Towards a magnetic semiconductor using Ca and Y co-substituted bismuth iron garnet thin films

Adrien Teurtrie

université PARIS-SACLAY

UNIVERSITÉ PARIS SUD
Comprendre le monde, construire l'avenir

NNT : 2019SACLS464

Thèse de doctorat

Towards a magnetic semiconductor using Ca and Y co-substituted bismuth iron garnet thin films

Thèse de doctorat de l'Université Paris-Saclay
préparée à Université Paris-Sud

École doctorale n°564 Ecole doctorale Physique en Ile-de-France (EDPIF)
Spécialité de doctorat : Physique

Thèse présentée et soutenue à Orsay, le 25/11/2019, par

ADRIEN TEURTRIE

Composition du Jury :

Agnès Bathélémy Professeure des Universités, Université Paris-Sud (Unité mixte de physique CNRS/Thales)	Présidente
Gianluigi Botton Professeur, McMaster University (Materials Science and Engineering)	Rapporteur
Nathalie Viart Professeure des Universités, Université de Strasbourg (Institut de Physique et Chimie des matériaux de Strasbourg)	Rapporteure
Amélie Juhin Chargée de recherche, CNRS (Institut de Minéralogie, de Physique des Matériaux et de Cosmochimie)	Examinatrice
Ulrike Lüders Directrice de recherche, CNRS (Laboratoire de Cristallographie et sciences des Matériaux)	Examinatrice
Alexandre Gloter Directeur de recherche, CNRS (Laboratoire de Physique des Solides)	Directeur de thèse
Elena Popova Ingénieure de recherche, CNRS (Groupe d'Etude de la Matière Condensée)	Co-directrice de thèse
Laura Bocher Chargée de recherche, CNRS (Laboratoire de Physique des Solides)	Co-encadrante de thèse

Contents

Chapter 1

Introduction

The oxide electronics is a fast growing field that already achieved high performances, for instance, in data storage units, solar cells or neuromorphic computing [1]. In this field, the transition metal oxides (TMO) have a central role. The presence of mixed-valence states, spin states, unpaired electrons, anisotropic $3d$ valence shells and a plethora of accessible structural symmetries make TMO highly versatile materials with tunable charge, spin, orbital and lattice orderings. These orderings and their interplay lead to a wide variety of interesting physical properties such as ferroelectricity, superconductivity and multiferroicity [2]. However, despite the richness of the TMO phases, the obtention of an oxide magnetic semiconductor (MS) suitable for applications at room temperature remains an unmet challenge to this date. A MS is a material where the charge carriers populate a spin-split band and induce the magnetic ordering [3]. Therefore, the control of magnetism is possible in a MS by modulating the concentration of charge carriers using an electric field in the same way as for conventional semiconductors [4]. Conversely, the control of the electrical properties is also possible by applying magnetic field. The development of such materials drew a lot of attention from the scientific community as it would drastically reduce the energy consumption of electronic devices. Coey [3] proposed a list of requirements for the MS to be suitable for applications at room temperature:

- A Curie temperature (T_C) above 500 K
- A coupling between the charge carriers and the magnetism
- The possibility to develop n- and p-type behavior
- A high mobility (>10 cm^2 V^{-1} s^{-1} [5]) and a long spin diffusion length (≈ 1 μm [6])
- The presence of a significant magnetic circular dichroism (≈ 1 deg μm^{-1})

- The presence of the anomalous Hall effect

To meet these requirements, both theoretical and experimental works have been carried out using two approaches: the dilute magnetic semiconductors (DMS) and the dilute magnetic oxides (DMO). Both approaches involve the doping of conventional semiconductors (e.g. GaAs for DMS) or semiconductor oxides (e.g. ZnO for DMO) with 3d magnetic cations such as Mn [7]. The successful coupling between charge carriers and magnetism and the subsequent physical properties was demonstrated in DMS only up to 190 K in (Ga,Mn)As [8]. On the other hand, DMO exhibit T_C of up to 850 K [9] but the magnetism in these materials is not coupled with the charge carriers and its origin is not fully understood yet [3]. To our knowledge, the only p-type magnetic semiconductor showing this coupling at room temperature was reported for $Co_{28.6}Fe_{12.4}Ta_{4.3}B_{8.7}O_{46}$ glass with a T_C of 600 K [10].

In this thesis, an alternative approach to obtain a material that is both magnetic and semiconductor has been developed where aliovalent and/or isovalent cations were substituted in an insulating oxide with robust magnetism to induce charge carriers. Bismuth iron garnet (BIG, $Bi_3Fe_5O_{12}$) is an insulating magnetic oxide with a T_C of 660 K [11] and a magnetization of 1600 G [12] resulting from the uncompensated magnetic moments between the tetrahedral and octahedral iron sublattices. BIG presents remarkable properties such as a giant Faraday rotation in the visible spectrum induced by the presence of Bi [13] and a linear magneto-electric coupling at room temperature [14]. Moreover, the calculated electronic density of states of BIG exhibits spin split states at the top of the valence band as well as at the bottom of the conduction band [15]. BIG has been chosen as a matrix to develop a MS as it already meets some of the requirements stated by Coey [3]. However, the growth of an iron garnet with a high concentration of Bi (> 2 Bi per formula unit) can only be achieved as an epitaxial thin film on an isostructural substrate. Yttrium (0.2 to 0.5 of Y per formula unit) and calcium (0.0 to 0.3 of Ca per formula unit) co-substituted BIG thin films, about 150-200 nm thick, have been synthesized by pulsed laser deposition (PLD) on gadolinium gallium garnet substrates. The Ca^{2+} substituted on the Bi^{3+} site is expected to induce $Fe^{3+/4+}$ that would lead to spin-polarized p-type conduction through the formation of holes at the top of the valence band. The substitution of a complementary amount of Y^{3+} on the Bi site should maintain a constant Bi content, i. e. $Bi_{2.5}$, to preserve the state-of-the-art magneto-optical properties of the films. The expected stoichiometry and charge distribution of the grown thin films are expressed :

$$Bi_{2.5}^{3+}Y_{0.5-x}^{3+}Ca_x^{2+}Fe_x^{4+}Fe_5^{3+}O_{12}^{2-} \text{ with } \{x = 0.0 \rightarrow 0.3\}$$

The electrical properties of Bi-rich iron garnets were not investigated previously and this work represents a first step towards the development of a MS based on BIG. The aim of this thesis is then to achieve the successful substitution of Ca and Y in the garnet matrix to improve the transport properties of BIG while preserving its functional properties such as the giant Faraday rotation. These goals can be formulated more specifically with the following questions:

- What is the impact of the co-substitution on the structural and microstructural properties ? What is the distribution of Ca and Y in the thin films ?
- Does the Ca and Y co-substitution improve the electrical transport properties of BIG ? How is the electronic structure of BIG changed upon the substitution ?
- How are the magnetic and magneto-optical properties of BIG influenced by the substitution ?

To answer these questions, the exploration of physical and structural properties of the thin films was carried out using a combination of macroscopic physical techniques, e.g. X-ray (XMCD) and optical (Faraday rotation) magnetic circular dichroisms, and of transmission electron microscopy (Cs-STEM) and with electron energy-loss spectroscopy (EELS) techniques. Coupling electron spectroscopy and microscopy techniques allows to study both the integration of the dopants into the garnet lattice and the charge compensation mechanisms down to the atomic scale.

The presentation of this work is divided into 6 chapters:

In the next chapter, the main elements showing that BIG is a promising base compound for the development of a MS are presented. We start by describing the growth of pure BIG thin films and their structural and physical properties. After a description of the molecular orbitals models that attempted to explain the origin of the giant Faraday rotation in BIG, we focus on the electronic density of states of BIG calculated by Federico Iori and with whom I collaborated. Then, the expected effect of Ca and Y co-substitution on the electrical and magnetic properties of BIG are detailed. This chapter ends by a review of the electrical properties of doped yttrium iron garnets

($Y_3Fe_5O_{12}$, YIG) that can be seen as reference systems due to the absence of literature on the electrical properties of Bi-rich iron garnets.

In the third chapter, we present the experimental and data analysis tools as well as a methodological development achieved during this thesis. In a first part, we detail the PLD setup used to grow the thin films and the experiments performed to measure their macroscopic physical and structural properties. The experimental techniques used to probe the microscopic properties of the thin films such as Cs-STEM/EELS are presented afterwards. In a second part, the data analysis techniques used to process the spectro-microscopy data are described. In a third part, we develop and test a clustering method to refine further the analysis of the Cs-STEM/EELS data.

The fourth chapter is composed of two parts. In the first one, we present the structural and the microstructural properties of the thin films. Afterwards, the distribution of Ca and Y dopants were studied using Cs-STEM/EELS to determine the solubility of the dopants within the garnet matrix.

In the first part of the fifth chapter, the electrical resistivity and thermopower of the thin films are investigated. The second part is devoted to the effect of the atmosphere and the temperature on the transport properties. In the third part, the charge distribution is first probed at the nanometric scale using spectro-microscopy techniques and the analysis is further refined down to the atomic scale using a combination of STEM/EELS and XMCD.

In the sixth chapter, we focus on the modification of the magneto-optical properties upon the substitution of Ca and Y. The evolution of the Curie temperature and of the magnetic anisotropy of the thin films were also investigated.

In chapter seven, we conclude by determining which of the requirements stated above are met. Perspectives on future work that is desirable to carry out after this study are then given.

Chapter 2

Iron garnets

In this thesis we aim to develop a material combining robust magnetism and a semiconductor conductivity at room temperature by substituting aliovalent and/or isovalent cations in a magnetic insulator to induce charge carriers. The Bi-rich iron garnets were chosen to achieve this goal because of their giant Faraday rotation and spin-split bands. In this chapter, the structural and magnetic properties of BIG are presented. After a short introduction of the magneto-optical (MO) effects and their origin in magnetic materials, the two molecular orbitals models attempting to explain the origin of the giant Faraday rotation in BIG are presented. The electronic density of states of BIG calculated by Federico Iori in relation with the present work is presented to demonstrate the presence of spin-split bands and further clarify the origin of the giant Faraday rotation. Then, the expected effect of Ca and Y co-substitution on the electrical and magnetic properties of BIG are described. Finally, the electrical properties of semiconductor doped YIGs are reviewed as reference systems due to the absence of literature on the electrical properties of Bi-rich iron garnets.

2.1 Bismuth iron garnet

The iron garnets are magnetic oxides with the following formula unit $R_3Fe_5O_{12}$ with e.g. R= Y, Lu, Yb, Gd. For instance, YIG was studied for its exceptionally long spin diffusion length [16]. It was evidenced in the 70s that the substitution of Bi in iron garnet yields a large increase of the Faraday rotation [17]. The commonly used technique to grow iron garnet thin films, liquid phase epitaxy (LPE), can only achieve $Y_{3-x}Bi_xIG$ films with $x \leq 2.3$ [18] which prevented the growth of highly Bi-substituted iron garnet thus limiting the maximum reachable Faraday rotation. Nevertheless, BIG thin films were grown for the first time by Okuda et al. [19] and Satoh et al. [20] in 1990 by reactive ion-beam-sputtering (RIBS) on a garnet substrate. The growth

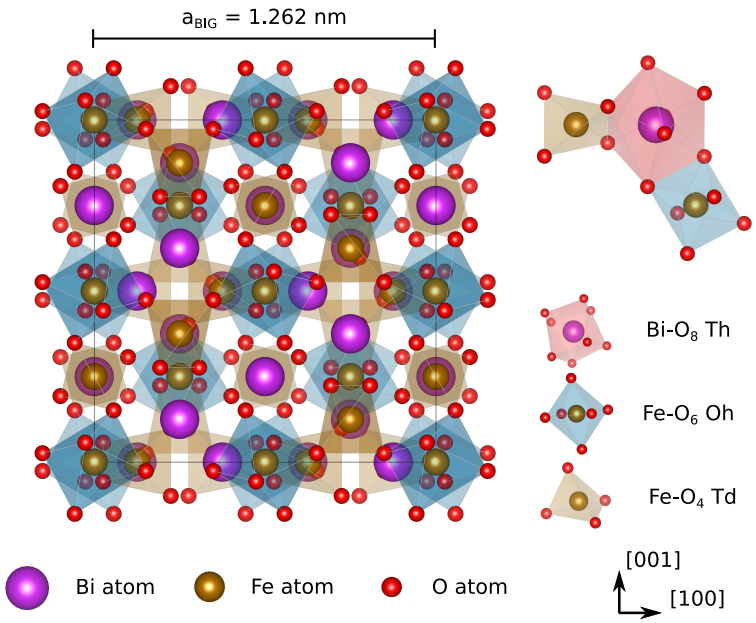

FIGURE 2.1: Representation of the theoretical unit cell projected along the [010] axis with the lattice parameter indicated on top. The Bi, Fe and O atoms are depicted in purple, brown and red respectively. An arrangement of Bi T_h site, Fe O_h site and Fe T_d site is shown at the top right corner. The T_h, O_h and T_d polyhedra are depicted in red, blue and brown, respectively.

of BIG is very recent since it can only be obtained in the form of thin films on isostructural substrates and mostly by out-of-thermodynamical equilibrium techniques such as RIBS, PLD [21, 22] or radio-frequency sputtering [23]. The only exception so far is the work of Jesenska et al. [24] in which the growth of BIG by metal organic decomposition is reported. During the BIG growth by PLD, Bi is a volatile element whose integration into the garnet structure is partly driven by the partial oxygen pressure (PO_2) in the growth environment. A single BIG phase is obtained in a narrow PO_2 range in between a few mTorr and a dozen mTorr depending on the growth chamber and on the oxygen injection method. For PO_2 above 30 mTorr, $BiFeO_3$ and $Bi_2Fe_4O_9$ secondary phases form [25, 12] while for PO_2 below 5 mTorr the formation of an unidentified secondary phase was reported by Kahl et al. [26]. The other important parameters that influence the integration of Bi in the iron garnet matrix are the fluence of the laser, the substrate temperature and the PLD target stoichiometry. For instance, stoichiometric BIG presents a Bi/Fe ratio of 0.6 which is obtained using PLD for Bi/Fe ratios of the target of $0.6 \leq \text{Bi/Fe}_{\text{target}} \leq 0.7$ [12].

2.1.1 Structural and physical properties of BIG

It is possible to grow single BIG phase by PLD with high structural quality [21] with a careful adjustment of the growth parameters. However, the experimental crystallographic structure of BIG is currently unknown due to the absence of bulk BIG [1]. As most iron garnet phases, BIG is expected to crystallize in the $Ia\bar{3}d$ cubic space group with a lattice parameter of 1.262 nm [21]. As shown in Fig. 2.1, there are three cations sublattices in the conventional unit cell that is made of 8 formula unit.

- 24 Bi sites surrounded by 8 O anions forming a dodecahedral (T_h) cage
- 24 Fe sites surrounded by 4 O anions forming a tetrahedral (T_d) cage
- 16 Fe sites surrounded by 6 O anions forming a octahedral (O_h) cage

In stoichiometric BIG, considering in first approximation that cations have an ionic character, they all have 3+ valency. Bi^{3+} ions have $6s^2$ closed shell and behave rather diamagnetically. Conversely, Fe^{3+} ions have $3d^5$ half-filled shell and have a high magnetic moment of 4.4 μ_B [2] [25] corresponding to the high-spin configuration. In iron garnets, the Fe T_d sublattice and the Fe O_h sublattice are antiferromagnetically coupled and the uncompensated magnetic moments of the 8 additional Fe T_d give rise to the macroscopic ferrimagnetism. BIG exhibits a strong magnetism with a saturation magnetization (M_s) of about 1600 G at 300 K [12] and a high Curie temperature (T_C) of around 660 K [11] (Fig. 2.2). These values are comparable to YIG thin films that exhibit a magnetization of 1800 G at room temperature and a T_C of 560 K [27]. The reduced dimensionality of thin films tends to put their easy magnetization axis parallel to the film/substrate interface, i.e. in-plane. Indeed, the easy magnetization axis of BIG thin films was reported to be in-plane for hundreds of nm thick films grown onto [001] oriented garnet substrates [28, 25].

The electrical transport properties of BIG were not investigated previously but its optical band gap of 2.3 eV [29] strongly suggests that BIG is an insulator. For comparison, YIG exhibits an optical band gap of 3.0 eV [30]. Recently, a linear magneto-electric coupling at room temperature was evidenced in undoped BIG [14] which is three orders of magnitude higher than the one of YIG [31].

[1] The crystallographic structure of BIG thin films might present a slight symetry breaking due to an effect of the substrate.

[2] μ_B is the Bohr magneton

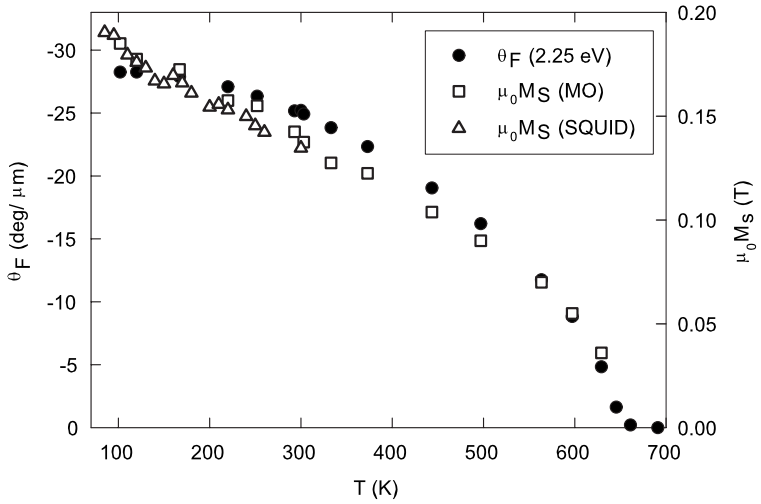

FIGURE 2.2: Temperature dependence of the Faraday rotation measured at 2.25 eV, of the saturation magnetization, and of the saturation magnetization measured by superconducting quantum interference device for a BIG thin film. This figure is adapted from ref [11]

As stated previously, BIG has motivated a large number of studies mainly because it possesses a giant Faraday rotation (θ_F) in the visible range with, for instance, $-17\,\mathrm{deg}\,\mu\mathrm{m}^{-1}$ at 550 nm [32, 24, 11, 29]. For comparison, YIG exhibits only around $0.3\,\mathrm{deg}\,\mu\mathrm{m}^{-1}$ at the same wavelength [33, 34]. The possibility to develop efficient magneto-optical photonic crystals [12, 35] and optical isolators [36] based on BIG systems has been already investigated successfully.

2.1.2 Origin of the giant Faraday rotation

In this section, we discuss the different proposed theoretical models describing the origin of the large increase of Faraday rotation in Bi-substituted YIG ($Y_{3-x}Bi_xIG$). The effect of a Bi substitution of 0.25 per f.u. on the MO properties of $Y_{2.75}Bi_{0.25}IG$ is shown in Fig. 2.3 (a) and the contribution of Bi is shown as the difference spectrum between $Y_{2.75}Bi_{0.25}IG$ and YIG [37]. This difference spectrum is compared to the normalized spectrum of BIG in Fig. 2.3 (b). Apart from the already observed red shift of the BIG spectrum [38] compared to $Y_{3-x}Bi_xIG$, the two spectra exhibit very similar features. These similarities imply that the conclusions drawn from the study of $Y_{3-x}Bi_xIG$ can be applied to BIG. Before describing these models we recall the definition of MO effects and their microscopic origin in materials.

[3] ϵ_1' (Fig. 2.3 (a), y axis)refers to the real part of the off-diagonal term of the dielectric tensor which is proportional to θ_F.

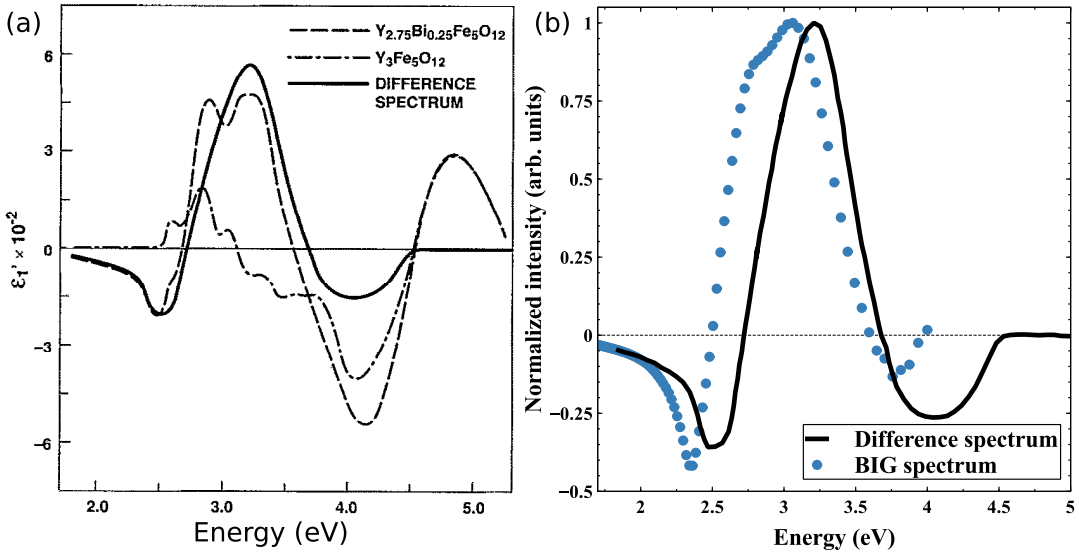

FIGURE 2.3: a) MO spectra [3] of $Y_{2.75}Bi_{0.25}IG$ (dashed line) and YIG (dotted dashed line) and difference spectrum between the ones of $Y_{2.75}Bi_{0.25}IG$ and YIG. b) Comparison between the normalized difference spectrum of (a) and the measured Faraday rotation spectrum of BIG. This figure is adapted from ref [37]

Origin of the MO effects

Magnetic circular dichroism (MCD) is the differential absorption measured between left (LCP) and right (RCP) circularly-polarized light induced in a material by a magnetic field oriented parallel to the direction of the light propagation. It occurs in paramagnetic or diamagnetic materials under the application of a magnetic field ($\vec{H}$) that breaks the time-reversal symmetry [39]. In a ferromagnetic or a ferrimagnetic material an additional internal field $\vec{H} = \vec{H}_{ext} + \mu_0\vec{M}(\vec{H})$ strengthens the MCD intensity.

In the visible spectrum, the MCD is at the origin of the MO Faraday effects: the Faraday ellipticity (ϵ_F) and the Faraday rotation (θ_F) that are linked by the Kramers-Kronig relations. For the sake of clarity, we mainly discuss the θ_F here since similar information can be drawn from ϵ_F and θ_F. The θ_F is the rotation of linearly-polarized light going through a material [4]. The rotation angle of the polarization is proportional to the film thickness and to the magnetic field strength. The Faraday rotation intensity can thus be quantitatively described for a ferrimagnetic material by the θ_F expressed in degree per micrometer at magnetic saturation [5].

[4] We recall here that linearly-polarized light is the sum of right and left circularly-polarized light. A phase difference between right and left circularly-polarized light results in the rotation of the linearly-polarized light axis by an angle of half the phase difference.

[5] We consider here that the optical absorption is negligible compared to the magnitude of MO effects.

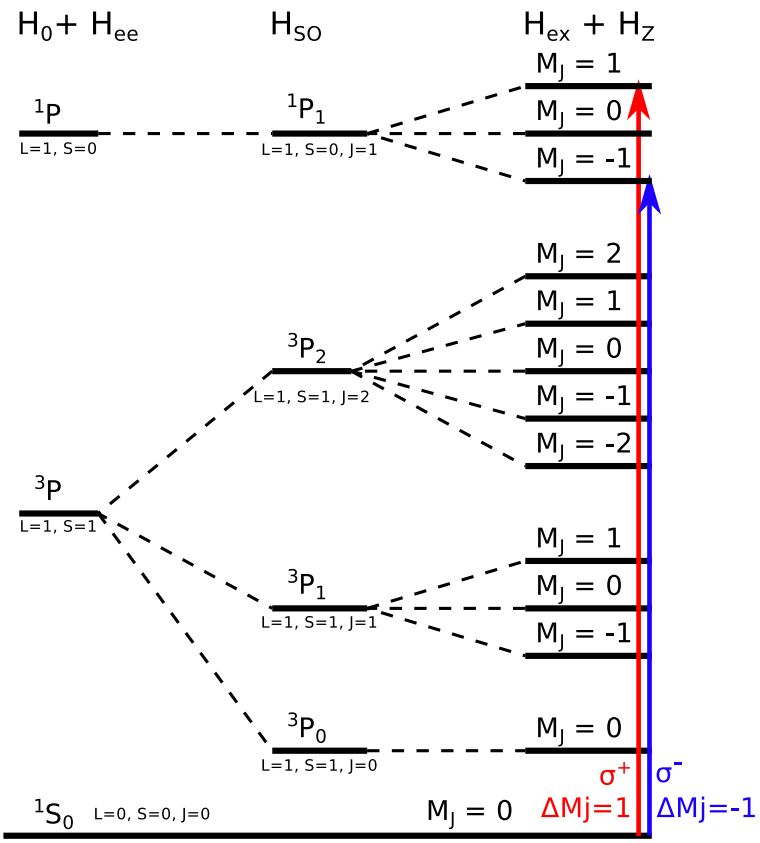

FIGURE 2.4: Atomic energy levels ($H_0 + H_{ee}$) split by the exchange interaction (H_{ex}), the SO interaction (H_{SO}) and the applied magnetic field ((H_Z). An example of two transitions with opposite circular polarization are displayed in red (RCP, σ^+) and blue (LCP, σ^-).

At the microscopic level, the origin of the MCD and thus the Faraday rotation results from an absorption difference between transitions with $\Delta m_J = \pm 1$. By convention, the LCP light is absorbed for $\Delta m_J = -1$ while the RCP light is absorbed for $\Delta m_J = 1$. As a simple example, we describe here the case of a dipolar transition with RCP and LCP light from a $1s^2$ ground state to $1s^1 2p^1$ excited states ($\Delta m_J = \pm 1$, $\Delta L = 1$ and $\Delta S = 0$) as depicted in Fig 2.4. The $1s^2 s$ ground state has a $^1S_0$ term ($L = 0$, $S = 0$ and $J = 0$) while the $1s^1 2p^1$ term has a $^1P_1$ term ($L = 1$, $S = 0$ and $J = 1$) and $^3P_{0,1,2}$ terms ($L = 1$, $S = 1$ and $0 \leq J \leq 2$). Due to the spin parity conservation only the transitions to the $^1P_1$ term are allowed. However, the $^3P_{0,1,2}$ are still shown to illustrate the effect of the spin-orbit (SO) interaction.

In the frame of atomic multi-electronic states, the high θ_F value originates from a strong splitting of the orbital momenta states, this splitting is driven by the following interactions :

$$H = H_0 + H_{ee} + H_{ex} + H_{SO} + H_Z \tag{2.1}$$

Here H_0 is the atomic hamiltonian with a spherical potential [6] and H_{ee} is the non-spherical part of the interaction between the electrons. These parts of the hamiltonian yield the ^{2S+1}L terms. H_{ex} is the exchange interaction that leads to the splitting of states according to their spin value. It should be noted that H_{ex} acts only on the spin part of the states and is not at the origin of MCD even though H_{ex} increases its intensity. H_{SO} is the spin-orbit Hamiltonian and leads to the additional splitting of the states in the $^{2S+1}L_J$ terms. H_Z is the Zeeman interaction that is responsible for the splitting of the orbital momenta m_J at the origin of the MCD. This simple atomistic description highlights the influence of the exchange and the SO interactions on the Faraday rotation for a given applied magnetic field.

At the macroscopic level, θ_F can be described by off-diagonal elements of the dielectric tensor (often called the gyration vector) that can be calculated from the MO transitions. When an energy difference between σ^+ and σ^- transitions is at the origin of the MCD, the corresponding MO transition is called a diamagnetic [7] transition. The two transitions highlighted in Fig. 2.4 yield the θ_F and ϵ_F spectra as shown in Fig. 2.5 (a) and (b), respectively. Any MO spectrum, even coming from a more complex ground state, will exhibit similar Δm_J selection rules among multiplet lines and can be decomposed as the linear combination of such curves (Fig. 2.5). Thus, the experimental Faraday rotation spectrum of a BIG thin film, displayed in Fig. 2.5 (c), can be well fitted by the contributions of two diamagnetic transitions. Such a model using the dielectric tensor is a very general theoretical framework that yields an accurate description of MO spectra and can be applied to any material. The challenge is then to determine the correct ground and excited states of the studied material.

Origin of the MO effects in Bi-substituted iron garnets

Considering now the atomic ground state of a Fe $3d$ in the high-spin configuration, it yields the LS term $^6S_{5/2}$ from Hund's rule. In BIG, this state becomes $^6A_{1g}$ and $^6A_1$ when the contributions from the crystal field of Fe-O_6 (O_h) and Fe-O_4 (T_d) are added, respectively. These states have $< L >= 0$ which implies that the excited states are mainly responsible for the high θ_F. In particular, it has to be mentioned that BIG and YIG have similar $^6A_{1g}$ and

[6] The approximation here is that H_0 is the sum of single particle hamiltonians.

[7] This name was attributed for historical reasons and is not linked to the magnetic behaviour of the probed material [39].

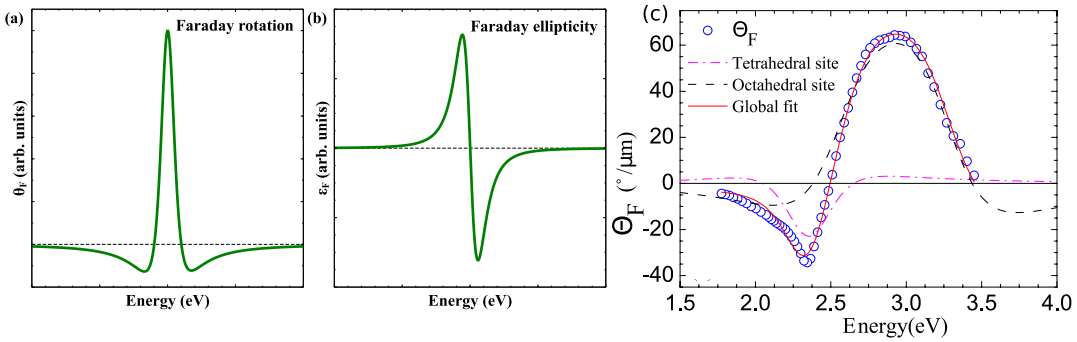

FIGURE 2.5: a) Theoretical Faraday rotation spectrum for a MO diamagnetic transition. b) Theoretical Faraday ellipticity spectrum for a MO diamagnetic transition. c) Experimental Faraday rotation spectrum of BIG (blue circles) with its corresponding theoretical model (red line) using two MO diamagnetic transitions. The black dashed and purple dashed dotted lines correspond to the octahedral and tetrahedral components of the theoretical model, respectively. This figure is adapted from ref [13].

$^6A_1$ ground states. However, the origin of the large increase of Faraday rotation upon Bi substitution in YIG is still controversial and thus have been discussed in the frame of two different molecular orbital theories [40, 41].

Dionne and Allen's [40] main interpretation is based on the direct hybridization of Fe $3d$ with Bi $6p$ that would be responsible for the increase in θ_F upon Bi substitution in iron garnets. The Fe atomic excited states (^4P) are split by the crystal field into $^4T_{1g}$ and $^4T_1$ states for O_h and T_d, respectively. The covalency between Fe $^4T_{1g}$ and $^4T_1$ states and Bi atomic excited states (^3P) yields the hybridized anti-bonding and bonding states. More precisely, only the Fe $^4T_{1g}$ and $^4T_1$ which are quenched by the exchange interaction to $m_s = -\frac{3}{2}$ are considered in this analysis due to their lower energy. These states, after hybridization with Bi $6p$, correspond to the bonding states (Φ_{Td} and Φ_{Oh} in Fig. 2.6). Their orbital moments $m_l = (-1, 0, 1)$ are further split due to the SO interaction. The effective SO interaction of the Fe $^4T_{1g}$ and $^4T_1$ states is further increased due to the hybridization with the Bi ^3P states. In this framework, the role of oxygen is considered only as a correction to the energy of the Fe atomic states and the transitions are thus mostly of intra-d shell type. The difference between BIG and YIG is then mostly related to the direct hybridization between Bi and Fe. Then, in Dionne and Allen's [40] interpretation, only two diamagnetic transitions are then needed to explain the Faraday rotation spectrum of BIG in the visible range, one for each Fe sublattice as shown in Fig. 2.6. This approach was used by many authors [37, 13, 42, 29, 43] to describe their experimental spectra.

Zenkov and Moskvin [41] consider the charge transfer transitions from the O $2p$ band to the Fe $3d$ band in both Fe-O_6 and Fe-O_4 clusters. The ground

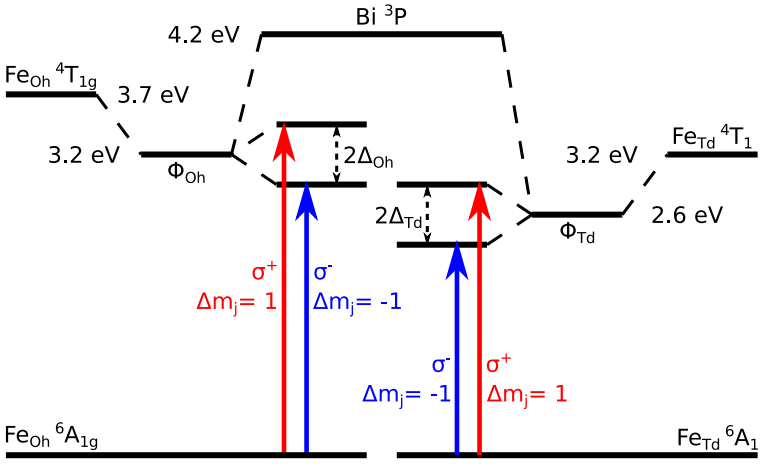

FIGURE 2.6: Theoretical energy levels scheme of Bi-substituted YIG as derived by Dionne and Allen [40]. The Fe$_{Oh}$ $^4T_{1g}$, Fe$_{Td}$ $^4T_1$ and Bi ^3P correspond to the Fe and Bi states before taking into account the hybridization between Fe and Bi orbitals. The four arrows correspond to two diamagnetic transitions ($\Delta m_j = \pm 1$) from the Fe$_{Oh}$ $^6A_{1g}$ and Fe$_{Td}$ $^6A_1$ states to the hybridized bonding states Φ_{Oh} and Φ_{Td} that are split by $2\Delta_{Oh}$ and $2\Delta_{Td}$ SO energies. This figure is adapted from ref. [40].

state is then $3d^5$ ($t_{2g}^3 e_g^2$ [8]) where the oxygen p orbitals are fully filled. The excited states have the configuration $\underline{L}_{2p} - 3d^6$ where $\underline{L}$ is the ligand hole. The $3d^6$ term is either $t_{2g}^4 e_g^2$ noted t_{2g} or $t_{2g}^3 e_g^3$ noted e_g depending if the additional electron goes in the t_{2g} or the e_g state, while the $\underline{L}_{2p}$ terms allowed by symmetry are for instance t_{2u} or t_{1u} [44]. A total of 13 allowed excited states in terms of selection rules and symmetry for the transitions from the $^6A_1$ and $^6A_{1g}$ ground states were reported by Zenkov and Moskvin [41]. Some of these transitions are listed in table 2.1 for the Fe-O_6 cluster. In this approach, the hybridization of Bi $6p$ orbitals with O $2p$ and Fe $3d$ orbitals yields excited states with enhanced effective SO noted ξ_{2p} and ξ_{3d}, respectively (see table 2.1). Thus, the increase in θ_F when substituting Bi in iron garnets is mainly originating from the ligand hole states with enhanced SO ξ_{2p} as a result of its stronger hybridization with Bi $6p$. This interpretation of the multiplet structure of Bi-substituted iron garnets was suggested earlier by several authors [45, 46, 47, 48] without a full theoretical modelisation. Since transitions from molecular orbitals of primarily ligand type are taken in account, the resulting multiplet states are numerous and the modelization of experimental spectra is a complex task. This approach was only applied to a few experimental spectra by Zenkov and Moskvin [41].

These calculations have already shown their utility for the analysis of experimental spectra [13], however the molecular orbital theory does not take

[8] e_g and t_{2g} are linear combination of 3d atomic orbitals that have the symmetry of the octahedral crystal field.

CT transitions	Effective spin-orbit coupling	Energy (eV)
$t_{2u} - t_{2g}$	$0.1\xi_{3d} + 0.05\xi_{2p}$	2.78
$t_{1u}(\pi) - t_{2g}$	$-0.1\xi_{3d} + 0.05\xi_{2p}$	3.6
$t_{2u} - e_g$	$-0.05\xi_{2p}$	4.3
$t_{1u}(\sigma) - t_{2g}$	$-0.1\xi_{3d}$	4.8

TABLE 2.1: Part of the magneto-optically active transitions in the octahedral cluster for Bi doped YIG. This table is adapted from the work of Zenkov and Moskvin [41].

into account the precise band structure of BIG. Density functional theory (DFT) calculations were carried out first by Oikawa, Suzuki, and Nakao [49] and more recently in relation with the present thesis work with Iori et al. [15] to find an even more accurate approach to describe and discriminate in between the two previous ones.

2.1.3 Calculated electronic structure

DFT is a theoretical framework for the computation of the ground state of many-body systems such as solids [50]. It is important to determine the ground state or density of states (DOS) as it represents the first step towards the understanding of the physical properties of a material such as MO spectra. The common approximations used by DFT to treat the many-body problem are the local density approximation (LDA) and the generalized gradient approximation (GGA). The LDA treat electrons as if they behaved like an homogeneous electron gas which is a good approximation for free electrons like in metals. The GGA is similar to a Taylor expansion of the homogeneous electron gas. These approximations do not yield accurate DOS in TMO since the $3d$ electrons are strongly correlated as they have both a ionic character (atomic like) and a covalent character (metal like) [9]. For instance, LDA and GGA tend to underestimate the band gap or even predict metallic DOS in insulators. To overcome this issue, a parameter U is introduced which corresponds to the energy of on-site Coulomb repulsion. U allows a better treatment of the ionic character of $3d$ electrons and in TMO a value of $U = 4eV$ usually yields good results [51]. An other approach is to use hybrid functionals [52] that compute a part of the many-body hamiltonian without approximations and the other part is computed using GGA which yields improved results at the cost of heavy computations.

[9] This mixing between ionic and covalent character is the hardest issue to solve in many-body physics. Theoretical approximations are much more efficient at treating fully ionic or fully covalent electrons.

BIG was first investigated using LDA and taking into account the effect of the spin-orbit coupling (SOC) [49] since Bi carries a very strong SO. In the present work, the DOS of BIG is further investigated using more sophisticated theoretical tools. The DOS calculated with hybrid functional is described first (Fig. 2.7). In this case the SOC is not taken into account as it reduces the symmetry of the systems and thus significantly extend the computing time. Then, the impact on the DOS of the U value is tested (Fig. 2.8) using GGA+U to better understand the effect of the electronic correlations. The effect of the SOC on the DOS calculated with GGA+U+SOC is discussed last (Fig 2.9). These results are compared with the calculation of the electronic structure of YIG using LDA+U [53] to highlight the effect of Bi in the iron garnet matrix.

BIG density of states

In the hybrid functional framework (Fig. 2.7 (a)), most of the occupied Fe 3d states and some O $2p$ states lie in between -7.5 eV and -6 eV separated from the valence band ranging from -6 eV to 0 eV that is characterized by a mixing of O $2p$, Bi $6s$ and Fe $3d$. The relatively strong exchange splitting of the top of the valence band mostly composed of Bi 6s and O $2p$ is a key figure of the BIG electronic structure (Fig. 2.7 (b)). This feature was not present in the calculated YIG electronic structure [54]. Such spin-splitting could contribute to the θ_F intensity as a ligand hole excitation. This hypothesis considers the same type of MO excitations as Zenkov and Moskvin [41] but with a different physical origin based on the exchange splitting rather than on the SO splitting of the O $2p$ states hybridized with Bi $6p$. It should be noted that in the specific case of hole doping, this spin-splitting at the top of the valence band could lead to a Fermi level with a strong spin polarization.

Considering now the conduction band, from 3eV to 5eV, it is dominated by the spin polarized Fe $3d$ similarly as in the work of Oikawa et al. [49]. The crystal field effects split the Fe $3d$ in a triple degenerate t_{2g} states and in doubly degenerate e_g states with different hierarchy for both sub-lattices. The clear separation of Fe $3d$ bands for the spin-up conduction band is due to a stronger O_h crystal field. For the minority spin, instead, the T_d crystal field is not strong enough to separate the e_g/t_{2g} contribution in the unoccupied part. This important difference of crystal field strengths for the O_h and the T_d symmetry was also experimentally reported in the case of YIG. Based on an analysis of the d-d optical transitions, a crystal field splitting of 1.52eV and 0.77eV in YIG were derived for the O_h and the T_d sites, respectively [55].

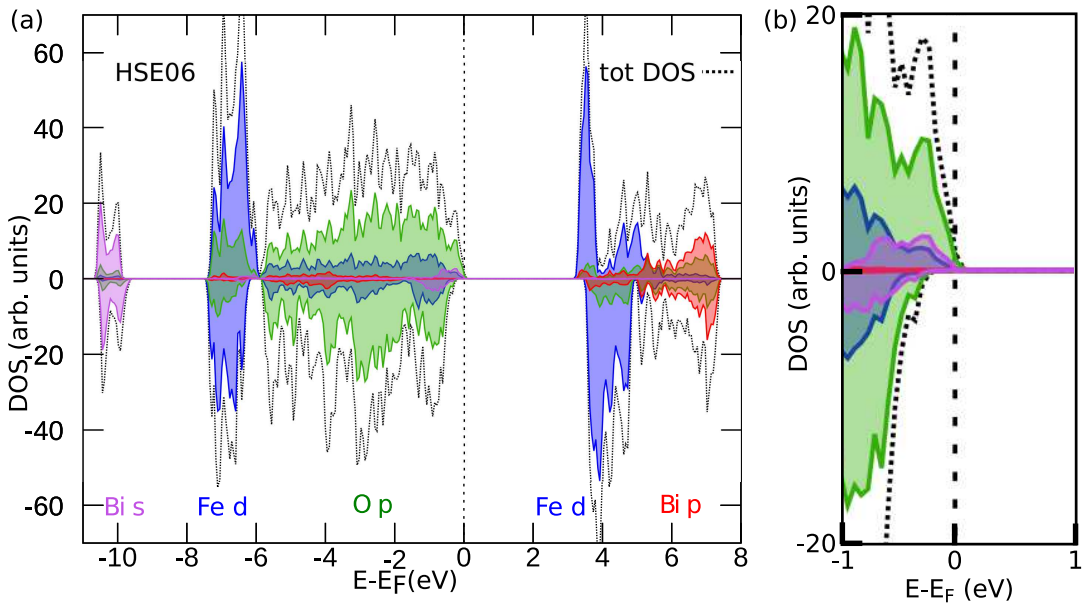

FIGURE 2.7: a) Hybrid functional calculation of the total DOS and the projected DOS. The different projected angular moment channels shown correspond to: Bi 6s in lilla, Fe 3*d* in blue, O 2*p* in green, Bi 6*p* in red. b) Zoom around the Fermi level of (a). This figure is adapted from Iori et al. [15].

The geometry of BIG [10] is at the origin of the 100% spin-polarized DOS that occurs at several energies in the DOS, e.g. around -6 eV, 0 eV, 3 eV and 4 eV. These spin gaps play an important role on the MO effects [32].

Effect of U

Therefore, the effect of the correlations U (from 0 eV to 4.5 eV) on the calculated spin gaps have been investigated (Fig. 2.8). In the valence band the iron 3*d* states are shifted downward in energy to around -7 eV for $U = 4eV$ and the top of the valence band becomes spin-split. In the conduction band, the spin gaps observed at the three energies A,B and C (Fig. 2.8 upper scheme with U=0) in the DOS tend to disappear for U above 2-3 eV. For the valence band, U aids to correct the delocalization error of pure DFT while for the conduction band it seems to induce a spurious artefact in the correct description of the hybridization between oxygen and the Fe states [56]. Such a spurious disappearance of the spin gaps for moderate U values might bias future first-principle calculations of the optical properties (e.g. θ_F). It would require the utilisation of hybrid functional that are much more demanding in terms of computation time.

[10] In BIG, the minority spin is in pure O_h site and majority spin is in pure T_d site for the occupied band.

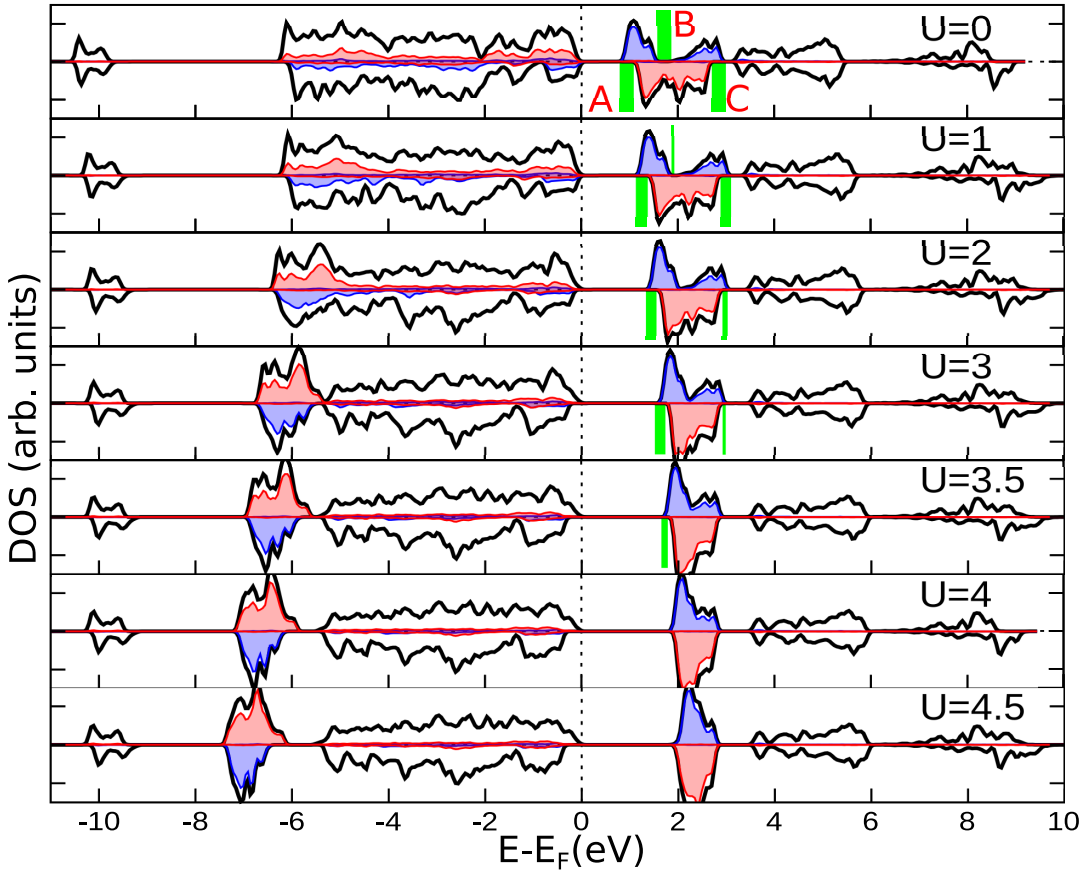

FIGURE 2.8: Evolution of the Fe 3*d* states (Fe O_h in blue and Fe T_d in red) and of the exchange splitting gaps (A,B,C - green lines) for U ranging from 0 eV to 4.5 eV. The total DOS is reported as reference in solid black line for each U. This figure is adapted from Iori et al. [15].

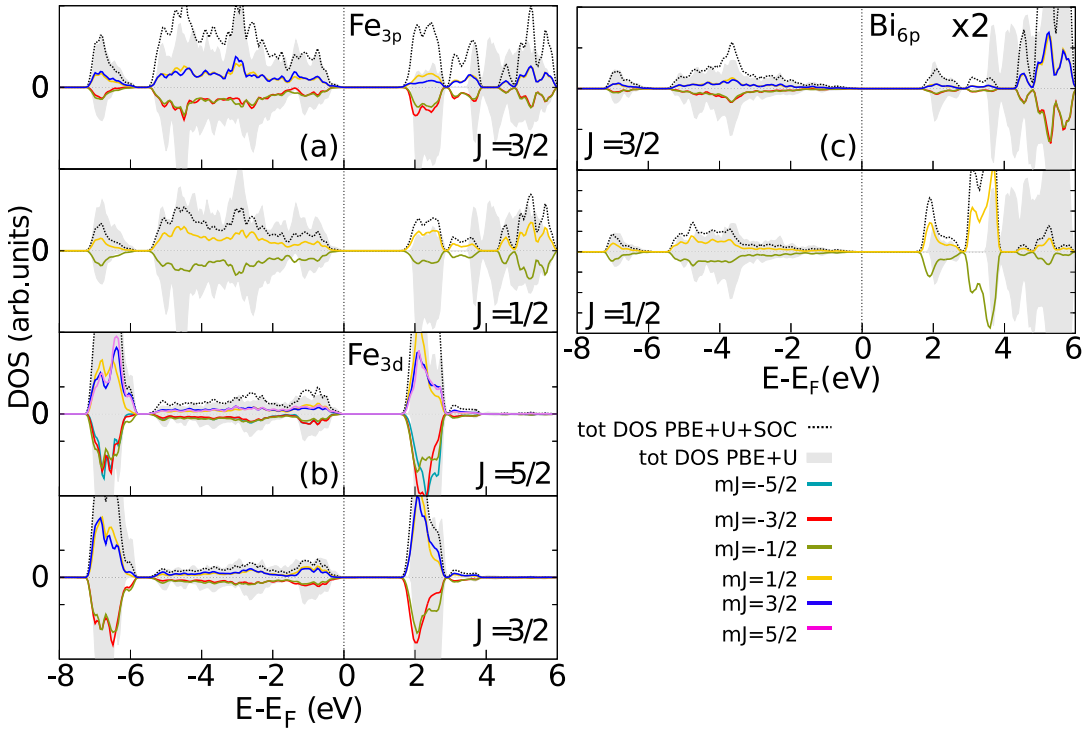

FIGURE 2.9: In panel a) the Fe $3p$, in panel b) the Fe $3d$, in panel c) the Bi $6p$ are the projected DOS for DFT+U and DFT+U+SOC. In each panel the total DOS for DFT+U and for DFT+U+SOC appear in grey and as dotted black line, respectively. The total l-resolved DOS per element (dotted black line) is the sum of all the corresponding m_j projections (solid coloured lines). This figure is adapted from Iori et al. [15].

Effect of the SO

Above 3 eV, the conduction band is mostly composed of Bi $6p$ states. These states have a very strong SO interaction and its effect has been evaluated by GGA+U+SOC. The atom-projected GGA+U DOS and the GGA+U+SOC DOS projected for different value of m_J are compared in Fig. 2.9. The SOC affects mainly the Bi $6p$ and only slightly the Fe $3p$ and Fe $3d$. In the GGA+U calculations (Fig. 2.8), the Bi $6p$ states were spanning from 3 to 6 eV. In contrast, the GGA+U+SOC calculated DOS results in a Bi $6p_{1/2}$ spanning from to 2 to 4 eV and the Bi $6p_{3/2}$ from 4 to 7 eV. The Fe $3p$ and Fe $3d$ state are then more hybridized with the Bi when the SOC is included via the Bi $6p_{1/2}$ states. The SO effect of Fe d states is instead very soft. In the Fe $3d$ valence band the SO splitting is 50 meV, while in the conduction band it is around 25 meV which is in good agreement with the experimental and calculated values reported by Oikawa et al. [49]. These results tend to support the idea of Dionne and Allen [40] that a part of the θ_F increase in BIG compared to YIG might be driven by the hybridization of Bi $6p$ with Fe $3d$ in the conduction band.

Conclusions

The strong splitting of the O $2p$ states at the top of the valence band in addition to the multiple spin gaps in the conduction band tends to favour the interpretation of the MO effects in BIG given by Zenkov and Moskvin [41] over the one given by Dionne and Allen [40]. In addition, the band structure calculation evidences a clear $p-d$ [11] band gap for BIG that is in line with the suggested charge transfer MO transitions from the work of Zenkov and Moskvin [41].

The two electronic structures of YIG and BIG have been schematized in Fig. 2.10 to better interpret the major difference in the Faraday rotation observed between both iron garnets. Spin gaps and SO coupling are already present in the electronic structure of YIG associated with the Fe $3d$ states. In the case of BIG, the exchange splitting of the valence band and the hybridization with the SO split Bi band appears. Based on these results, DFT calculation of the dielectric tensor for both BIG and YIG phases should bring further elements to discriminate between the theories of Zenkov and Moskvin [41] (Strong SO in ligand hole type excitations) and of Dionne and Allen [40] (direct Bi-Fe hybridization in final states) and bring new insight to understand the origin of the giant Faraday rotation in BIG. To calculate the Faraday rotation, the SOC and the non-diagonal elements of the dielectric tensor have to be computed. Unfortunately, combining the calculation of these quantities with the electronic correlations correction and the large number of atoms per formula unit of the garnet structure is out of the scope of this thesis work.

In addition to the magneto-optical properties, it is important to emphasize the presence of a spin-polarized DOS at the top of the valence band and at the bottom of the conduction band in the electronic structure of BIG. Taking advantage of this particularity of the electronic structure while inducing a semiconductor behavior in BIG opens interesting perspectives for the development of spintronics devices operating at room temperature.

2.2 Ca and Y co-substituted BIG

2.2.1 Improving the electrical properties of BIG

Its strong magnetism and its giant Faraday rotation make BIG a potential candidate as a multifunctional material for oxide-based electronics. However, stoichiometric BIG is expected to be an insulator similarly as YIG (10^{12} Ω cm

[11] A $p-d$ transition is a charge transfer transition.

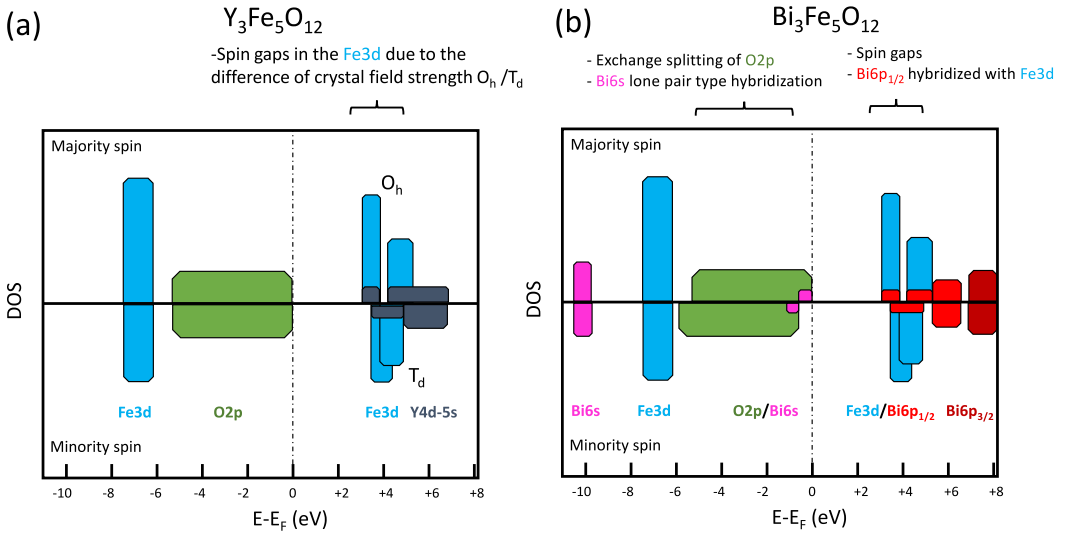

FIGURE 2.10: Schematic density of states of a) YIG adapted from [53] and of b) BIG adapted from Iori's calculations [15]. The main features and differences are indicated.

at 300 K) [57]. Tailoring BIG transport properties from insulator to n- and p-type semiconductor will provide new prospectives of integration into magneto-plasmonic structures or spin-polarized BIG-based heterostructures. In this thesis, we focus on enhancing the electrical properties of substituted-BIG phases by applying a site-selective co-substitution of Ca^{2+} and Y^{3+} in do-decahedral Bi sites. This will aim at combining in a single oxide material a relatively high electrical conductivity and a robust magnetism at 300 K while preserving its initial functionalities [58]. Ca substitution aims at improving the electrical conductivity of BIG via the introduction of hole charge carriers. According to Iori et al. [15] (Fig. 2.11), Ca should be at the origin of an almost 100% spin polarized density of states at the Fermi level. The expected mech-anism is the formation of $Fe^{3+/4+}$ mixed valence states leading to a p-type spin-polarized conduction:

$$Bi^{3+}_{2.5}Y^{3+}_{0.5-x}Ca^{2+}_{x}Fe^{4+}_{x}Fe^{3+}_{5-x}O^{2-}_{12} \text{ with } \{x = 0.0, 0.1, 0.2, 0.3\} \tag{2.2}$$

The co-substitution of a complementary amount of Y is designed to main-tain a constant Bi concentration at high value of 2.5 per f.u. (Eq. 2.2) since Bi is known to govern the Faraday rotation intensity [42]. This work presents the first investigations on the high temperature transport properties of Bi-rich iron garnets [58].

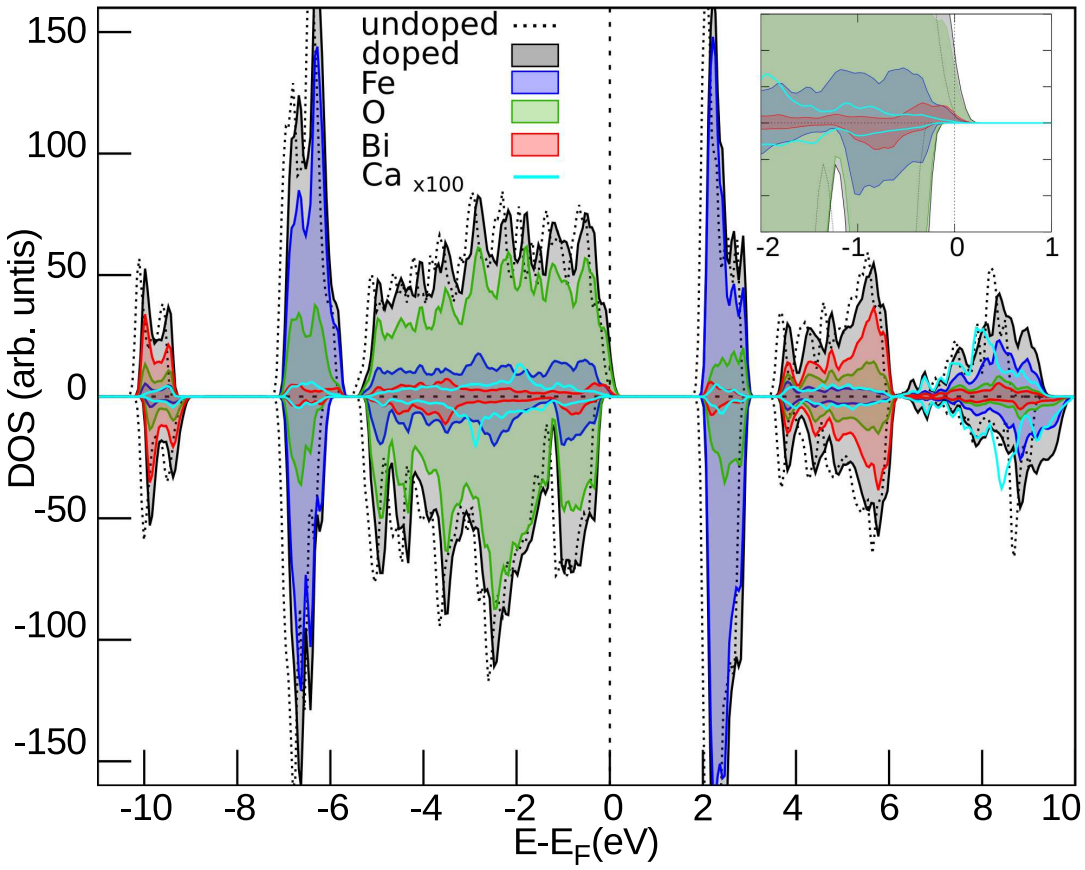

FIGURE 2.11: DFT+U (U=4 eV) total and projected DOS of Ca-doped BIG with a Ca concentration of 4%. (Ca projected DOS has been magnified by 100). The dotted black line corresponds to the undoped BIG total DOS, while the Ca-doped total DOS is in grey. The inset shows a magnification around the Fermi energy between -2 and 1 eV. This figure is adapted from Iori et al. [15].

2.2.2 $B_{3-x}Y_xIG$

In $B_{3-x}Y_xIG$, Bi plays an important role on the structural and physical properties of this system and is notably responsible for a large enhancement of the Faraday rotation (see section 2.1.2). A crystalline thin film can be obtained for most of the Bi/Y ratios [21, 59, 22, 24] with a lattice parameter increasing with increasing Bi concentration as expected from the large ionic radius of Bi^{3+} [60]. A red shift of the MO response from YIG to BIG is also observed [38], that is reflected in the decrease of the optical band gap. Indeed, from YIG to BIG, the optical band gap changes from 3.0 eV [30] to 2.3 eV [29]. Apart from this decrease of the band gap, the Y^{3+} substitution in the BIG matrix should not result in additional charges, unlike Ca^{2+}. Concerning the magnetic properties, the T_C of $B_{3-x}Y_xIG$ are also a growing function of the bismuth concentration which is consistent with a higher exchange interaction as calculated by Iori et al. [15]. The fractional population of Bi on the dodecahedral site gives rise to an additional magnetic anisotropy term, the so-called growth anisotropy term [61, 62]. This anisotropy tends to put the easy magnetization axis of the thin films out-of-plane leading to perpendicular magnetic anisotropy as demonstrated in the recent work of Soumah et al. [59]. As stated previously, the electrical transport properties of Bi-rich iron garnet were not investigated. Therefore, the doped YIGs are considered, in this work, as reference compounds for their electrical transport properties.

2.3 Doped semiconductor YIGs as reference systems

2.3.1 N- and p-type doped YIGs

Doping solely with aliovalent cations was investigated previously on the parent compound, i.e. YIG. YIG is also a ferrimagnetic insulator (10^{12} Ω cm at 300 K) [57, 63, 64] exhibiting a much weaker MO signal in the visible range than BIG and possessing most remarkably the lowest known magnetic damping [65]. Doped-YIG phases were usually synthesized either by applying the flux growth technique for single crystals or the LPE method for films thicker than 1μm. Tetravalent cations such as Hf^{4+} [66], Sn^{4+} [67], and Si^{4+} (e.g. Fig. 2.12 (a)) [68, 69, 70], were successfully substituted into the YIG lattice yielding n-type semiconductors with electrical resistivity values between

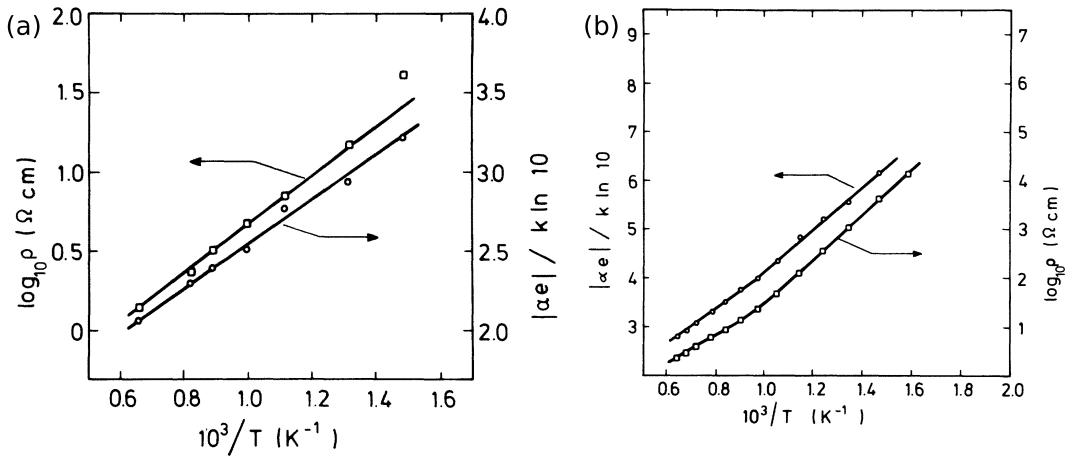

FIGURE 2.12: a) Resistivity and absolute value of the normalized Seebeck coefficient [12] as a function of temperature for a n-type YIG. b) Resistivity and Seebeck coefficient as a function of temperature for a p-type YIG. This figure is adapted from ref. [69].

10^3 and 10^5 Ω cm at room temperature. Conversely, divalent cationic substitutions such as Zn^{2+} [69], Mg^{2+} [71], Pb^{2+} [72], or Ca^{2+} (e.g. Fig. 2.12 (b)) [69, 70, 71, 73] in YIG yield p-type semiconductors with electrical resistivities ranging from 10^7 Ω cm to 10^3 Ω cm at 300 K; the best of them [73] being comparable to the n-type doped YIG. The electrical resistivity and Seebeck coefficient measurements as a function of temperature lead to the conclusion that both n- and p-type doped YIGs follow a band conduction mechanism in the temperature range 300 - 600 K [67, 74]. Such findings show that n- and p-type semiconductor can be obtained from YIG and open interesting perspectives for the investigation of BIG-based semiconductors.

2.3.2 Defects in doped YIGs

The electrical properties of doped YIG are modified by the presence of defects in the garnet structure. Thus, for both n- and p-type YIG grown by LPE, chemical impurities such as Pb^{2+}, F^- or B^{3+} (up to 0.1 per f.u.) are unintentionally incorporated during the growth process. These defects act as extrinsic acceptors or donors that can partially account for differences in the electrical resistivity for a given carrier type and concentration. The presence of oxygen vacancies that can act as intrinsic donors in complex oxides also plays a key role in their transport properties. Oxygen concentration is directly linked to the growth conditions, but cationic substitutions can also influence the oxygen stoichiometry in a single oxide phase. In doped-YIG phases, it is known that the substitution of tetravalent cations prevents the formation of oxygen

[12] α is the Seebeck coefficient, e is the charge of the electron and k is the Boltzmann constant.

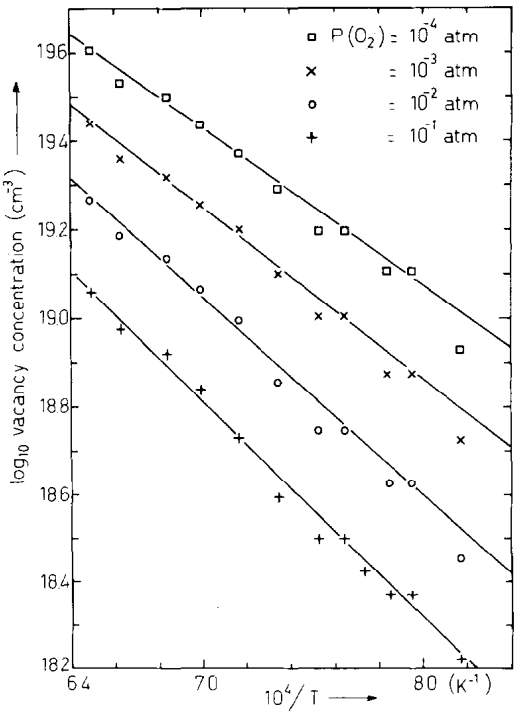

FIGURE 2.13: Concentration of oxygen vacancies calculated from thermogravimetry experiments as a function of the inverse temperature and the partial oxygen pressure. These experiments were performed on a Ca-doped YIG. This figure is adapted from ref. [75].

vacancies [69, 75]. Conversely, divalent cationic doping favours the presence of oxygen vacancies in p-type YIGs that alter their electrical properties [76]. For instance, oxygen migration was further evidenced in p-type YIG through annealing at $T > 1100$ K under inert/oxidizing atmosphere leading to small reversible resistivity changes, i.e. less than an order of magnitude [69, 75]. An applied voltage of roughly 100 V lead to a room temperature high conductivity state in p-type YIG indicating the migration of oxygen vacancies in an electric field [77]. The measurement of $I - V$ curves on these thin films [73] show that their behavior corresponds to the space-charge limited current model [78]. This behavior can lead to resistive switching as in, for instance, $Pr_{0.7}Ca_{0.3}MnO_3$ [79] or $La_{0.7}Ca_{0.3}MnO_3$ [80].

Although thin films are ideal for integration into advanced nanoelectronics, they are even more prone to defects inclusions than single crystals and thus YIG-based thin films have been less widely investigated. However, 20 nm thick YIG films with a p-type conductivity of ca. 10^7 Ω cm at 300 K were grown recently by LPE [81]. The authors suggest that this relatively

low resistivity for undoped iron garnet originates either from the low dimensionality of the film or from the chemical impurities incorporated during the growth process. Overall, the microscopic origin of the electrical properties of doped YIGs and more generally iron garnets were mostly investigated by indirect means such as chemical or optical characterizations. The present work aims at filling that gap by probing the nature of defects and the charge compensation mechanisms using, in particular, transmission electron spectro-microscopy techniques (STEM/EELS) and X-ray magnetic circular dichroism (XMCD).

Summary of chapter 2

In this chapter, the structural and physical properties of BIG and $Bi_{3-x}Y_xIG$ were presented including their MO properties. The origin of their MO properties were investigated using DFT calculations and this theoretical study was compared to previous works on this subject that were based on molecular-orbital calculations. The substitution of Ca is expected to enhance the electrical transport properties of BIG and the co-substitution of Y is expected stabilize the MO properties between the different Ca substitution levels. Since the electrical properties of $B(Ca_xY_{0.5-x})IG$ were not studied previously the electrical properties of n- and p-type doped YIG were reviewed as reference systems. The presence in BIG of a $T_C > 500$ K, of the giant Faraday rotation, of the spin-split bands around the Fermi level and the possibility to develop n- and p-type semiconductors in doped YIG are encouraging results towards the development of a magnetic semiconductor based on BIG.

Chapter 3

Experimental techniques and data analysis tools and developments

In a first part of this chapter, we present all the experimental setups that were operated to measure the electrical and magnetic properties of Ca and Y co-substituted BIG thin films. Different experimental techniques were combined during this thesis to reveal the structural, microstructural, physical properties of the synthesized substituted BIG thin films from the macroscopic scale down to the atomic scale. The thin films were grown using pulsed laser deposition (PLD) and their physical and structural properties were investigated by electrical transport measurements and X-ray diffraction (XRD). Faraday rotation spectroscopy, scanning transmission electron microscopy (STEM) coupled with electron energy-loss spectroscopy (EELS) and X-ray magnetic circular dichroïsm (XMCD) were performed to study the microstructural and microscopic properties of the thin films.

In a second part, the operating principle of the data analysis tools applied on the STEM/EELS data are presented. The local strain distribution was determined using geometric phase analysis (GPA) on STEM images. Most of the STEM/EELS elemental maps presented in this manuscript were denoised using principal component analysis (PCA).

In a third part, we describe the cluster analysis that was used to study in detail the subtles changes of EELS fine structures. The cluster analysis has not been applied to such problematics yet. Therefore, the domain of application and the performance of this technique to retrieve EELS signatures were tested first. Finally, the clustering was applied on Co_3O_4 selected as a model system.

3.1 Experimental techniques

3.1.1 Thin film growth and post-growth processing

PLD growth

The investigated thin films were all deposited at the GEMaC laboratory[1] using PLD. PLD is a well-establised growth technique yielding cristalline epitaxial thin films of complex oxides under controlled atmosphere and pressure conditions [82]. In this technique, a high power laser periodically fires very short light pulses on a ceramic target having the desired stoichiometry. This light pulse is intense enough ($\approx$ 60 MW cm^{-2}) to eject ions, atoms or particulates from the ceramic target and create a plasma called a plume. The species in the plasma are then deposited on the substrate placed in front of the target. The PLD chamber is equipped with several in-situ experimental setups that are used either to tune the deposition conditions or to measure the structural and optical properties of the growing film as shown in Fig. 3.1. The homogeneity of the ablation of the target is ensured by its simultaneous rotation and vertical movements. In addition to the oxygen gas valve that allows the deposition in an oxygen partial pressure, a O^+ plasma source and a pulsed oxygen gas valve allow the growth of thin films in highly tunable conditions. The base pressure in the chamber is 5×10^{-6} mTorr. The temperature of the substrate is controlled by a heater located at the back of the substrate and can reach 1220 K[2]. The distance between the target and the substrate is 5.5 cm. The structural properties of the thin films can be measured in-situ during growth by reflection high-energy electron diffraction (RHEED). The optical properties are also measured in-situ by ellipsometry providing an estimation of the film thickness in real time.

The $Bi_{2.5}Ca_xY_{0.5-x}Fe_5O_{12-\delta}$ (B($Ca_xY_{0.5-x}$)IG) with x={0.0; 0.1; 0.2; 0.3} and $Bi_{2.0}Y_{1.0}Fe_5O_{12-\delta}$ (B($Y_{1.0}$)IG) thin films were grown on $Gd_3Ga_5O_{12}$ (GGG) (100) with thicknesses ranging roughly from 150 nm to 200 nm. The deposition rate is of $\approx$ 8 nm min^{-1} and the substrate size was 10×10 mm^2. The BIG targets substituted with Ca and Y have been prepared from high purity powders (99.99% for Ca precursor and 99.999% for all other precursors) using the standard ceramic processing method [21, 28]. The Bi is preferentially evaporated compared to other species such as Ca [83] which tends to deplete the Bi content from the target during the deposition. To avoid this effect, the

[1] All the samples were deposited by Elena Popova.

[2] The temperature of the front of the substrate cannot be measured easily and is probably up to 200 K less than the temperature measured at its back.

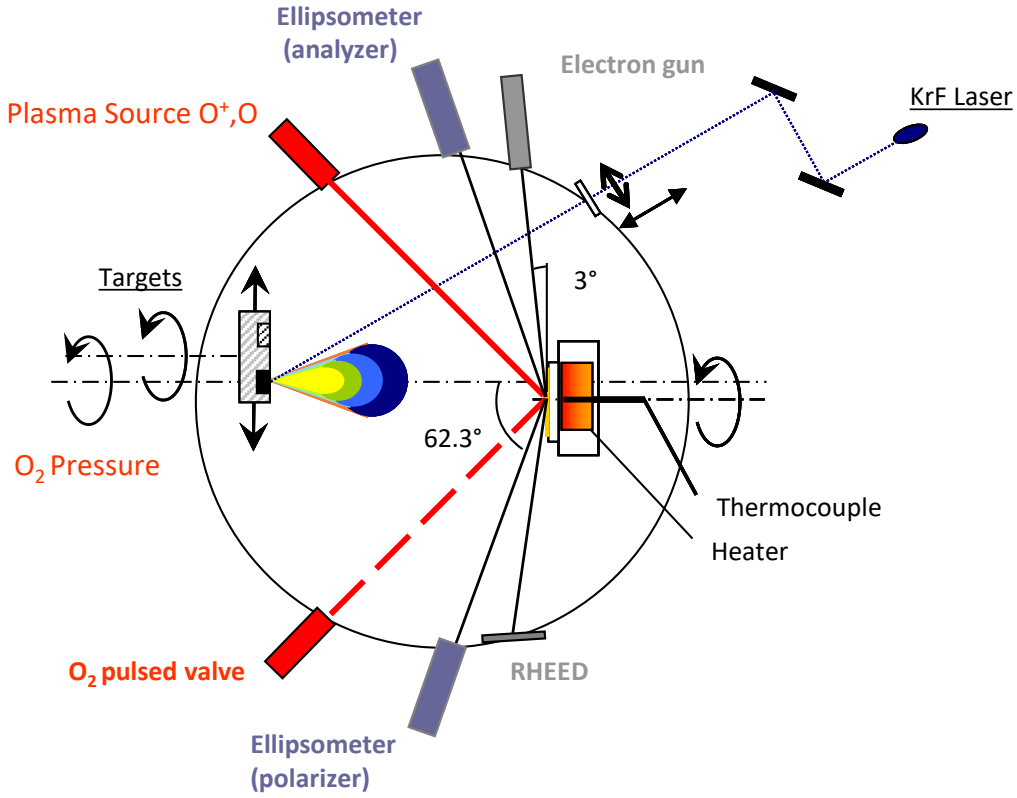

FIGURE 3.1: Scheme of the pulsed laser deposition setup. Courtesy of Bruno Berini (GEMaC).

surface of the target is polished between two depositions which removes the Bi depleted layer. An excimer KrF laser with a wavelength of 248 nm and pulse duration of 20 ns was used for film deposition. The laser fluency and frequency were maintained at about 1.2 J cm^{-2} and 2 Hz respectively for all the samples. The films were grown onto the substrates heated to 1050 K in a stable oxygen pressure of 5 mTorr. After the growth, the samples were cooled down to room temperature in the growth atmosphere in about 3.5 hours.

Thin film post-annealing

Post-annealing under controlled oxygen flux was performed in a dedicated furnace to obtain oxygen stoichiometric thin film. The samples were annealed at 820 K under oxygen flux of 50 mL min^{-1} for 48 hours once (TA48) or twice (TA96).

3.1.2 X-Ray Diffraction

The X-ray diffraction (XRD) was systematically measured before and after the post-annealing to ensure that the thin films are well crystallized. The Ca and Y co-substituted thin films are expected to crystallize in the garnet space

group $Ia\bar{3}d$. The samples were probed by XRD using a Seifert XRD3000 4-circles diffractometer at the GEMaC laboratory. The incident X-ray beam is monochromated at the Cu $K\alpha 1$ peak. The diffractometer's angular resolution is 0.0005 deg. To extract the out-of-plane lattice parameter the $(0, 0, l)$ reflection set is measured, while for the in-plane lattice parameter the $(0, k, 2k)$ reflection set is measured as shown in Fig. 3.2 [3]. The diffraction patterns were acquired usually acquired from 20 deg to up to 100 deg in 2θ with a step of 0.01 deg and a dwell time of 1s.

From a diffraction pattern a few other information can be extracted in addition to the lattice parameter.

- The Full Width at Half Maximum (FWHM) of a given reflection peak gives an estimation of the mosaicity (i.e. the dispersion of crystallographic orientation) of grains within the film.
- The presence of Laue oscillations attests that a coherent crystal structure exists over the whole probed volume.
- Since the 2θ values of the garnet reflections are known, any additional peak may be the signature of secondary phase inclusions. However, this is limited to a certain volume of well crystallised secondary phases that have to be in diffraction condition in the explored range of the reciprocal space.

3.1.3 Electrical transport and thermopower measurements at high temperatures

Electrical resistivity

The electrical resistivity measurements were performed on the substituted BIG thin films over a wide temperature range (300 K < T < 700 K) under inert/oxidizing atmospheres during heating/cooling cycles on a custom designed setup at the GEMaC laboratory. A full heating and cooling cycle with a 5 K step takes about 20 hours to measure.

The electrical resistivity ρ of a material is the ratio of the applied electric field on this material divided by the current density flowing through it. It is expressed in Ω cm and describes the flow of electrons through the material. It should be noted that the presence of defects such as grain boundaries affect the electron conduction and therefore impact the resistivity measurement.

[3] The in-plane lattice parameter were only determined for a few films.

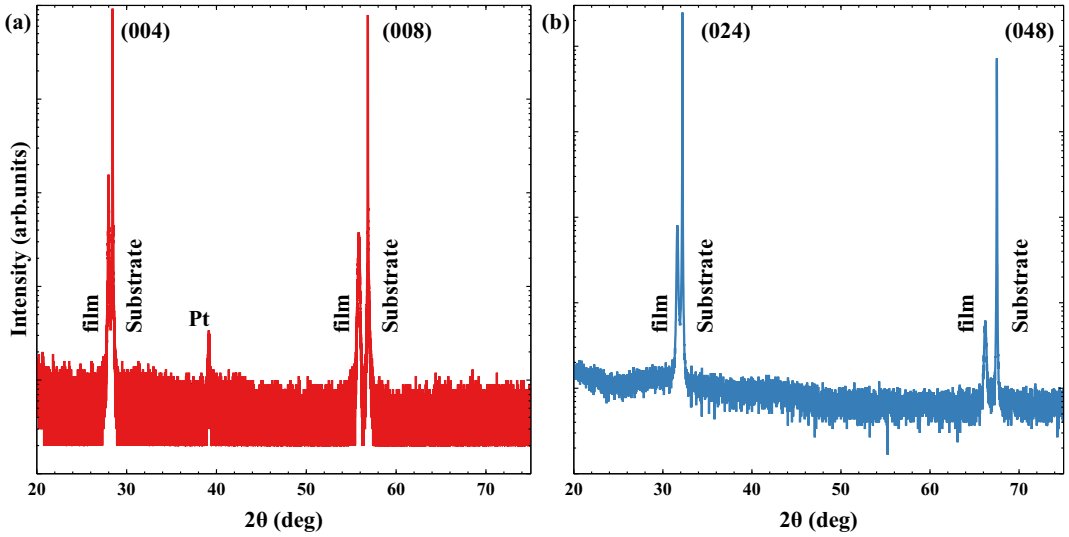

FIGURE 3.2: Typical XRD patterns of Ca and Y co-substituted BIG films acquired along the $(0,k,2k)$ direction in blue and along the $(0,0,l)$ direction in red. A diffraction peak of the Pt contact pads is observed in the $(0,0,l)$ direction.

The electrical resistivity of the thin films was measured by the four point-probe technique developed by Van der Pauw[84]. The advantage of using this four point-probes technique is to negate the effect of the resistance at the interface between the metallic electrodes and the semiconducting thin film on the resistivity measurement (hereafter : contact resistance). A scheme of the electrical resistivity experiment is displayed in Fig. 3.3, showing the four contact pads on the film. A current I is applied and measured between two electrodes (e.g. A and B) while the other two electrodes measure the associated voltage V (e.g. C and D). This process is repeated with a circular permutation of the electrodes and the resistivity of the film is calculated as follows :

$$\rho = \frac{\pi d}{\ln 2} \frac{R_{AB,CD} + R_{BC,DA}}{2} f \tag{3.1}$$

Here d is the film thickness, $R_{ij,kl}$ is the measured resistance with applied current between electrodes i and j and with voltage measured between k and l electrodes and f is a correction factor. The factor f is a monotonous decreasing function of the ratio $R_{AB,CD}/R_{BC,DA}$ taking values between 0 and 1.

For the measurement of the electrical properties of the films, the samples were cut into four pieces of 5×5 mm^2. Metallic contact pads were deposited by RF-sputtering at the four corners of 5×5 mm^2 pieces. Pt circular pads that were roughly 250 nm thick and 1mm wide were deposited onto the film [4]. The separation between two pads is roughly 2 mm (Fig. 3.3). Each Pt pads

[4]The deposition of Pt was performed by Bruno Berini.

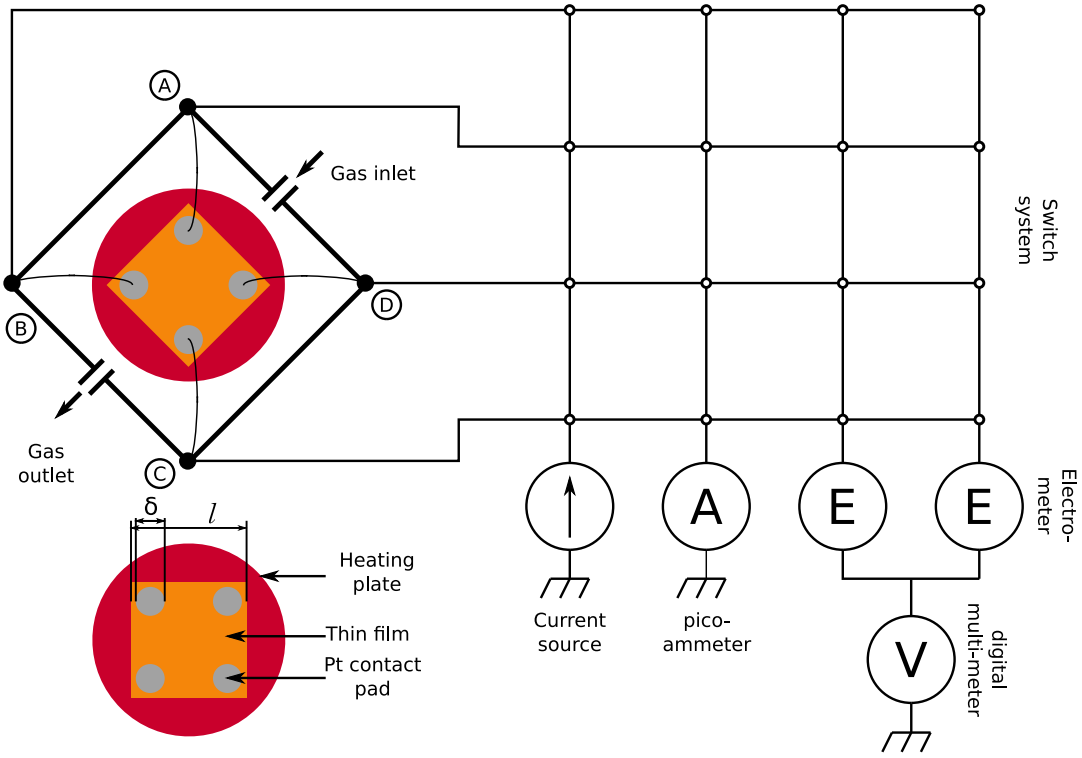

FIGURE 3.3: Scheme of the High Impedance High Temperature setup.

are separated of 2 mm from each other. Pt was chosen as contact material as the interface between the films and the Pt contact exhibits an ohmic electrical behaviour.

To determine the resistivity of oxide semiconductors and insulators with high impedance ($R > 10^8\Omega$), a custom setup with a high internal impedance which reaches high temperature ($T > 400$ K) is required. Besides, at high temperatures, oxides might exchange oxygen with the atmosphere, therefore a controlled atmosphere is also required. The voltage was measured by two 6514 Keithley electrometers with two probes while the current was injected by a 6221 Keithley current source and measured by a 6487 Keithley picoammeter with the other two probes. These signals were then digitized by a 2700 Keithley multimeter and the switch between the different four-probe configurations was performed by a 7001 Keithley system. With this setup it is possible to measure samples with up to 200 GΩ impedance and currents as low as 10^{-10} A. The present electrical measurements were performed by applying 1 nA current in a THMS600 temperature controlled stage (Linkam Scientific Instruments Limited) at temperatures ranging from 300 K to 700 K under ambient atmosphere or N_2/Ar flux of at least 200 mL min^{-1}. At each temperature, a current of 1 nA is applied for 180 s prior to the resistivity measurement to reach a steady current regime.

The instruments yield measurements with very low imprecisions of about 2%. However, the Van der Pauw measurement has a few intrisic sources of inaccuracy[5]. To obtain Eq. 3.1, the contact resistance has to follow an Ohmic behaviour. Therefore, the resistances $R_{AB,CD}$, $R_{BC,DA}$, $R_{CD,AB}$ and $R_{DA,BC}$ are measured every time to ensure that V changes sign with I, following the Ohmic behaviour. In the Van der Pauw method, the contact size is assumed to be infinitesimal which is experimentally not the case. The size of the contact is usually expressed as δ/l, where δ is the characteristic size of the contact and l is the length of a side of the sample. However, the finite size of the contacts yields inaccuracy on the resistivity measurement of up to 15% for δ/l ratio of 0.25 [85]. In our work, the δ/l ratio is around 0.1. Heterogeneities in the form of a non percolating secondary phase inclusions in the film that have higher resistivity also have an impact on the resistivity determination with an inaccuracy that can reach 70% [86]. In this work, the resistivity of the thin films varies over several orders of magnitude in the explored temperature range which is a very large variation compared to inaccuracies of even up to 100%. Therefore, the inaccuracies are not take into account in the interpretation of the resistivity measurement.

Thermopower

We probed the thermopower of the thin films to better understand the nature of the charge carriers and therefore the corresponding charge compensation mechanisms. Under the application of a steady thermal gradient (ΔT), the chemical potential of a material varies across it inducing an accumulation of charges at the coldest end of the probed material. S is an intrinsic physical property of the material describing the diffusion of charges through it. The electrical potential difference (ΔV) induced by an accumulation of charges is proportionally linked to ΔT by the thermopower also named the Seebeck coefficient S and calculated as follows:

$$S = -\frac{V_{hot} - V_{cold}}{T_{hot} - T_{cold}} = -\frac{\Delta V}{\Delta T} \tag{3.2}$$

Here, V_{hot} and V_{cold} are the voltages at the high temperature (T_{hot}) and at the low temperature (T_{cold}) sides, respectively. The charges, either hole or electrons, accumulate at the cold side and yield the inequality $|V_{hot}| < |V_{cold}|$. Then $\Delta V > 0$ and $S < 0$ for electron as majority carrier. Conversely, $\Delta V < 0$

[5]Inaccuracy corresponds to an offset in the measurement compared to the true value. Imprecision corresponds to the statistical distribution around the measured value.

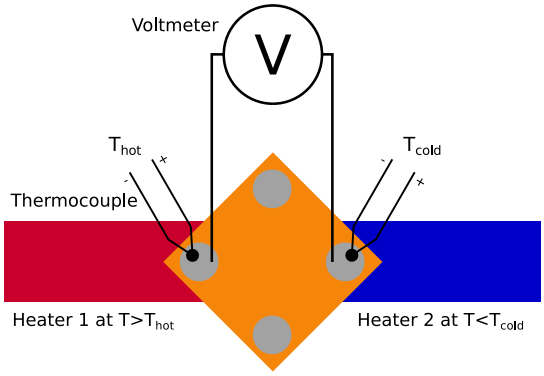

FIGURE 3.4: Scheme of the Seebeck coefficient measurement setup.

and $S > 0$ for hole as majority carrier. The thermopower is then a probe of the majority carrier type.

The Seebeck coefficients were determined with the two point-probe method using another custom-designed experimental setup under air atmosphere at the GEMaC laboratory. A scheme of the experimental setup is displayed in Fig. 3.4. The temperature gradients ΔT were set using a RTD2 thermoregulator (Omicron technologies) with two heaters, separated by 6.5 mm from each other, placed below the substrate while voltage and temperature were both probed onto the film surface above the heaters. ΔT were measured using two K-type thermocouples and reached positive or negative values between 5 K and 30 K with ± 2 K fluctuations during voltage measurements. Voltage at both hot and cold sides were measured using a Keithley 4200 SCS with $10^{13}\Omega$ internal impedance. The ΔV was measured for several ΔT values. The S value was extracted as the slope of a linear fit on these $(\Delta T, \Delta V)$ points.

One should note that the measured Seebeck coefficient is the sum of S_{film} of the film and of S_{probe} of the wires used for the measurement. For a quantitative measurement of the Seebeck coefficient, the S_{probe} has to be taken into account. In this work, the thermopower was mainly used to obtain qualitative information i.e. the sign of the majority carrier (either p- or n-type) and a rough estimate of the charge carrier density using the Heikes formula [87]. The Hall effect is another probe of the carrier type. However, if this technique is especially well suited for high mobility and low resistivity materials such as metals, its application is much more complex on materials with high resistivity and low mobility [88]. Therefore, the Hall effect is not investigated in this work.

3.1.4 Magneto-optical measurements

Faraday spectroscopy and Curie temperature

The out-of-plane MO spectra were measured before and after post-annealing for all the thin films to understand the evolution of the MO properties upon Ca and/or Y substitution. The temperature dependence of the MO signals at 550 nm was also systematically measured to obtain the T_C of the films. In this setup, both the applied field direction and the light beam are collinear to the out-of-plane axis.

The Faraday rotation (θ_F) and ellipticity (ϵ_F) spectra were measured at the GEMaC laboratory using a custom designed experimental setup depicted in Fig. 3.5 [89]. The light source is a LOT-Oriel Xe 75 W lamp with a constant emission spectrum in the 300 to 900 nm range. With the polarizer, the photo-elastic modulator (PEM) produces oscillating left and right circularly polarized light at a frequency $f = 50$ kHz. The PEM (I/FS50 model by Hinds-instruments) birefringence parameters are set to operate as a $\lambda/4$ lamella at the selected monochromated wavelength. The modulated light goes through the magnetic coil and through the sample with normal incidence. The magnetic coil can produce a field of up to 1.3 T collinear to the optical axis and a Hall probe inside the pole piece of the coil measures the applied field. The outgoing light is then monochromated by a SP2557 monochromator and detected with a photomultiplicator of the Hamamatsu brand with similar performances to the Hamamatsu R375. The measured intensity can be written as follows :

$$I = I_0 + I_f \sin(2\pi f t) + I_{2f} \sin(4\pi f t) \tag{3.3}$$

It can be demonstrated that I_f and I_{2f} are proportional to ϵ_F and θ_F, respectively [89]. A lock-in amplifier at f and another lock-in amplifier at $2f$ extract the I_f and I_{2f} signals.

To measure the temperature dependence of the Faraday effect, it is possible to insert a furnace in between the two pole pieces of the magnet. The furnace can operate at temperatures ranging from 300 K to 1000 K.

To obtain a typical Faraday spectrum, the MO signal is measured at each wavelength while a saturating magnetic field is applied ($\approx$ 0.5 T). Since the signal is measured in transmission through the film and the substrate, a paramagnetic component originating from the GGG substrate is superimposed on the magneto-optical response of the film (Fig. 3.6). To overcome this issue, every data point is acquired for positive and negative magnetic fields.

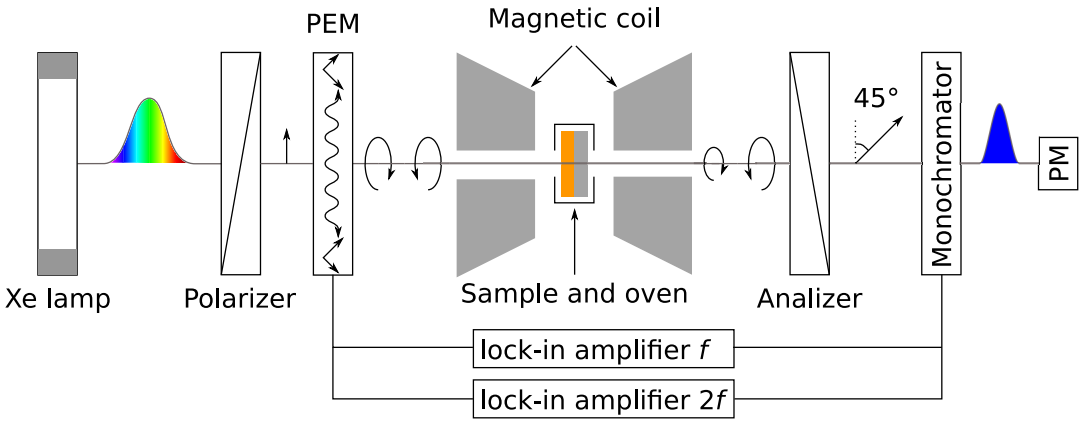

FIGURE 3.5: Scheme of the experimental setup. The polarization state are depicted by arrows. This figure is adapted from ref. [89].

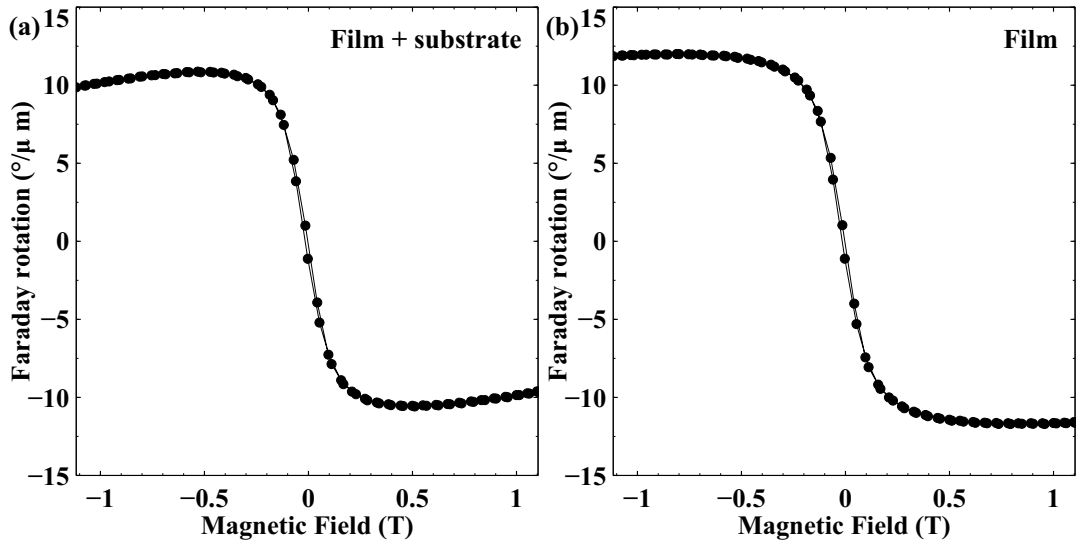

FIGURE 3.6: a) Faraday rotation magnetic hysteresis cycle at 550 nm with contributions from the thin film and the substrate. b) Cycle (a) after removal of the substrate paramagnetic contribution.

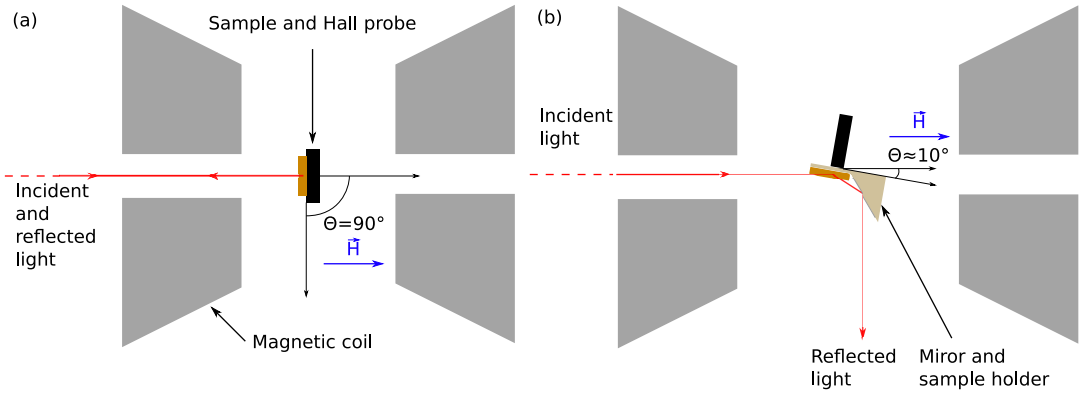

FIGURE 3.7: a) Scheme of the experimental Kerr setup in the polar configuration. b) Scheme of the experimental Kerr setup in the longitudinal configuration.

Longitudinal and polar MO Kerr effect

The MO Kerr effect is the same physical phenomenon as the MO Faraday effect measured using a reflected wave instead of a transmitted one. To probe the magnetic anisotropy of some of the films (section 6.2.2), the magneto-optical Kerr effect was probed in longitudinal and polar configurations i.e. along the in-plane and out-of-plane directions, respectively.

The MO Kerr effect is measured with a polarizer/analyzer couple and a PEM coupled to a lock-in amplifier the same way as the Faraday setup described in section 3.1.4 [6]. The main differences of the Kerr experimental setup with respect to the Faraday setup are the following:

- The light source is a He-Ne laser emitting at 633 nm. Limiting the experiments to magnetic hysteresis loop at fixed wavelength.
- The setup was operated either in polar (see Fig. 3.7 (a)) or longitudinal (see Fig. 3.7 (b)) configurations
- The applied magnetic field is limited to 0.4 T in the polar mode and to 0.3 T in the longitudinal mode.

3.1.5 Electron Microscopy and Spectroscopy

Bi-rich iron garnets can only be synthesized as thin films on isostructural substrates. Transmission electron microscopy is then a key technique to investigate the structural, chemical and electronic properties of such materials with reduced dimensions. In this thesis, we have made important efforts in

[6] Alexandra Mougin (IDMAG team at LPS) helped us to carry out the MO Kerr experiments and adviced us for the interpretation of these data.

understanding the electronic properties of Ca and Y co-substituted BIG thin films in link with their local dopant concentration and their electrical transport properties using electron spectro-microscopy techniques.

Electrons are charged particles that interact with atoms, when passing through a material, via electrostatic interactions. The interaction with nuclei mostly scatters the electrons elastically and are used for imaging in this thesis. Conversely, the electrons that interact with the electrons of the solid are scattered inelastically. These scattering events can lead to individual excitations of core electrons, to collective excitations such as phonons or plasmons or to interband transitions. In this work, we use the excitations of core electrons to extract information of the electronic and chemical properties of the films.

Scanning Transmission Electron Microscopy (STEM)

The aberration corrected scanning transmission electron microscope (Cs-STEM) is a tool that provides information on the structural, chemical and electronic properties of the observed specimen down to the atomic scale. In STEM, a convergent electron beam accelerated at a few hundreds of kV is focused by magnetic round lenses and multipoles and then scanned across the specimen. Transmitted scattered electrons are collected by detectors covering different radial sections around the optic axis. Electrons detected at each pixel of the scan form the image. The sample has to be transparent to the electrons i.e. it has to be ≤ 100 nm thick to be probed in transmission.

Spatial resolution

Before going into the details of the microscope operated during this work, the spatial resolution limit of the Cs-STEM is described. Mainly three factors play a role on the achievable spatial resolution in a transmission electron microscope: the aberrations of the lenses, the diffraction of electrons and the source size. The effects of the diffraction and the aberrations are discussed first. The Rayleigh criterion describes the highest resolution achievable (d_d) by an optical system that is only limited by diffraction as:

$$d_d = 0.611\frac{\lambda}{\alpha} \tag{3.4}$$

Here, λ is the electron wavelength and α is the aperture half-angle that is equivalent to the convergence half-angle (Fig. 3.9 (b)). The values of α typically range from a few mrads to a few tens of mrads. In the case of STEM

imaging, d_d corresponds to the smallest achievable probe size. A lower d_d is reached for higher α and for lower λ as seen in Eq. 3.4. In this work, the microscope was operated at 100 keV which corresponds to $\lambda = 3.7$ pm. For a typical value of $\alpha = 30$ mrad we will obtain a theoretical $d_d = 75$ pm. λ is very small and therefore it is not the main limiting factor. However, the value of α is constrained by the optical system that is limited by aberrations.

Indeed, round lenses for electron optics are intrinsically not stimagtic [7] systems notably due to their cylindrical symmetry [90]. An ideal spherical wavefront would focus the electron beam into a probe with size only limited by diffraction. However, the aberrations of lenses induce a phase change of the electron wavefront (χ) that distort the wavefront and enlarge the minimum probe size. The aberrations fall in two categories: geometric and chromatic.

Only taking into account the geometric aberrations with cylindrical symmetry and the chromatic aberration, χ takes the following expression [91]:

$$\chi(\theta) = \frac{\theta^2}{2}\Delta f + \frac{\theta^2}{2}\frac{\Delta E}{E_0}C_c + \frac{\theta^4}{4}C_s + o(\theta^6, \theta \to 0) \tag{3.5}$$

Where θ is the angle between the optical axis and propagating electrons and so $0 \leq \theta \leq \alpha$. Δf and C_s are the defocus and the spherical aberration, respectively. ΔE is the energy spread of the electron source, E_0 is the energy of the electron beam and C_c is the chromatic aberration. The C_s is always positive for round lenses and tends to over focus electrons passing away from the optical axis. The C_c results from the lens focusing differently electrons with different energies. The effects of C_s and C_c are illustrated in Fig. 3.8. χ is a fast growing function of θ and to reduce the effect of aberrations it is necessary to decrease α. Indeed, there is a competition between the diffraction limit and the aberrations and α can be optimized to minimize the probe size. For uncorrected STEMs, the C_s is the most limiting aberration and the defocus can be used to compensate partially for C_s [92]. In Cs-STEM, the geometric aberrations can be corrected and compensated up to the 5^{th} order by a system of magnetic multipoles. The correction of aberrations is possible using optical elements that break the cylindrical symmetry. The aberration correctors are either made of a set of octupoles and quadrupoles (NION [93]) or by a set of haxapoles (CEOS [94]). The limiting factor for the Cs-STEM optical system is therefore the chromatic aberration. However, the C_c increases as θ^2 and is therefore much less limiting than the C_s which implies that α can be set to

[7] In a stigmatic system the image of a point is a point.

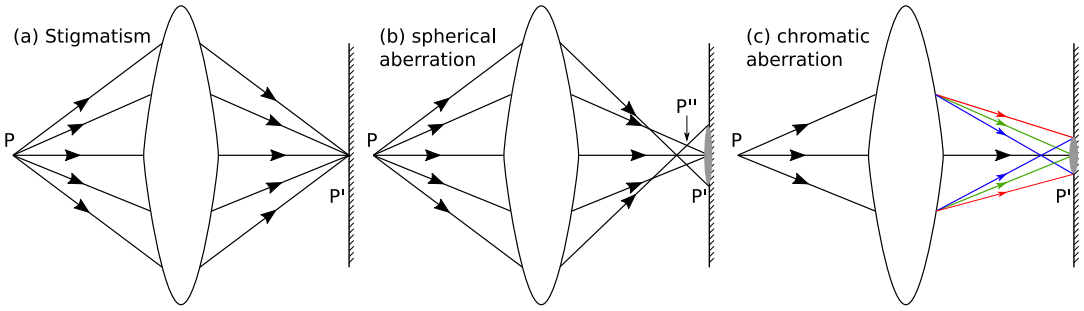

FIGURE 3.8: a) Scheme of an ideal stigmatic round lense where P is the object and P′ is the image of P on the screen. b) Scheme of a round lense with a non-zero spherical aberration. The image P′ is not a point anymore but a partial compensation of C_s is possible using a negative Δf yielding a narrower image P″. b) Scheme of a round lense with non zero chromatic aberration. Rays of different colors represent different wavelength.

higher values in Cs-STEMs compared to uncorrected STEMs. The effect of C_c can be reduced using a monochromator (e.g. CHROMATEM) [95] or with a C_c corrector [96].

An additional factor limiting the probe size is the source size. The practical probe d size is defined by [97]:

$$d = \sqrt{d_a^2 + d_s^2} \tag{3.6}$$

Where d_a is the probe size considering the effect of the aberrations and d_s is the source size. d_s is linked to the probe current I by the following equation [97]:

$$I = \frac{B\pi^2 d_s^2 \alpha^2}{4} \tag{3.7}$$

Where B is the brightness of the electron source [8]. It should be also noted that the higher α, the higher I, so the higher the signal-to-noise ratio (SNR). In Cs-STEMs, high resolution images can be obtained with corresponding large values of α ($\approx$ 30 mrad) and higher probe current ($I \approx$ 50 pA) than uncorrected STEM.

NION UltraSTEM 200

The Cs-STEM operated in this work was the Nion UltraSTEM 200 equipped with a C3/C5 NION corrector which technical scheme is shown in Fig. 3.9 (a) [98]. In this part, we discuss the path of electrons in the column of the UltraSTEM 200 from the gun to the detectors. This microscope is equipped with a cold field electron gun (c-FEG) that has a high brightness of 10^9 A cm^{-2}

[8] The brightness is characteristic of the electron emitter and describes the current density in the probe.

sr^{-1} and a spectral broadening limited to 0.35 eV [99]. With its low spectral broadening a c-FEG reduces the effect of the C_c and is then particularly well suited for high spectral and spatial resolution experiments. Thanks to the high brightness c-FEG, high probe current are achieved. During this work the microscope was operated at 100 kV to limit the damages such as sputtering of oxygen that might become strong at 200 keV. The probe is formed by the condenser system (3 condenser lenses CL1 to CL3 in Fig. 3.9 (a)) and the objective lens (OL in Fig. 3.9 (a)). The aberrations are corrected by a set of magnetic octupoles and quadrupoles [93] labeled as C_3/C_5 corrector in Fig. 3.9 (a). In this corrector, the C_s is tuned to compensate for the C_5 which is the cylindrical symmetric θ^6 order aberration. Typical C_s aberrations of a few micrometers are set to compensate for a residual C_5 cylindrical aberration of several millimetres. The non-cylindrical aberrations are also minimized and compensated by the corrector. The C_3/C_5 corrector is optically coupled to the objective lens by a set of quadrupole (QLM in Fig. 3.9 (a)). With such an instrument, the optimal convergence half-angle reaches $\alpha = 30$ mrad and the probe size is then of $d = 0.8$ Å[97] with $I \approx 50$ pA at 100 kV that is enough to perform atomically-resolved images.

High stability sample holders are also required to achieve a high spatial resolution. Thus, a stage drift as low as 1 Å min^{-1} can be reached with the system operated during this thesis [98]. The sample holders also provide the possibility to tilt of up to $\pm$ 30 deg along 2 orthogonal axes. This feature is critical to orient with an accuracy of 0.1 mrad the thin film specimen along the high symmetry direction of the crystal (zone axis) where atomic columns can be observed. In this work, the thin films are observed along the [010] direction of the garnet lattice. Moreover, the atmosphere at the sample holder is maintained at at room temperature [9] and at around 10^{-5} mTorr. After the sample, the transmitted beam is optically coupled to the high-angle annular dark-field (HAADF) detector by the projector system (4 projector lenses PL1 to PL4 in Fig. 3.9 (a)). The bright-field (BF) and the medium-angle annular dark-field (MAADF) detectors and the electron energy-loss spectrometer (EELS) are coupled with the transmitted beam by the projector system and the quadrupole-octupole coupling module (QOCM in Fig. 3.9 (a)). In the next sections, we describe the main acquired signals in this work, i.e. first HAADF and then EELS.

[9] It is also possible to heat up the sample.

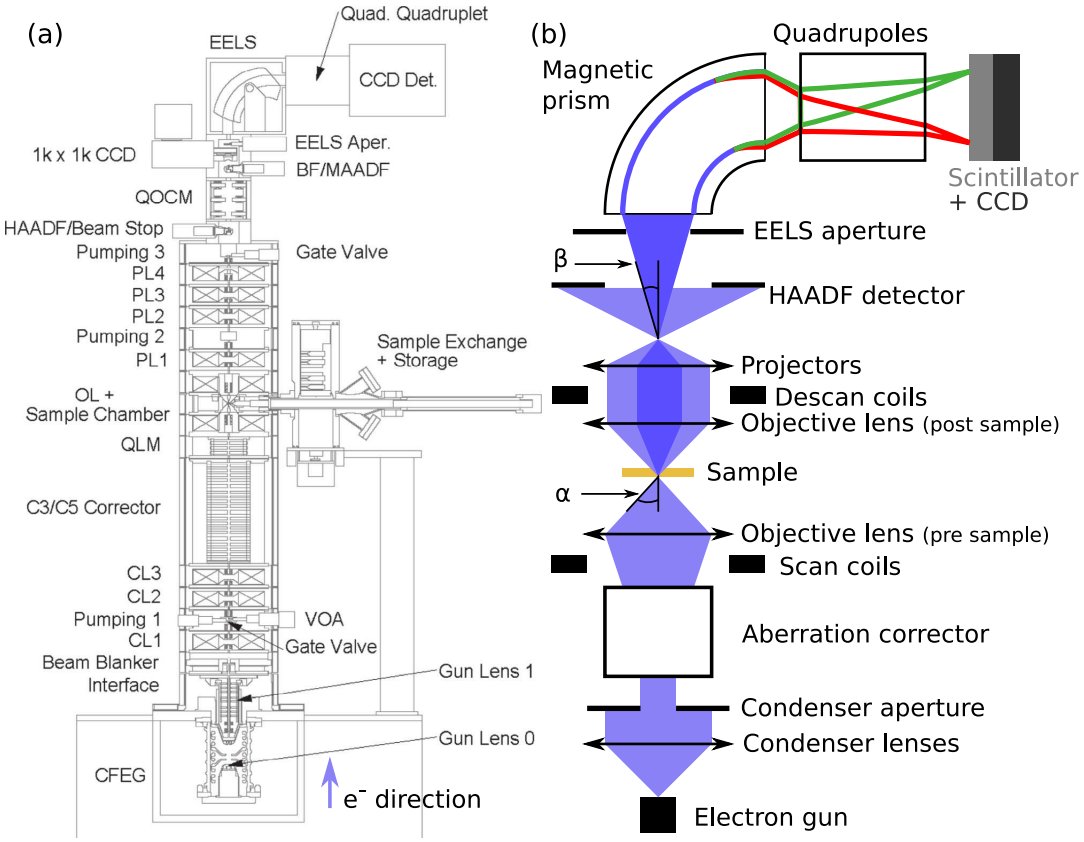

FIGURE 3.9: a) Scheme of the UltraSTEM 200 column from the NION company. b) Simplified scheme of typical aberration-corrected STEM. This figure is adaptated from refs. [98, 100]

High-angle annular dark-field (HAADF) imaging mode

The high-angle annular dark-field detector is a ring-shaped detector which covers a radial section around the optical axis which, in our case, ranges from 80 mrad to 240 mrad [97]. The HAADF imaging mode is incoherent, due in particular to the large area of the detector which averages the residual diffracted intensity [101]. Hence, HAADF images are much more straightforward to interpret than typical BF intensity that contains a difficult to estimate phase term.

At high angles, electron scattering is dominated by interactions with atomic nuclei [102] of the observed solid. For this type of interactions, the electrons are mostly elastically scattered as a result of the large difference of mass between electrons and nuclei ($m_N \approx 1000 \times m_e$). Thus, the cross-section of the high-angle scattered electrons varies roughly as $Z^{1.7}$ [103] where Z is the atomic number. An atomic scale HAADF image of B($Ca_{0.3}Y_{0.2}$)IG is shown in Fig. 3.10. The atomic columns containing elements with high atomic number such as Bi ($Z = 83$) and Fe ($Z = 28$) appear as bright contrast in Fig. 3.10 [10]. In the case of Ca substitution ($Z = 20$) on the Bi site, the presence of Ca in an atomic column will tend to decrease its intensity in HAADF (atomic column a in Fig. 3.10). Besides, HAADF images have the advantage to suffer no contrast reversal over a wide range of focus values and sample thicknesses [104]. However, the HAADF intensity increases with the sample thickness and is therefore sensitive to thickness variations.

At the atomic scale, the HAADF was used in this thesis to obtain an easily interpretable image of the cationic lattice (Fig. 3.10). These images of atomic columns also provide a way to measure the strain distribution in the film using GPA (section 3.2.1). The large inner radius of the HAADF detector allows the simultaneous detection of inelastic scattering that occurs at lower angles by the EELS system.

3.1.6 Electron Energy Loss Spectroscopy (EELS)

In this thesis, EELS was used first at low energy dispersion ($\approx$ 1 eV ch^{-1}) to perform elemental mapping, in particular at the film substrate interface. At higher energy dispersion ($\approx$ 0.06 eV ch^{-1}), EELS was used to probe the valence state of Fe at the local scale in relation with the electrical properties of the different Ca and Y co-substituted BIG thin films.

[10] For this reason, HAADF is often also called Z-contrast

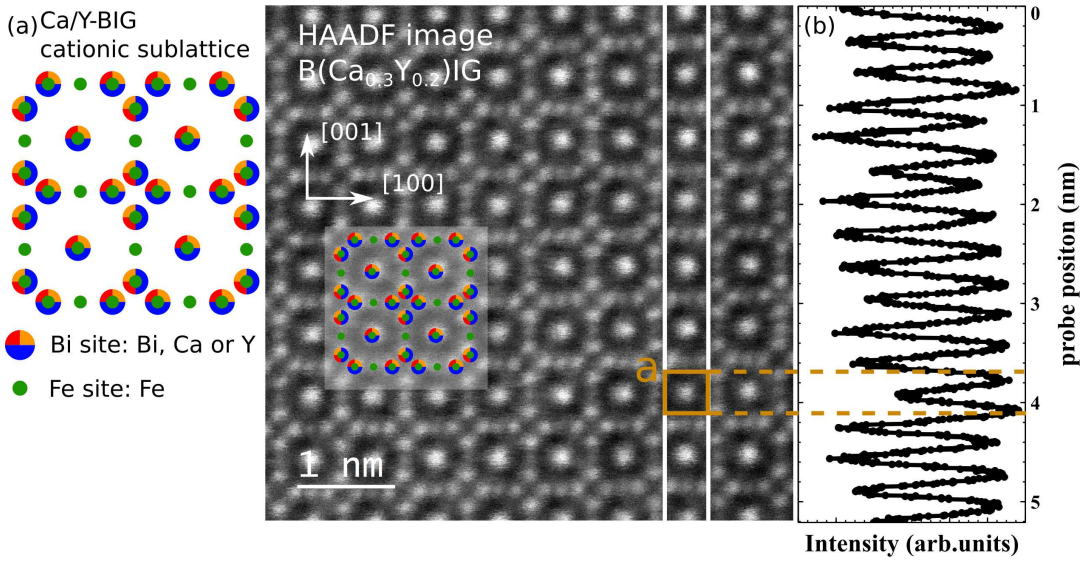

FIGURE 3.10: a) Atomic scale HAADF image of $B(Ca_{0.3}Y_{0.2})IG$ thin film. A model of the cationic sublattice is displayed on the left and on top of the HAADF image. An atomic column a, highlighted in orange, has a lower intensity of $\approx 5\%$ which might indicate the presence of Ca. b) Intensity profile of image (a) integrated in between the two white lines displayed in (a).

EELS spectrometer

Electron energy-loss spectroscopy (EELS) is the measure of the energy lost by electrons upon inelastic scattering in the observed specimen. The spectrometer operated to disperse the electrons according to their energy losses is a Gatan Enfina [97] fitted with a high sensitivity fast CCD (ProEM 1600). Transmitted electrons that enter the spectrometer are deflected depending on their energy by its magnetic prism (Fig. 3.9 (a)). More precisely, the more electrons lose energy upon inelastic scattering in the sample, the more they are deflected. Besides, electrons entering the prism at different angles but with the same energy are focused in a line by the prism. A set of quadrupoles located after the prism modulate the energy dispersion to achieve higher energy resolution (Fig. 3.9 (b)). The electron counts in the direction of energy dispersion form the EEL spectrum on the CCD camera. In this work, the CCD camera was used in its low read-out frequency of 100 kHz to reduce the noise level (typical three e^- rms read noise noise per channel at full binning).

In this thesis, the dispersion of EEL spectra ranges from 0.063 eV per channel to 1.25 eV per channel. As any optics in the electron microscope, the spectrometer has to be aberration corrected not to broaden the measured spectral features. In the NionUltraSTEM200, the aberrations are corrected up to the third order by the QOCM (see Fig. 3.9 (a)) [97]. The EELS aperture defines the collection angle (β) which ranges from 20 mrad to 60 mrad. While a large collection angles is useful to increase the SNR, it can introduce additional

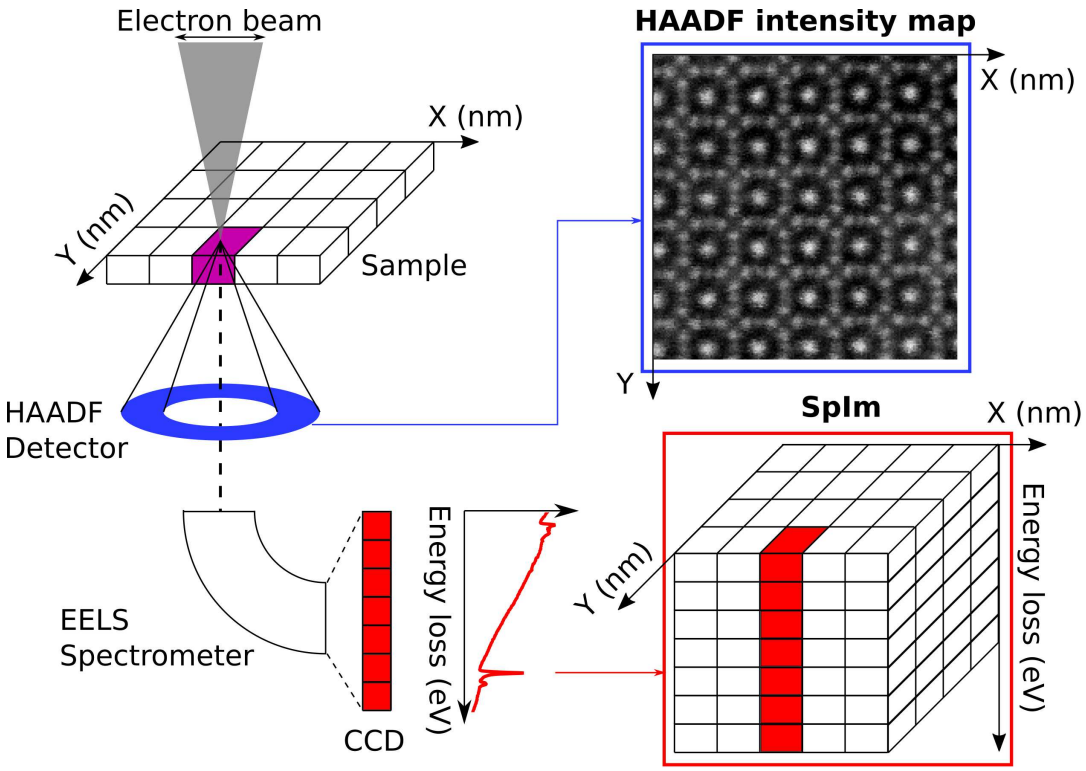

FIGURE 3.11: Scheme of the acquisition of a SpIm. The electron beam is scanned over a chosen region of the sample. At each position of the beam, the scattered electrons are simultaneously collected by the HAADF detector and by the EELS spectrometer. An image is formed using the HAADF signals while the EELS signals forms an array of spectra. An HAADF intensity corresponds to each spectrum of the SpIm. Figure adaptated from ref [106].

aberrations. A combination of a low β, an aberration correction to the third order and a large enough energy dispersion are required to achieve an high energy resolution. Overall, the energy resolution of the EELS spectrometer is limited to about 0.5 eV.

Spectrum Image (SpIm)

Coupling the STEM imaging mode while probing EELS allows the simultaneous acquisition of the HAADF contrast and EELS spectrum during the scan. The resulting dataset, called a spectrum-image (SpIm), is a data-cube (Fig. 3.11(a)) where the channels of each spectrum at position (x, y) are stored along the z direction; each (x, y) pixel has a corresponding HAADF intensity. Mapping the energy-loss features can be performed down to the atomic scale thanks to this acquisition method [105].

EELS spectrum

Inelastic scattering of electrons in solids is mostly caused by interactions with

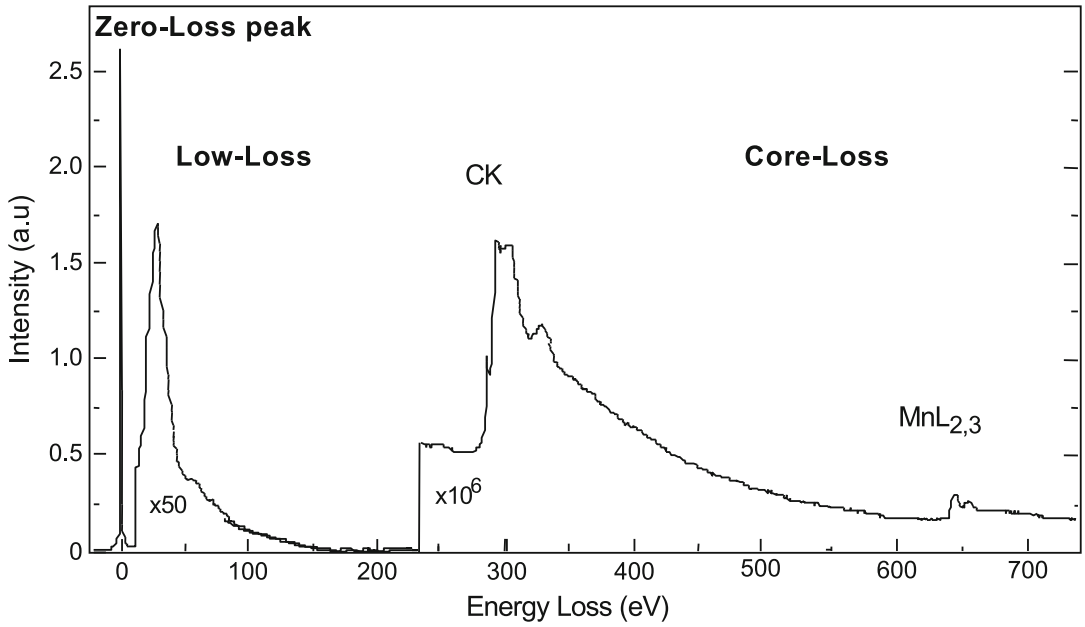

FIGURE 3.12: Typical EELS spectrum covering the low loss and core loss regions. This figure is adapted from ref. [100].

the electrons of the solid. An EELS spectrum is composed of two energy regions. The low losses region corresponds to the excitation of phonons, excitons, interband transitions or plasmons which occur from 0 to roughly 50 eV (Fig. 3.12 (a)). An intense peak is observed at 0 eV (called the zero-loss peak) which corresponds to the electrons having lost less energy than the energy resolution of the EELS system. The core losses region correspond to excitations of the inner shell of atoms which starts, typically, above 50 eV energy loss. The cross-section of electron inelastic scattering decreases rapidly with increasing energy [102], limiting the range of detectable spectral features to roughly 3 keV.

Core losses

In this work, only the core losses were studied. The excitation of an inner shell by a 100 keV beam induces a transition to empty states. These excitation yield an high intensity ionization threshold at energy losses that correspond to the energy difference between the core shell and the first empty states. After an ionization threshold, the intensity decays as a power law. In the dipolar approximation, i.e. no momentum transfer, the cross section of core-loss EELS is proportional to the one of X-ray absorption spectroscopy (XAS) [107]. XAS spectra are therefore occasionally used through this manuscript in direct comparison with EELS spectra.

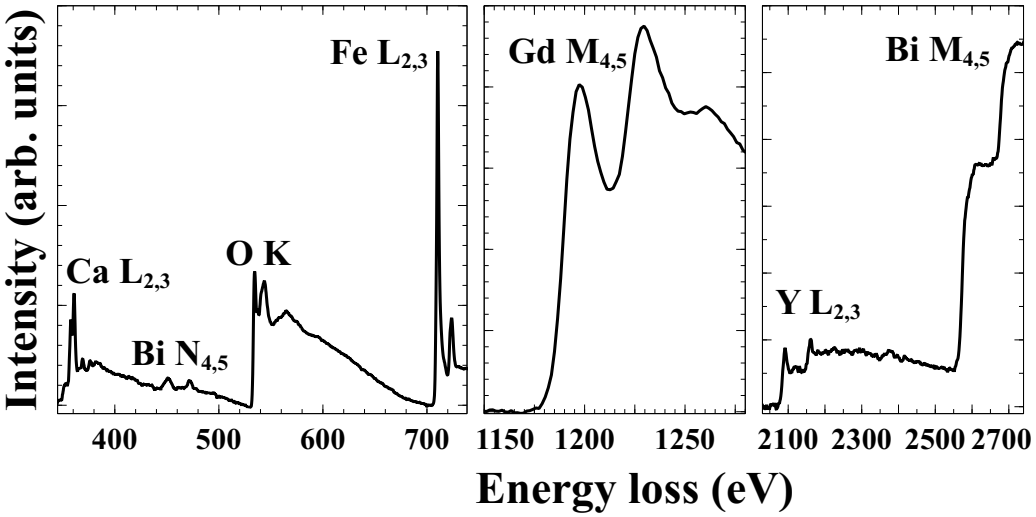

FIGURE 3.13: Typical EELS spectra acquired in B($Ca_{0.3}Y_{0.2}$)IG (right panel), in GGG substrate (middle panel) and in B($Ca_{0.0}Y_{0.5}$)IG (left panel).

Elemental mapping: In this work, the EELS were first used for elemental mapping as each ionization threshold occurs at an energy that is specific of the probed atoms and enables elemental identification. The main edges investigated in this work are: Ca $L_{2,3}$ at 346 eV, O K at 532 eV, Fe $L_{2,3}$ at 710 eV, Gd $M_{4,5}$ at 1185 eV, Y $L_{2,3}$ at 2080 eV and the Bi $M_{4,5}$ at 2580 eV edges (Fig. 3.13). The Ca/Fe elemental ratios were calculated using tabulated cross-section: Hydrogenic cross-section for $L_{2,3}$ edges [11] [108].

Several factors play a role on the spatial resolution of elemental maps. Inelastic scattering events with higher q (q is the momentum transfer in nm^{-1}) are more localized. Hence, a β of 60 mrad was used to increase the collection of inelastic scattering events [109]. Besides, a characteristic excitation length (l_{loc}) can be assigned to each core-loss ionization, describing the distance from which the electron probe excites the transition. An upper boundary to the l_{loc} can be estimated as : $l_{loc} \approx 0.71\lambda \left(\frac{E_0}{E}\right)^{3/4}$ [110] where λ and E_0 correspond to the wavelength and energy of the electron beam and E corresponds to the excitation energy. The l_{loc} ranges from 1.8 Å for Ca $L_{2,3}$ to 0.4 Å for Bi $M_{4,5}$ at 100 kV and should limit the spatial resolution. Additionally, the spatial resolution in EELS mapping is obviously limited by the electron probe characteristics. The large α values related to the small probe size tend to delocalize the electron probe, especially for thick (>50 nm) samples [111, 104]. However, the electrons undergo a channeling effect which tends to localize them along atomic columns during their propagation through the

[11] A special correction for $L_{2,3}$ edges to the hydrogenic cross-section was applied.

sample [112] [12]. The acquisition of atomically resolved elemental maps is made possible by Cs-STEM as a result of the high achievable currents in sub-angström sized probe and was demonstrated in several works [105, 113, 114, 115, 116].

Energy-loss near-edge structure: At higher energy resolution, the core-losses present fine structures from 0 to 30 eV after the ionization edge called energy-loss near-edge structures. In this thesis, we investigated the fine structures of the O *K* and Fe $L_{2,3}$ edges to better understand the electronic structure of the probed thin films. Thus, the Fe $L_{2,3}$ carries detailed information on the valence and spin states and on the site symmetry of Fe. On the other hand, the information about the hybridization of O with Fe (and Bi) are contained within the O K edge fine structures. The spectral signatures of valence, site symmetry, spin and hybridization are recognizable as energy shifts and/or shape changes of the fine structures [116]. These fine structure changes are subtle and therefore require EEL spectra to be acquired at large spectral dispersion (0.063 eV ch^{-1}). Even though the task is more challenging than elemental mapping, several authors have already shown that it is possible to map the coordination [117, 118] or the valence states [119, 120, 121] of transition metals down to the atomic scale.

The O *K* edge originates from $1s \rightarrow 2p$ transitions. The Fe *L* is split by the spin-orbit of the $2p$ states into the L_3 and L_2 peaks originating from $2p_{3/2} \rightarrow 3d$ and $2p_{1/2} \rightarrow 3d$ transitions, respectively. The $L_{2,3}$ edges (Fig. 3.14) are called white lines due to their high cross-section related to the large overlap between the $2p$ core hole and $3d$ states [107]. The transitions responsible for the O *K* and Fe $L_{2,3}$ edges are mostly dipolar with a small momentum transfer [102]. Hence, to avoid the spectral broadening from residual aberrations in the spectrometer and additional non-dipolar transitions the fine structures were probed with $\beta = 20$ mrad.

There are no EELS reference for BIG in the literature. We will thus discuss the fine structures of Fe $L_{2,3}$ for iron oxides with comparable density and Fe ground states (spin states and hybridization amount). Hence, the analysis of the fine structures of Fe $L_{2,3}$ are transferable from one oxyde to another [122]. Thus, the different fine structures related to the Fe^{4+}, Fe^{3+} in O_h and T_d coordinations and Fe^{2+} are described here.

- **Fe^{3+} O_h**: The spectral shape of Fe^{3+} is known to be dominated by excitations from a $3d^5$ ground state. The EELS spectrum of O_h Fe^{3+} is shown

[12] A quantification of the resolution of atomic scale EELS mapping is possible using a simulation of the electrons propagation.

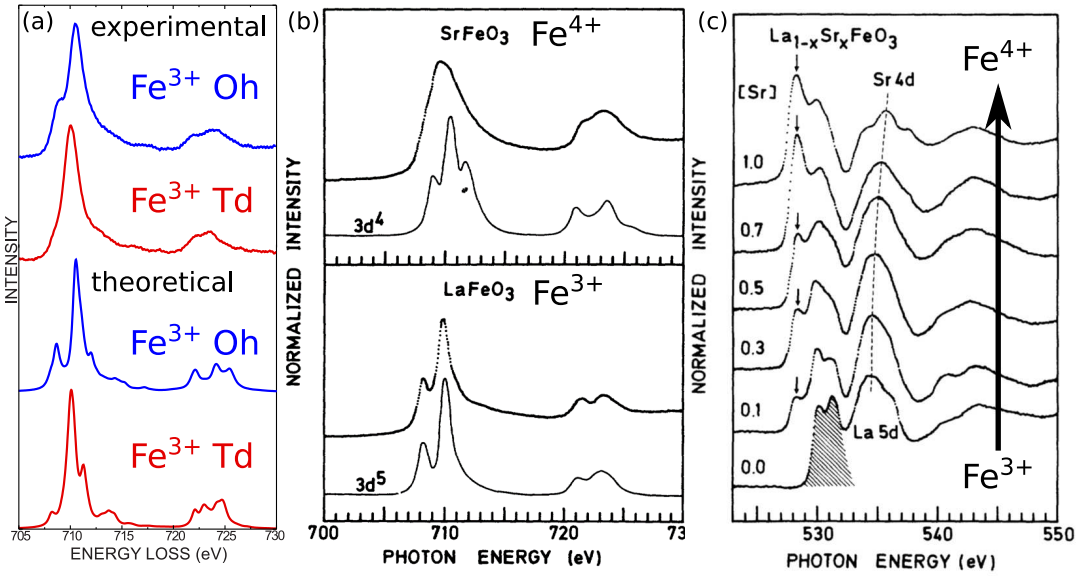

FIGURE 3.14: a) Experimental and theoretical EELS spectra of Fe^{3+} $L_{2,3}$ edge in O_h and T_d coordination probed in $NiFe_2O_4$ b) Experimental and theoretical spectra of O_h Fe^{3+} and O_h Fe^{4+} $L_{2,3}$ edges in $LaFeO_3$ and $SrFeO_3$ respectively. c) Experimental EELS spectra of the O K edge in the $La_{1-x}Sr_xFeO_3$. This figure is adapted from ref. [123] for $La_{1-x}Sr_xFeO_3$ and ref. [124] for $NiFe_2O_4$

in Fig. 3.14 (a) [124]. The O_h L_3 peak has a maximum at ca. 710 eV and a shoulder at ca. 708 eV. These two features are well separated due to the strong crystal field of the O_h configuration. The O_h L_2 is mostly composed of 2 peaks at 721 and 723 eV, the latter being slightly more intense [125, 126, 127].

- **Fe^{3+} T_d**: The spectral shape of T_d Fe $3d^5$ is shown in Fig. 3.14 (a) [124]. The T_d L_3 peak maximum is shifted to 0.4 eV lower energy with respect to the maximum of the O_h L_3. In many T_d environments, the shoulder of the T_d L_3 is less intense than the one of the O_h L_3 (associated to lower crystal field intensity in T_d environment and to different e_g/t_{2g} hierarchy.) [124, 122]. The T_d L_2 is very similar to the O_h L_2 except that it is spread on a narrower energy range [117, 118].

- **Fe^{4+}**: The Fe^{4+} has a mixed ground state of $3d^4$ and $3d^5\underline{L}$ where $\underline{L}$ is a ligand hole. Hence, the Fe^{4+} fine structure changes with respect to Fe $3d^5$ are very subtle on the Fe $L_{2,3}$ edge. This is shown in Fig. 3.14 (b) for Fe in O_h coordination in the $La_{1-x}Sr_xFeO_3$ solid solution where $La^{3+}Fe^{3+}O_3$ has Fe^{3+} and $Sr^{2+}Fe^{4+}O_3$ has Fe^{4+}[123]. It especially challenging if only a fraction of Fe_{4+} is present in the probed specimen. Nevertheless, the $\underline{L}$ is responsible for a strong pre-peak on the O K edge as shown in

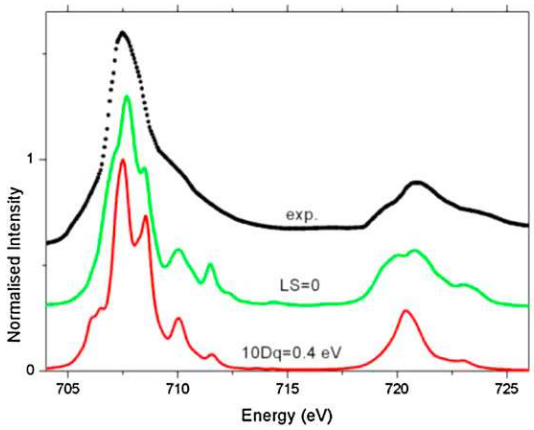

FIGURE 3.15: Experimental and theoretical EEL spectra of O_h Fe^{2+} $L_{2,3}$ edge in FeO. This figure is adapted from ref. [122]

Fig. 3.14 (c) for the $La_{1-x}Sr_xFeO_3$. In this work, the presence of Fe^{4+} is then mainly investigated by EELS on the O *K* edge [128, 129, 130, 131].

- **Fe^{2+}**: The spectral shape of Fe $3d^6$ is shown in Fig. 3.15 for FeO (O_h coordination) [122]. The maximum of the L_3 peak is shifted to around 708 eV that is almost 2 eV to lower energy. The principal shoulder of the L_3 peak is at around 710 eV at higher energy than the L_3 maximum in contrast to the $3d^5$ configuration. The L_2 peak is also shifted of about 2 eV to lower energy and is mainly composed of one strong peak [125, 132, 126].

In this work, the fine structures of the O *K* edge are investigated to assess the presence of Fe^{4+} in Ca and Y co-substituted thin films. The presence of oxygen vacancies that induce the formation of Fe^{2+} is studied using the Fe $L_{2,3}$ edge. The Fe $L_{2,3}$ edge was also probed at the atomic scale to unveil the possible link the coordination and charge state of Fe.

3.1.7 Sample preparation of films for electron microscopy

The samples for electron microscopy studies were prepared in the cross-section geometry by focused ion beam (FIB) using a Scios DualBeam equipement (ThermoFischer) in the NANOTEM platform (EquipEx TEMPOS project) [13]. The FIB is equipped with a source of Ga ions accelerated at a few kV which is used to extract a few μm^2 lamella for STEM observation for the film. The obtained lamella is a cross section of the film and the substrate that is approximately 70 nm thick. During the FIB extraction, Bi atoms can evaporate and

[13] The FIB lamella were prepared by Laura Bocher.

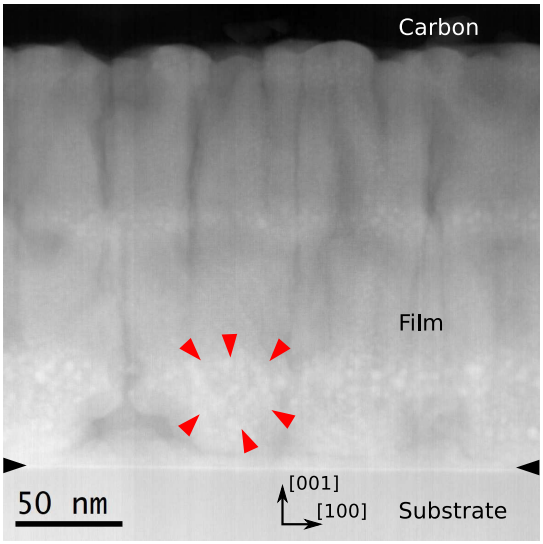

FIGURE 3.16: HAADF image of a Bi-rich iron garnet thin film. The film/substrate interface is highlighted by black arrowheads. A typical area with the Bi redeposits is highlighted with red arrowheads.

redeposit as clusters on the surface of the lamella. The Bi redeposits can be seen as circular higher contrast spots in Fig. 3.16. This effect can be limited by cleaning the lamella with a low energy ion beam (i.e. 2 kV and 27 pA). Using the FIB preparation, lamella of constant thickness can be extracted which is important for EELS and image analysis (section 3.2.1). The FIB also allows the extraction of lamellas along specific crystallographic axes or specific areas e.g. with a Pt contact pad.

3.1.8 X-ray magnetic circular dichroism (XMCD)

The XMCD studies were performed on the ALICE beamline [133, 134] at the BESSY II synchrotron which acts as a high brightness X-ray source [14]. The XMCD was probed on a few selected thin films: as-grown B($Ca_{0.3}Y_{0.2}$)IG, as-grown B($Ca_{0.0}Y_{0.5}$)IG, TA96 B($Y_{1.0}$)IG and BIG as a reference sample.

X-ray magnetic circular dichroism (XMCD) is analoguous to the Faraday ellipticity described in section 2.1.2 (or the Kerr ellipticity depending on the geometry) but in the X-ray range. The absorption difference of right- and left-circularly polarized X-rays yields the XMCD signal. XMCD at the Fe $L_{2,3}$ edge probes similar transition as in EELS, that are described in section 3.1.6, and additional Fe specific MO information can be obtained. This tool is notably useful to disentangle the spectroscopic contributions from coordination

[14] The beamline operation was supervised by Radu Abrudan and Sergio Valencia.

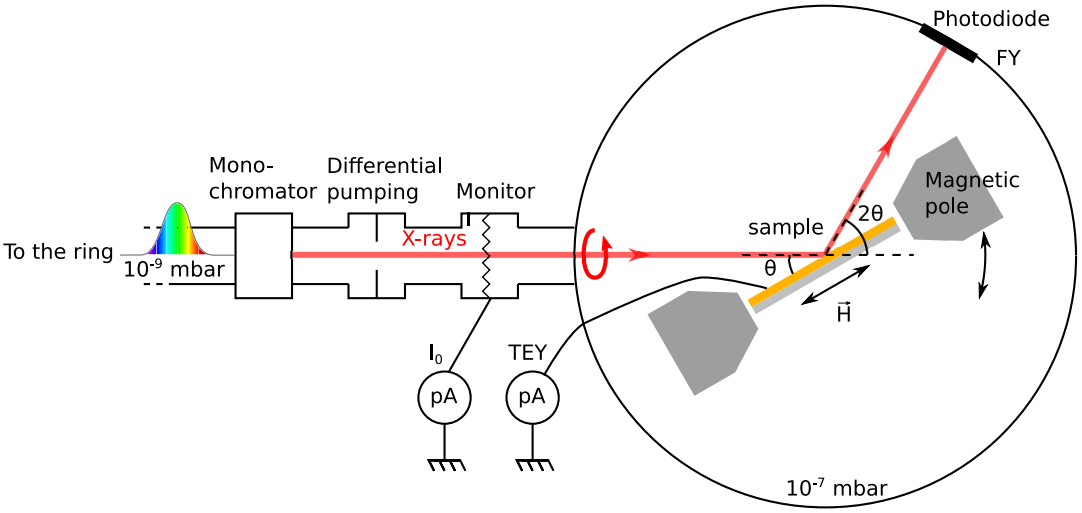

FIGURE 3.17: Simplified scheme of the ALICE beamline at the BESSY II synchrotron.

and charge [135]. In this work the XMCD signals of the Fe $L_{2,3}$ and Ca $L_{2,3}$ edges were investigated.

A scheme of the ALICE beamline is shown in Fig. 3.17. The beamline works with circularly polarized soft X-rays in the range 20 to 1900 eV. A 0.1-0.2 eV energy resolution is achieved with the monochromator (Fig. 3.17). In the sample chamber a pressure of around 10^{-4} mTorr is maintained to prevent X-ray absorption from air. To correct for the intensity fluctuations of the beam, the current in a X-ray transparent gold mesh (I_0 in Fig. 3.17) is measured by a Keithley pico Ampere-meter for normalization. The specimen makes an angle θ with the incident X-ray (Fig. 3.17) and θ can vary between -180 and 180 deg. An electro magnet that can rotate independantly is used to apply an in-plane (parallel to the film/substrate interface) magnetic field of up to $\pm$ 370 mT. This magnetic field is enough to saturate Bi-rich iron garnets. The interaction of X-rays with the sample can be measured in two ways:

- The total electron yield (TEY) is the measure of electrons emerging from the surface of the sample after the interaction with X-rays. Due to the low mean free path of electrons in solids TEY is mostly surface sensitive (about 5 nm [133]). The signal is collected through a wire glued with silver paste on the surface of the sample and measured by a Keithley pico Ampere-meter. This method yields quantitative results that are very similar to X-ray absorption spectroscopy (XAS) and EELS. A magnetic field cannot be applied during the TEY measurement as the electrons would interact with it. The TEY XMCD is then measured solely in remanence.

- The fluorescence yield (FY) is the measure of X-rays originating from the fluorescence decay. In contrast to TEY, the mean free path of X-rays in solids is much larger with a probing depth of around 100 nm [133]. The signal is collected at an angle 2θ with the incident beam by an IRD silicon photodiode [133] that can rotate around the sample from -175 to 175 deg. During the FY measurements an applied magnetic field can be applied and the magnetic hysteresis cycles were performed in FY. The FY only yields qualitative results [136, 137, 138].

In practice, the XMCD signal is obtained by measuring twice only one circular polarization but once with a parallel applied magnetic field (σ^+) and a second time with an anti-parallel (σ^-) applied magnetic field. This method yields the same results as using left- and right-circular polarizations. Both I_{σ^+} and I_{σ^-} are always normalized by I_0. The XMCD spectra are obtained calculating $I_{XMCD} = I_{\sigma^+} - I_{\sigma^-}$ and I_{XMCD} is normalized using $I_{XAS} = I_{\sigma^+} + I_{\sigma^-}$. The O *K* was also measured during the experiments but the results are not discussed in this thesis. The gold mesh used for intensity normalization was slightly oxidized, then the O *K* of the mesh appears in I_0 which prevents the normalization of the signal. The intensity of the hysteresis cycles were also not normalized by I_0 as the strong magnetic field of the magnet also perturbs the I_0.

3.2 Data analysis tools

3.2.1 Geometric phase analysis (GPA)

The studied thin films undergo a compressive strain of up to 2% from the substrate. The strain distribution and the strain relaxation mechanisms were investigated using GPA on atomically-resolved HAADF images of the film/substrate interface.

Principle

The GPA is an image processing method developed by Hÿtch, Snoeck, and Kilaas [139] for the analysis of strain and structural defects in crystal lattices in High Resolution TEM. It is also possible to use this technique on atomically resolved HAADF images. The GPA is using reciprocal space filtering to determine the local displacement of atomic columns (or strain) in the image.

The strain is determined with respect to a reference area picked in the image which, in our case, is the substrate.

The operating principle of the GPA is presented in Fig. 3.18. First, a Fourier transform (Fig. 3.18 (b)) of the image (Fig. 3.18 (a)) is performed. A mask is applied on two selected reciprocal lattice reflections. The phase part inside these masks is used to extract an image of the real-space phase for each reflection (Fig. 3.18 (c)). Maps of the strain are computed using the phase images (Fig. 3.18 (d)). The link between the phase images and the strain maps are detailed in appendix B. The position of the masks in the reciprocal space are optimized so that strain is zero in the reference area.

Application to atomically-resolved HAADF images

The instrument used here is a Cs-STEM described in section 3.1.5 and the atomically-resolved images are acquired with a HAADF detector. HAADF images have the advantage of suffering no contrast reversal over a wide range of focus values and sample thicknesses in contrast to HRTEM images [104]. The HAADF images are then straightforward to interpret and analyse over relatively large field of view even in the case where the thickness of the sample is slightly inhomogeneous.

However, STEM imaging obviously implies to scan over the region of interest which is at the origin of additional noise for the strain analysis compared to HRTEM images. The main source of errors occurs when the probe goes from one pixel row to the next one, which corresponds to the slow scan direction (in opposition to the fast scan direction that is along a row). Along the slow scan direction, both sample drift and fly-back errors result in a contraction or a dilatation of the image yielding an incorrect strain. To overcome this effect, for every GPA processing, a set of two images of the same region of interest are acquired with a 90 deg angle relative to each other [140]. The strain profiles were always integrated along the direction perpendicular to the computed strain component to avoid processing noise. Then the image acquisition parameters were chosen to ensure a sufficient signal to noise ratio and sampling rate while limiting the sample and hardware temporal instabilities.

The GPA were performed on images of 4096×4096 px^2 on a field of view of 80×80 nm^2 with a pixel dwell time of 19μs. For the geometric phase analysis, a mask size of 0.4 nm^{-1} was chosen, which corresponds roughly to $1/2a_{sub}$ ($a_{sub} = 1.2383$ nm). This mask size is a compromise between spatial resolution and noise level as both these parameters increase with the size of

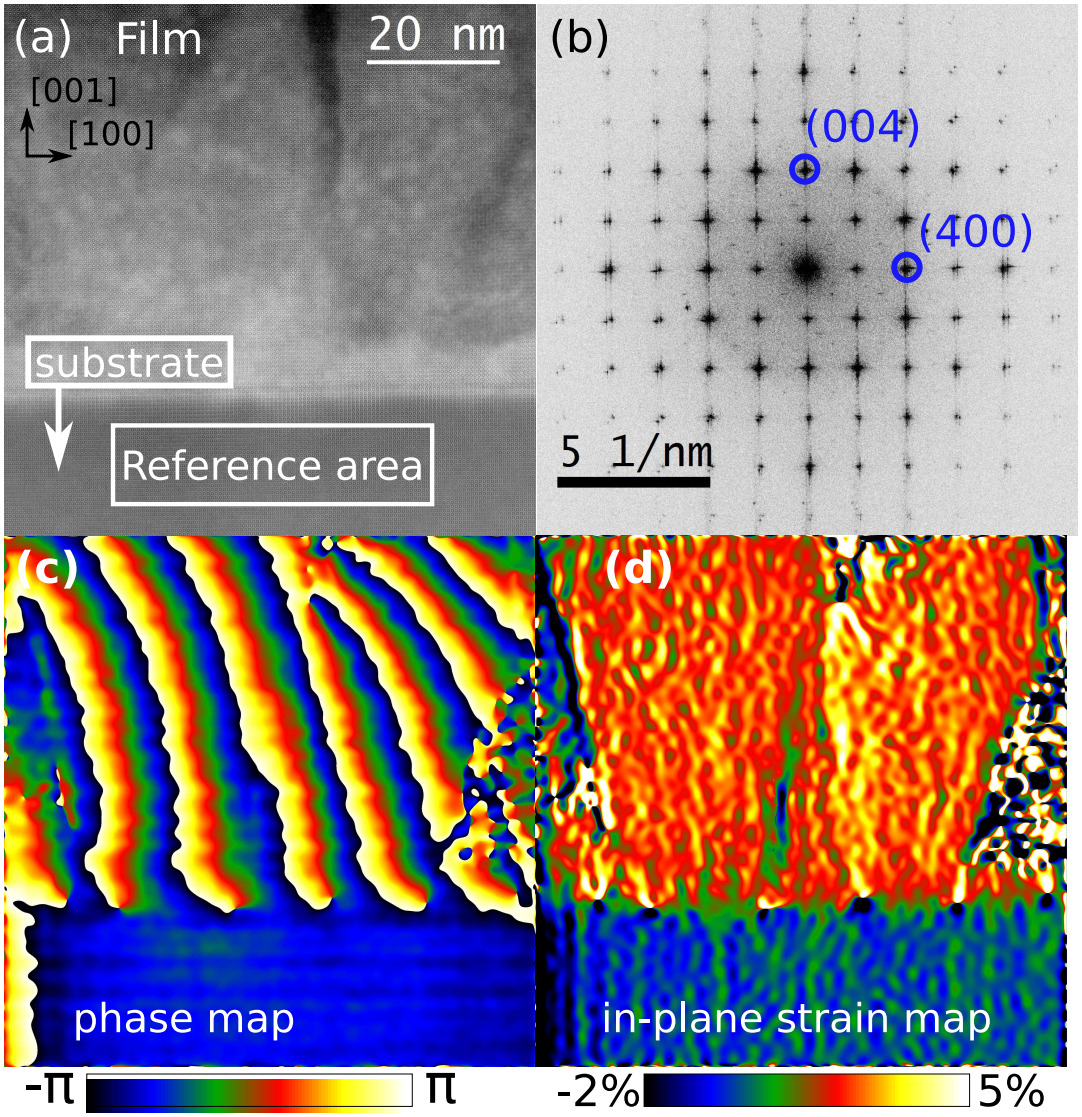

FIGURE 3.18: a) atomically resolved HAADF image of the film/substrate interface. The reference area used during GPA is indicated by a white rectangle. b) Fourier transform of (a). The (400) reflection in blue was used to extract (c) and (d) and the mask is indicated by a blue circle. c) phase map obtained after filtering of (b). d) In-plane strain map computed using (c).

the mask [140]. The masks were applied on the (004) and (040) reciprocal lattice reflections. The profiles of i-p relative strain and o-o-p relative strain with integration direction parallel to the film/substrate interface were then used for data analysis [140]. The acquired images always contain about 20 nm of the substrate which is used as reference area. The mask position is optimized so that the strain in the substrate is 0% in average.

3.2.2 Principal component analysis (PCA)

To achieve atomically resolved elemental maps, the acquisition time at each pixel of the SpIm is limited by the drift of the sample and by the damage induced by the electron probe. Therefore, each EELS spectrum of the SpIm is noisy with a mixture of gaussian and poissonian distributions and the PCA is used to overcome this issue.

Principle

The PCA is generally used for interpretation and reduction of the data. In this work, it was only used to denoise the STEM/EELS elemental map. This technique is commonly used in a variety of scientific fields and EELS is one of them [141].

A dataset can be describe in a n-dimensional space in which a set of coordinates can be attributed to each data point. The PCA is based on the hypothesis that signals[15] in a dataset have high variance while noise have lower variance. The algorithm changes the basis set on which the data are projected and finds new basis vectors that point in the directions of decreasing variance. The first vector of this new basis set therefore contains most of the variance of the complete dataset. A vector of the new basis set is called a component. Components with high variance, called "principal components", describe most of the signal while the other components describe only noise. By keeping only the principal components, a reduced dataset is built and contains most of the variance of the original dataset (explained variance). In the present work, the PCA was applied using the Hyperspy Python library [142] designed for the processing of multi-dimensional data. The algorithm used to perform PCA in Hyperspy is the singular values decomposition which is a generalized way of diagonalizing a non-square matrix of real numbers.

[15] By signals, we mean spectral features containing a physical meaning.

Application to EELS hyperspectral data

The electron scattering events through the observed material follow a Poisson's law. That is why the noise in EELS is primarily following a poissonian distribution which variance scales with electron count. The electron detection suffers from dark current noise (Poissonian) and read-out noises (Gaussian) that add up on the measured signal. A dedicated PCA algorithm, i.e. weighted PCA [143] was used on EELS SpIm taking in account the mixed poissonian and gaussian nature of the noise. In Fig. 3.19, typical results of PCA processing on an elemental map are shown.

The key part of the PCA processing is to choose the correct number of principal components that contain most of the explained variance without rejecting any minor signal. For this purpose, we present here several visualisation tools to discriminate between signal and residual noise:

- The scree plot (Fig. 3.19 a)) shows the explained variance corresponding to each component, in most cases the first few components, i.e. less than 10, contain all the relevant signal and there is an inflexion point in the plot after which mostly noise is remaining.

- The decomposition factors are the different components obtained by PCA. The first principal component is shown in Fig 3.19 (b) which corresponds to the negative average spectrum of the SpIm. Thus, the average Fe $L_{2,3}$ edge is recognizable (Fig 3.19 (b) inset). The 9^{th} component seems to describe only high frequency noise and no core-loss edge is identifiable (Fig 3.19 (d)).

- The decomposition loadings show maps of the weight of each component. The map of the first principal component is shown in Fig. 3.19 (c) while a map of a component containing only noise is shown in Fig. 3.19 (e).

The principal components are then chosen after the inspection of decomposition factors and decomposition loadings, leaving factors and loadings containing only noise. In the scree plot, the point after which the remaining points follow a linear behavior is usually a good estimation of the number of components. The factors are a linear combination of the signals contained in the dataset and are difficult to interpret because they do not correspond to real physical EELS spectra. The PCA algorithm tends to spread the variance over a high number of components in the case of low SNR, which results in the loss of information [144]. Furthermore, the PCA is an algorithm that uses

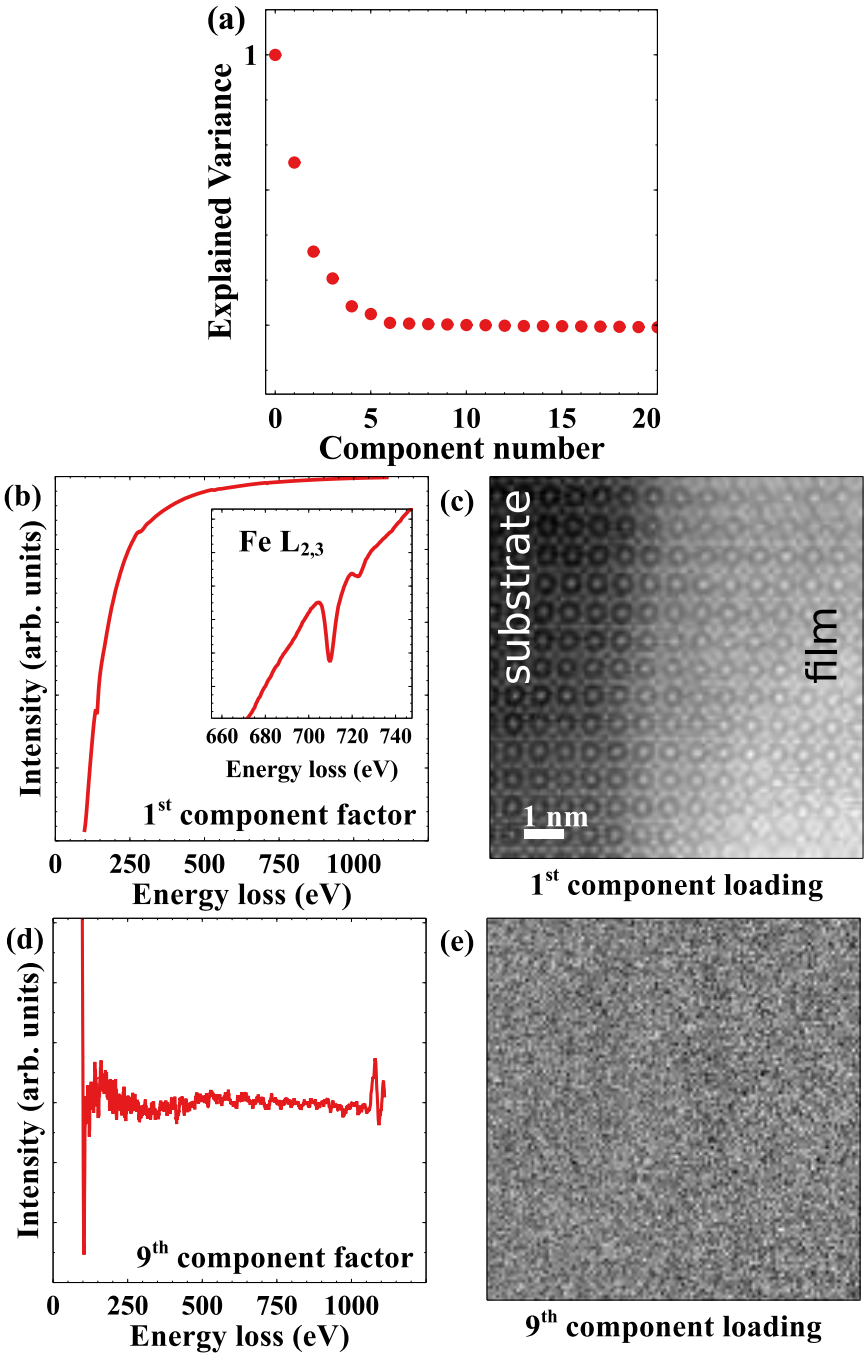

FIGURE 3.19: Determination of the number of components for the PCA of an elemental map at the film/substrate interface. a) Scree plot of the explained variance. b) Decomposition factor corresponding to the 1st component. A zoom on the Fe $L_{2,3}$ edge of the 1st component is shown in inset. c) Weight map of (b). c) and d) 9th component factor and its correspoding weight map, respectively.

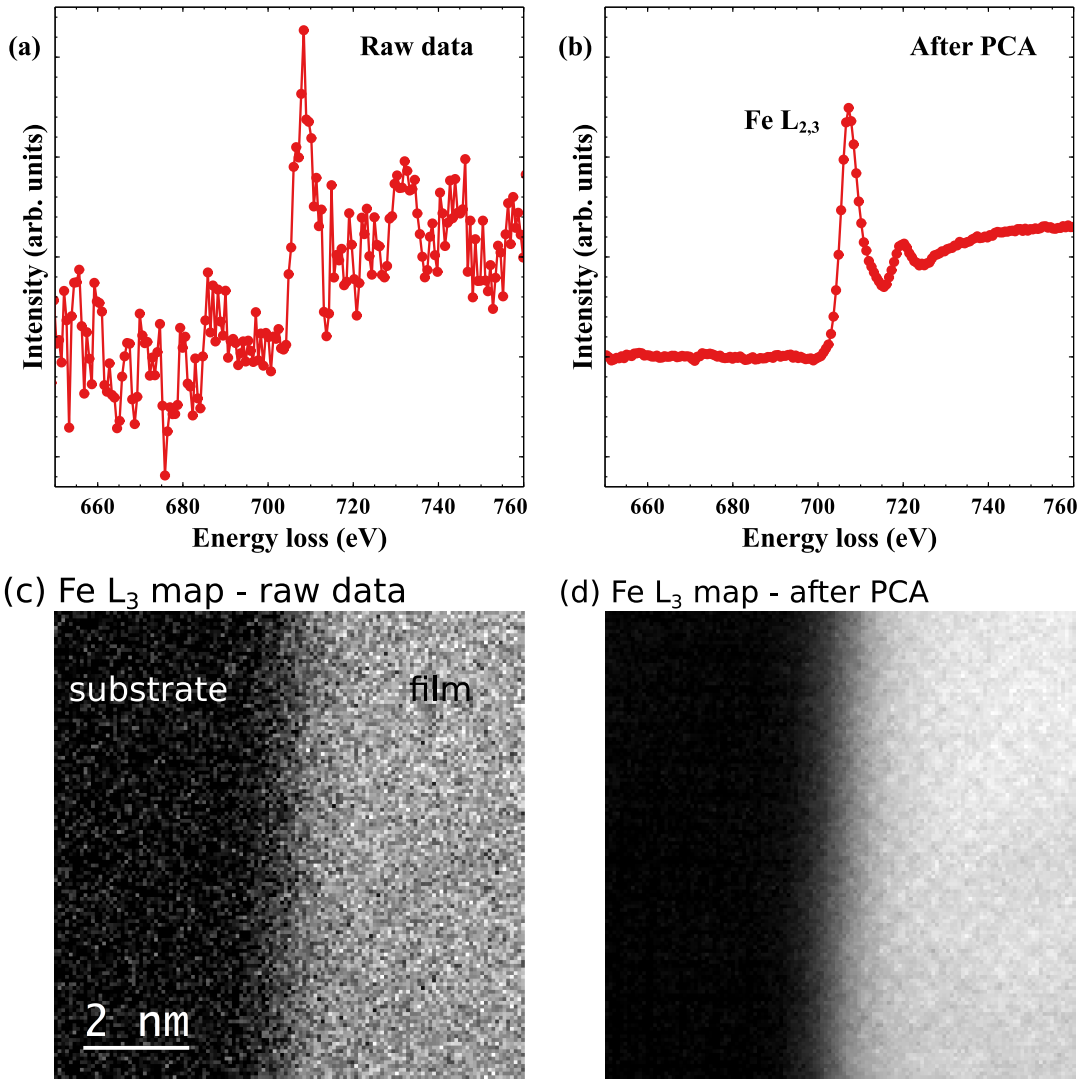

FIGURE 3.20: Comparison of elemental maps at the film/substrate interface before and after PCA retaining 8 components. a) and b) Fe $L_{2,3}$ edge of a typical pixel acquired in 30 ms before and after PCA, respectively. a) and b) Fe $L_{2,3}$ edge intensity maps before and after PCA, respectively.

linear algebra and therefore tends to produce artefacts when there are non-linearities in the data such as plural electron scattering or core-loss edges fine structures variations. Therefore, in the present work, PCA was only applied for elemental mapping such as the one presented in Fig 3.20.

3.3 Data analysis developments

3.3.1 Cluster analysis

Introduction

While it is difficult to analyze STEM/EELS elemental maps at the atomic scale, it is even more challenging to map subtle changes in the fine structures of core-loss edges due to the limited SNR. Here, the goal is to identify and localize the spectral signatures (e.g. Fe^{3+} O_h) within an atomically resolved SpIm despite the mixing of these spectral signatures due to the delocalization and the noise. Spectral unmixing techniques such as independent component analysis (ICA) [145] or vertex component analysis (VCA) [146] were already developed and applied on this type of data. However, ICA assumes that the different spectral signatures are statistically independent and VCA assumes that the dataset contains pure pixels which contain only one of the different spectral signatures. Both techniques also make the hypothesis that the mixing of the spectral signatures is linear.

We developed [16] the cluster analysis (or clustering) for the interpretation of fine structures in SpIms which uses less restrictive hypothesis on the structure of the explored dataset. The cluster analysis is a well-known technique in the field of data-science [147] that aims at grouping spectra according to their similarity. However, this technique was only used very recently in the EELS community [148, 149, 150] and mostly for the analysis of elemental maps, i.e. with well separated spectral signatures and higher SNR, but already yield interesting results. Here, first tests were applied on the analysis of the fine structures of Co L_3 through the cluster analysis on a model system, Co_3O_4, as a proof of principle to validate the clustering method applied on mixed-valence states and O_h/T_d sites mapped using STEM/EELS.

First, the clustering algorithm used in this study, K-means++, is introduced. Then, we describe the atomic and electronic structures of Co_3O_4 to clarify how it is a suitable model system to test the validity of the clustering approach for the further study of Fe L_3 in iron garnets (section 5.3.2). Synthetic SpIm are created to assess the performance of the K-means++ algorithm and its domain of application in terms of SNR. We evaluate the statistical distribution of experimental spectra to estimate the expected results of clustering. Finally, the results of clustering on an experimental atomically-resolved SpIm of Co_3O_4 are presented.

[16] Nathalie Brun (LPS) helped us to develop the cluster analysis.

K-means++ algorithm

When performing the clustering, the aim is to assign a label (k) to every spectrum of the dataset so that they belong to the clusters C_k [17]. Within each cluster, the spectra should be as similar as possible while spectra from different clusters should be as different as possible. In this work, the similarity between spectra was determined by computing the Euclidian distance between spectra of the dataset. A SpIm of $x \times y = N$ spectra that have p energy-loss channels are considered as a collection of N points in a p dimensional space, i.e. each spectrum is a point and the intensities in each channel are p coordinates. The Euclidian distance between spectrum a $(a_1, a_2, \ldots, a_p)$ and spectrum b $(b_1, b_2, \ldots, b_p)$ is then $d_E = \sqrt{(a_1 - b_1)^2 + (a_2 - b_2)^2 + \cdots + (a_p - b_p)^2}$. The smaller the d_E value, the more similar are the spectra.

The cluster analysis was performed using the K-means++ algorithm of the scikit-learn Python library [151]. To perform this algorithm, the user sets the number of clusters n and a tolerance value. It implies that generally some prior knowledge is required to guess the number of spectral signatures in the SpIm, e.g. two valence states or two coordination sites. In this study, the default tolerance value of 0.0001 was used as it yield good results. The steps of the K-means++ algorithm are described here:

- **Initialization** A set of n points of the p dimensional space is set randomly. These points are called centroids.
- **Assignment** Each data point is associated to its nearest centroid.
- **Update** The average of the spectra contained within each cluster is computed and the centroids are assigned to these new positions. If the centroids moved less than the tolerance value then the algorithm goes to the next step. Otherwise, the algorithm goes back to the **Assignment** step.
- **Randomization** The results depend strongly on the **Initialization** step. Therefore, the **Assignment** and **Update** loop is computed for several **Initialization**. The final output is the average of the results.

The computation time of K-means++ scales linearly with the size of the dataset [147] and is then a fast algorithm. For instance, cluster analysis with $n = 3$ of a SPIM with $N = 2600$ and $p = 250$ takes less than a second to compute. Its working principle and its outputs are fairly simple which help the

[17] This is not exactly true as some clustering algorithms are designed to exclude outliers.

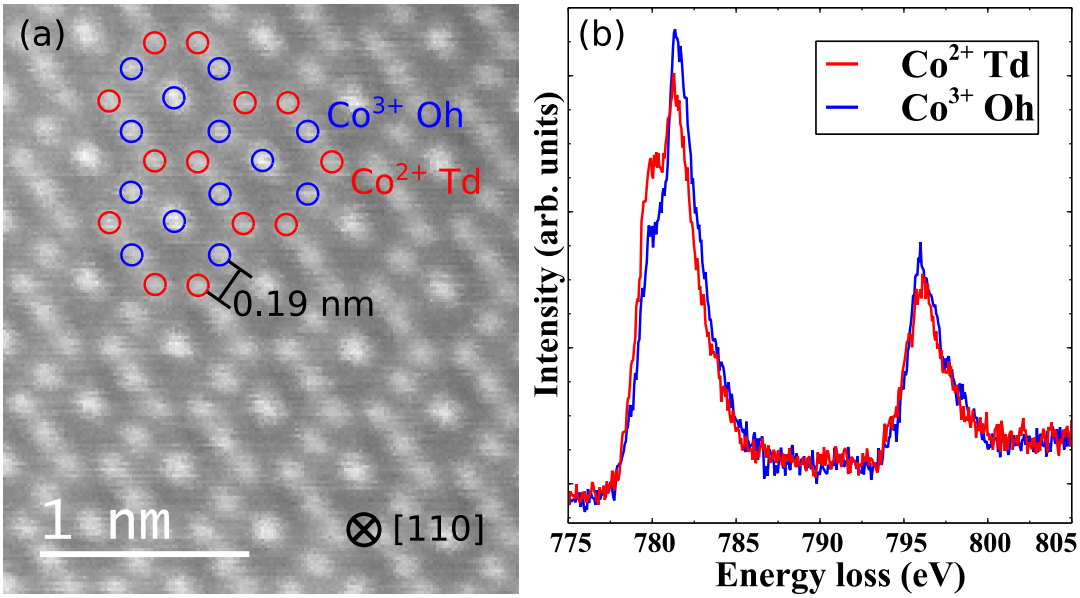

FIGURE 3.21: a) Atomic scale STEM-HAADF image of Co_3O_4. The Co^{3+} O_h columns are highlighted in blue and the Co^{2+} T_d columns are highlighted in red. b) Sum of 80 spectra extracted from Co^{3+} O_h columns and Co^{2+} T_d columns. The energy dispersion used was 0.063 eV ch^{-1} and each spectrum was acquired in 20 ms.

interpretation of the results. However, the clusters obtained with K-means++ are isotropic. This is a problem, for instance, for SpIm with thickness variations as the collection of spectra would take a hyper-line shape. Here, we work with atomically resolved SpIm which should reduce the impact of the thickness variations.

Co_3O_4 as a model system

The Co_3O_4 is used as a model system because it is a mixed valences states compound and the distribution of the Co valence states is well-known. Here a typical SpIm probed on a Co_3O_4 nanoparticle at the UltraSTEM200 [18] was first tested to validate the clustering approach.

Co_3O_4 is a binary oxide that crystallises in the normal spinel structure with the *Fd*3*m* space group and a lattice parameter of 0.8065 nm [152]. In the unit cell, two thirds of the Co ions are in the O_h site with 3+ valence while one third of the Co ion is located in the T_d site with 2+ valence. In the studied SpIm, the Co_3O_4 nanoparticle is observed along the [110] zone axis. Along [110] the atomic columns are purely composed of either Co^{2+} T_d or Co^{3+} O_h, these columns are indicated in Fig. 3.21 (a). Raw spectra extracted from the atomic columns corresponding to Co^{3+} and Co^{2+} are displayed in Fig. 3.21 (b).

[18] This experiment was carried out by Laura Bocher.

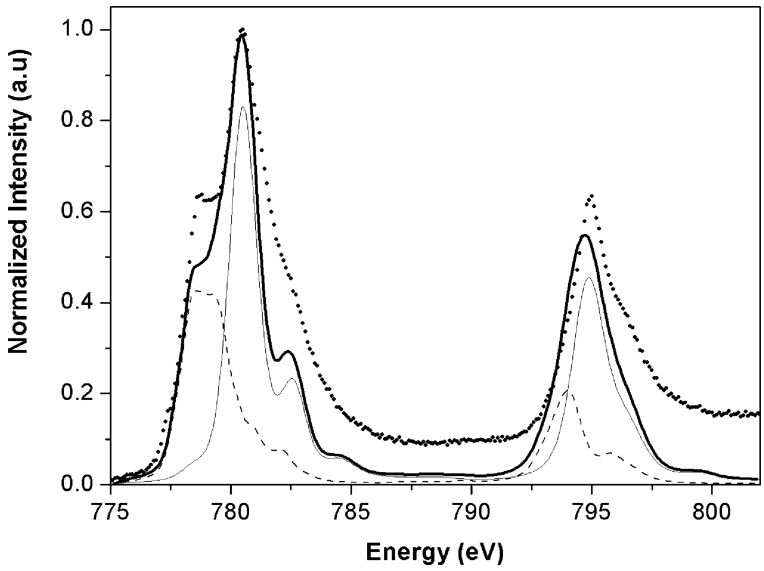

FIGURE 3.22: The experimental X-ray absorption spectrum of Co_3O_4 is displayed as dots. The theoretical spectrum is shown as a thick solid line and is the sum of the Co^{3+} spectral signature as a thin solid line and of the Co^{2+} spectral signature as a dashed line. This figure is adapted from ref. [153].

Co is the transition metal with a $L_{2,3}$ absorption edge at 780 eV that exhibit similar fine structures as the Fe $L_{2,3}$ edge. The XAS of Co_3O_4 $L_{2,3}$ edge is displayed in Fig. 3.22 together with simulated Co^{3+} and Co^{2+} $L_{2,3}$ edges [153]. Similarly as Fe fine structures, the Co^{2+} L_3 edge is at approximately 1 eV lower energy compared to the Co^{3+} L_3 edge. Therefore, the intensity of the shoulder of the Co L_3 edge in Co_3O_4 scales with the presence of Co^{2+}. The sum of spectra from T_d and O_h sites (Fig. 3.21 (b)) show a behavior similar to that expected in theory [153].

Co_3O_4 is a suitable model system to compare with iron garnets as fine structure variations of Co L_3 are rather analogous to the ones expected on the Fe L_3 edge in iron garnets. Moreover, the minimum distance between Co^{3+} O_h and Co^{2+} T_d columns is 1.9 Å which is in the same range as the distance between Fe T_d and Fe O_h in iron garnets ([100]), i.e. 1.6 Å. However, in spinel oxides, the contributions from the different coordination sites cannot be disentangled from the contributions of the mixed valence state. In this section, we will evaluate the capacity of clustering to retrieve the known distribution of valence states in Co_3O_4.

Synthetic SpIm

Synthetic SpIm were designed and generated to test the performances of the K-means++ algorithm with controled parameters. With this method, the true

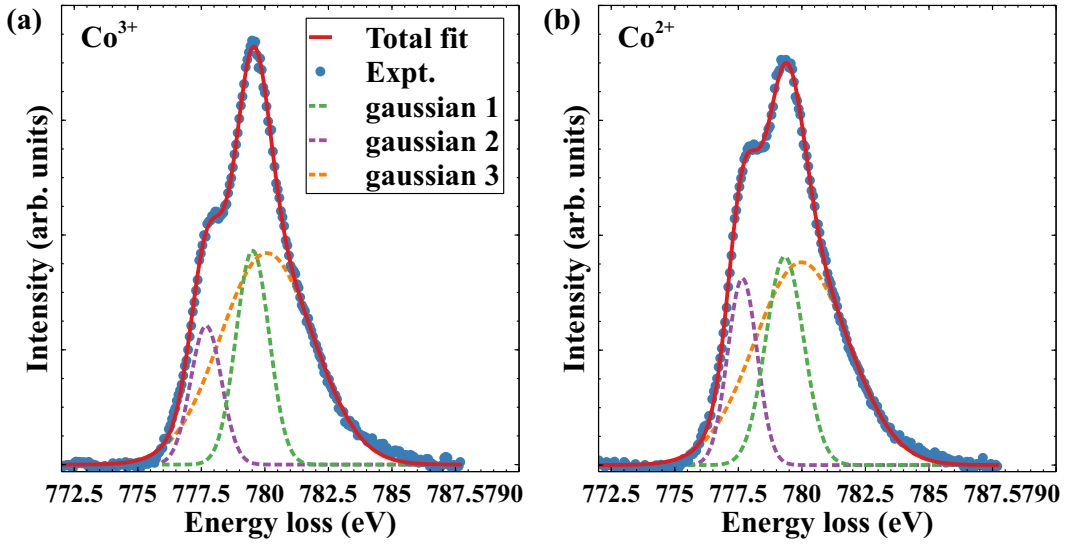

FIGURE 3.23: a) and b) Fit of the Co^{3+} and Co^{2+} L_3 edges with three gaussian components, respectively.

labels of clusters are known and the correctness of the clusters assignement by K-means++ can be measured.

When using the K-means++ algorithm, the numbers of clusters, n, must be defined by the user. The results of the cluster analysis strongly depends on n and we attempt here to define a criterion to set the optimal n value for the analysis of EELS fine structures. First, the effect of the SNR is investigated. The changes in EELS fine structures are also investigated in terms of intensity changes, e.g. intensity of the Co L_3 edge, energy shifts, e.g energy shift between Co^{2+} and Co^{3+}, or overall distance between spectra. The aim is to determine a threshold, for these quantities, below which the assignment of spectra to clusters by K-means++ is not better than the random assignment.

For that purpose, synthetic SpIms of the Co L_3 edge were created with 60 $\times$ 60 pixels where the 30 top rows contain one spectral signature while the 30 bottom rows present another spectral feature. For the sake of simplicity in the interpretation of the results, only the L_3 edge compose the spectral signatures of the artificial SpIms. The experimental Co L_3 edges were simulated using 3 gaussians as shown in Fig. 3.23 (a) and (b) for Co^{3+} and Co^{2+}, respectively [19]. The noise in the spectra is simulated by a sum of gaussian noise and of poissonian noise [154]. The standard deviation of the gaussian noise (σ) is generally selected to match the noise level of the experimental data. A typical spectrum obtained in 20 ms of the experimental SpIm and of the simulated SpIm are shown in Fig. 3.24 and show good agreement.

[19] The background is also subtracted to further simplify the problem.

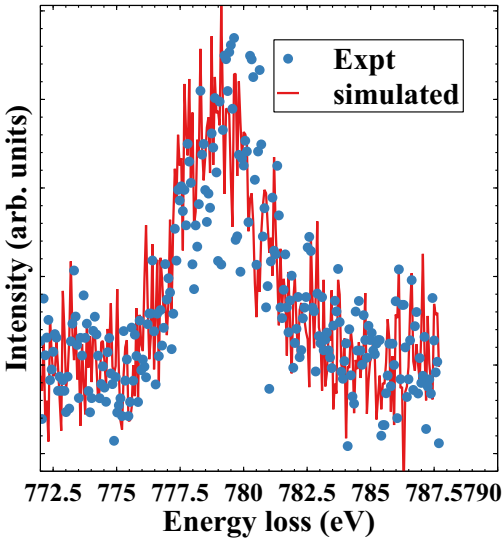

FIGURE 3.24: Comparison between an experimental spectrum (dots) and a simulated spectrum (solid line) showing a comparable noise level.

The performance of the cluster analysis on the synthetic SpIms is assessed by calculating the percentage of wrong attribution. The 30 upper lines should be labeled $k = 0$ while the 30 lower lines should be labeled $k = 1$, any mis-allocation is then easy to detect. A score of 100% corresponds to a perfect assignment while a score of 50% corresponds to a random assignment.

K-means++ performance tests

The synthetic SpIms were first used to test the required SNR to separate EELS fine structures using clustering. Then, we determine the lowest intensity change or energy shift which can be accurately separated using the cluster analysis.

Signal-to-noise ratio

For this test, the 30 upper lines of the simulated SpIm consist of a Co^{3+} L_3 edge and its 30 lower lines of a Co^{2+} L_3 edge. The clustering algorithm is then computed on multiple synthetic SpIm with varying values of σ simulating varying SNR. The SNR is calculated as SNR $= \frac{\sum_{i=0}^{p} y(i)^2}{\sigma^2}$ where $y(i)$ is the intensity in each channel i and σ is the standard deviation of the noise. Torruella et al. [148] showed that performing the clustering on data pre-processed by PCA improves the overall performances of the cluster analysis. The effect of a PCA pre-processing of the simulated SpIm was then also tested. For the synthetic SpIm tested using a denoising step, PCA is applied

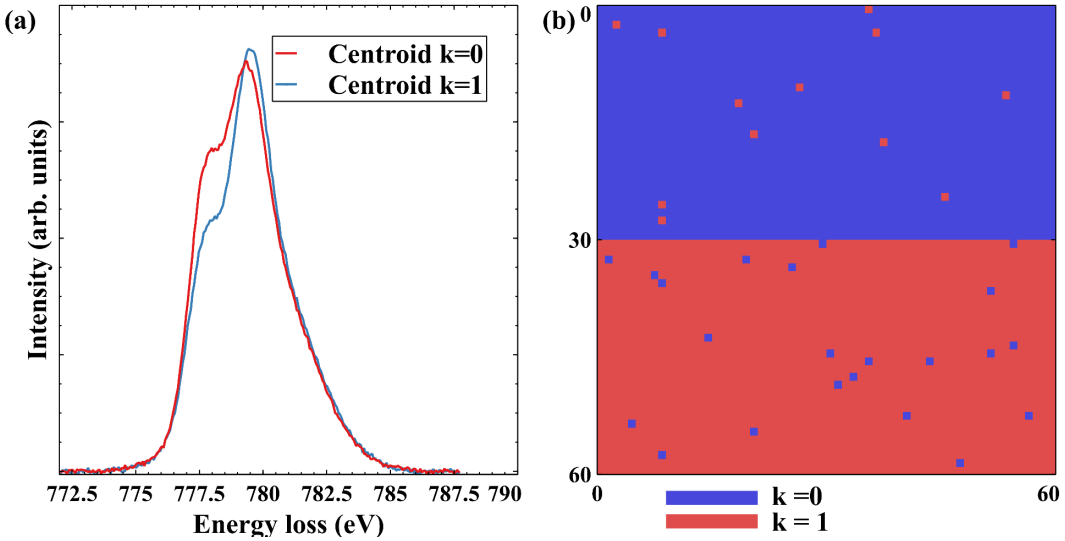

FIGURE 3.25: a) centroids output of the K-means++ algorithm on a synthetic SpIm. b) map of the labels of a synthetic SpIm as computed by the cluster analysis.

before clustering keeping only the 2 first components and K-means++ is then computed.

An example of cluster analysis results is displayed in Fig. 3.25 (a) and (b) for a SNR of 377 and the scores of the clustering for a wide range of SNR are displayed in Fig. 3.26. As expected, the results show that the cluster assignment fails below a certain SNR threshold. Below a SNR of 90 the cluster analysis is less than 90% accurate without PCA pre-processing. Surprisingly, the threshold increases to a SNR of 140 when applying PCA before clustering which implies that the PCA pre-processing hinders the performance of K-means++. In contrast with the work of Torruella et al. [148] that focuses mainly on elemental analysis, subtle variations of the EELS fine structures are studied at the atomic scale in the present work. At this scale, the $Co^{2+/3+}$ spectral signatures overlap due to the delocalization of the electron probe which results in a blurring of EELS fine structures. Thus, under a certain SNR value, the PCA can result in the loss of information [144].

Energy shifts and intensity changes

The subsequent tests aim at determining the minimum detectable energy shift and intensity change. A series of synthetic SpIm was created with the Co^{3+} L_3 edge as reference for the 30 top rows and an additional Co^{3+} L_3 edge with an energy shift that varies for each SpIm of the series for the 30 bottom rows. A similar series was prepared to test the effect of intensity changes. In that case, the intensity of the 2^{nd} gaussian (Fig. 3.23 (a)) was varied to mimic

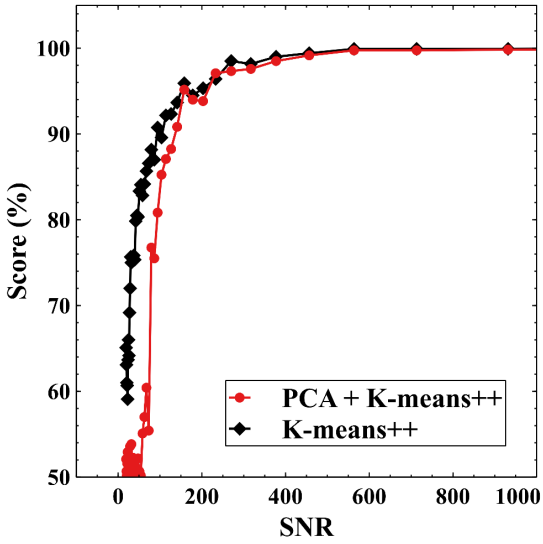

FIGURE 3.26: Score of the cluster analysis as a function of the noise level of the synthetic SpIm with (red) and without (black) PCA pre-processing.

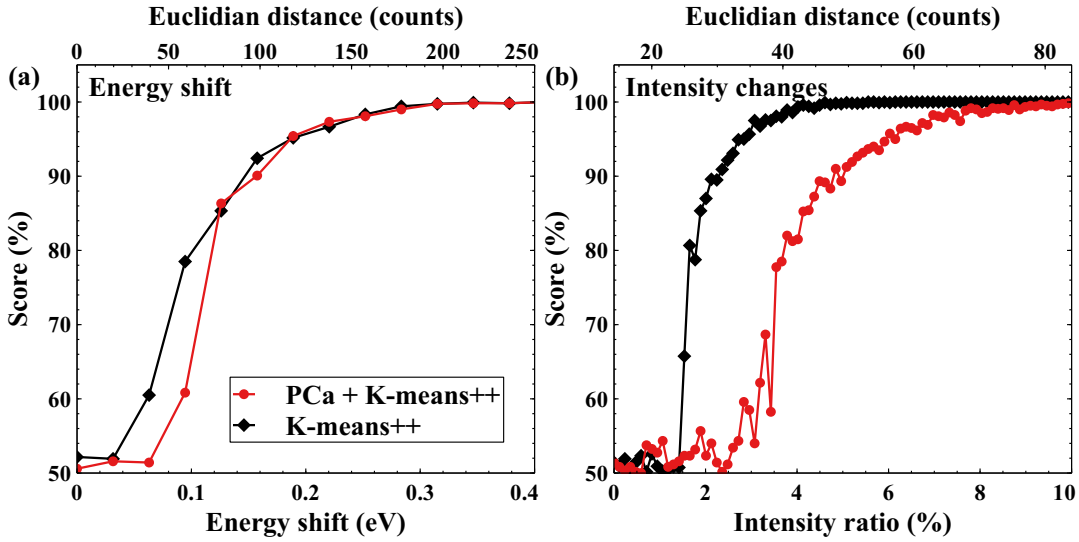

FIGURE 3.27: a) and b) Score of the cluster analysis as a function of the energy shift and of the intensity ratio, respectively. The effect of the PCA pre-processing is shown by the red curves.

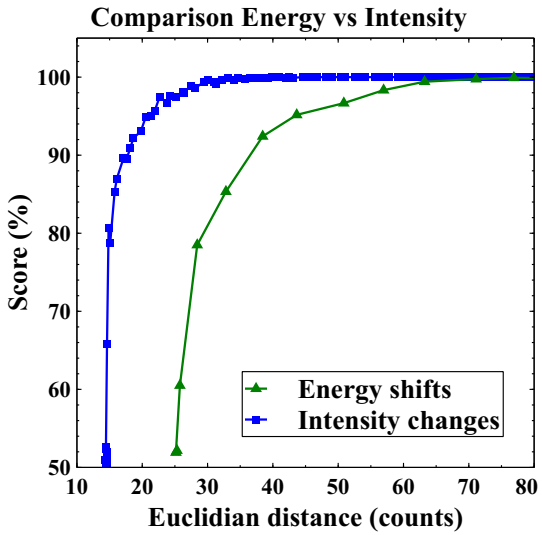

FIGURE 3.28: Score of the cluster analysis as a function of the Euclidian distance for varying energy shifts (green) and intensity changes (blue).

a variable concentration of Co^{2+}. The Euclidian distance between the two resulting centroids was also computed and the effect of a PCA pre-processing of the data was further tested. The results are shown in Fig. 3.27 (a) and (b). As expected, the threshold effect is also observed for these tests and the PCA pre-processing also hinders the performances of the cluster analysis. The cluster analysis is 90% accurate for an energy shift of 0.15 eV (distance of 75 counts) and for an intensity ratio of 2% (distance of 30 counts). Fig. 3.28 illustrates how K-means++ is more sensitive to intensity changes than energy shifts. For instance, energy shifts might produce clusters with anisotropic shape that are not well handled by the K-means++ algorithm.

Evaluation of the clusters distribution

Here, we will try to understand what is the statistical distribution of the spectra to assess the separation of spectra clusters. We will derive from this analysis the expected clustering behavior. Since the spectra composing the SpIm are either Co^{3+} O_h or Co^{2+} T_d, we should then expect two clusters. It is nonetheless useful to compute the pairwise distances histogram between spectra as it gives insights on what is computed in the cluster analysis. The diagram in Fig. 3.29 presents the histograms of pairwise distances in the simplified case of a 2-channel spectrum collection [20]. For one cluster, the distribution is gaussian peaked at d_c which is the radius of the cluster. When

[20] We make the assumption that the spectra inside one cluster follow a random distribution around a central point. It is not true in the presence of varying thickness for example.

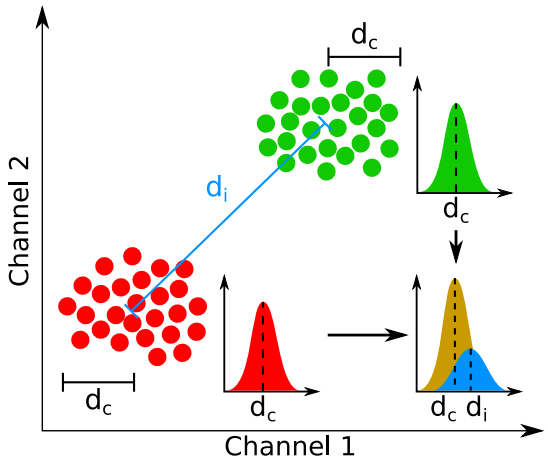

FIGURE 3.29: Simplified scheme of 2 clusters in a 2-dimensional space. The distribution of pairwise distances of individual clusters is displayed at their left. The total distribution of pairwise distances considering the 2 clusters is displayed at the bottom left.

a second cluster is added at a distance d_i with the same gaussian distribution, the total distribution is then asymmetric and composed of a gaussian distribution peaked at d_c with an increased height and another gaussian distribution peaked at d_i. The histogram of the pairwise distances for the Co_3O_4 SpIm is shown in Fig. 3.30 (a) and (b). The fit of this histogram by only one gaussian in Fig. 3.30 (a) shows the asymmetry of the distribution and a much better agreement is obtained using two gaussians as shown in Fig. 3.30 (b). These results indicate that the SpIm is at least composed of two spectral signatures. However, this method does only give a lower bound to the number of expected clusters as the pair-wise distance histogram can be fitted with infinitely many gaussians.

Clustering on an experimental SpIm

The clustering algorithm was tested on an experimental atomically-resolved SpIm acquired on a Co_3O_4 nanoparticle, as presented in Fig. 3.31. The SNR of a typical spectrum of this SpIm was estimated to be about 400 and is therefore suitable for the clustering. The number of clusters was optimized so that the output centroids exhibit either intensity or energy shift differences above the threshold determined in the previous section. Thus, the number of clusters for this SpIm is set to 3. With this parameter the intensity difference between two centroids is of at least 3.3%. The three resulting centroids correspond to: an O_h Co^{3+} spectral signature (orange), a T_d Co^{2+} spectral signature shifted of 0.2 eV to lower energy (black) and a mixed $Co^{2+/3+}$ spectral feature (brown) with a strong L_3 shoulder. The $Co^{2+/3+}$ mixing of the spectral signatures might be related to delocalization or channeling effects. However,

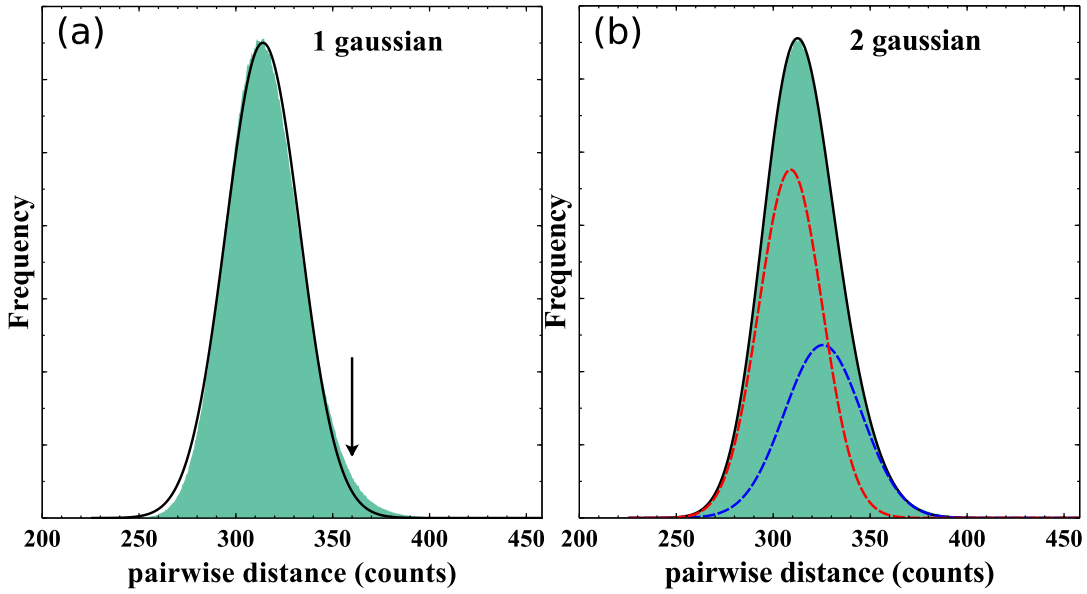

FIGURE 3.30: a) and b) Histogram of pairwise distances of the SpIm (filled turquoise), total gaussian fit (black solid line). In b), the two gaussians that compose the fit are displayed in red and blue dashed lines.

the charge ordering of Co_3O_4 is successfully retrieved, demonstrating the efficiency of the cluster analysis. This method will be applied on atomically-resolved SpIm of Bi-rich iron garnets to disentangle the contributions of Fe valences states from the one of T_d/O_h coordinations in the fine structures of the Fe $L_{2,3}$ edge (section 5.3.2).

Summary of chapter 3

In the first part of this chapter, we presented the different experimental techniques that were used to grow the thin films and measure their structural and physical properties, e.g. resistivity measurements. In a second part, we present the analysis of STEM/EELS data using PCA and GPA.

In the third part of this chapter, we present the development of an uncommon data processing technique: the clustering. This technique was applied to the analysis of subtle changes in EELS fine structures such as mixed-valence states. The validity and the performances of the cluster analysis were tested on a model system: Co_3O_4. These tests were successfull as it was possible to retrieve the valence state distribution of Co in Co_3O_4 using clustering.

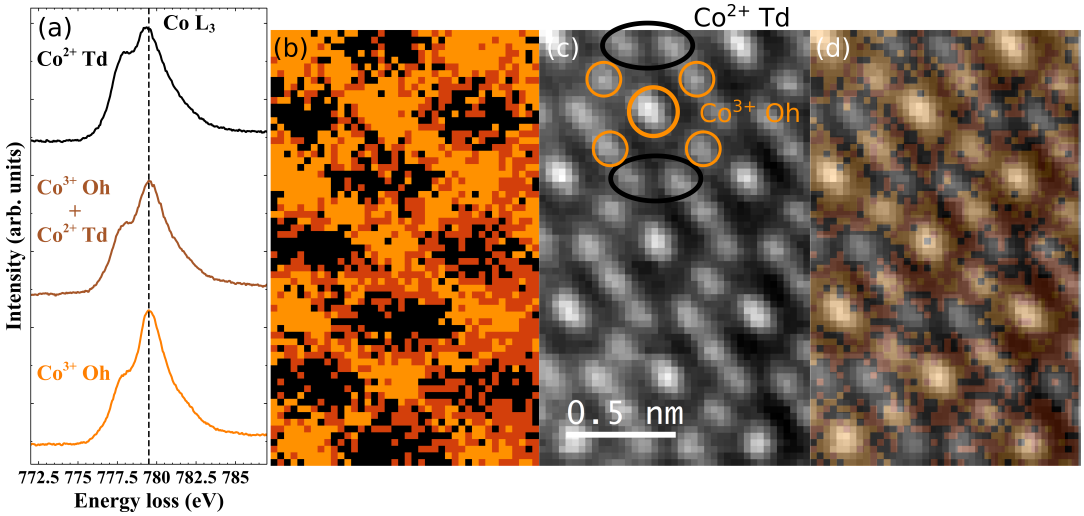

FIGURE 3.31: K-means++ results on an atomically-resolved Co_3O_4 SpIm. a) Centroids output by the K-means++ algorithm. b) Map of the labels output by the cluster analysis. The colors of the map have their corresponding centroids with the same color. c) STEM-HAADF intensity map of the SpIm. The different atomic columns are highlighted with colors corresponding to the map of the labels. d) Superimposition of (b) and (c) to highlight the matching between the cluster analysis and the Co_3O_4 atomic structure.

Chapter 4

Structure, microstructure and dopants distribution

As described in section 3.1.1, a series of B($Ca_xY_{0.5-x}$)IG with x = {0.0 ; 0.1 ; 0.2 ; 0.3} and B($Y_{1.0}$)IG thin films were grown by PLD on GGG (001) substrates. In this chapter, the macroscopic structural features of these films are first investigated using XRD. Then, the detailed microstructure is probed at both nanometric and atomic scales by Cs-STEM/EELS. The local strain distribution in the films is derived from GPA. Finally, the distribution of Ca and Y dopants are also studied by Cs-STEM/EELS to determine the solubility of the dopants within the garnet matrix.

4.1 Structure of Ca and Y co-substituted BIG

Structural quality

The as-grown B($Ca_xY_{0.5-x}$)IG and as-grown B($Y_{1.0}$)IG thin films tend to present oxygen off-stoichiometry. Hence, post-annealing under oxygen flux (TA48 and TA96) was performed to obtain oxygen stoichiometric thin films.

Fig. 4.1 (a) presents typical $\theta - 2\theta$ X-ray diffraction patterns obtained for as-grown and post-annealed B($Ca_{0.0}Y_{0.5}$)IGs. All the diffraction reflections belong to the garnet phase oriented along [001] with FWHM below 0.15 deg in 2θ. These FWHM values are 0.05 to 0.10 deg lower than previous values reported in the literature [23, 11, 26], indicating that the films presented here have a lower mosaicity. Fig. 4.1 (b) displays a zoom on the (004) reflection of the as-grown and post-annealed B($Ca_{0.0}Y_{0.5}$)IG. Laue oscillations visible in Fig. 4.1 reveal that these films have a coherent crystal structure over the probed volume, i.e. hundreds of nm^3. It should be noted that Laue oscillations were only reported for much lower concentrations of Bi, i.e. up to 1.5 Bi per f.u., in Bi-doped YIG systems either grown by PLD [38] or by liquid

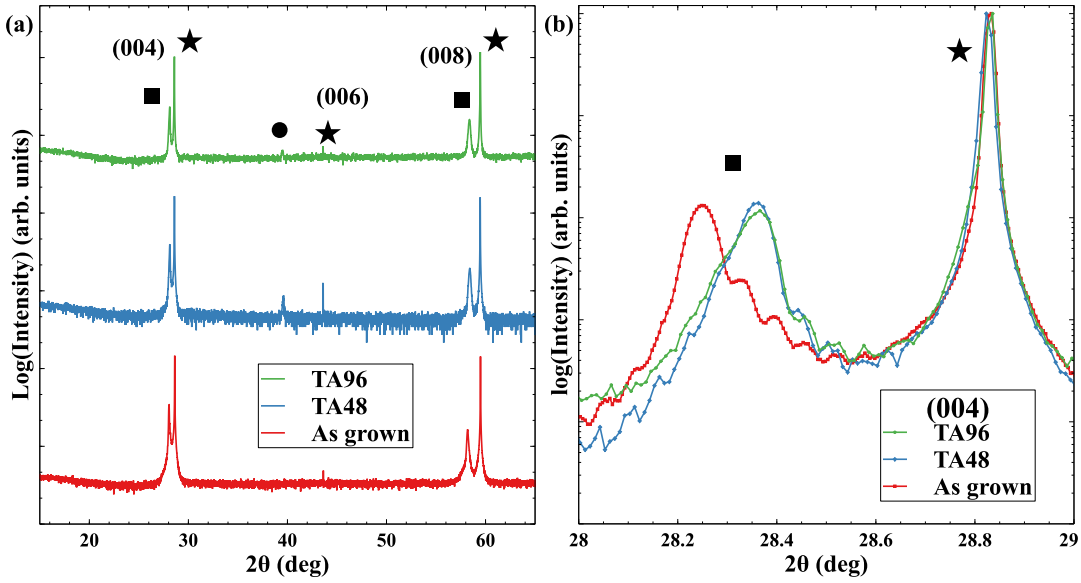

FIGURE 4.1: a) $\theta - 2\theta$ XRD scans of B($Ca_{0.0}Y_{0.5}$)IG before and after TA48 and TA96. b) Zoom of a) on the (004) reflection. The B($Ca_{0.0}Y_{0.5}$)IG, GGG and Pt contact pads peaks are highlighted by a square, a star and a circle, respectively.

phase epitaxy [59]. These oscillations are detected for the film without Ca or with a low Ca concentration i.e. B($Ca_{0.1}Y_{0.4}$)IG, B($Ca_{0.0}Y_{0.5}$)IG and B($Y_{1.0}$)IG. The absence of Laue oscillations for higher Ca content indicates a possible higher disorder. After TA48 and TA96, all the films keep the same structural features and crystal symmetry as for as-grown films. This is shown in Fig. 4.1 (a) and (b) for B($Ca_{0.0}Y_{0.5}$)IG. The presence of Laue oscillation in combination with the low FWHM confirms the high structural quality of the films based on the XRD results.

Reflection high energy electron diffraction (RHEED) measurements were performed on each sample [1]. Several images along different azimuths were systematically taken on a substrate before the growth and on the film after the cooling. Relatively high oxygen pressure during the film growth does not allow the measurement of RHEED while depositing a film. Fig. 4.2 shows representative RHEED patterns taken on the GGG substrate and the B($Y_{1.0}$)IG film in [100] and [120] directions. The films are epitaxial with, as expected, slightly larger lattice parameter than the substrate. The average rms roughness of the films is measured using atomic force microscopy and is found to be about 5 nm.

Lattice parameters

All the as-grown films of the B($Ca_xY_{0.5-x}$)IG series possess a slightly larger

[1] The RHEED was measured by Elena Popova.

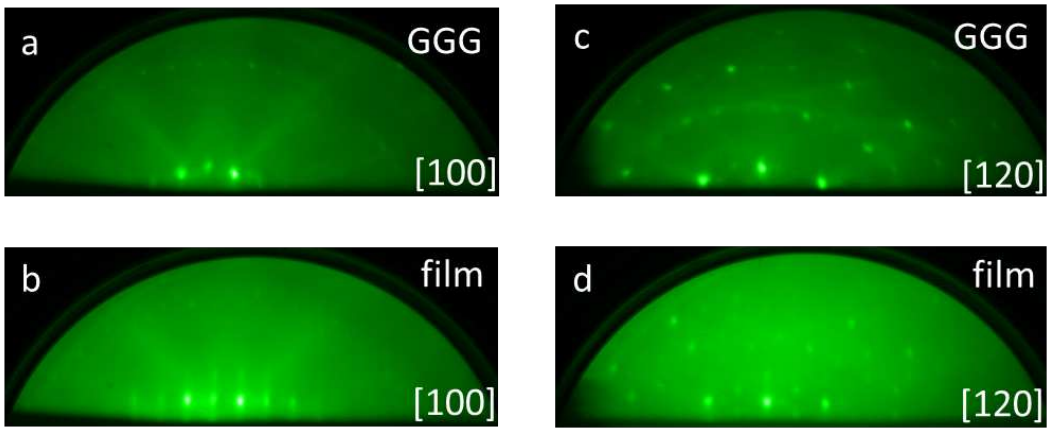

FIGURE 4.2: Typical RHEED images of the GGG(001) substrate and a doped BIG film. The corresponding azimuths are indicated in the images.

or equal out-of-plane (o-o-p) lattice parameter than stoichiometric BIG[21] (Fig. 4.3). A priori, this trend is unexpected since Bi^{3+} is larger than Y^{3+} and Ca^{2+} ($r_{Y^{3+}}$ = 104 pm < $r_{Ca^{2+}}$ = 114 pm < $r_{Bi^{3+}}$ = 117 pm)[60] and Y-doped BIG was already experimentally reported with a smaller volume[22] assuming a cubic unit cell. Indeed, the in-plane lattice parameter of TA96 B($Ca_{0.0}Y_{0.5}$)IG was also measured and it is not significantly different than the out-of-plane lattice parameter. These large o-o-p lattice parameters strongly indicate that the films are oxygen off-stoichiometric [155]. B($Ca_xY_{0.5-x}$)IG TA48 films present a decrease of 0.1-0.3% of their o-o-p lattice parameters compared to their as-grown state indicating the effective filling of the oxygen sub-lattice. After TA96 the o-o-p does not significantly decrease within the error margins suggesting that the oxygen sub-lattice was already completely filled after TA48.

The as-grown B($Y_{1.0}$)IG thin film have a 0.4% smaller o-o-p lattice parameter than BIG due to its lower Bi concentration (Fig. 4.3). Nevertheless, a decrease of the o-o-p lattice parameter of 0.4% for TA48 B($Y_{1.0}$)IG compared to its as-grown value is measured. These results indicate that as-grown B($Y_{1.0}$)IG thin films are oxygen off-stoichiometric similarly to the B($Ca_xY_{0.5-x}$)IG series. For both as-grown and TA48, the Ca-doped thin films have a 0.5% larger o-o-p lattice parameter than B($Ca_{0.0}Y_{0.5}$)IG that indicates the effective substitution of Ca in the garnet lattice [156]. With increasing Ca concentration, the o-o-p lattice parameter stays constant in contrast to the expected linear increase.

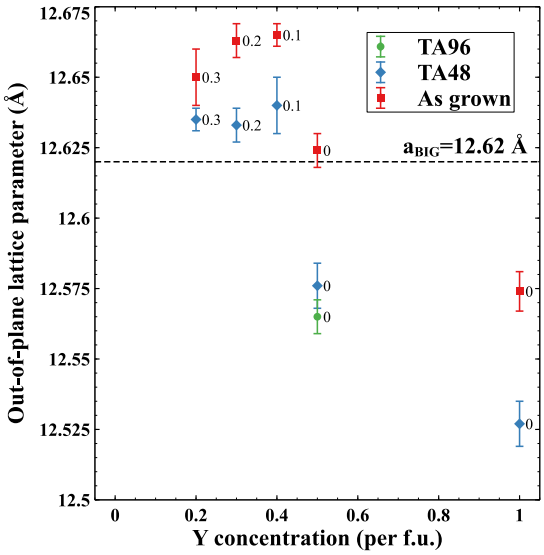

FIGURE 4.3: Evolution of the out-of-plane lattice parameter with the nominal Y concentration for as-grown, TA48 and TA96 thin films. The nominal Ca concentration of the thin films is indicated at the right of every data point.

4.2 Microstructure of Ca and Y co-substituted BIG

4.2.1 Secondary phase inclusions

Size and distribution

Selected phases: as-grown and TA96 B($Ca_{0.0}Y_{0.5}$)IG, as-grown B($Ca_{0.3}Y_{0.2}$)IG were further investigated by TEM and Cs-STEM/EELS studies. Fig. 4.4 (a) shows a typical low magnification TEM-BF image of the as-grown B($Ca_{0.0}Y_{0.5}$)IG that is representative of the studied films. The XRD patterns have shown a garnet phase with high structural quality as confirmed by the selected area electron diffraction pattern in Fig. 4.4. A typical STEM-BF image is displayed in Fig. 4.4 (c) showing that B($Ca_{0.0}Y_{0.5}$)IG exhibits a columnar growth, with column widths of ca. 40 nm. Secondary phase nanoneedles are observed mostly in between garnet grains, one of them is highlighted by two white arrowheads in Fig. 4.4 (c). Their widths varies from 5 to 30 nm. They start to form at about 20 nm above the film/substrate interface and reach the film surface. The nanocrystallites are still present after TA96.

Chemical and electronic natures

The chemical and electronic natures of the nanoneedles were further locally probed by STEM-EELS. The O *K* and Fe $L_{2,3}$ absorption edges of the nanocrystallites are compared with those of pure BIG films and of a hematite reference(α-Fe_2O_3) in Fig. 4.5 (a). The O *K* edge of α-Fe_2O_3 consists of the A1 peak at 530 eV and the B peak at 540 eV [157]. A1 corresponds to the hybridization of O

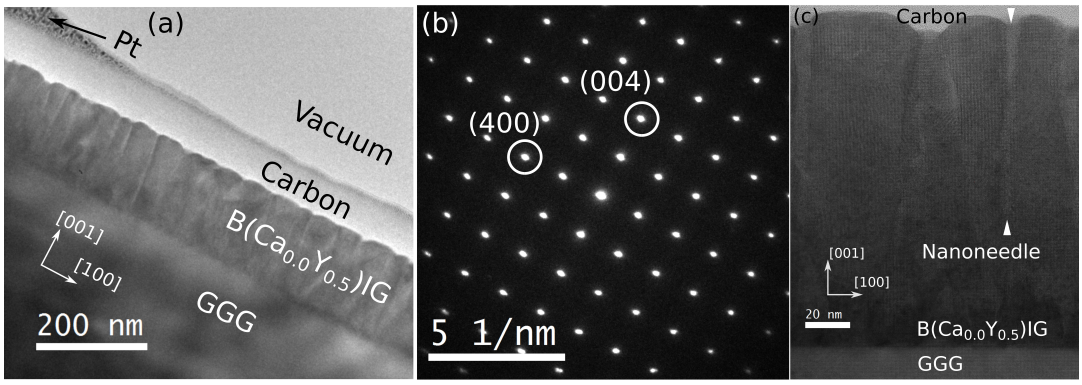

FIGURE 4.4: a) TEM bright field low magnification image of as-grown $B(Ca_{0.0}Y_{0.5})IG$. b) Diffraction pattern of a selected area in the film shown in a). The (004) and (400) reflections are highlighted by white circles. c) STEM bright field image of as-grown $B(Ca_{0.0}Y_{0.5})IG$. The presence of a nanocrystallite is highlighted by two white arrowheads.

$2p$ states with Fe $3d$ states while B is assigned to the hybridization of O $2p$ states with Fe $4s$ and $4p$ states [158]. In BIG, the O K edge has an additional peak at 533 eV labelled A2 that corresponds notably to the hybridization of O 2p states with Bi $6p$ states [159]. The O K edge of nanoneedles does not possess the A2 peak and the B peak is more intense than the A1 peak, similar to α-Fe_2O_3. The Bi $M_{4,5}$ edge was also probed in the nanocrystallites and exhibited a large intensity decay (not shown here). A part of the garnet phase is always probed by EELS along with the nanoneedles as their diameters are thinner than the thickness of the FIB lamella ($\approx$ 70 nm). Thus, a residual intensity of the Bi $M_{4,5}$ edge is observed in the nanocrystallites. The absence of the A2 peak, together with the lower Bi $M_{4,5}$ intensity indicate a strong Bi depletion in the nanocrystallites. Besides, the Fe $L_{2,3}$ edges of pure BIG, nanocrystallite and α-Fe_2O_3 (Fig. 4.5 (a) right panel) show the typical fine structures of Fe^{3+} [122]. These results strongly indicate that the nanocrystallites are mainly composed of binary ferric oxide.

Structural properties

A STEM-HAADF image with atomic-scale resolution is presented in Fig. 4.5 (b) at the boundary between the garnet and the secondary phases. A typical nanocrystallite appears as a low intensity area marked by white arrowheads in line with the observed Bi depletion. Atomic planes of the nanocrystallite are visible but they often appear with faint contrast or show disorder. It indicates that the ferric iron oxide is rather weakly crystallized and this feature could explain the absence of α-Fe_2O_3 peaks in the XRD patterns. In

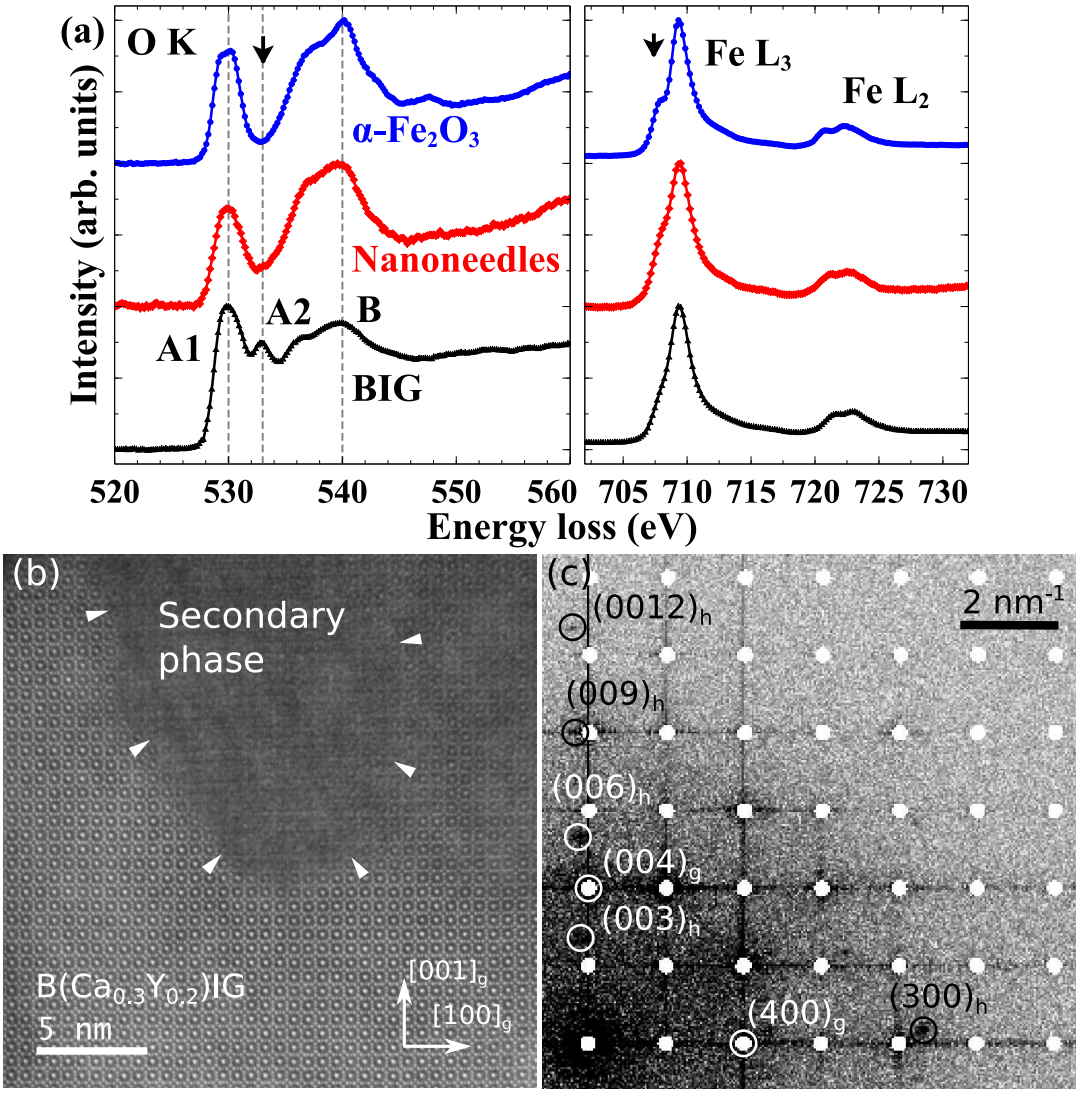

FIGURE 4.5: a) Sum of O-K and Fe-L edges spectra acquired in α-Fe_2O_3, nanocrystallites and pure BIG in blue, red and black, respectively. The nanocrystallite spectrum is the sum of 1500 spectra of 30 ms each with a dispersion of 0.18 eV ch^{-1}. The two other spectra are the sum of 15000 spectra acquired the same way. b) STEM-HAADF image of as-grown $B(Ca_{0.3}Y_{0.2})IG$ and a part of nanocrystallite highlighted by white arrowheads. c) Fourier transform modulus of b) with inverse grayscale contrasts. The reflections from the nanocrystallite are noted $(mnp)_h$ and those of the garnet are noted $(mnp)_g$.

Fig. 4.5 (c), the fast Fourier transform (FFT) of Fig. 4.5 (b) exhibits the reflections of the garnet lattice (with a g subscript) and additional reflections (with a h subscript) from the nanocrystallite. In Fig. 4.5 (c), the reflections of the nanocrystallites correspond to a hematite ($R\bar{3}c$) observed along the $[120]_h$ zone axis. These results, correlated with the EELS study, strongly indicate that the secondary phase has the α-Fe_2O_3 structure.

As shown in Fig 4.5 (c) the hematite $(009)_h$ planes (interplanar distance of 0.159 nm) almost coincide with the garnet $(008)_g$ planes (interplanar distance of 0.158 nm) resulting in an interfacial relationship as observed in Fig 4.5 (b). More generally, it is observed that the $[001]_h$ axis of many observed nanocrystallites makes an angle ranging roughly from 2 to 25 degrees with the $[001]_g$ axis of the garnet phase as derived from the FFTs of Cs-STEM-HAADF images. The secondary phase is then made of poorly crystallized hematite nanocrystallites with a textured orientation with respect to the garnet grains. It is interesting to note that the presence of the nanocrystallites is not detected by conventional macroscopic techniques such as XRD. This underlines the importance of transmission electron spectro-microscopy studies for the detailed chemical and crystallographic analysis of the microstructural features of materials; it is especially true when they do not exist as bulk.

Secondary phase inclusions in BIG

The occurrence of secondary phase inclusions were already reported in pure BIG. These inclusions are most often composed of $BiFeO_3$ (BFO) [11, 25] and $Bi_2Fe_4O_9$ [12]. Their formation occurs at high ($PO_2 > 130$ mTorr) or low ($PO_2 < 1$ mTorr) oxygen partial pressure during the growth and they are usually detected directly by XRD. The only example of secondary phase inclusions not detectable by XRD was reported by Kahl et al. [26] in BIG grown by PLD on GGG. However, in the work of Kahl et al., the structural and chemical natures of the inclusions were not identified.

Secondary phase inclusions in $BiFeO_3$

Secondary phase inclusions are often observed in bismuth iron oxides. A classic example of such well-studied oxide is $BiFeO_3$. As for BIG, the PLD growth of BFO still remains a complex topic and is only possible in a narrow range of partial oxygen pressures. For PO_2 below ca. 5 mTorr, inclusions of α-Fe_2O_3, maghemite (γ -Fe_2O_3) or more scarcely magnetite (Fe_3O_4) form, while for PO_2 above ca. 20 mTorr the formation of Bi_2O_3 occurs [161, 162, 163]. These effects originate mainly from the high volatility of Bi ions

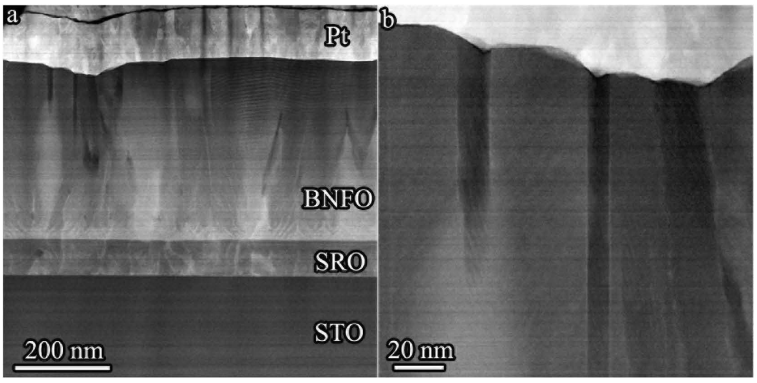

FIGURE 4.6: a) Low magnification STEM-HAADF image of Nd and Ti co-substituted BFO (BNFO) film grown on $SrRuO_3$(SRO)/$SrTiO_3$(STO). b) Enlarged image of a region of (a) at the top of the film. The BNFO thin film presents secondary phase nanoneedles that are similar to the ones we evidenced in Ca/Y-doped BIG thin films. This figure is extracted from the work of Zhang et al. [160].

[162] and it is likely that the same mechanism is present in the growth of BIG. In some cases, these secondary phase inclusions can be nanometric in size and remain undetectable by conventional macroscopic techniques such as XRD [160]. In the case of BFO, the addition of dopants change the PLD growth conditions necessary to obtain single phase thin films [160, 164, 165]. It should be noted that well crystallized secondary phase inclusions of Fe_2O_3 with the perovskite structure were reported by Zhang et al. [160]. The microstructure of these BNFO thin films is shown in Fig. 4.6 and is remarkably similar to the microstructure of the present doped-BIG films, thus, changes of the growth conditions might lead either to similar crystallisation or the absence of nanocrystallites in doped BIGs. By comparison with the growth characteristics of BFO, it can thus be concluded that the B($Ca_xY_{0.5-x}$)IG thin films were grown in a too low PO_2 range that lead to the unexpected formation of α-Fe_2O_3.

4.2.2 Strain relaxation

GPA were performed to determine the local lattice parameter variations of the garnet phase in both i-p and o-o-p directions, especially at the film/substrate interface. A typical STEM-HAADF image of as-grown B($Ca_{0.0}Y_{0.5}$)IG used for the GPA is shown in Fig. 4.7 (a). The extracted i-p and o-o-p relative strain maps of the film are displayed in Fig. 4.7 (b) and (c). Extracted profiles from the o-o-p and i-p strain maps of as-grown and TA96 B($Ca_{0.0}Y_{0.5}$)IG and of TA48 B($Y_{1.0}$)IG are displayed in Fig. 4.8 (a),(b) and (c), respectively. The o-o-p lattice parameters determined using XRD are used here as references to determine the expected lattice mismatches with the substrate (Table. 4.1).

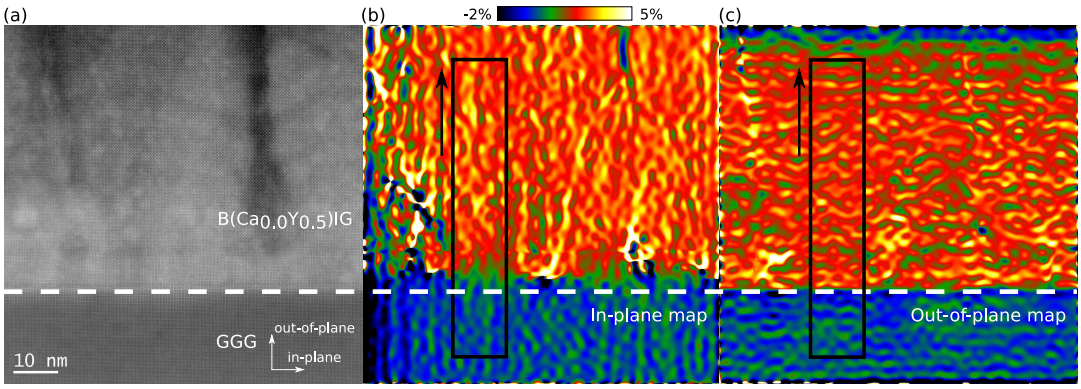

FIGURE 4.7: a) High resolution HAADF image of the film substrate interface for as-grown $B(Ca_{0.0}Y_{0.5})IG$. Extracted in-plane b) and out of plane c) relative strain maps from GPA on a) where the substrate is taken as reference.

Thus, a decreasing strain is expected from as-grown $B(Ca_{0.0}Y_{0.5})IG$ to TA96 $B(Ca_{0.0}Y_{0.5})IG$ until TA48 $B(Y_{1.0})IG$. For all the characterized films, the strain relaxation mechanisms are similar. As expected, the compressive strain induced by the substrate ($a_{GGG} = 1.2383$ nm) is fully relaxed on a length of up to 27 nm from the film/substrate interface by in-plane pseudo-periodic dislocations. The o-o-p lattice parameter is fully relaxed immediately at the film/substrate contrarily to the i-p lattice parameter[2]. This difference of relaxation lengths induces locally a deformation of the unit cell that changes the symmetry from cubic to tetragonal. In this strained region, an o-o-p/i-p lattice parameters ratio of up to 2% (Fig. 4.8) is observed. Besides, the unit cell of the films remains cubic in the relaxed region supporting the assumption that the unit cell volume can be derived solely from o-o-p lattice parameter. This strain relaxation mechanism is analogous to that of BIG on substituted-GGG [001] [21].

The GPA results are summarized in Table 4.1. The lower concentration of dislocations and the larger relaxation length of TA96 $B(Ca_{0.0}Y_{0.5})IG$ compared to as-grown $B(Ca_{0.0}Y_{0.5})IG$ are in line with expected lower strains. After relaxation of the strain, the garnet grains of the $B(Ca_{0.0}Y_{0.5})IG$ films are structurally homogeneous and the i-p and the o-o-p lattice parameters determined using GPA are close to the XRD ones. The TA48 $B(Y_{1.0})IG$, despite its expected lower strain, exhibits a concentration of dislocations and a relaxation length similar to those of as-grown $B(Ca_{0.0}Y_{0.5})IG$. For $B(Y_{1.0})IG$, it cannot be excluded that the secondary phase inclusions play a role on the

[2] At the film/substrate interface overshoots in the o-o-p strain, as large as the mask size, can be observed. This feature is an artefact of the GPA [140] due to the discontinuity of the interface [166].

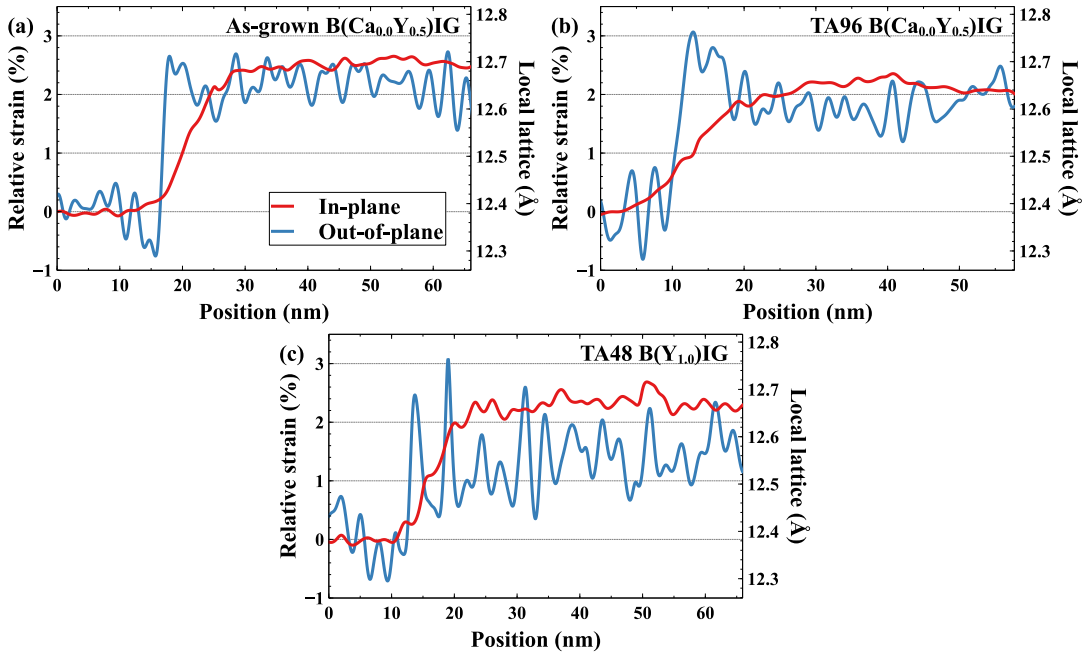

FIGURE 4.8: a) Extracted profiles for as-grown $B(Ca_{0.0}Y_{0.5})IG$ from the i-p and o-o-p relative strain maps of Fig. 4.7 (b) and (c), respectively. b) and c) Extracted profiles for TA96 $B(Ca_{0.0}Y_{0.5})IG$ and TA48 $B(Y_{1.0})IG$ from the i-p and o-o-p relative strain maps derived from GPA.

strain relaxation. Such an effect was reported in the BFO/hematite composite where the regions in between the hematite inclusions help to relax more strain compared to the single phase BFO thin films [167].

4.3 Dopants distribution

The atomic scale structural features and the EELS features of the studied thin films are recalled here to present the STEM/EELS results. A typical atomically resolved STEM-HAADF image of BIG observed along [010] is shown in

	$B(Ca_{0.0}Y_{0.5})IG$		$B(Y_{1.0})IG$
	As grown	TA96	TA48
i-p dislocations frequency (nm)	18	27	20
i-p relaxation length (nm)	13	21	15
i-p lattice parameter (nm)	1.270	1.265	1.267
o-o-p lattice parameter (nm)	1.266	1.261	1.256
XRD o-o-p lattice parameter (nm)	1.2624 ± 0.0006	1.2565 ± 0.0006	1.2527 ± 0.0008
XRD Lattice mismatch	1.95%	1.47%	1.16%

TABLE 4.1: Summary of the GPA results for as-grown and TA96 $B(Ca_{0.0}Y_{0.5})IG$ and for TA48 $B(Y_{1.0})IG$. The lattice parameters of the films derived from GPA are calculated after the strain relaxation. The o-o-p lattice parameters measured by XRD are shown in the lower row for comparison.

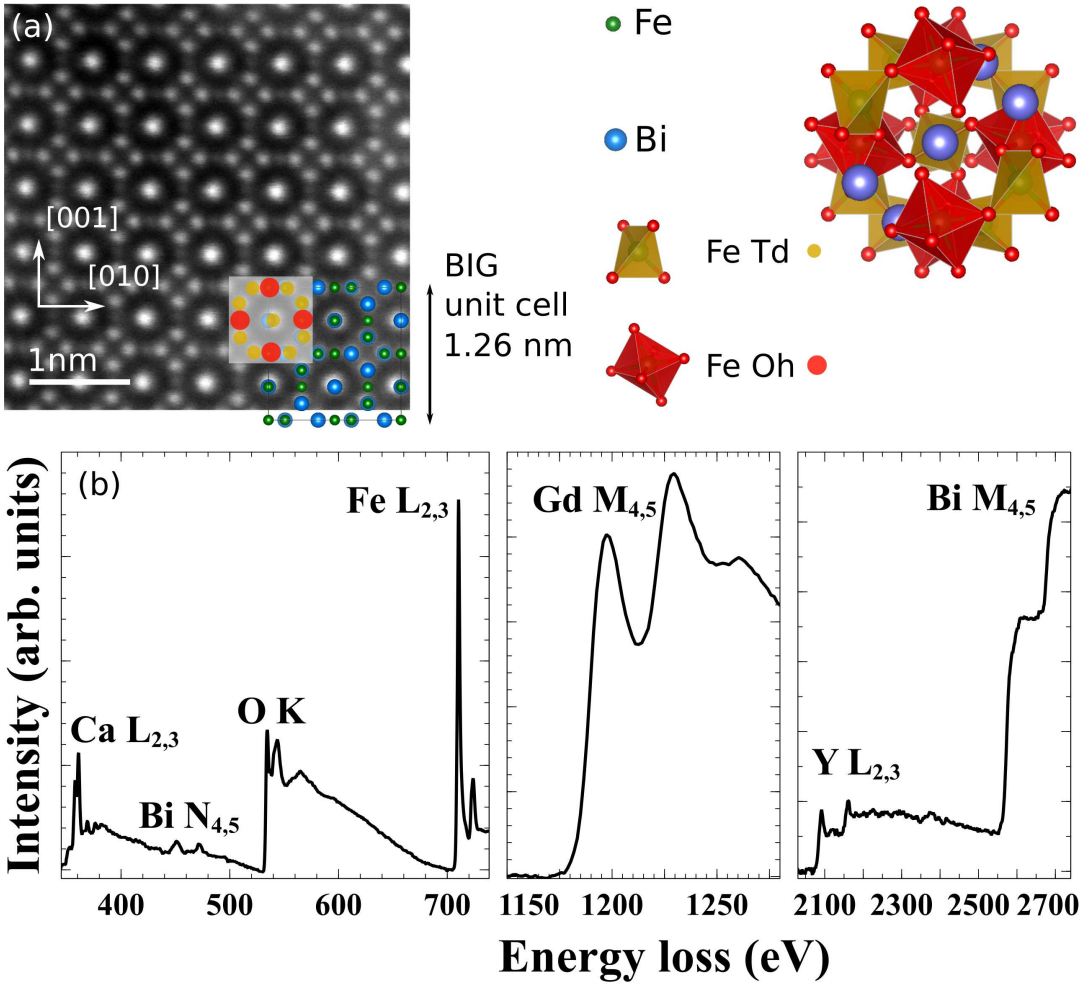

FIGURE 4.9: a) Atomically-resolved STEM-HAADF image of BIG. The atomic model of cation sub-cell along with the Fe coordination model of the garnet structure are overlaid on the HAADF image. Fe and Bi atoms are depicted in green and blue, respectively, while Fe-O_h and Fe-T_d are depicted in red and orange, respectively. b) Typical EELS spectra acquired in B($Ca_{0.3}Y_{0.2}$)IG (right panel), in GGG substrate (middle panel) and in B($Ca_{0.0}Y_{0.5}$)IG (left panel).

Fig. 4.9 (a). Projected along the [010] zone axis, the BIG structure presents 8 Fe (green) atomic columns with Fe in octahedral coordination (red) and 20 mixed Bi (blue) and Fe atomic columns with Fe in tetrahedral coordination (orange). EELS spectra acquired in B($Ca_{0.3}Y_{0.2}$)IG, in GGG substrate and in B($Ca_{0.0}Y_{0.5}$)IG are displayed in Fig. 4.9 (b). The Ca $L_{2,3}$ and the Y $L_{2,3}$ edges were probed to take advantage of the high cross-section of $L_{2,3}$ edges. However, the cross-section of the Y $L_{2,3}$ is lower than the one of Ca $L_{2,3}$ edge due to its higher energy which makes Y more challenging to probe. For Bi, its $N_{4,5}$ edge at 440 eV has a very low cross section. The Bi $M_{4,5}$ edge at 2580 eV is then used for elemental mapping.

Before mapping the distribution of dopants the average Ca/Fe ratio was determined by EELS for B($Ca_{0.3}Y_{0.2}$)IG thin film. The spectra were acquired

over a garnet grain (typically hundreds of nm^2) or over a nanocrystallite (typically tens of nm^2). The Ca $L_{2,3}$ and Fe $L_{2,3}$ edges integrated over a 30 eV window to determine the Ca/Fe ratios and hydrogenic calculated (corrected for white lines) cross-sections were used. The nominal Ca/Fe in B($Ca_{0.3}Y_{0.2}$)IG is 6%. A slightly higher than nominal Ca/Fe ratio of (8%) is observed in the garnet phase while a low (4%) Ca/Fe ratio is observed in the nanoneedles. It should be noted that the nanocrystallites are thinner than the lamella observed in STEM/EELS which implies that the Ca found in the secondary phase inclusions might originate from a superimposed garnet grain. These results indicate that the Ca dopants do not segregate within the secondary phase inclusions. The Y/Bi ratios were not quantified because the cross-section ratio of the Y $L_{2,3}$ and the Bi $M_{4,5}$ edges are inaccurately computed in Digital Micrograph (Gatan).

4.3.1 Y distribution

Atomically-resolved EELS chemical mapping was performed on the as-grown B($Ca_{0.0}Y_{0.5}$)IG film at the film/substrate interface as shown in Fig. 4.10. Elemental maps of Fig. 4.10 (c), (d) and (e) show a homogeneous distribution of Y, Fe and Bi, respectively, from the film/substrate interface, and up to 20 nm above i.e. below the distance at which nanoneedles start to form. Fig. 4.10 displays the normalized profiles of these maps, showing that the chemical interdiffusion at the interface is limited at most to the first 2 nm, i.e. less than two garnet unit cells and might be even thinner as the Cs-STEM/EELS spatial resolution is limited by the probe broadening and the inelastic delocalization [168]. In YIG/GGG systems, discrepancies were reported regarding the thickness of the chemical interdiffusion region ranging from 2 nm [169, 170] to 6 nm [171]. Here, the B($Ca_{0.0}Y_{0.5}$)IG/GGG interface interdiffusion matches with the best of those systems.

An analogous EELS elemental mapping was performed at the TA48 B($Y_{1.0}$)IG/GGG interface as shown in Fig. 4.11 and the Y and Bi elemental maps are shown in Fig. 4.11 (c) and (d), respectively. Similarly as as-grown B($Ca_{0.0}Y_{0.5}$)IG, an homogeneous distribution of Y and Bi is observed from the film/substrate interface to 20 nm in the film i.e. below the distance at which nanoneedles start to form. Besides, the interdiffusion at the interface is limited to at most 5 nm (Fig. 4.11 (e)), i.e. less than four unit cells, which indicates that even after annealing the interdiffusion at the film/substrate remains localized to the first few unit cells.

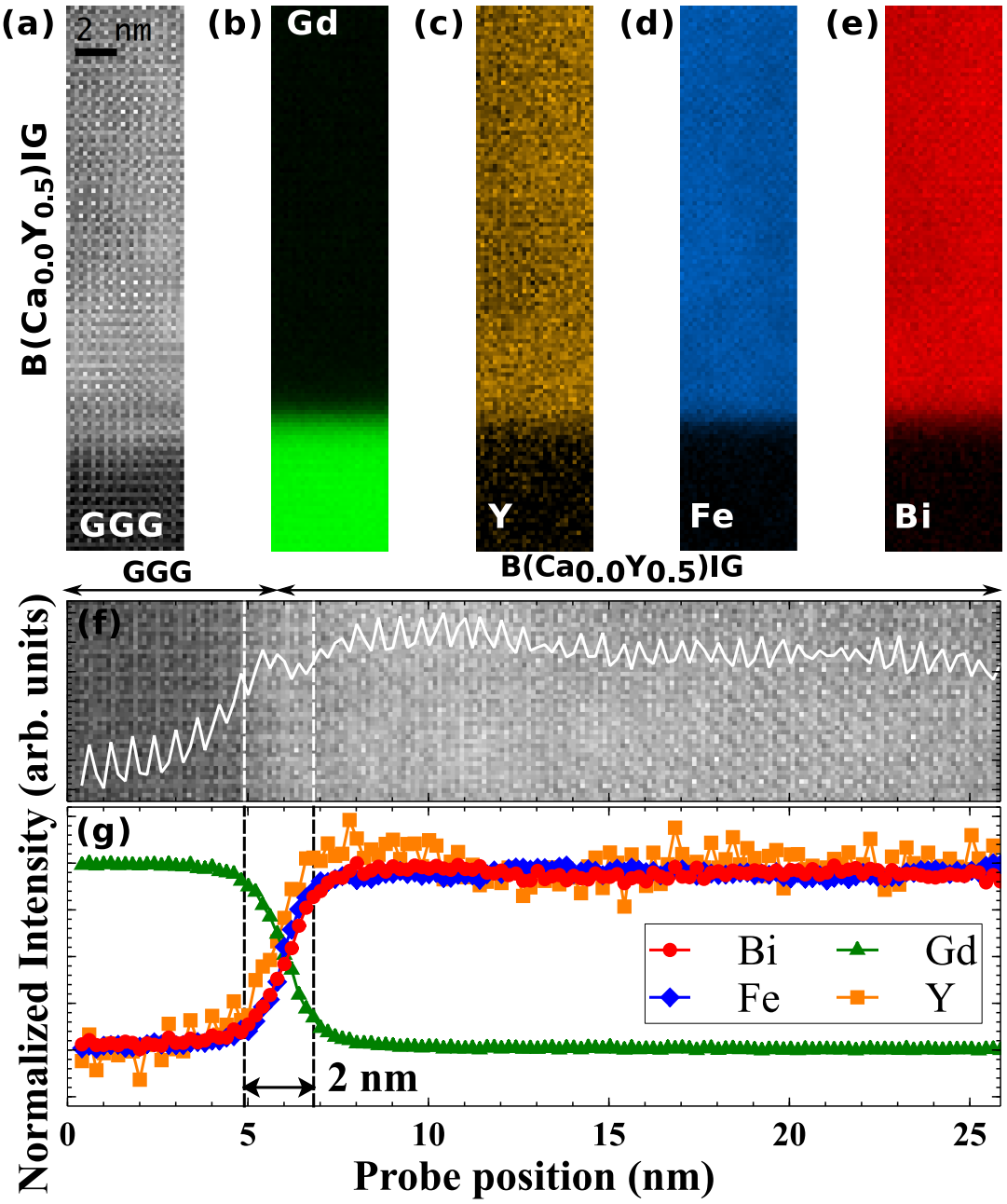

FIGURE 4.10: a) HAADF intensity recorded simultaneously with the EELS map in as-grown $B(Ca_{0.0}Y_{0.5})IG$ at the film/substrate interface. b), c), d) and e) Gd $M_{4,5}$,Y $L_{2,3}$, Fe $L_{2,3}$ and Bi $M_{4,5}$ integrated intensity maps. f) HAADF survey image together with its summed profile. g) Normalized summed profiles of (b), (c), (d) and (e) elemental maps. The energy dispersion used was 1.54 eV ch^{-1} and each spectrum was acquired in 200 ms.

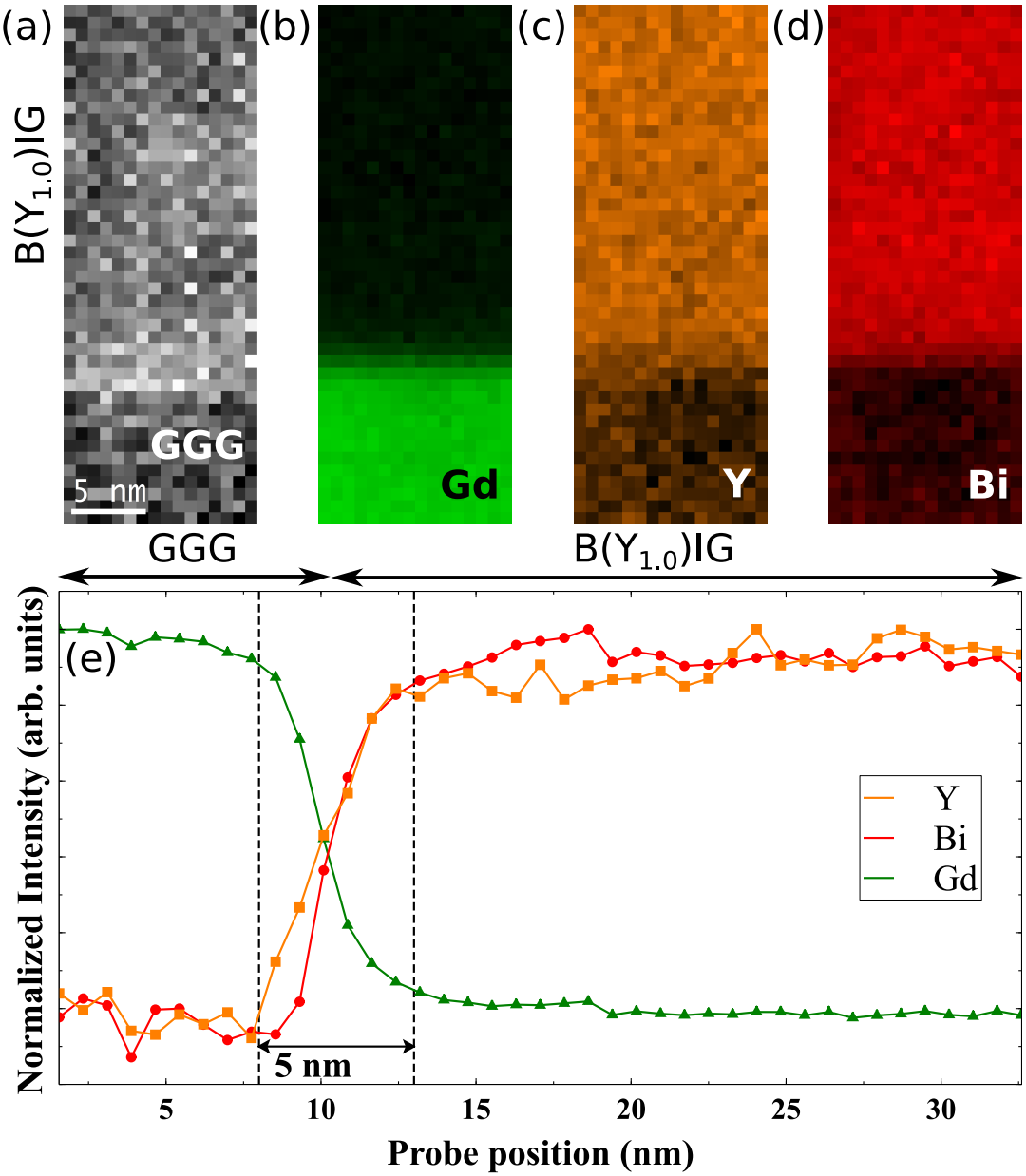

FIGURE 4.11: a) HAADF intensity recorded simultaneously with the EELS map in TA48 B($Y_{1.0}$)IG at the film/substrate interface. b), c) and d) Gd $M_{4,5}$,Y $L_{2,3}$ and Bi $M_{4,5}$ integrated intensity maps. e) Normalized summed profiles of (b), (c) and (d) elemental maps. The energy dispersion used was 1.54 eV ch^{-1} and each spectrum was acquired in 20 ms.

4.3.2 Ca distribution

A Ca $L_{2,3}$ intensity map performed along a B($Ca_{0.3}Y_{0.2}$)IG grain is shown in Fig. 4.12. An inhomogeneity of two percentage points in the Ca distribution was systematically observed at the nanometric scale as an oscillation of Ca concentration along the growth direction. This feature has typically a pseudo-period of 10-15 nm, i. e. 8-12 unit cells, and the Ca/Fe concentration ratio yields values between ca. 7.0% (area 2 in Fig. 4.12) and ca. 9.0% (area 1 in Fig. 4.12). These oscillations were also confirmed by secondary ions mass spectrometry. A possible explanation for this phenomenon resides in the PLD growth. The target simultaneously rotates along one axis and transfer vertically (Fig. 3.1) to homogenize the laser ablation. Nevertheless, if there are points impacted more frequently by the laser this can lead to fluctuations in concentration. A more complete study would be required but it should be noted that small variations of dopants in thin films are rarely discussed and are difficult to investigate.

To determine whether Ca substitutes within the garnet matrix, atomic-scale STEM/EELS was then performed in a Ca-rich region as shown in Fig. 4.13 and in Fig. 4.14. First, the STEM-HAADF image is considered, its intensity scales roughly as $Z^{1.7}$ [103] where Z is the average atomic number of the probed atoms. Ca being a lighter element than Bi and Fe, it yields less intense HAADF signal. A few atomic columns such as column 1, with up to 10% lower HAADF intensity than average (Fig. 4.13 (b)), exhibit a higher Ca $L_{2,3}$ intensity (Fig. 4.13 (c)) which indicates that Ca is inserted into the BIG matrix and notably in a mixed Bi-Fe column.

To evaluate whether the presence of Ca-rich/Ca-depleted atomic columns was related to clusters of Ca or to the statistical distribution of Ca atoms in the garnet lattice, atomically-resolved EELS elemental mapping of the Ca $L_{2,3}$ edge was performed at the finest spatial scale and at a larger field of view. A typical example is shown in Fig. 4.14 where a Ca $L_{2,3}$ intensity map (in red) superimposed on a HAADF intensity map (in blue) shows areas (zones 1 and 2) with size of ca. two garnet unit cells, with different Ca/Fe ratios as probed by EELS (Fig. 4.14 (b) and (c)). The maximum difference reaches 0.1 per f.u. (Fig. 4.14 (c)) which confirms that the Ca substitution within the BIG matrix is of statistical origin and indicates a good solubility of the low-level Ca doping.

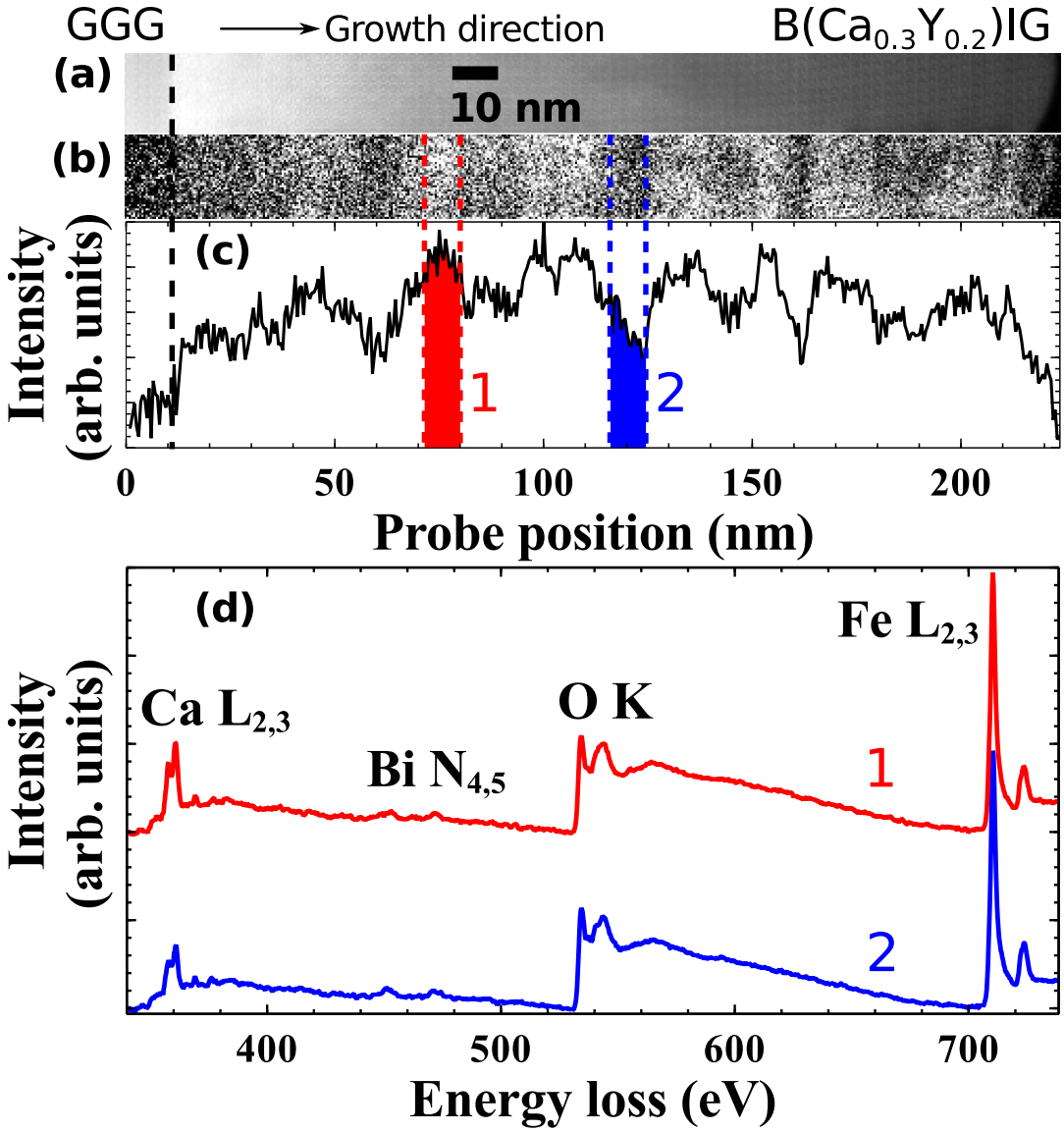

FIGURE 4.12: a) HAADF intensity recorded simultaneously with the EELS map. b) Ca $L_{2,3}$ integrated intensity map. c) Summed profile of map (b). A Ca-rich region (1) is highlighted in red while a Ca-depleted region (2) is highlighted in blue. d) EEL spectra corresponding to area 1 (red) and 2 (blue). The energy dispersion used was 0.26 eV ch_{-1} and each spectrum was acquired in 30 ms.

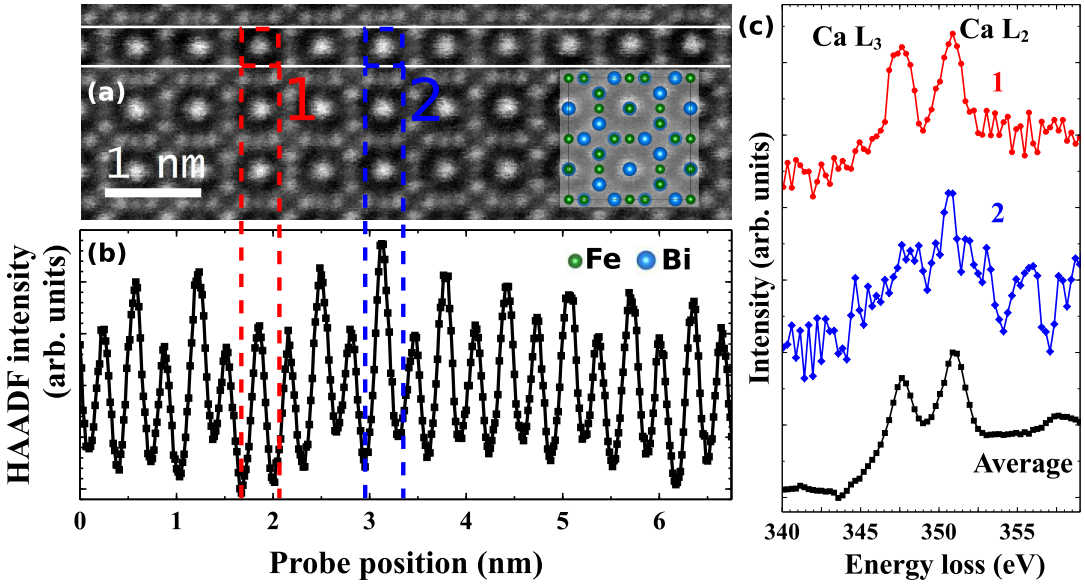

FIGURE 4.13: a) Atomically-resolved STEM-HAADF survey image of B($Ca_{0.3}Y_{0.2}$)IG acquired in a Ca-rich region. Atomic model of cation sub-cell of the garnet structure is overlaid on the HAADF image (Fe and Bi atoms are depicted in green and blue respectively). b) Profile of the HAADF intensity integrated in between the two horizontal white lines of (a). c) Sum of 9 raw spectra of Ca $L_{2,3}$ edges probed in site 1 (red dotted line) and 2 (blue dotted line) in (d) are shown along with the normalized sum (black dotted line) of 14160 spectra in this region. The energy dispersion used was 0.26 eV ch^{-1} and each spectrum was acquired in 30 ms.

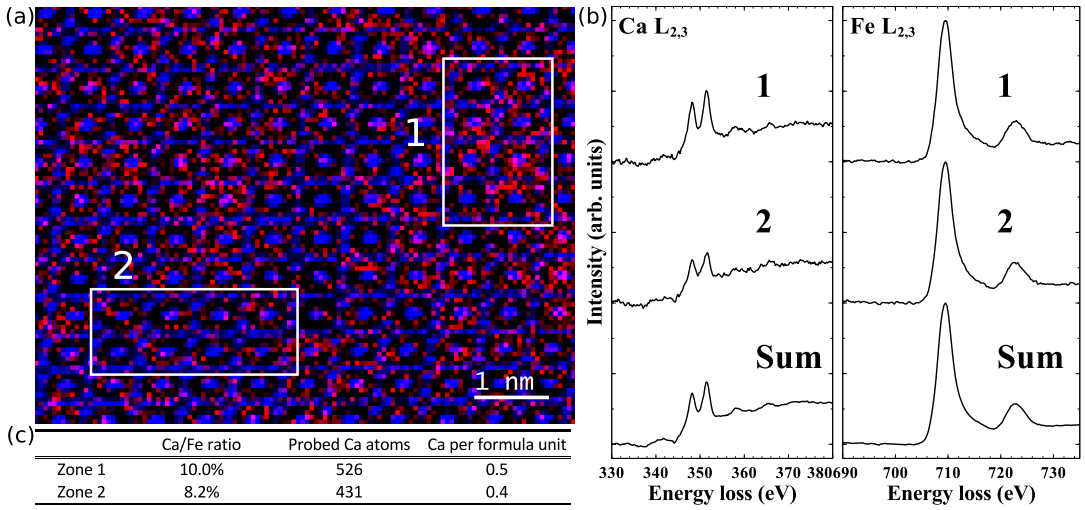

FIGURE 4.14: a) Ca $L_{2,3}$ integrated intensity map (red) superimposed on the simultaneously-recorded HAADF intensity map (blue). b) Ca $L_{2,3}$ and Fe $L_{2,3}$ edges extracted from area 1, area 2 and from the complete SpIm. c) Table summarizing the Ca/Fe ratio determined in zone 1 (based on 786 spectra) and zone 2 (based on 731 spectra), each zone corresponding to the area of two garnet unit cells. The energy dispersion used was 0.26 eV ch^{-1} and each spectrum was acquired in 30 ms.

Summary of chapter 4

In this chapter the structural and microstructural features of the films along with the dopant integration in the garnet lattice were investigated. The films are mostly composed of a well-crystallized epitaxial garnet phase with a low mosaicity but they present minor weakly crystallized and textured hematite nanocrystallites inclusions in between the garnet grains. These nanocrystallites are not detectable by XRD but the growth conditions that would prevent the formation of the nanocrystallites are discussed in this thesis. The strain analysis by GPA indicate a complete strain relaxation over few tens of nm. The as-grown thin films are oxygen off-stoichiometric and the complete filling of the oxygen sub-lattice is achievable by annealing while preserving the structural and microstructural features of the film. Besides, an homogeneous distribution of Y is observed in the films indicating a good solubility of Y in the garnet matrix. In contrast, the Ca distribution at the nanometric scale oscillates along the growth direction. Nevertheless, the integration of Ca in the garnet structure is demonstrated at the atomic scale.

Chapter 5

Electrical properties and charge distribution

In section 4.1, we demonstrate the excellent structural properties of the thin films exhibiting a single crystal garnet phase with a cube-on-cube epitaxy. The presence of a weakly-crystallized ferric oxide secondary phase should not hinder the electrical resistivity of the films as it is non-percolating. The solubility of both Ca and Y was successfully evidenced by STEM/EELS (section 4.3). In this chapter, the electrical resistivity of Ca/Y-substituted BIG and Y-substituted thin films are investigated first. The Y-substituted thin films are studied further regarding their electrical transport properties under different atmospheres. Then, the distribution of charges in as-grown B($Ca_{0.3}Y_{0.2}$)IG, TA96 B($Ca_{0.0}Y_{0.5}$)IG and TA48 B($Y_{1.0}$)IG are probed by STEM/EELS at the nanometric scale. Finally, a combination of XMCD and Cs-STEM/EELS is used to resolve the charge distribution in TA48 B($Y_{1.0}$)IG and TA96 B($Ca_{0.0}Y_{0.5}$)IG down to the atomic scale. The results presented in sections 5.1 to 5.3.2 are published in ref. [58].

	$\rho_{300\ K}(\Omega\ cm)$	$\rho_{450\ K}(\Omega\ cm)$	$S_{340\ K}(\mu V\ K^{-1})$
YIG	1×10^{13}		-5×10^4
BIG		8×10^3	
B($Ca_{0.3}Y_{0.2}$)IG		3.7×10^3	300
B($Ca_{0.0}Y_{0.5}$)IG	9.6×10^2	4.1×10^1	-18
B($Y_{1.0}$)IG	4×10^3		

TABLE 5.1: Summary of the measured electrical transport properties of various iron garnets. The electrical properties of YIG are extracted from ref. [64].

5.1 N- and p-type semiconductors

Fig. 5.1 presents the electrical transport properties measured at high temperatures ($T > 300$ K) under air atmosphere for as-grown BIG and B($Ca_{0.3}Y_{0.2}$)IG and for TA96 B($Ca_{0.0}Y_{0.5}$)IG thin films. The electrical resistivity values for all garnet films increase with decreasing temperature, indicating a semiconducting behavior ($\frac{\partial \rho}{\partial T} < 0$). The typical resistivity values are displayed in Table 5.1. These results represent a large improvement in the transport properties of iron garnet phases, with resistivities up to ten orders of magnitude lower than those of its parent compound, YIG [63, 64]. These findings also confirm that doping BIG thin films with Ca and/or Y leads to an additional functionality exploiting their electrical conductivity. In particular, B($Ca_{0.0}Y_{0.5}$)IG films present resistivity values as low as $\rho = 9.6 \times 10^2\ \Omega$ cm at room temperature with an activation energy of $E_a = 0.25$ eV in between 300 K and 400 K. The Seebeck coefficients as an intrinsic probe to determine the type of majority carriers were also measured in Ca/Y-substituted BIG films. B($Ca_{0.0}Y_{0.5}$)IG presents a negative Seebeck coefficient with $|S|$ around $15 - 25 \mu V\ K^{-1}$ at 340 K (Fig. 5.2), indicating electrons as the predominant charge carriers with a concentration that can be estimated roughly to $10^{20} - 10^{21} cm^{-3}$ based on the Heikes formula [87]. Such carrier concentration should lead to mobilities of ca. $10^{-2} - 10^{-3} cm^2 V^{-1} s^{-1}$ which is somewhat too low for accurate Hall effect measurements. Among the n-type iron garnet systems, this B($Ca_{0.0}Y_{0.5}$)IG phase exhibits so far one of the lowest electrical resistivity value at 300 K ; previously a comparable value has only been reported for an n-type Sn-doped YIG single crystal ($10^3 \Omega$cm at 300 K and $E_a = 0.3$eV), in which additional charge carriers are introduced via tetravalent cationic substitutions [67]. The similar E_a values tend to indicate that Sn-doped YIG and B($Ca_{0.0}Y_{0.5}$)IG have the same transport mechanisms, i.e. band conduction [74]. Here, the transport properties of the n-type B($Ca_{0.0}Y_{0.5}$)IG phase appear to originate solely from the presence of oxygen vacancies acting as donors and inducing Fe^{2+} as expressed in eq. 5.1:

$$Bi_{2.5}Y_{0.5}Fe_5O_{12-\delta} \rightarrow Bi^{3+}_{2.5}Y^{3+}_{0.5}Fe^{3+}_{5-2\delta}Fe^{2+}_{2\delta}O_{12-\delta} \tag{5.1}$$

The point defect equilibrium that describes the formation of oxygen vacancies in the n-type B($Ca_{0.0}Y_{0.5}$)IG can be described using the Kröger-Vink notation [172] as :

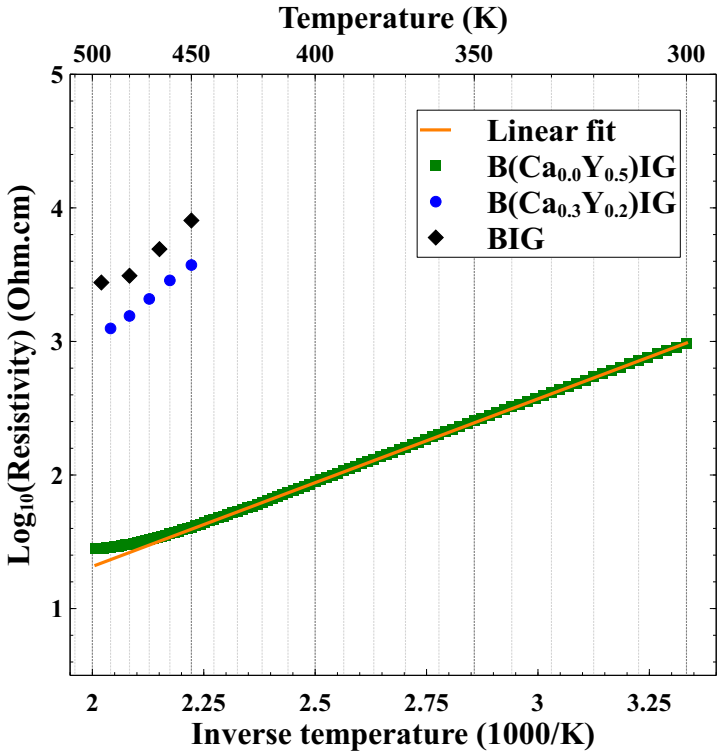

FIGURE 5.1: Logarithm of the resistivity as a function of the reciprocal temperature for the $B(Ca_xY_{0.5-x})IG$ series and BIG under air atmosphere. A linear fit was applied to extract the activation energy on $B(Ca_{0.0}Y_{0.5})IG$ over the range 300 to 450K.

$$5Fe_{Fe}^{x} + (12-\delta)O_{O}^{x} \rightleftharpoons (5-2\delta)Fe_{Fe}^{x} + 2\delta Fe_{Fe}^{'} + \delta V_{O}^{\cdot\cdot} + \frac{\delta}{2}O_{2(g)} \tag{5.2}$$

Where $V_{O}^{\cdot\cdot}$, Fe_{Fe}^{x} and $Fe_{Fe}^{'}$ denote an oxygen vacancy with relative charge +2, the neutrally effective charged Fe^{3+} and the Fe^{2+} cations both at the Fe site, respectively.

$B(Ca_{0.3}Y_{0.2})IG$ exhibits overall higher electrical resistivity values than the Y-substituted films. The substitution of 0.3 Ca per f.u. was chosen for resistivity measurements to match dopant concentration of the best p-type YIG [73]. At that concentration, the electrical resistivity of $B(Ca_{0.3}Y_{0.2})IG$ could be measured only above 450 K due to its high impedance values and reaches almost 4×10^3 Ω cm at that temperature. $B(Ca_{0.3}Y_{0.2})IG$ films exhibit a large positive Seebeck coefficients with $|S|$ in the range of $300\mu V\,K^{-1}$ at 340 K (Fig. 5.2), indicating that holes are the predominant charge carriers with a concentration that can be estimated roughly to $10^{19} - 10^{20}$ cm^{-3} using the Heikes formula [87]. This positive Seebeck coefficient is consistent with the Ca^{2+} substitution acting as an acceptor that should induce the presence of Fe^{4+} in $B(Ca_{0.3}Y_{0.2})IG$. These resistivity values are one order of magnitude

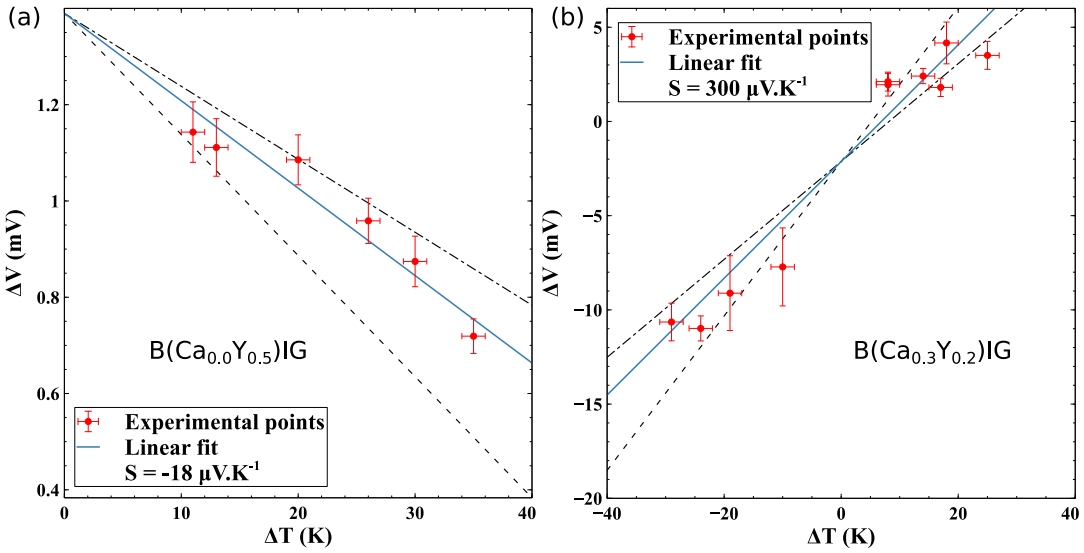

FIGURE 5.2: Determination of Seebeck coefficient at 340K of B($Ca_{0.0}Y_{0.5}$)IG (a) and B($Ca_{0.3}Y_{0.2}$)IG (b). To guide the reader regarding errors on the thermopower determination, maximum S values (dashed lines) and minimum S values (dashed-dotted lines) were plotted.

higher than those of the best Ca-doped YIG film obtained by LPE, i.e. around 10^2 Ω cm resistivity at 450 K [73]. The difference might originate from a stronger self-compensation [173] of Ca^{2+} with oxygen vacancies in the thin films. The scenario of the self-compensation mechanism can be written as follows :

$$Bi_{2.5}Y_{0.2}Ca_{0.3}Fe_5O_{12-\delta} \rightarrow Bi^{3+}_{2.5}Y^{3+}_{0.2}Ca^{2+}_{0.3}Fe^{3+}_{4.7+2\delta}Fe^{4+}_{0.3-2\delta}O_{12-\delta} \tag{5.3}$$

which in the Kröger-Vink notation becomes:

$$0.3Ca^{\cdot}_{Bi} + 5Fe^{x}_{Fe} + (12-\delta)O^{x}_{O} \rightharpoonup (4.7-2\delta)Fe^{x}_{Fe} + (0.3-2\delta)Fe^{\cdot}_{Fe} + \delta V^{\cdot\cdot}_{O} + \frac{\delta}{2}O_{2(g)} \tag{5.4}$$

Where $V^{\cdot\cdot}_{O}$, Fe^{x}_{Fe} and $Fe^{\cdot}_{Fe}$ denote an oxygen vacancy with relative charge +2, the neutrally effective charged Fe^{3+} and the Fe^{4+} cations both at the Fe site, respectively[1]. For both n-type B($Ca_{0.0}Y_{0.5}$)IG and p-type B($Ca_{0.3}Y_{0.2}$)IG thin films, oxygen vacancies act as intrinsic donors and appear to play a key role in their electrical transport properties as highlighted in Eq. 5.2 and 5.4.

[1]Eq. 5.4 is valid for $\delta \leq 0.15$.

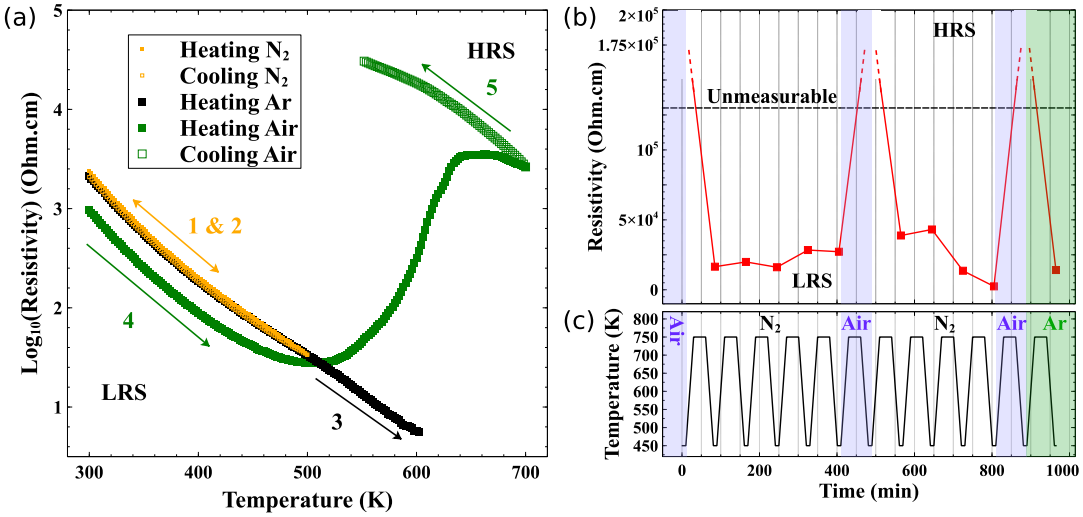

FIGURE 5.3: a) Heating/cooling resistivity cycles under inert (N_2, Ar) and oxidizing (Air) atmospheres exhibiting LRS and HRS. b) Resistivity measured at 450 K after annealing at 750 K under different atmospheres. The thermal cycling procedure is shown in c) along with the used atmospheres (Air in blue, N2 in white and Ar in green).

5.2 Reversible resistivity change

Since they exhibit a lower resistivity, n-type B($Ca_{0.0}Y_{0.5}$)IG films were further investigated under inert and oxidizing post-annealing conditions (Fig. 5.3 (a)) to understand the influence of the oxygen vacancies. Heating/cooling cycles (1 and 2 in Fig. 5.3 a)) were applied first under N_2 atmosphere demonstrating that a low-resistance state (LRS) with $\rho(300K) = 10^3\ \Omega$ cm is still preserved at 500 K. Heating under Ar atmosphere (3 in Fig. 5.3 (a)) keeps the B($Ca_{0.0}Y_{0.5}$)IG films in the LRS until 600 K. However, thermal cycles under air above 500 K induce a transition to a high-resistance state (HRS). The HRS persists after cooling down to room temperature with impedance larger than our measurement capabilities ($> 200\ G\Omega$). This resistive change of at least three orders of magnitude achieved under post-annealing in inert/oxidizing atmospheres tends to confirm the key role of oxygen vacancies in the transport mechanisms. The LRS and HRS are both stable in time at ambient temperature and pressure and XRD data confirm that the garnet phase is preserved in both states after thermal cycling as shown in Fig. 5.4. Resistivity changes and reversibility capabilities were examined further through subsequent thermal cycles performed in different atmospheres. Fig. 5.3 (b) illustrates that the resistivity switch between the two states is totally reversible when alternating high-temperature annealing under inert/oxidizing atmospheres. A similar reversible resistive change is also observed for B($Y_{1.0}$)IG. It suggests that the same mechanisms as those of B($Ca_{0.0}Y_{0.5}$)IG films are

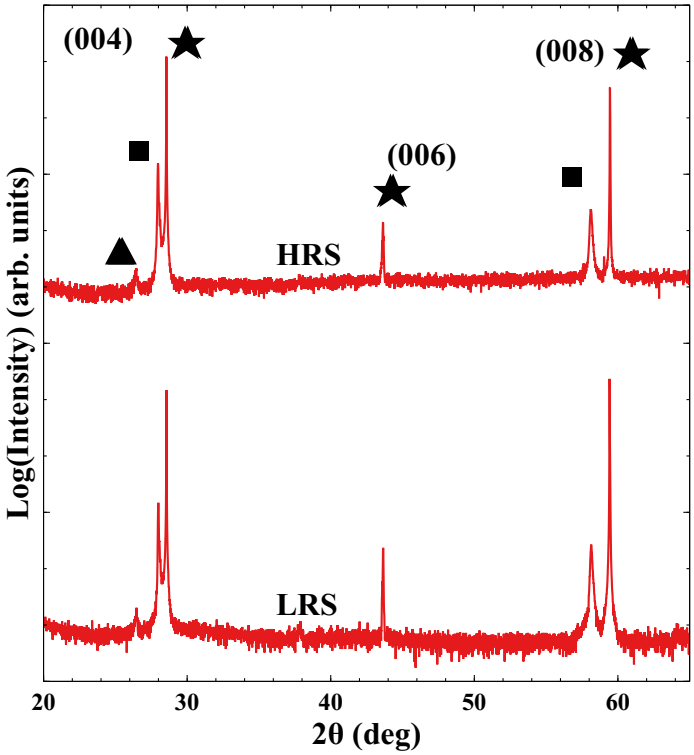

FIGURE 5.4: Intensities of $\Theta - 2\Theta$ XRD scans (Cu-$K\alpha 1$) of HRS and LRS n-type B($Ca_{0.0}Y_{0.5}$)IG in logarithmic scale. The reflections of the films and the GGG substrate are highlighted with squares and stars, respectively. A graphite plate used for thermal conduction during electrical transport measurements produces a peak indicated by a triangle.

present in B($Y_{1.0}$)IG films. This reversible resistivity change of large amplitude makes Y-substituted BIG a promising material for gas sensing applications [174].

The electrical resistivity behavior of B($Ca_{0.3}Y_{0.2}$)IG in air atmosphere was also studied under successive heating and cooling cycles as shown in Fig. 5.5. The resistivity increases from $\rho(450\text{K}) = 5.3 \times 10^3 \Omega\text{cm}$ to $\rho(450\text{K}) = 1.7 \times 10^4 \Omega\text{cm}$ after two heating/cooling cycles between 450 K and 500 K. The B($Ca_{0.3}Y_{0.2}$)IG thin film is p-type, then this resistivity increase corresponds to a decrease of the net number of holes. It tends to indicate that annealing at $T > 450$ K under air atmosphere induces the formation of oxygen vacancies that compensate with the holes brought by Ca^{2+}. In contrast, at high temperatures the air atmosphere acts as an oxidizing atmosphere for n-type B($Ca_{0.0}Y_{0.5}$)IG. However, these two opposite behaviours are not in contradiction as it is known that acceptors tend to lower the formation energy of oxygen vacancies [175]. Similar temperature cycles in inert atmosphere, which should favor even more the formation of oxygen vacancies, were performed for the p-type Ca-substituted thin films and the same resistivity increase was observed as expected.

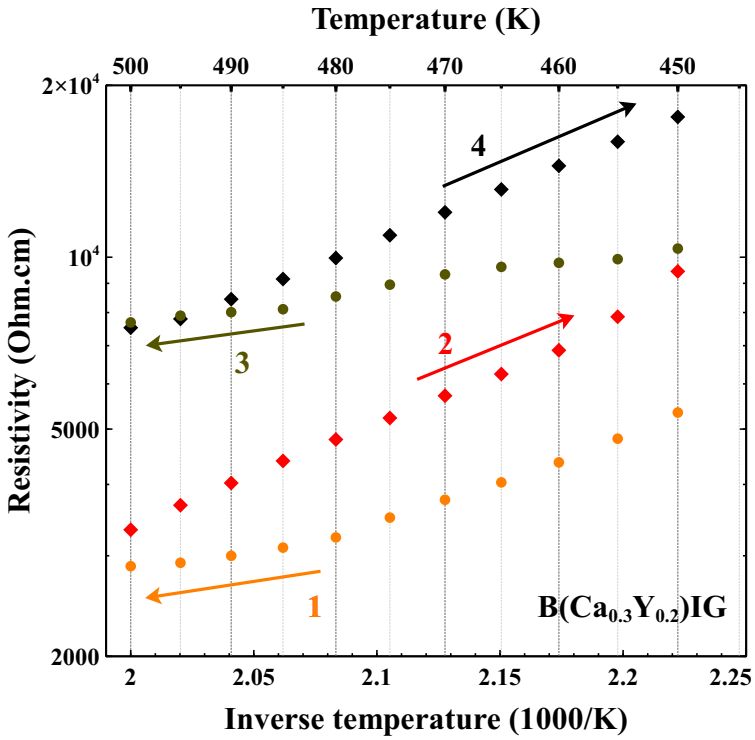

FIGURE 5.5: Resistivity (logarithmic scale) as a function of inverse temperature for $B(Ca_{0.3}Y_{0.2})IG$ under air atmosphere during heating (1 and 3) and cooling (2 and 4). The numbers (1,2,3 and 4) indicate the order in which the measurements were done.

5.3 Charge distribution

The distribution of charges in TA96 $B(Ca_{0.0}Y_{0.5})IG$, TA48 $B(Y_{1.0})IG$ and as-grown $B(Ca_{0.3}Y_{0.2})IG$ thin films were first probed by STEM/EELS to assess the origin and the nature of their electrical properties. With an energy resolution of 500 meV, the local charge variation can be derived through the analysis of the EELS spectral fine structures as described in section 3.1.6. The amount of Fe^{2+} can be identified by differences in Fe $L_{2,3}$ fine structures with respect to Fe^{3+} (section 3.1.6) [125]. Fe^{4+} has two spectral signatures, the main one is a pre-peak on the O K edge because of the primary $3d^5\underline{L}$ nature of Fe^{4+} and another one on the Fe $L_{2,3}$ edge as a result of its partial $3d^4$ nature [128, 123, 176]. Then, the films were studied further by XAS and XMCD that provides a wealth of information on charge and coordination. The charge distribution of p-type $B(Ca_{0.3}Y_{0.2})IG$ is discussed first and the one of $B(Ca_{0.0}Y_{0.5})IG$ and $B(Y_{1.0})IG$ are discussed next.

5.3.1 Holes in B($Ca_{0.3}Y_{0.2}$)IG

The evolution of the O *K* edge together with the Ca $L_{2,3}$ edge was probed in B($Ca_{0.3}Y_{0.2}$)IG through the Ca oscillations along the growth direction. While the absolute quantification of the valence is often difficult, relative variations of the valence are easier to determine. Thus, we took advantage of the Ca heterogeneity to investigate the possible relative charge evolution in correlation with the Ca concentration. In Fig. 5.6 (b), the Ca $L_{2,3}$ edge intensity map shows a modulation similar to Fig. 4.12 (b) (section 4.3.2). Spectra from Ca-rich (A) and Ca-depleted (B) regions are shown in Fig. 5.6 (d) together with spectra acquired in pure BIG as a reference. A Ca-rich region is expected to induce locally more holes and therefore a higher intensity pre-peak or a lower energy of the onset of the O *K* edge. However, the O *K* edges probed in regions A and B have the same fine structures as those of BIG; their edge onsets are at the same energy-loss and none of these spectra exhibit any pre-peak. Additionally, a comparison of the O *K* edges of B($Ca_{0.3}Y_{0.2}$)IG and BIG probed by XAS did not reveal the presence of a pre-peak for the p-type film (not shown here).

One should note that probing low Fe^{4+} densities by spectroscopy techniques is challenging because of the low O *K* cross-section and the mixed $3d^5\underline{L}/3d^4$ natures of the Fe^{4+} configuration. The quantification of holes in transition metal oxides by STEM/EELS has rarely been reported and mostly in the case of a heavily hole-doped cuprates [121]. Nevertheless, this absence of Fe^{4+} signature, despite the solubility of the Ca in the garnet matrix (section 4.3.2), indicates that most of the Ca dopants do not introduce holes. This is consistent with the large positive Seebeck coefficient probed in as-grown B($Ca_{0.3}Y_{0.2}$)IG (section 5.1) and tends to corroborate the strong compensation of holes induced by Ca^{2+} with oxygen vacancies as described in Eq. 5.4. Both pure and substituted-BIG thin films present larger unit cells than their parent compound i.e. YIG. This may promote a decrease in the formation energy of oxygen vacancies in BIG systems resulting in a stronger self-compensation of the divalent dopant. This trend is expected from the known chemical expansion caused by oxygen vacancies and has been demonstrated for others TMO thin films where the tensile strain increases the concentration of oxygen vacancies [177]. On that aspect, the co-substitution can also act for controlling the cell volume and could be a strategy to govern the self-compensation mechanism when fine-tuning p- and n-type BIG as demonstrated in the case of ZnO [173].

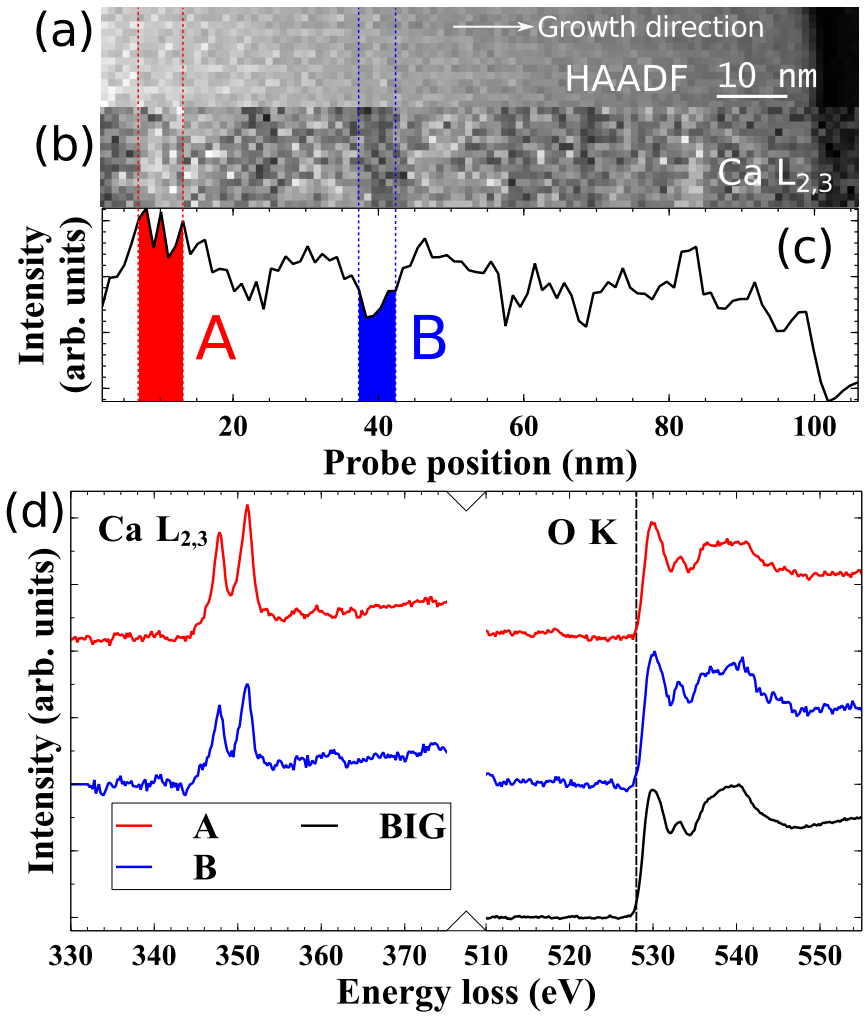

FIGURE 5.6: a) HAADF intensity recorded simultaneously with the EELS map in B($Ca_{0.3}Y_{0.2}$)IG. b) and c) Ca $L_{2,3}$ integrated intensity map and summed profile respectively. d) 70 raw spectra Ca $L_{2,3}$ and O K edges probed in Ca-rich region 1 (red line) and Ca-depleted region 2 (blue line) as shown in c). A sum of 15000 O K edge spectra of BIG (black line) is shown for comparison. The energy dispersion used was 0.19 eV ch^{-1} and each spectrum was acquired in 200 ms.

5.3.2 Electrons in Y-substituted BIG

Charge distribution at the nanometric scale

As it was shown in section 4.3.1, the film/substrate interface is sharp and the cationic distribution is homogeneous. The chemical homogeneity of the garnet phase is expected to induce an homogeneous charge distribution. Hence, EELS core-loss fine structures were investigated in grains of TA96 B($Ca_{0.0}Y_{0.5}$)IG over areas of a few hundred nm^2 for each resistivity state, i.e. LRS and HRS. In LRS, the presence of oxygen vacancies are expected to induce Fe^{2+} which has a recognizable $L_{2,3}$ edge spectral signature. Fig. 5.7 (a) and (b) display Fe L_3 and Fe L_2 edges, respectively, probed in HRS and LRS films. While the HRS system exhibits the typical fine structures of Fe^{3+} in a mixed T_d and O_h environments as expected from an iron garnet structure [125, 178], the LRS spectrum presents additional Fe^{2+} fine structures, highlighted by arrows in Fig. 5.7 (a) and (b) [119]. The presence of Fe^{2+} in the LRS is the clear signature of additional electrons that induce an increased n-type conductivity when the samples are annealed under inert atmosphere.

To quantify the concentration of the induced charge carriers in the LRS relatively to the HRS, the LRS Fe L_3 edge was fitted as a linear combination of siderite as an Fe^{2+} reference and the HRS as an internal Fe^{3+} reference using a least-square fitting method Fig. 5.7 c) [179, 119, 180]. The Fe site in siderite is solely in O_h coordination but the Fe^{2+} being a minority component in LRS, the lack of T_d fine structures does not impact the fitting procedure. This results in an $Fe^{2+}/\Sigma Fe$ ratio of $13 \pm 2\%$, which corresponds to 0.65 Fe^{2+} per f.u., a $\delta = 0.325$ based on Eq. 5.2 and 2.6×10^{21} cm^{-3} electrons; corroborating further the carrier concentrations estimated from the Seebeck coefficient measurement. The TA48 B($Y_{1.0}$)IG films in LRS was also studied by STEM/EELS and revealed the presence of Fe^{2+} as well. The same fitting procedure was applied resulting in a $Fe^{2+}/\Sigma Fe$ ratio of $12 \pm 2\%$.

In earlier work, concentrations of 0.07 Fe^{2+} per f.u. were reported in Sn^{4+} doped YIG by means of chemical titration on flux grown samples [67]. Such a low Fe^{2+} value might be attributed to the presence of impurities induced by the flux growth technique or the titration method that assumes no oxygen vacancies. More recently, in YIG ceramics, concentrations from 0.2 up to 1.25 Fe^{2+} per f.u.[181, 178] were determined by direct X-ray photo-electron and X-ray absorption spectroscopy techniques. The Fe^{2+} concentration probed in the present work lies in the middle of the range of these reports. This indicates that the garnet structure might accommodate even more oxygen

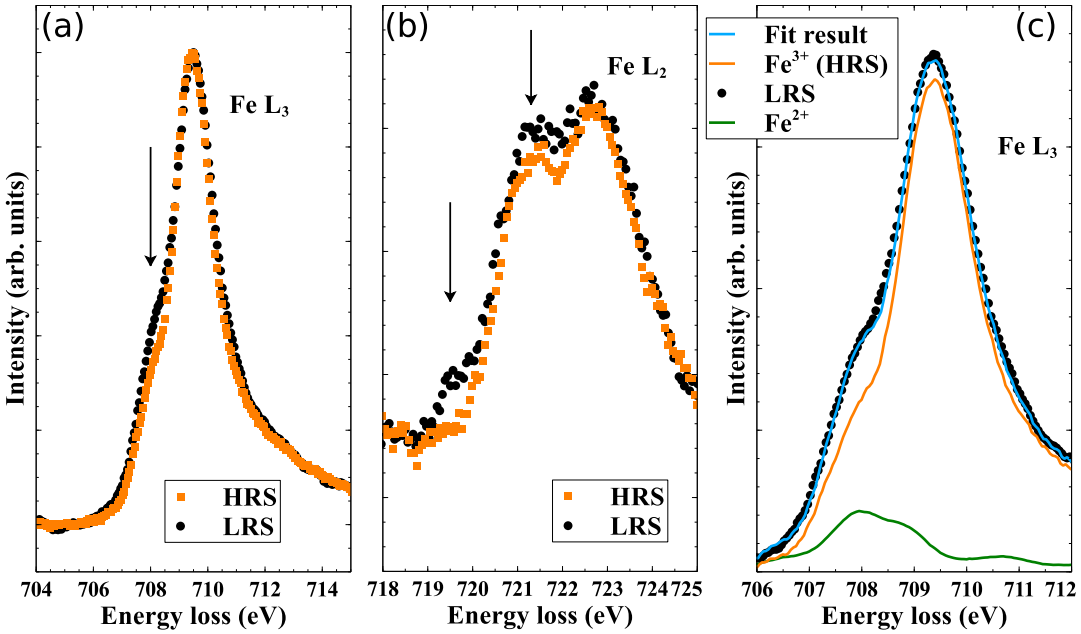

FIGURE 5.7: a) and b) Sum of spectra of Fe L_3 and Fe L_2 edges, respectively, acquired with a 0.06ev ch^{-1} dispersion and a 100 ms exposure time on about a few hundred of nm^2 area in a grain of B($Ca_{0.0}Y_{0.5}$)IG in HRS (192 spectra, black dot) and in LRS (756 spectra, orange square). Characteristic Fe^{2+} fine structures in LRS are indicated by black arrows. c) The LRS Fe L_3 edge was fitted from 706 to 712 eV as a linear combination (blue line) of the HRS spectral signature as Fe^{3+} reference (orange line) and of the siderite as a Fe^{2+} reference (green line).

vacancies. Further annealing in inert atmosphere might then induce a larger charge carrier concentration leading to an enhanced n-type conduction state.

Charge distribution at the atomic scale

The Fe $L_{2,3}$ fine structures were probed at the atomic scale in garnet grains[2] to unveil a possible correlation between the charge distribution and the coordination of iron. In iron garnets, there are two iron sub-lattices, T_d and O_h, that have different spectral signatures shown in section 3.1.6. In the studied thin films, there are additionally two valence states of iron, i.e. mostly Fe^{3+} and minor amount of Fe^{2+} (see Eq. 5.2), each having a different spectral signature which are shown in section 3.1.6. Here, the aim is to determine whether the Fe^{2+} are preferentially located on the T_d, on the O_h sites or randomly distributed.

[2]The following spectra were probed as far as possible from the secondary phase inclusions to obtain spectra purely originating from the garnet phase.

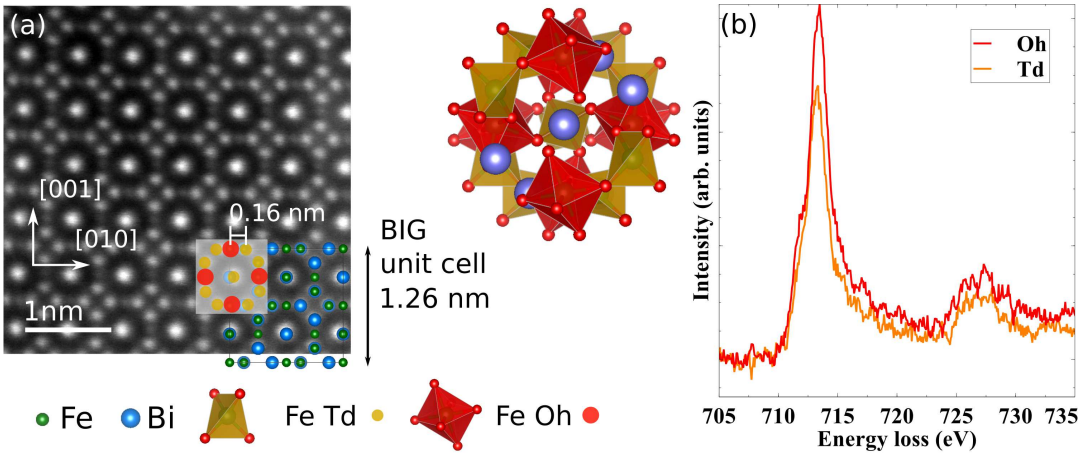

FIGURE 5.8: a) atomically-resolved STEM-HAADF image of BIG. The atomic model of cation sub-cell along with the Fe coordination model of the garnet structure are overlaid on the HAADF image. Fe and Bi atoms are depicted in green and blue, respectively, while Fe-O_h and Fe-T_d are depicted in red and orange, respectively. b) Fe $L_{2,3}$ edges of B($Ca_{0.0}Y_{0.5}$)IG HRS extracted from the O_h (red) and T_d (orange) sites. Each spectrum is the sum of 72 spectra acquired with a 0.06ev ch^{-1} dispersion and a 100 ms exposure time.

B($Ca_{0.0}Y_{0.5}$)IG HRS

To this end, the TA96 B($Ca_{0.0}Y_{0.5}$)IG in HRS (i.e. after annealing in oxidizing atmosphere) and in LRS (i.e. after annealing in inert atmosphere) and the B($Y_{1.0}$)IG in LRS were probed using Cs-STEM/EELS along the [001] zone axis. The cluster analysis using the K-means++ algorithm (section 3.3.1) was applied on the Fe L_3 edge to disentangle the different fine structures associated to each iron state. The acquired SpIm of the three Y-substituted films present a SNR of approximately 300 which makes them suitable candidates for cluster analysis. We first applied the analysis to the B($Ca_{0.0}Y_{0.5}$)IG HRS. The distribution of Fe O_h and Fe T_d atomic columns along with the sum of raw spectra extracted from O_h and T_d columns are shown in Fig. 5.8. The O_h Fe L_3 edge is more intense than the T_d Fe L_3 edge due to the higher Fe density in the O_h columns. The shoulder of the O_h Fe L_3 peak is more visible than for the T_d Fe L_3 and the T_d Fe L_3 is slightly shifted towards lower energy loss. These facts are consistent with what was shown in section 3.1.6. For the clustering, the procedure described in section 3.3.1 is applied to determine the optimal number of clusters to perform the K-means++ algorithm.

The results of the clustering with three clusters are shown in Fig. 5.9. One cluster corresponds to the O_h sites (blue) and exhibits a higher intensity, as expected. The other two clusters correspond to the T_d sites (T_d 1 red and T_d 2 brown). They have different intensities which might be related to different proportions of elastic scattering corresponding to these particular imaging

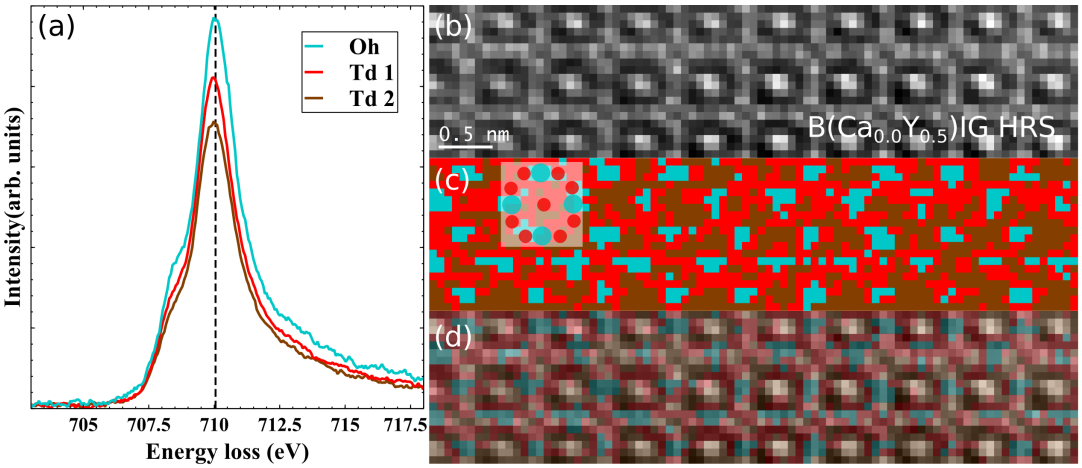

FIGURE 5.9: Clustering results on the B($Ca_{0.0}Y_{0.5}$)IG HRS. a) Centroids corresponding to the computed clusters. b) HAADF intensity map recorded simultaneously with the EELS map. c) Map of the clusters labels. A scheme of the site occupancy is superimposed on this map. d) Superimposition of (c) and half transparent (b) to highlight the structure of the cluster labels. The spectra were acquired with a 0.06ev ch^{-1} dispersion and a 100 ms exposure time.

conditions [3]. The minimum intensity difference between two centroids is 5% and the T_d centroids are both shifted of 0.07 ± 0.01 eV to lower energy than the O_h centroid. The B($Ca_{0.0}Y_{0.5}$)IG presents then two T_d Fe^{3+} clusters with different intensities and an O_h Fe^{3+} cluster.

B($Ca_{0.0}Y_{0.5}$)IG LRS

For the B($Ca_{0.0}Y_{0.5}$)IG LRS, the results of the cluster analysis with two clusters are shown in Fig. 5.10. One cluster corresponds to the O_h sites (blue) and the other one corresponds to the T_d sites (brown). The intensity difference between the two centroids is 4% and the T_d centroid is shifted of 0.13 ± 0.01 eV to a lower energy than the O_h centroid. The additional energy shift of the LRS T_d centroid compared to the HRS T_d centroids tends to indicate that the Fe^{2+} are preferentially located on the T_d sites. The two centroids correspond then to a T_d $Fe^{2+/3+}$ and a O_h Fe^{3+}.

B($Y_{1.0}$)IG LRS

For the B($Y_{1.0}$)IG LRS, the results of the cluster analysis with four clusters are shown in Fig. 5.11. One cluster corresponds to the O_h sites (blue) and the other clusters correspond to the T_d sites (T_d 1 brown, T_d 2 red and T_d 3 turquoise). The minimum intensity difference between two centroids is 5%.

[3] Elastic scattering is more likely to produce events at larger angles than inelastic scattering. If a strong proportion of beam intensity is elastically scattered, the intensity of the inelastically scattered signal is therefore reduced.

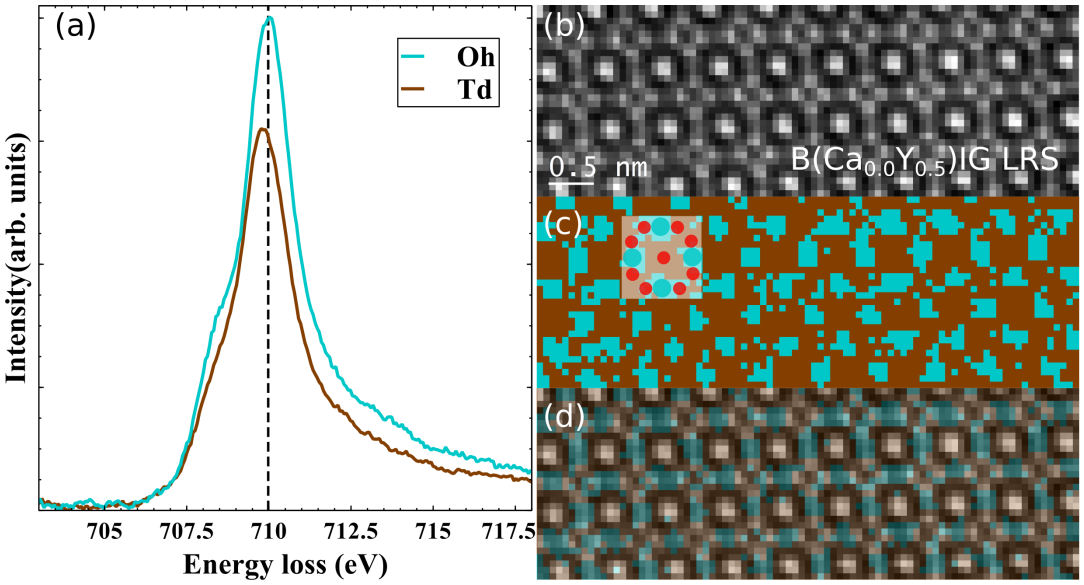

FIGURE 5.10: Clustering results on the B($Ca_{0.0}Y_{0.5}$)IG LRS. a) Centroids corresponding to the computed clusters. b) HAADF intensity map recorded simultaneously with the EELS map. c) Map of the clusters labels. A scheme of the site occupancy is superimposed on this map. d) Superimposition of (c) and half transparent (b) to highlight the structure of the cluster labels. The spectra were acquired with a 0.06ev ch^{-1} dispersion and a 80 ms exposure time.

The T_d centroids are shifted of 0.10 ± 0.01 eV (T_d 2 red and T_d 3 brown) and 0.08 ± 0.01 eV (T_d 1 turquoise) to a lower energy than the O_h centroid. The T_d 1 (turquoise) centroid is mainly located around the O_h site and has the highest intensity and the lowest energy shift. These results tend to indicate that the T_d 1 (turquoise) cluster corresponds to a mixing of the T_d and O_h sites due to the delocalization of the probe. On the other hand, the T_d 2 and T_d 3 (red and brown, respectively) clusters correspond to T_d $Fe^{2+/3+}$ as they exhibit a larger energy shift. The difference in intensity between these two centroids might also be related to different proportions of elastic scattering.

Overall the analysis of Cs-STEM/EELS data using clustering tend to show that Fe^{2+} films are more likely to be located on the T_d sites in LRS for both B($Ca_{0.0}Y_{0.5}$)IG and B($Y_{1.0}$)IG. This behavior is further investigated in the next section using XMCD.

5.3.3 Site specific spectroscopy using XMCD

In this work, the Fe $L_{2,3}$ edge of BIG, as-grown B($Ca_{0.3}Y_{0.2}$)IG, as-grown B($Ca_{0.0}Y_{0.5}$)IG in HRS and TA48 B($Y_{1.0}$)IG in LRS were also studied using XAS and XMCD in TEY. However, we found that XMCD was more sensitive to minor changes of Fe valence states and therefore most of the study focuses on the XMCD results. As in magneto-optics, the magnetic field induces an

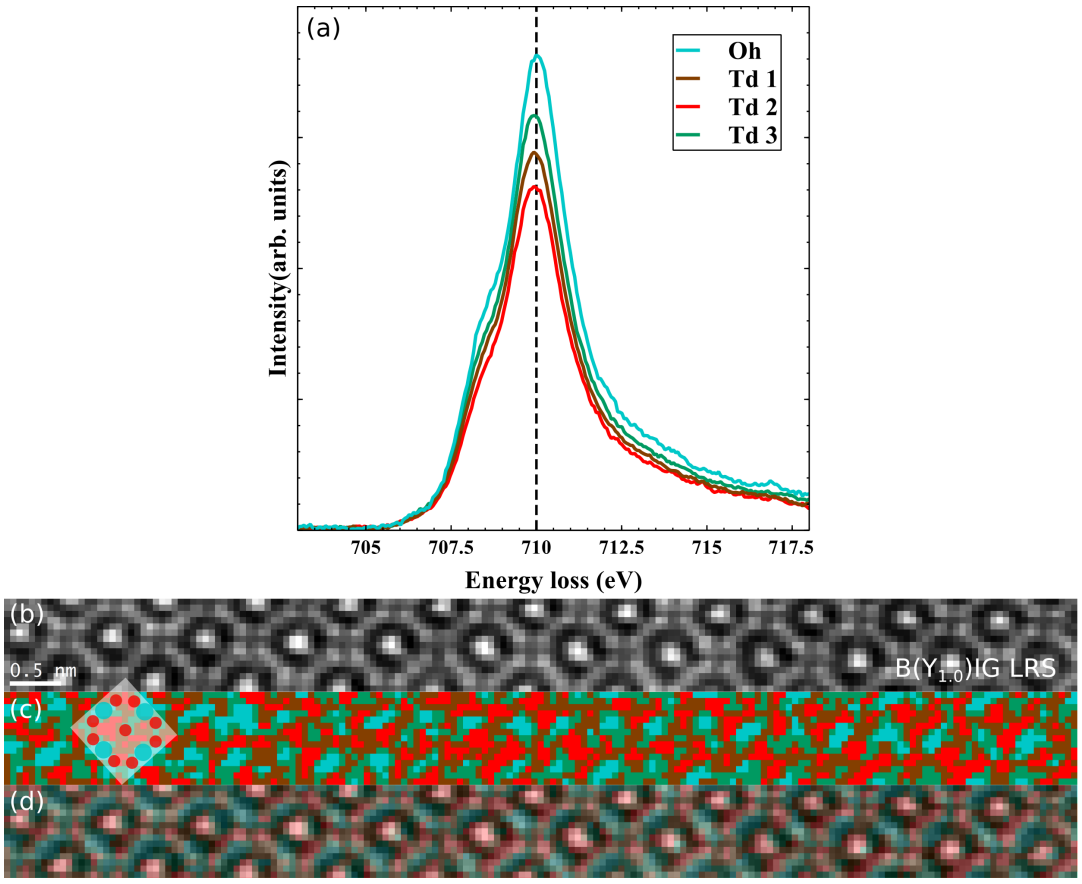

FIGURE 5.11: Clustering results on the $B_{(1.0)}$IG LRS. a) Centroids corresponding to the computed clusters. b) HAADF intensity map recorded simultaneously with the EELS map. c) Map of the clusters labels. A scheme of the site occupancy is superimposed on this map. d) Superimposition of (c) and half transparent (b) to highlight the structure of the cluster labels. The spectra were acquired with a 0.06ev ch^{-1} dispersion and a 50 ms exposure time.

additional energy splitting between the electronic states that is probed using XMCD which increases the sensitivity of this technique to subtle changes in the electronic structure.

XMCD spectral signatures identification

The Fe $L_{2,3}$ edge of iron garnets were rarely studied using XMCD [182, 183]. Hence, the fine structure of Fe $L_{2,3}$ as probed using XMCD are also analysed with the help of the literature on more widely studied iron spinels such as Fe_3O_4 (magnetite). Fe_3O_4 presents O_h and T_d iron sites with a Fe^{2+} O_h: Fe^{3+} O_h : Fe^{3+} T_d ratio of 1: 1: 1. γ-Fe_2O_3 (maghemite) also presents T_d and O_h sites but they both have Fe^{3+}. Magnetite and maghemite, with these Fe mixed-valence states and/or Fe mixed sites coordinations have a similar multiplet structure and thus similar XMCD fine structures as iron garnets. They will be used as references systems for the study of XMCD fine structures of the iron garnets of this work.

An experimental XMCD spectrum of YIG and Ce-doped YIG [183], a calculated XMCD spectrum of Fe_3O_4 [184] and experimental XAS and XMCD spectra of γ-Fe_2O_3 are displayed in Fig. 5.12 (a), (b) and (c), respectively. The different individual spectral signatures of XMCD spectra, e.g. Fe^{3+} T_d, can be identified by a main central peak and minor additional side peaks. In the experimental XMCD spectrum, each peak can be attributed to a main individual spectral signature with minor contributions from the other spectral signatures. Thus, the theoretical spectra in Fig. 5.12 (b), the L_3 peaks labeled a_1 and a_2 correspond mainly to Fe^{2+} in O_h coordination and to Fe^{3+} in O_h coordination, respectively, while the peak labeled d corresponds mainly to Fe^{3+} in T_d coordination [185, 186]. The spectrum of maghemite can be labeled the same way. Nevertheless, the a_1 peak of maghemite is less intense due to the absence of Fe^{2+} on the O_h site and it is composed of a minor contribution from the Fe^{3+} O_h.

The YIG and Ce doped YIG XMCD fine structures can also be labeled similarly as the Fe_3O_4 and γ-Fe_2O_3 spectra. However, in iron garnets, the d peak has a much higher intensity than a_1 and a_2 and the peaks have a different sign because T_d Fe carries the majority magnetic moment unlike Fe_3O_4. For the iron garnets, the a_1 peak has a lower intensity than the a_2 peak as a result of the absence of Fe^{2+} on the O_h site. The presence of Fe^{2+} in T_d coordination was reported in γ-Fe_2O_3 [187] and in Ti-doped Fe_3O_4 [188]

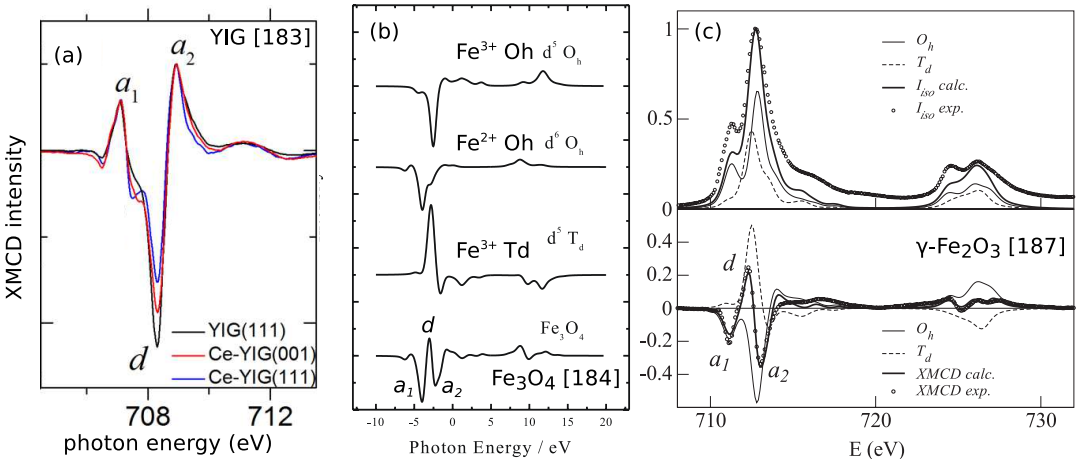

FIGURE 5.12: a) XMCD intensity of YIG (111) and Ce-doped YIG (111) and (001). b) Calculated Fe^{3+} O_h, Fe^{2+} O_h and Fe^{3+} XMCD spectra (top three spectra). Calculated Fe_3O_4 XMCD spectrum (bottom spectrum) using the sum of the top three spectra. c) Experimental XAS (dotted top) and XMCD (dotted bottom) spectra of γ-Fe_2O_3 and their theoretical simulation (thick solid line). The T_d and O_h Fe^{3+} components of the theoretical model are shown in dashed line and thin solid line, respectively. This figure is adapted from refs. [183, 184, 187].

as peak at lower energy than the a_1 peak [4].

XMCD results on Ca and Y co-substituted BIG

Typical XAS spectra with $\sigma+$ and $\sigma-$ polarization were used to obtain the XMCD signal, as shown in Fig. 5.13 (a). The XMCD of the Fe L_3 edge are shown in Fig. 5.13 (b). The Fe L_2 edge has a too low intensity for conclusions on the Fe valence states to be drawn from it. All the films exhibit a similar spectral shape as YIG, indicating that they have mostly Fe^{3+}. An additional peak, labeled δ in Fig. 5.13, at lower energy than a_1 is observed for BIG and B($Y_{1.0}$)IG LRS. In particular, there is a clear difference between the B($Y_{1.0}$)IG LRS spectrum and the B($Ca_{0.0}Y_{0.5}$)IG HRS spectrum at low energy. The energy and sign of the δ peak correspond to the T_d Fe^{2+} spectral signature [188, 187]. Moreover, since the δ peak has an opposite sign compared to the a_1 peak the more intense the δ peak is, the lower the value of the a_1/a_2 ratio is. YIG has only Fe^{3+} and exhibits a a_1/a_2 ratio of 0.54 that was calculated using Fig. 3 (a) of ref. [183].

- The B($Ca_{0.3}Y_{0.2}$)IG does not exhibit the δ peak and its a_1/a_2 ratio is 0.6. This film has mostly Fe^{3+} and a minor amount of Fe^{4+} evidenced by thermopower measurements (see Eq. 5.4). The XMCD results show a complete absence of Fe^{2+}.

[4] according to Vasili et al. [183], the presence of T_d Fe^{2+} is related to a shoulder on the d peak. However, the energy difference between the T_d Fe^{2+} and the T_d Fe^{3+} seems unrealistic.

- The B($Ca_{0.0}Y_{0.5}$)IG HRS does not exhibit the δ peak either and its a_1/a_2 ratio is 0.5. This film was annealed in oxidizing atmosphere before the XMCD experiment and presents only a Fe^{3+} spectral signature.

- The pure BIG exhibits a δ peak and its a_1/a_2 ratio is 0.3. In section 4.2, we show that the films were grown in low PO_2 that could induce oxygen off-stoichiometry. The Fe^{2+} spectral signature probed using XMCD might be induced by this off-stoichiometry. These results may explain why BIG does not present the typical resistivity of an insulator, i.e. $\rho = 10^{12}\ \Omega$ cm (see Fig. 5.1).

- The B($Y_{1.0}$)IG LRS exhibits the most intense δ peak and possesses the highest a_1/a_2 ratio which is 0.22. This strong T_d Fe^{2+} signature tends to indicate the Fe^{2+} is mainly located on the T_d site which is consistent with the Cs-STEM/EELS analysis combined with clustering in section 5.3.2. The magnetic moment associated with the Fe^{2+} T_d is ferromagnetically coupled with the Fe^{3+} T_d.

To summarize, the B($Ca_{0.3}Y_{0.2}$)IG and B($Ca_{0.0}Y_{0.5}$)IG HRS present only a Fe^{3+} spectral signature while the BIG and B($Y_{1.0}$)IG LRS present an additional Fe^{2+} spectral signature mainly located on the T_d site. Moreover, these results are consistent with electrical transport and Cs-STEM/EELS results.

Summary of chapter 5

In this chapter the electrical transport properties of the thin films were investigated and the corresponding charge distributions were probed using Cs-STEM/EELS and XMCD. The Ca and Y co-substituted thin films present a p-type semiconductor behavior with $\rho(450\text{K}) = 3.7 \times 10^3\ \Omega$ cm while the Y-substituted films present a n-type semiconductor behavior with $\rho(450\text{K}) = 4.1 \times 10^1\ \Omega$ cm that is 10^{10} less than the resistivity of YIG. A reversible resistivity change of three orders of magnitude upon inert/oxidizing atmosphere annealing was evidenced in the n-type films. In the p-type films the spectroscopic signature of charge carriers is not detectable either using EELS or XAS as a result of the strong self-compensation by oxygen vacancies. In the n-type films, the presence of 0.65 Fe^{2+} per f.u. was evidenced and both EELS and XMCD tend to show that these charge carriers are mainly located on the Fe T_d sites. In all films, the oxygen vacancies play a major role as intrinsic donors either in the formation or in the compensation of charge carriers.

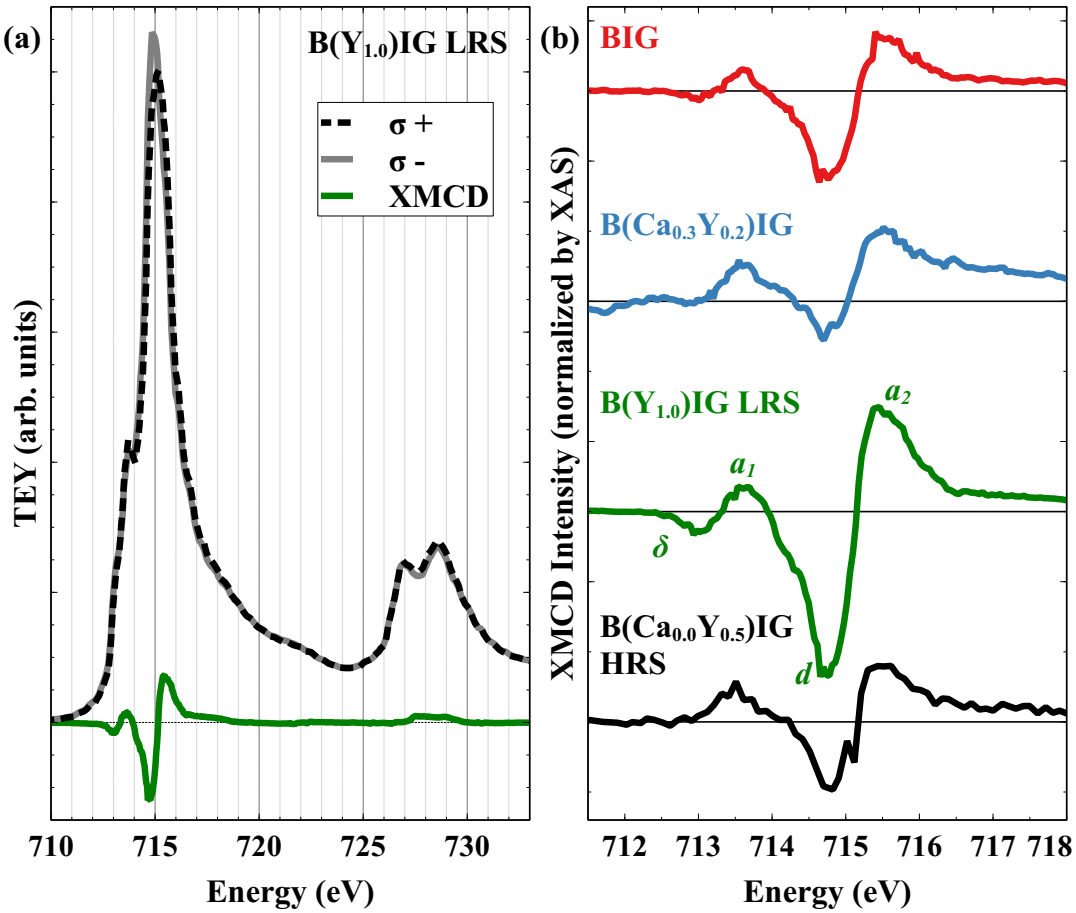

FIGURE 5.13: a) XAS and XMCD spectra of $B(Y_{1.0})IG$ LRS. b) XMCD spectra of BIG (red), $B(Ca_{0.3}Y_{0.2})IG$ (blue), $B(Y_{1.0})IG$ LRS (green) and $B(Ca_{0.0}Y_{0.5})IG$ HRS (black).

Chapter 6

Magneto-optical and magnetic properties

After demonstrating the structural and chemical homogeneity of the main garnet phase in the studied thin films (section 4.1), the electrical transport properties of the films were investigated in section 5.1. The as-grown B($Ca_{0.3}Y_{0.2}$)IG is a p-type semiconductor while the TA96 B($Ca_{0.0}Y_{0.5}$)IG and TA48 B($Y_{1.0}$)IG are n-type semiconductors. Both Y-substituted BIG films exhibit a 3 orders of magnitude reversible resistivity change under atmosphere switch at high temperature. If their magneto-optical (MO) properties are preserved upon doping, these electrical transport properties make the grown thin films potential candidates for future integration in oxytronic devices. In this chapter, the evolution of the MO properties upon doping are investigated by Faraday rotation spectroscopy. Then, the evolution of the Curie temperature (T_C) and of the magnetic anisotropy are discussed in terms of the doping level, the presence of secondary phase inclusions and the structural properties of the films.

6.1 Giant Faraday effect

The Faraday rotation spectra between 1.5 eV and 4 eV were acquired for as-grown and TA48 B($Ca_xY_{0.5-x}$)IG and B($Y_{1.0}$)IG as shown in Fig. 6.1 (a) and (b), respectively. All the spectra of the substituted garnets show overall spectral shapes and intensities similar to BIG Faraday rotation spectrum despite the presence of the secondary phase inclusions. Besides, except for B($Ca_{0.3}Y_{0.2}$)IG, an increase of the Faraday rotation intensity between 8% to 14% is observed upon annealing for the doped thin films. The effect of this post-annealing could not be verified for BIG, since the garnet phase in undoped film is not stable under TA48 but at least the θ_F does not evolve upon

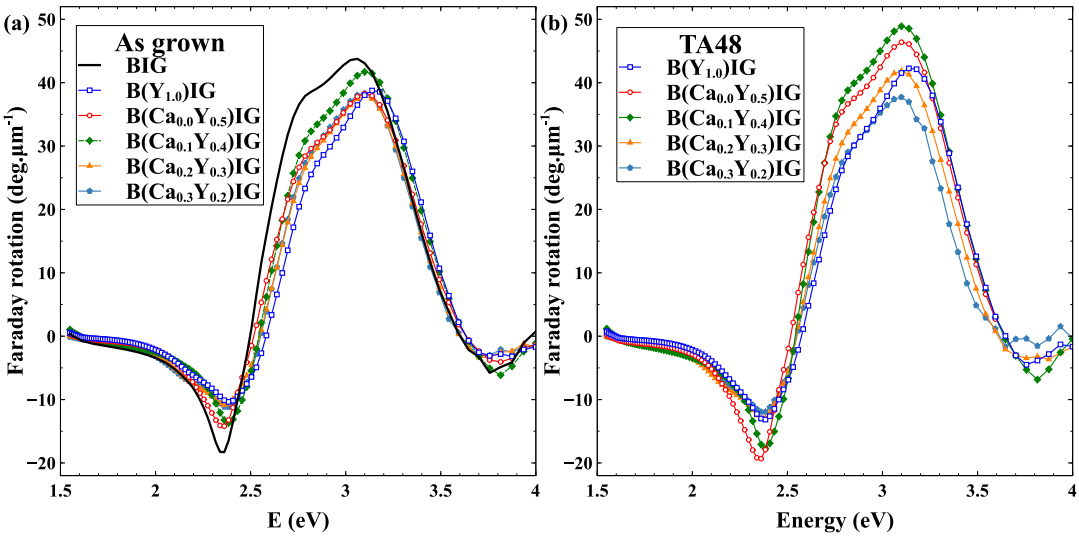

FIGURE 6.1: a) Faraday rotation spectra for as-grown thin films. b) Faraday rotation spectra for TA48 thin films. The open symbols correspond the films solely doped with Y.

annealing 48 hours at 625 K under an O_2 flux of 50 ml min^{-1}. A blue shift is also observed for the Ca and Y co-substituted BIG MO spectra.

In order to quantify the evolution of the Faraday rotation intensity and energy shift while doping the garnet structure, the experimental data were fitted using a model based on two diamagnetic transitions, used by Deb et al. [13], which corresponds to the Dionne and Allen's model described in section 2.1.2. In that model, a diamagnetic transition is parametrized by a transition energy (E), an energy splitting (Δ), a line-width (Γ) and the product (Nf) of the number of active centers (N) and oscillator strength (f). Γ and Δ drive the shape and the intensity of the transition while Nf is only linked to its intensity. The transition at around E_{Oh} = 3.0 eV is associated with the Fe O_h sublattice while the transition at around E_{Td} = 2.5 eV is linked to the Fe T_d sublattice [37, 13]. A typical fit is presented in Fig. 6.2 and the extracted parameters (Nf and E) are shown in Table 6.1. One should note that the least-square fitting of T_d transition yields noisier results due to its lower intensity, therefore the main interpretation is based on the O_h transition parameters.

An average blue shift of Δ E_{Oh}=70 meV with respect to BIG is observed for the $B(Ca_xY_{0.5-x})IG$ series. A larger blue shift of Δ E_{Oh}=110 meV is found for $B(Y_{1.0})IG$. These blue shifts are consistent with what was reported for $Y_{3-x}Bi_xFe_5O_{12}$ thin films and confirms the lower concentration of Bi in the doped thin films [13, 38]. This feature can be explained by the band gap increase from BIG (2.3 eV [29]) to YIG (3.0 eV [30]). For as-grown films, the transition intensity Nf is lower than BIG as this quantity scales with the Bi concentration. However, for TA48 films Nf_{Oh} increases as shown in Table 6.1 and

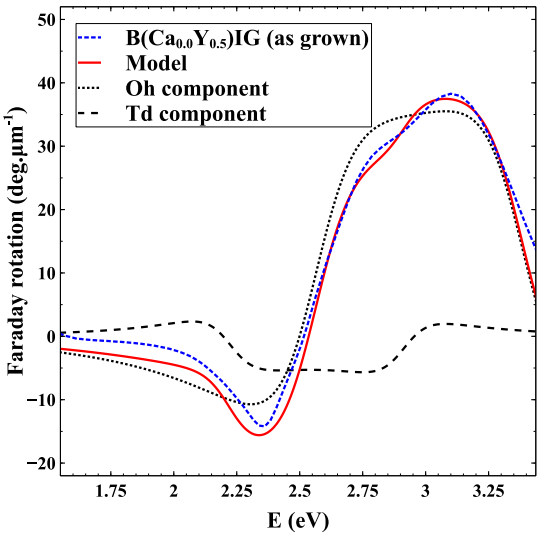

FIGURE 6.2: Experimental Faraday rotation spectrum of $B(Ca_{0.0}Y_{0.3})IG$ (blue dashed line) with its corresponding theoretical model (red line). The black dotted and dashed lines correspond to the octahedral and tetrahedral components, respectively, of the theoretical model.

the Faraday rotation reaches even higher values than BIG for $B(Ca_{0.1}Y_{0.4})IG$ and $B(Ca_{0.0}Y_{0.5})IG$. These high Nf_{Oh} values can be related to the decrease of the unit cell volume upon annealing which increases the hybridization between the Bi, O and Fe electronic states. As-grown thin films might also present Fe^{2+} [58] that could reduce the MO effects while in TA48 films, all Fe should tend to 3+ valence yielding an enhanced Faraday rotation.

The detailed spectral features of as-grown $B(Ca_{0.2}Y_{0.3})IG$ and $B(Ca_{0.3}Y_{0.2})IG$ were further investigated to better understand the effect of Ca substitution on the MO properties. A comparison of the normalized MO spectra of $B(Ca_{0.2}Y_{0.3})IG$ and $B(Ca_{0.3}Y_{0.2})IG$ with the one of undoped BIG is displayed in Fig. 6.3 (a). The spectra of the Ca containing films exhibit a strong additional feature at around 2.2 eV (highlighted by a black arrow in Fig. 6.3 (a)). This additional feature in θ_F reflects an additional spin-split density of states close to the band gap energy of pure BIG. According to the nature of the band gap ($p-d$ transition) and the DFT calculations (section 2.1.3) showing an exchange split upper part of the valence band, these additional spectral signatures may confirm the presence of spin-polarized holes associated with Ca. In section 5, we searched, without success, for Fe^{4+} spectral signatures having $3d^4$ ground state on Fe $L_{2,3}$ edge and having $3d^5\underline{L}$ ground state on O K edge using EELS, XAS and XMCD. In contrast, this signature is detectable in the θ_F. It should be noted that Bi-rich iron garnets exhibit a giant Faraday rotation and are thus very sensitive to variations in the amount of spin-polarized states near the band gap.

	As-grown				TA48			
	Nf (10^{17}cm^{-3})		Energy (eV)		Nf (10^{17}cm^{-3})		Energy (eV)	
	O_h	T_d	O_h	T_d	O_h	T_d	O_h	T_d
BIG	3.89	1.11	2.91	2.47				
B($Y_{1.0}$)IG	3.51	0.19	3.03	2.61	3.91	0.32	3.02	2.62
B($Ca_{0.0}Y_{0.5}$)IG	3.47	0.38	2.97	2.57	4.04	0.72	2.96	2.52
B($Ca_{0.1}Y_{0.4}$)IG	3.67	0.25	2.99	2.61	4.25	0.31	2.99	2.61
B($Ca_{0.2}Y_{0.3}$)IG	3.57	0.21	2.99	2.56	3.98	0.33	2.98	2.55
B($Ca_{0.3}Y_{0.2}$)IG	3.75	0.34	2.99	2.63	4.25	0.60	2.96	2.57

TABLE 6.1: Transition energies and Nf values of the O_h and T_d components of the fitted theoretical model before and after TA48 for all thin films. The transitions energies and Nf values of BIG are also displayed for comparison.

Besides, XMCD experiments on the Ca L edge of as-grown B($Ca_{0.3}Y_{0.2}$) (Fig. 6.3 (b)) were carried on and show that Ca possesses a magnetic moment that is ferromagnetically coupled to the magnetic moment of Fe T_d (section 5.3.3). This result is an additional indication that Ca substitutes well within the garnet matrix.

6.2 Magnetic properties

6.2.1 Curie temperature

The variations of the Curie temperatures for the B($Ca_xY_{0.5-x}$)IG series and B($Y_{1.0}$)IG are displayed in Fig. 6.4 (a) as a function of the nominal Y stoichiometry and in Fig. 6.4 (b) as a function of the o-o-p lattice parameter. The films have T_C between 591 to 658 K as expected since the T_C of the parent phases ranges from 560 K for YIG to 660 K for BIG. Indeed, in the yttrium/bismuth iron garnet solid solution, the T_C depends strongly on the Bi concentration with a monotonous increase from YIG to BIG [38]. According to our previous analysis of Faraday rotation spectra, the B($_{1.0}$)IG film has the lowest Bi concentration. Thus, the measured T_C for the as-grown films decreases by 37 K with decreasing Bi concentration consistently with the literature [11, 33, 38]. Upon annealing, the T_C increases for all thin films by maximum 43 K. The annealing decreases the volume of the unit cell which implies that O 2p and Fe 3d orbitals are more overlapped. Therefore, the

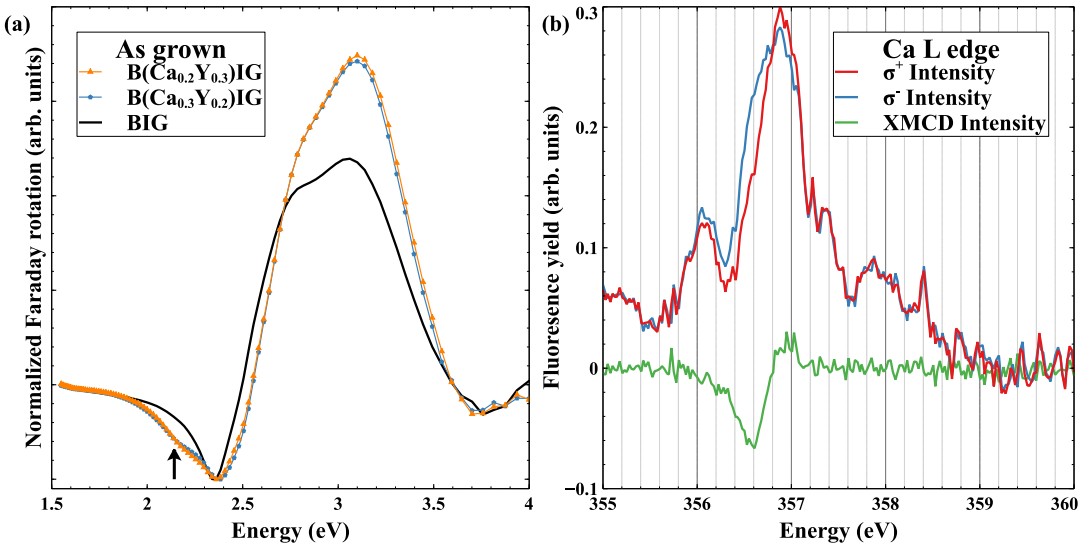

FIGURE 6.3: a) Normalized Faraday rotation spectra of $B(Ca_{0.2}Y_{0.3})IG$, $B(Ca_{0.3}Y_{0.2})IG$ and BIG. The spectra are normalized by their respective minimum. b) Fluorescence yield circularly polarized light in positive magnetic field (σ^+, red) and negative magnetic field (σ^-, blue) on Ca L edge of as grown $B(Ca_{0.3}Y_{0.2})IG$. The XMCD signal (green) is obtained as the difference between σ^+ and σ^-.

superexchange interaction is enhanced and results in a direct increase of the T_C. This behavior is illustrated in Fig. 6.4 (b) where the effect of the volume of the unit cell is underlined for a given nominal Bi stoichiometry. Besides, the evolution of the Fe-O-Fe angles also influence the superexchange interaction [189]. These results confirm that magnetism in $B(Ca_xY_{0.5-x})IG$ remains robust despite the Ca and Y co-substitution, the presence of minor secondary phase inclusions and the oxygen off-stoichiometry.

6.2.2 Magnetic anisotropy

For TA48 $B(Y_{1.0})IG$, as-grown $B(Ca_{0.0}Y_{0.5})IG$, as-grown $B(Ca_{0.3}Y_{0.2})IG$ and as-grown BIG, the longitudinal (i-p direction) and polar (o-o-p direction) MO Kerr effect were measured as shown in Fig. 6.5 (a) and (b), respectively. The o-o-p saturation field ranges from 130 mT for $B(Ca_{0.3}Y_{0.2})IG$ to more than 300 mT for BIG. The i-p saturation field varies from 120 mT for BIG to 230 mT for $B(Ca_{0.3}Y_{0.2})IG$.

For a few hundreds of nm thick thin films of BIG, its easy magnetization axis is parallel to the i-p direction [25, 28]. While for Ca and Y co-substituted BIG films, their easy magnetization axis tends to be more in the o-o-p direction. For all films, the GGG substrate applies a compressive strain. This strain is at the origin of a negative magneto-elastic anisotropy that tends to put the easy magnetization i-p [59] and is therefore not responsible for the change in

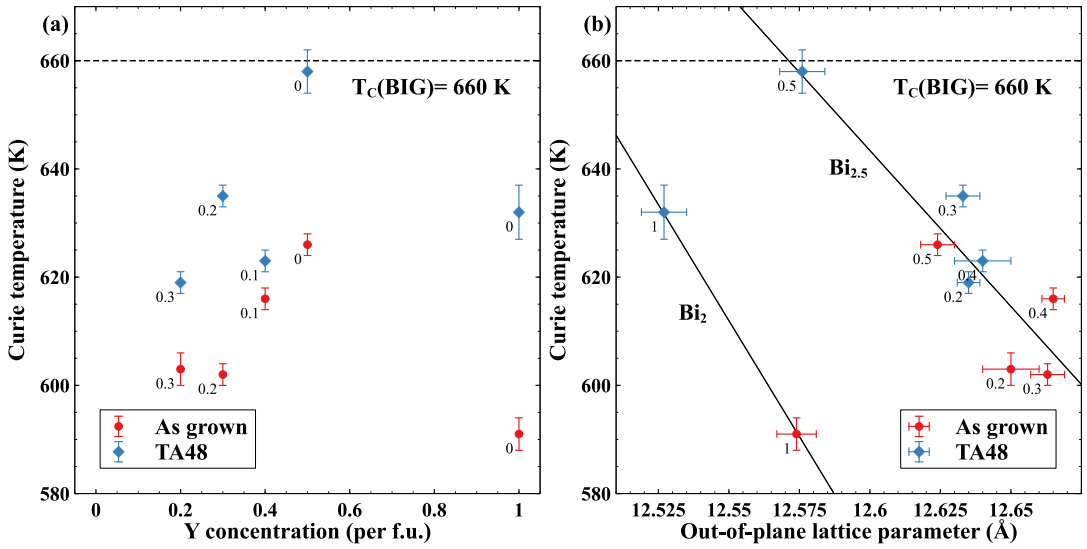

FIGURE 6.4: a) T_c as a function of the nominal Y concentration for all thin films before and after TA48. b) T_c as a function of the o-o-p lattice parameter for all thin films before and after TA48. Two solid lines linking the points corresponding to one nominal Bi concentration are displayed as a guide for the eyes. The nominal Ca concentration is indicated at the bottom right of every point in (a) and (b). The T_C of BIG is indicated by a dashed line for comparison.

anisotropy. Similarly, the shape anisotropy is negative for a thin film and is not reponsible for the o-o-p anisotropy. Then this anisotropy change could be explained by an additional anisotropy issued from the nanocrystallites. The hematite nanocrystallites are textured antiferromagnets and their interaction with the main ferrimagnetic garnet phase could yield an exchange anisotropy [190]. To probe a possible exchange bias issued from the weakly-crystallized secondary phase, Faraday rotation field cooling experiments were performed from 700 K to 300 K but yield no detectable signature. Another possibility resides in a change of the growth anisotropy upon doping as evidenced in Bi-substituted YIG [59]. The garnet thin films have nonequivalent dodecahedral sites due to the preferential direction induced by epitaxial growth [191]. The Bi population difference between these nonequivalent sites yields the growth anisotropy that tends to rotate the easy magnetization axis in the o-o-p direction [61, 62]. In BIG, all the dodecahedral sites are filled and then there is no growth anisotropy which implies that the easy magnetization axis remains i-p. Hence, in Ca and Y co-substituted BIG a growth anisotropy could also participate to the change of easy magnetization axis.

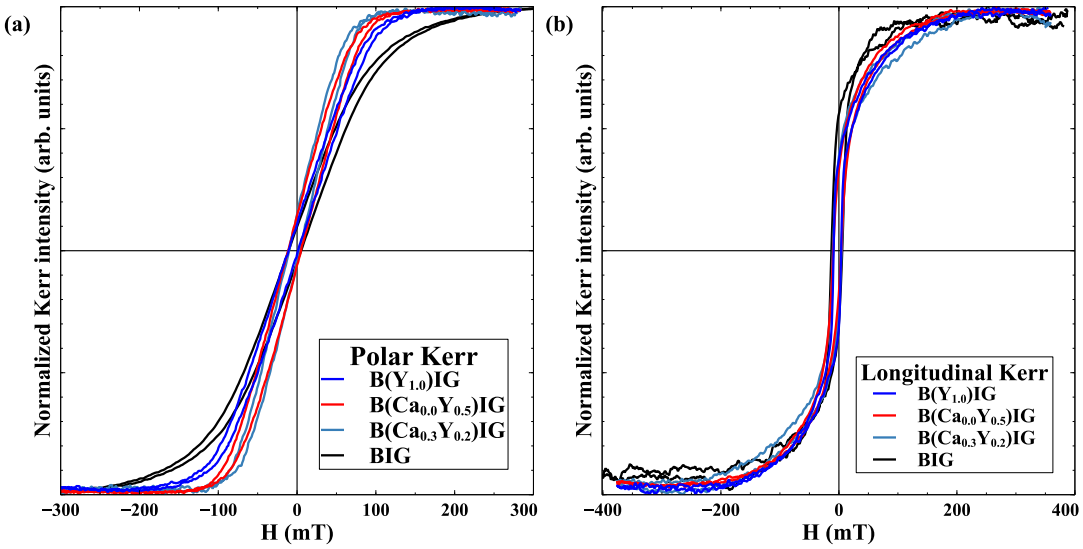

FIGURE 6.5: a) Kerr effect hysteresis cycles of TA48 $B(Y_{1.0})IG$, as-grown $B(Ca_{0.0}Y_{0.5})IG$, as-grown $B(Ca_{0.3}Y_{0.2})IG$ and as-grown BIG in polar (o-o-p) configuration. b) a) Kerr effect hysteresis cycles of the same films in longitudinal (i-p) configuration.

Summary of chapter 6

In this chapter the MO and magnetic properties of the thin films were investigated. The Ca and Y co-substituted BIG thin films exhibit preserved MO and magnetic properties with Faraday rotation of intensities similar to that of BIG and $T_C > 600$ K. Faraday rotation intensities even higher than that of BIG can be achieved through annealing in oxidizing atmosphere. The solubility of Ca within the garnet lattice is further confirmed by the presence of an additional feature in the MO spectrum and of a magnetic moment on Ca. An additional MO feature at the energy of the band gap suggests an additional spin-polarized density of states at the top of the valence band associated to Ca substitution. The direction of the easy magnetization axis is favored in the o-o-p direction in Ca and Y co-substituted thin films compared to undoped BIG. These results show that the functional properties of BIG were preserved upon substitution.

Chapter 7

Conclusions and perspectives

7.1 Conclusions

In this thesis, we attempted to lay the experimental and theoretical foundations for the development of a magnetic semiconductor based on Bi-rich iron garnets. The realization of a magnetic semiconductor suitable for applications at room temperature would be an important step towards more energy-efficient electronics. First, we recall the requirements that have to be met for a magnetic semiconductor to be suitable for applications at room temperature as stated by Coey [3]:

1) A T_C above 500 K

2) A coupling between the charge carriers and the magnetism

3) The possibility to develop n- and p-type behavior

4) A high mobility (>10 cm^2 V^{-1} s^{-1} [5]) and a long spin diffusion length ($\approx 1\mu$ m [6])

5) The presence of a significant magnetic circular dichroism (≈ 1 deg μm^{-1})

6) The presence of anomalous Hall effect

BIG possesses, among other properties, a T_C of 660 K and a giant Faraday rotation. In chapter 2, DFT calculations, performed by Iori in collaboration with this work, showed that the electronic structure of BIG presents a spin-polarized density of states at the top of the valence band [15]. This feature, not present in YIG, is related to the presence of Bi in the garnet lattice. It was also shown, using DFT, that Ca substitution in the garnet matrix would induce a p-type spin-polarized semiconductor behavior.

Hence, Ca and Y co-substituted BIG thin films with a high content of Bi (above 2.0 per f.u.) were then grown using PLD to induce charge carriers

in BIG and thus obtain a magnetic semiconductor. Ca is expected to induce $Fe^{3+/4+}$ to increase the conductivity of the films while the complementary amount of Y is expected to control the magnetic and magneto-optical properties by keeping constant the Bi concentration. This mechanism can be expressed:

$$Bi_{2.5}^{3+}Y_{0.5-x}^{3+}Ca_x^{2+}Fe_x^{4+}Fe_5^{3+}O_{12}^{2-} \text{ with } \{x = 0.0 \rightarrow 0.3\}$$

In chapter 4, we show that Ca and Y co-substituted BIG thin films are mostly composed of a well-crystallized garnet phase oriented along the [001] direction. It was also evidenced by Cs-STEM/EELS that the films are also composed of a minor secondary phase undetectable by XRD. These secondary phases inclusions are poorly-crystallized textured hematite nanoneedles as identified by an extensive characterization. The presence of these nanoneedles does not seem to hinder the physical properties of the thin films since no percolation path is formed. The Ca concentration in Ca and Y co-substituted BIG oscillates along the growth direction over a pseudo-period of e.g. about 12 nm in B($Ca_{0.3}Y_{0.2}$)IG. Nevertheless, at the atomic scale, both the Ca and the Y substitute well within the garnet matrix. These results tend to show that it is possible to grow well-crystallized Bi-rich iron garnet phases substituted with aliovalent and/or isovalent cations.

In chapter 5, we evidenced that Ca and Y co-substituted BIG thin films exhibit a p-type semiconductor behavior while Y-substituted BIG thin films exhibit a n-type behavior with resistivities two orders of magnitude lower than the p-type films. Overall, the measured resistivities are up to ten orders of magnitude lower than the resistivity of YIG thin films yielding at best $\rho_{300\ K} = 9.6 \times 10^2 \Omega$ cm for Y-substituted BIG. In Y-substituted thin films, a reversible resistivity change of three orders of magnitude was also evidenced upon annealing in inert/oxidizing atmospheres. The charge compensation mechanisms were investigated using a combination of Cs-STEM/EELS and XMCD techniques. These studies revealed that the increased conductivity in n-type thin films was related to the presence of Fe^{2+} (0.65 per f.u.) mainly located on the Fe T_d site while the spectral signature of Fe^{4+} remained undetectable. In both n- or p-type thin films, the oxygen vacancies play a key role as intrinsic donors either compensating holes or inducing the formation of electrons.

In chapter 6, the magnetic and magneto-optical properties of the thin films were investigated. The films exhibit a preserved giant Faraday rotation and a T_C above 600 K despite the presence of the nanoneedles and the Y and Ca

dopants. An additional feature in MO spectra related to the presence of Ca tends to indicate the presence of a spin-polarized density of state at the band gap energy. The magnetic moment of Ca evidenced by XMCD further support the substitution of Ca in the garnet matrix. Upon doping, the easy magnetization axis direction is favored in the out-of-plane direction, in contrast to the in-plane anisotropy of pure BIG thin films. This magnetic anisotropy change is an interesting feature from the point of view of spintronics [59].

With these results, how far are we from developing a magnetic semiconductor using Ca and Y co-substituted BIG thin films ?

The studied thin films fulfill three of Coey's requirements as they exhibit: a T_C> 600 K (1), n- and p-type semiconductor behaviors (3) and a preserved giant Faraday rotation (5). However, the magneto-transport properties of these films were not investigated in this work and the fulfillment of requirements (2), (4) and (6) remains undetermined. Nevertheless, the MO feature indicating a spin-polarized density of states at the band gap energy is an encouraging sign towards the coupling between charge carriers and magnetism (2). The spin-polarized density of states at the top of the valence band, as calculated in BIG by DFT, also suggests that charge carriers should be coupled to magnetism (2) in Ca and Y co-substituted BIG films. The mobilities of the charge carriers estimated using electrical resistivity and thermopower measurements are probably lowered by the presence of the nanoneedles while thin films composed a single garnet phase may exhibit higher mobilities (4).

7.2 Perspectives

Ca and Y co-substituted BIG thin films are promising candidates for the development of magnetic semiconductors suitable for room temperature applications. This is the first work investigating the electrical properties of the Bi-rich iron garnets. Therefore, there is still room for improvement and many unresolved issues remain on this subject.

Growth optimization

The presence of secondary phase inclusions (section 4.2.1) most probably limits the mobility of the charge carriers and the achievable resistivity. To obtain single phase thin films, we propose first to increase the PO_2 during the PLD growth and the cooling step to up to hundreds of mTorr (section 4.2.1) which would also mitigate the self-compensation of divalent cations. Using substrates with lower lattice mismatch, such as gadolinum scandium gallium

garnet with $a = 1.2576$ nm, would also help to prevent the formation of the nanoneedles [192]. The Bi is known to evaporate quicker than other elements such as Ca [83] and to avoid the possible Bi off-stoichiometry, the thickness of the films will be reduced to approximately 20 nm and the substrate temperature will also be optimized to avoid a Bi re-evaporation. These investigations should lead to the growth of single phase and single crystalline substituted BIG thin films.

Physical properties

The magneto-resistance is a key property of the magnetic semiconductors. Unfortunately, the magneto-transport properties were not investigated in this thesis due to the low mobility of the charge carriers of the films. On the single phase thin films with expected higher mobilities, the direct coupling between charge carriers and magnetism should be tested by magneto-transport experiments. Moreover, Hall effect measurements would demonstrate the possible presence of the anomalous Hall effect (requirement (6) [3]). Nevertheless, special care has to be taken to accurately measure the Hall effect on films with high resistance [88] on the custom setup described in section 3.1.3. It should be noted that the measurement of anomalous Hall effect was not reported directly in iron garnets. However, iron garnets such as YIG, are mostly used to induce anomalous Hall effect in non-magnetic metals such as Pt [193].

The growth of single phase thin films would also allow the quantitative determination of their structure using XRD in synchrotron. During this thesis, we attempted to determine the structure of undoped BIG on the SIXS beamline at SOLEIL[1] and the related work is still in progress.

Our first XMCD run motivates us to perform further experiments using this technique. It would be especially interesting to probe the evolution of charge carriers on the O K or Fe $L_{2,3}$ edges in the single phase thin films under different stimuli: temperature or applied voltage [194]. An analysis of the hysteresis cycles acquired during the first run is ongoing. We aim at extracting the different magnetic contributions of a collection of noisy hysteresis cyles (Fe T_d, Fe O_h and additional contributions) using an uncommon approach based on VCA [146].

[1] The crystallographic structure refinement is carried out by Florence Porcher (Laboratoire Léon Brillouin).

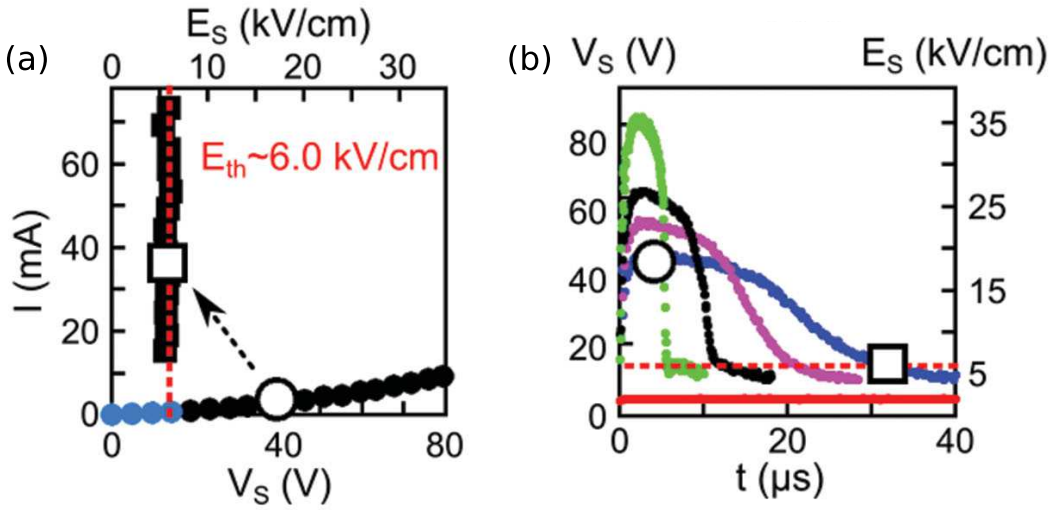

FIGURE 7.1: a) Dielectric breakdown I(V) curve. E_{th} corresponds to the threshold electric field below which no breakdown is observed. b) Time dependance of the applied voltage. The experiments were performed at 164 K on $V_{1.7}Cr_{0.3}O_3$. This Figure is adapted from ref. [195].

Towards applications for short, middle and long terms

As short term investigations, the promising non-volatile and reversible resistivity changes demonstrated in Y-substituted BIG under annealing in oxidizing/inert atmosphere calls for the next development step by applying a voltage to induce resistive switching. Such switching between HRS and LRS would enable information storage and finding a material with such a functionality is an active field of research [195]. A change of resistivity upon an applied voltage that follows the space charge limited current mechanism was already reported for Ca-doped YIG thin films [73] which is rather encouraging for Y-substituted BIG thin films. Future experiments will aim at determining figures of merit of the resistive switching property: a typical I(V) curve, an electric field threshold, and a relaxation time (Fig. 7.1). Besides resistive switching, this atmosphere-induced resistivity change is also promising for gas sensing applications [174].

At middle term, once the presence of anomalous Hall effect in single phase thin films has been demonstrated, we will propose to investigate the electric field control of magnetic domain walls which would result in low power electronics. Such a property was only evidenced in iron garnets for intense electric fields (2-3 kV) [196].

At a longer term, magnetic p/n junctions could be obtained with both n- and p-type doped-BIG phases that possess comparable electrical properties in the same temperature range. Such junctions offer a wide range of functionalities by coupling equilibrium magnetism and non-equilibrium spins.

They can present a giant magneto-resistance and act as spin valves that block or not a charge current depending on the direction of the applied magnetic field [197]. This effect can be used for memory devices or for magnetic field sensitive detector. Moreover, iron oxides exhibit an important absorption in the ultraviolet-visible to near infrared spectral range and a p/n junction would be interesting in itself. A magnetic p/n junction would generate spin-polarized currents when illuminated by circularly-polarized light [198]. This effect should be especially strong in doped BIGs due to their giant Faraday rotation.

Beyond BIG

One rather radical perspective to overcome the issues associated to the formation of p-type charge carriers in iron garnets would be to investigate the possibility of obtaining a Mn based garnet. Such $Bi_3Mn_5O_{12}$ (BMG) is believed to be unstable [199] but BIG is also theoretically unstable in bulk form and it is nevertheless possible to grow it as thin film on isostructural substrates.

Manganese oxides already lead to applications in the field of spintronic. For instance, $La_{0.7}Sr_{0.3}MnO_3$ is a good candidate as spin injector with its half-metallic nature and its small magnetic damping [200]. Iron garnets present similarly a small damping that may also be preserved in Mn based garnet.

BMG should also keep the interesting features of the electronic structures of iron garnets since these features mostly originate from the garnet structure and from the distribution of majority spin in T_d site and minority spin in O_h sites. Fe^{3+} has the advantage of having a strong magnetic moment (4.4 μB, garnet structure [25]) but the $Mn^{3+/4+}$ still exhibits a rather large magnetic moment (3.6 μB, perovskite structure [201]). In the iron garnets, the crystal field difference for O_h and T_d is large enough to result in the appearance of spin gap in the conduction band. Preliminary ab-initio calculation done using LDA+U (U = 3eV) indicate that BMG is ferrimagnetic and present three spin gaps in the conduction band like in BIG and YIG (Fig. 7.2) [2].

The advantage of manganese garnets with respect to iron garnets would be the easier $Mn^{3+/4+}$ control as compared to the $Fe^{3+/4+}$ control. Indeed, we have shown that the substitution of Ca can lead to the formation of Fe^{4+} (section 5.1) in Ca and Y co-substituted BIG thin films. However, the amount of Fe^{4+} is too low to be detected using spectroscopy techniques as a result of

[2] DOS calculated by Alexandre Gloter.

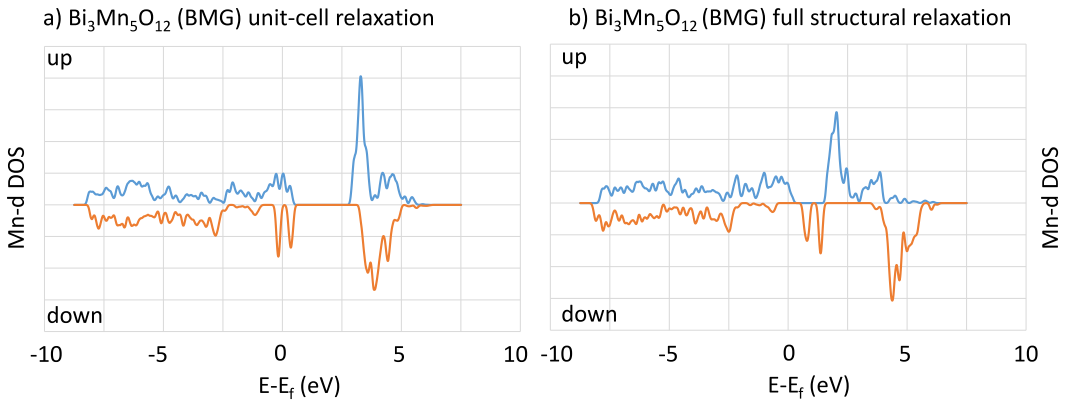

FIGURE 7.2: Mn-*d* projected densities of states of BMG as obtained by LDA+U (U=3 eV) calculations. (a) the Mn-*d* DOS with atomic positions identical to those of BIG structure showing very similar conduction band to that of BIG. b) the Mn-*d* DOS after full structural relaxation show an increase of the size of the spin-gaps.

a strong self-compensation by oxygen vacancies. This behavior is not specific of iron garnets. For instance, $SrMnO_3$ [202] does not require a complex post-treatment to stabilize a 4+ valence compared to $SrFeO_3$ [203]. It would then be interesting to grow Ca substituted bismuth manganese garnet ($Bi_{3-x}Ca_xMn_5O_{12}$) which may present an increased concentration of transition metal with 4+ valence, i.e. charge transfer hole, compared to Ca-substituted BIG.

Electron spectro-microscopy techniques

A large part of this thesis was devoted to Cs-STEM-EELS related techniques and we hope that some perspectives might also be drawn on that aspect. A highly monochromated Cs-STEM, the NION CHROMATEM 200MC, was recently acquired in the STEM group. With this instrument, it is possible to reach a sub-Å spatial resolution and 50-80 meV spectral resolution for the study of core-loss EELS [204]. Such a high spectral resolution will enable us to probe subtle changes of EELS fine structures such as energy shifts of the O *K* that were not detectable without a monochromator. At lower energy losses, it would also be interesting to map the local band gap variations with an energy resolution of up to 5meV. The CHROMATEM is also designed to accept tuneable temperature and electrical biasing stages to perform in-situ experiments.

The electrical biasing in-situ experiments would complement the investigations on the possible resistive switching behavior in Y-substituted BIGs. It could, for example, demonstrate whether the resistive switching originates from the local migration of oxygen vacancies [205] or from the nucleation

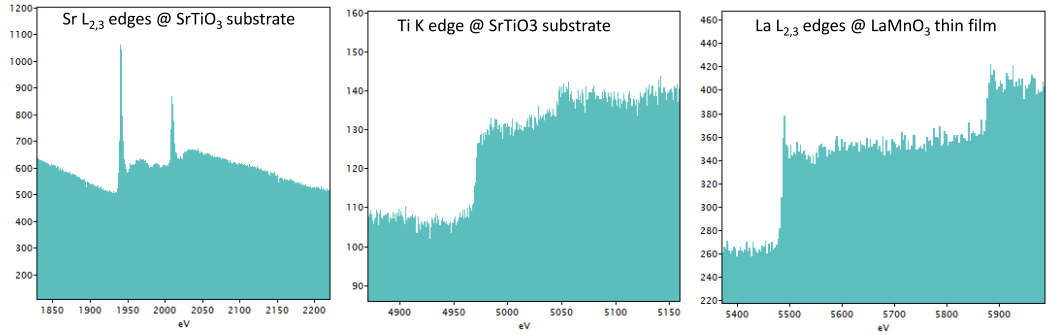

FIGURE 7.3: Example of energy-loss spectra obtained with the Medipix detector on a transition metal oxydes, here an heterostructure comprising $LaMnO_3$(film)/$SrTiO_3$(substrate).

and propagation of filamentary paths [206] by probing the O *K* or TM $L_{2,3}$ edges at the local scale. It would be very interesting to observe the motion of magnetic domain walls in single-phase doped BIG magnetic semiconductor under applied bias using in-situ electron holography [207]. Indeed, the magnetic domain structure of pure BIG was also investigated during this thesis using electron holography at the Centre d'Elaboration de Matériaux et d'Etudes Structurale[3]. The typical size of the domains (about 40 nm) prevent their observation using MO Kerr effect or magnetic force microscopy.

The EELS experiments were carried out using an EM-CCD detector developed by Marcel Tencé at the LPS. The detection quality of such equipement is overpassing most of the EELS commercial system available in the last decade, but it is still subjected to readout noise, dark current and gain variations [154]. These issues can be avoided using a recently available detector in the STEM group (Marcel Tencé, first tests in september 2019): the Medipix3 detector that even allows the couting of individual electrons [208]. With this more efficient detector, we expect a significant improvement of the possibilities in EELS. In the study of doped garnets, small variations associated to doping might become more visible (quantitative elemental mapping of e.g. Y $L_{2,3}$, detection of Fe^{4+} signatures, etc.). More generally, the detector is especially useful in the case of transition metal oxides, where for instance, transition metal K edges might become detectable despite their high energy loss (5-9keV). These K edge contain information on, for instance, the hybridization of 3*d* metals with the oxygen [209]. The feasibility of such measurements collecting the EELS spectral signature of $LaMnO_3$ thin film at the La $L_{2,3}$ edges at 6 keV while maintaining a nanometer-scale resolution is shown in Fig. 7.3.

We have demonstrated that clustering techniques enable a rather rapid

[3]The electron holography experiments and their analysis were carried out by Christophe Gatel within a METSA project.

and efficient ranking of the fine structure distributions, even if the differences of these features are small in between the spectral components. This is of particular interest for transition metal oxides where the electronic structure can evolve from one column to the others leaving only a small spectral fingerprint in the transition metal $L_{2,3}$ edges. We can, for example, cite the case of small charge ordering/disproportionation where only a fraction of electron $+\delta/-\delta$ with $\delta \approx 0.1$ is changing from one columns to the others, such as in the so called Co^{3+}/Co^{4+} charge disproportionation in $Na_{1/2}CoO_2$ [210]. However, the fine structures gradients at interfaces (such as a film/substrate interface) will produce anisotropic clusters which are not well treated by the K-means++ clustering algorithm used in this thesis. This issue may be overcome by other clustering algorithms that would require further developments.

Chapter 8

Résumé

Ce travail de thèse s'intéresse au développement du domaine des oxydes multifonctionnels pour l'électronique tout-oxyde dans lequel notamment un matériau semi-conducteur magnétique adapté aux applications à température ambiante n'existe pas encore. En effet, un semi-conducteur magnétique permettrait, par exemple, le contrôle du magnétisme par un champ électrique ou le déplacement de parois de domaines magnétiques induit par un courant électrique pour réduire la consommation d'énergie de l'électronique. Le développement d'un tel matériau a donc suscité un vif intérêt dans la communauté scientifique. Dans ce but, de nombreux travaux à la fois théoriques et expérimentaux ont effectivement été réalisés sur le dopage des semi-conducteurs classiques comme GaAs ou des oxydes semi-conducteurs comme ZnO par des cations magnétiques 3d tel que Mn. Les matériaux ainsi obtenus sont respectivement dénommés semi-conducteurs magnétiques dilués (DMS) et oxydes magnétiques dilués (DMO). Néanmoins, la température de Curie (T_C) maximale mesurée dans un DMS est de 190 K ce qui limite fortement l'utilisation de ce type de matériau pour des applications industrielles. Dans le cas des DMO, des T_C allant jusqu'à 900 K ont été obtenues mais le mécanisme à l'origine de l'ordre magnétique est encore mal compris et aucun lien clair n'a été tiré entre les porteurs de charge et le ferromagnétisme dans ces matériaux. Il a été récemment démontré qu'il était possible d'obtenir un semi-conducteur magnétique montrant un couplage magnéto-électrique fort à température dans un oxyde ferromagnétique amorphe ($Co_{28.6}Fe_{12.4}Ta_{4.3}B_{8.7}O_{46}$) avec une T_C de 600 K. Ces travaux ouvrent des perspectives prometteuses pour le développement de semi-conducteurs magnétiques à température ambiante basés sur les oxydes.

Dans cette thèse une approche alternative pour l'obtention d'un matériau à la fois magnétique et semi-conducteur a été développée. En effet, des oxydes isolants présentant un magnétisme robuste ont été dopés par des cations aliovalents et/ou isovalents afin d'induire des porteurs de charge. Le grenat

de bismuth fer (BIG en anglais pour Bismuth Iron Garnet) a été sélectionné car il présente de nombreuses propriétés remarquables telles que la rotation Faraday géante dans le spectre visible (induite par la présence de bismuth) et un couplage magnéto-électrique linéaire à température ambiante. Dans les grenats de fer, l'ordre magnétique a pour origine le couplage ferrimagnétique entre les sites de Fe tétraédriques et octaédriques ce qui induit une T_C de 660 K pour le BIG. De plus, de récents calculs théoriques montrent que le BIG possède un haut de bande de valence fortement polarisé en spin ce qui devrait favoriser un transport électronique fortement polarisé en spin.

La croissance d'un grenat de fer avec une forte concentration de Bi (> 2 Bi par unité de formule) ne peut être réalisée que sous forme de film mince épitaxié sur un substrat isostructural. Des films de BIG co-dopés à l'yttrium (0.2 à 0.5 d'Y par unité de formule) et au calcium (0.0 à 0.3 de Ca par unité de formule) d'environ 150-200 nm d'épaisseur ont été synthétisés par dépôt laser pulsé sur un substrat de grenat de gadolinium gallium. Le Ca^{2+} substitué sur le site du Bi^{3+} tend à induire la formation de $Fe^{3+/4+}$ et une conduction de type p tandis que la substitution d'une quantité complémentaire d'Y^{3+} sur le site du Bi permet de maintenir une teneur en Bi constante (c'est-à-dire $Bi_{2.5}$) afin de préserver la rotation Faraday géante des films. Étant donné la faible quantité de matière constituant les films minces, l'exploration de leurs propriétés physiques et structurales a été menée via une combinaison de techniques physiques macroscopiques adaptées (par exemple le dichroïsme circulaire magnétique optique (rotation Faraday) et des rayons X (XMCD)) et de techniques avancées de microscopie (Cs-STEM) et spectroscopie (EELS) électronique en transmission. Le couplage de ces deux techniques de microscopie et de spectroscopie permet notamment l'étude de l'intégration des dopants au sein de la maille de grenat ainsi que l'étude des mécanismes de compensation de charge et ce jusqu'à l'échelle atomique. Pour détecter des changements subtils de structures fines sur les seuils L des métaux de transition, tels que des états de valences mixtes, nous avons développé l'analyse des données EELS par clustering. La validité et les performances d'une telle approche ont été testée en utilisant un système modèle : le Co_3O_4. Il a notamment été possible de retrouver l'ordre de charge présent dans Co_3O_4 par clustering sur des données expérimentales.

Les films, étudiés par diffraction des rayons X et Cs-STEM, présentent une phase grenat majoritaire bien cristallisée et epitaxiée dont la contrainte compressive due au substrat est totalement relaxée en environ 15-25 nm depuis l'interface film/substrat. En outre, l'étude des films par STEM/EELS a mis en

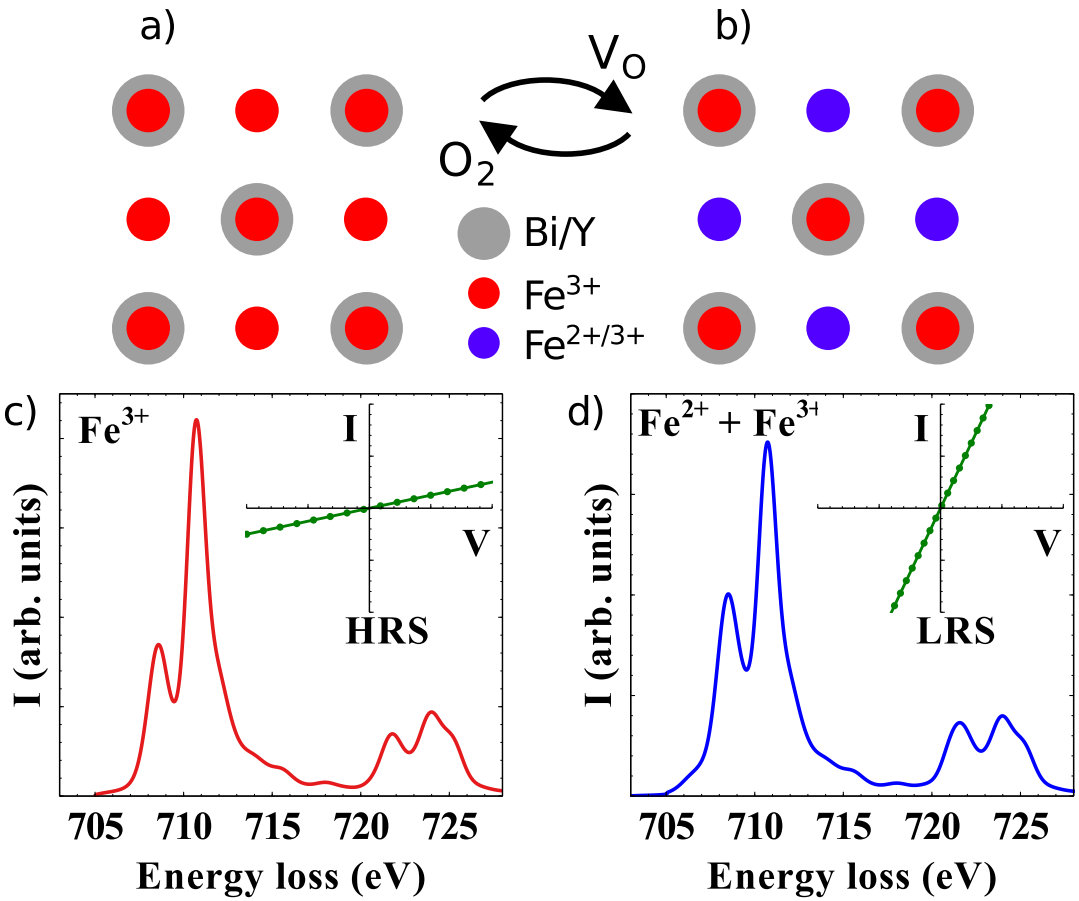

FIGURE 8.1: Schéma d'un des résultats principaux de ce manuscrit. a) et b) modèles cationique d'un quart de la maille du BIG dopé à l'yttrium respectivement dans l'état HRS et LRS. c) et d) Seuils d'absorption Fe-L théoriques respectivement dans l'état HRS et LRS. Les encarts montrent les courbes I(V) théoriques obtenues dans l'état LRS et HRS.

évidence que les dopants (Ca and Y) se substituent dans la maille de grenat et ne forment pas d'agrégats. Cependant, une phase minoritaire d'hématite faiblement cristallisée et texturée non détectable par diffraction des rayons X est aussi présente sous forme de nanocristallites entre les grains de grenat sans former de chemin de percolation. La présence de cette phase n'est pas délétère pour les propriétés physiques des films. Des pistes pour éviter la formation de ces nanocristallites sont proposées.

Les films présentent une sous-stœchiométrie en oxygène mais il est possible de remplir le sous-réseau d'oxygène par un recuit post-croissance qui conserve par ailleurs les propriétés structurales et micro-structurales des films. Les films ayant été co-dopés avec succès, leurs propriétés de transport électrique ont été étudiées à haute température et sous différentes atmosphères. Les grenats co-dopés au Ca et à l'Y présentent un comportement semi-conducteur de type p avec une résistivité de 3.3×10^4 Ω cm à 450 K tandis que le BIG

dopé à l'Y uniquement présente un comportement semi-conducteur de type n avec une résistivité de 4.1×10^1 Ω cm à 450 K. Ces résistivités correspondent à une amélioration de jusqu'à 10 ordres de grandeur par rapport au grenat d'yttrium fer isolant. Les films de type n montrent en plus un changement de résistivité réversible d'au moins trois ordres de grandeur lors de recuits sous une atmosphère inerte ou oxydante. Ce changement de résistivité est induit par la formation ou le remplissage de lacunes d'oxygène. Concernant la distribution de charges en lien avec les propriétés de transport, la présence de Fe^{4+} n'a pas pu être mise en évidence par des techniques de spectroscopie à l'échelle locale ce qui tend à démontrer que les trous dans les films de type p sont fortement compensés par des lacunes d'oxygène. Néanmoins, l'analyse des spectres de rotation Faraday montre la présence d'une densité d'état polarisée en spin en haut de bande de valence associée à la présence de Ca. En utlisant le changement réversible de résistivité des films de type n nous avons mis en évidence la présence de 12% de Fe^{2+} supplémentaire dans l'état de basse résistivité. À l'aide de l'analyse clustering nous avons démontré que le Fe^{2+} est principalement localisés sur le site tétraédrique du fer. Ce résultat a été confirmé par XMCD sur le seuil L du Fe. L'obtention de semi-conducteurs à partir de BIG est donc possible par co-dopage tout en préservant ses propriétés magnéto-optiques remarquables comme démontré dans ce travail. Les films conservent une rotation Faraday géante dans le spectre visible avec jusqu'à $-13\,\mathrm{deg}\,\mu\mathrm{m}^{-1}$ à 550 nm ainsi qu'une $T_C > 600K$. Un changement d'axe facile d'aimantation est aussi observé lors du dopage. La préservation du couplage ferrimagnétique entre les deux sous-réseaux de fer a été démontré par XMCD ainsi qu'une signature magnétique supplémentaire possiblement liée à un effet de la phase secondaire.

La présence simultanée d'un comportement semi-conducteur de type p ou n, d'une T_C supérieure à 600 K, de la rotation Faraday géante ainsi que d'une forte polarisation en spin du haut de bande de valence font des films de BIG co-dopés à l'Y et au Ca des candidats prometteurs pour l'obtention d'un semi-conducteur magnétique. Ils représentent également une perspective intéressante pour l'élaboration d'hétérostructures p/n artificielles ou même pour une utilisation potentielle dans des applications pour la détection de gaz.

Chapter 9

Remerciements

9.1 Préambule

Je me permets d'ajouter, avant de commencer les remerciements, que je ne dispose malheureusement pas d'une fibre littéraire très développée et que, par conséquent, les remerciements qui vont suivre paraîtront probablement froids aux éventuels lecteurs. Les lecteurs les plus avisés y verront là une marque de pudeur tandis que les lecteurs les plus mesquins y verront là de la fainéantise. Néanmoins, j'affirme avec sincérité que j'ai eu beaucoup de chance pendant ma thèse, et plus généralement ma vie, de n'avoir rencontré que des gens intelligents, gentils, beau, etc... autrement dit "bien sous tous rapports". La médiocrité de ma prose ne retranscrira donc que partiellement la qualité intrinsèque des personnes citées ci-dessous.

9.2 Prose

Je voudrais tout d'abord commencer par remercier mes rapporteurs, Nathalie Viart et Gianluigi Botton, qui ont eu la patience et l'amabilité de lire mon manuscrit et de venir à ma soutenance de thèse. Je remercie aussi Amélie Juhin, Ulrike Luders et Agnès Barthélémy d'avoir participé en tant que jury à ma soutenance de thèse. Je tiens à remercier ce jury pour la qualité des questions qu'ils m'ont posé et qui ont pu me permettre de pousser encore plus loin la réflexion sur mon travail.

Je souhaite bien entendu remercier aussi mes encadrants Alexandre Gloter, Laura Bocher et Elena Popova qui m'ont accompagné, guidé et soutenu tout au long de ma thèse et avec qui il a été très agréable de travailler. Je me permets de souligner leur rigueur intellectuelle et leurs qualités humaines qui m'ont permis d'évoluer à la fois sur le plan professionnel et sur le plan personnel. J'ai énormément appris à leur côtés et je leur souhaite de réussir leur

projets futurs. Concernant mon encadrement, j'aimerai aussi remercier tout particulièrement Niels Keller qui a pris un temps, pourtant précieux, pour assister aux réunions et pour me prodiguer de bons conseils.

Je souhaite maintenant remercier Federico Iori, Nathalie Brun, Alexandra Mougin et Ibrahim Koita qui ont contribué à ce travail. J'ai beaucoup apprécié travailler avec Federico sur les calculs de DFT. Malgré les la difficulté des calculs sur le BIG, Federico a su garder sa bonne humeur et son humour. Nathalie a eu l'idée d'utiliser le clustering sur nos données d'EELS. Ca a été très agréable de collaborer avec Nathalie car elle a été motivée et motivante pour développer de nouvelles techniques d'analyse de données. Son avis et ses questions pertinentes ont été un moteur pour mes travaux sur le clustering. Merci à Alexandra qui m'a beaucoup aidé lors de la réalisation et l'analyse des expérience d'effet Kerr. Je tiens à remercier aussi Ibrahim qui sait faire le grand écart entre l'espièglerie et la rigueur scientifique. Je pense et je souhaite qu'Ibrahim ira loin dans sa vie notamment grâce aux deux qualités mentionnées précedemment. Il a fourni un travail important, que j'ai en partie supervisé, sur le débruitage des cartes chimiques par PCA.

Les deux premières années de ma thèses sont passées beaucoup plus vite que prévu grâce à mon TAC (Hugo Lourenco-Martins[1]) qui s'est tellement plaint du temps, des trains, de sa thèse, etc ... que ça m'a permis de beaucoup relativiser quant à ma propre thèse. Je reprends ses mots car il a raison : Nous avons passés des moments d'anthologie à Balaruc les bains ou Berlin notamment. J'espère sincèrement que cet homme aura son poste CNRS tant convoité.

Un grand merci va à l'équipe STEM qui m'a accueillie pendant ces trois ans. Merci à Odile Stéphan qui m'a soutenue lors de moments critiques par des conseils avisés. Merci à Marcel Tencé qui a été un excellent coloc de bureau avec qui j'ai pu apercevoir un petit bout de la compléxité de Swift. Merci à Christian Colliex pour son enthousiasme quant à mes travaux. Merci à Michael Walls qui a supporté mes moqueries effrontées avec humour. Merci à Mathieu dont le rire peut parfois s'entendre depuis le LPS jusqu'à la gare du guichet. Merci à Marta pour sa gentillesse et son écoute. Merci à Jean-Denis Blazit qui apporte (entre autres) la bonne humeur et la rigolade dans l'équipe. Et merci encore à Jean-Denis qui s'est décarcasser pour présenter un show de qualité à la fête de la science. Merci à Xiaoyan Li pour son aide sur les microscope et j'espère que l'heureux évenement se passera très bien.

[1] Tant pis pour la cédille...

Merci à Steffi Woo qui nous a régalé avec ses talents culinaires hors-pairs. Merci à Néomie Bonnet pour le fromage en général.

Un second grand merci va au Groupe d'Etude de la Matière Condensée qui m'a aussi accueilli pendant ces trois ans. Merci à Ekaterina Chikoidze pour m'avoir montré comment mesurer le transport électrique sur HTHZ. Merci à Bruno Berini pour avoir déposé les contacts de platine sur mes échantillons. Merci à François Jomard d'avoir fait une expérience de SIMS sur nos échantillons. Merci à Yves Dumont pour son soutien pendant ma thèse. Merci à Christèle Vilar pour son aide lors de la découpe des échantillons.

Je voudrais aussi remercier Sergio Valencia et Radu Abrudan qui nous ont apporté leur aide et leur conseils lors des expériences de XMCD à Bessy II et ce malgré le grand froid de janvier à Berlin.

Lors de cette thèse, j'ai aussi travaillé sur des projets annexes tels que la détermination de la structure du BIG ou l'imagerie des domaines magnétiques dans le BIG par microscopie Lorentz. Je voudrais donc remercier Florence Porcher et l'équipe de la beamline SIXS avec lesquels on a tenté de déterminer la structure cristallographique du BIG au synchrotron Soleil. Je voudrais aussi remercier Christophe Gatel qui a pu révéler une partie de la compléxité de la structure de domaines magnétiques du BIG. Lors de ces projets annexes, j'ai toujours eu affaire à des gens sympathiques et professionnel.

Je remercie mes camarades de master puis de thèse Ewen, Eloi, Alicia (que thèse du coup malheureusement) et Geoffrey qui ont partagé ces trois années avec moi au LPS. Merci pour toutes nos discussions autour d'un café, soirées parisiennes, weekend thésards, etc..

Je remercie aussi mes super colocs : Vincent Denechaud, Anais Molineri, Antoine Laudrain, Cécile Carcy et Morgane Farradèche. On a passé 3 années de colocs magiques et je pense que sans eux la thèse aurait été bien plus difficile.

Je voudrais aussi remercier tout particulièrement mes amis : Aurore, Jean-Baptiste, Gros Ben et Yohann. Je pense aussi à Marianne, Anouck, Louison, Chloé, Pierre, Lucas, Jérémy et Mathilde. Ils ont eux aussi rendu mes années de fac et de Lycée magiques. Je n'en dirai pas plus pour ne pas choquer les lecteurs...

Un grand merci aussi à Enzo, Tom, Nicolas, Marion, P'tit Ben, Elise, Audrey, Camille et Merry avec qui j'ai passé plein de moments tout à fait mémorables.

Je tiens bien évidemment à remercier ma famille : Papa, Maman, Jean, Mamie, Sylvain, Saloua, Eliane, Jacques, Marie-Laure, Christel, Lionel, Rémy,

Thérèse, Patrick, Pascal et Martine. C'est un peu téléphonné mais ils m'ont aidé à me construire tout au long de ma vie et pour ça merci encore.

Appendix A

DFT calculations methods

In this appendix we present, the methods used in our article accepted in physical review B [15] to calculate the density of states presented in chapter 2.

We have used ab-initio calculations based on Kohn-Sham Density Functional Theory (DFT) [211, 212] in a planewave pseudopotential approach as implemented in QuantumEspresso [213]. Scalar and full relativistic ultrasoft pseudopotential, including semicore states and spin-orbit coupling for Bi and Fe, have been obtained from the PSLibrary designed by Dal Corso [214]. An energy cutoff of 50 Ry for plane-wave basis expansion and of 400 Ry to describe the charge density and the potential have been respectively used. Geometry has been relaxed at the Gamma k-point until reaching a maximum force on each atom smaller than 10^{-4} eV Å^{-1}. Charge density has been converged with $2 \times 2 \times 2$ and $4 \times 4 \times 4$ k-points and the density of states with a total mesh of 64 k-points in total. We applied a spin-polarized generalized gradient approximation in the Perdew-Burke-Ernzerhof (PBE) [215, 216] formulation and in its version optimized for solids (PBEsol) [217]. To improve the treatment of electronic correlation in the description of the correlated subset of Fe d states we apply a "Hubbard+U" scheme, where U represent the ad-hoc Hubbard on-site Coulomb repulsion parameter. We used the effective "Hubbard-U" in the simplified formulation of Cococcioni and Gironcoli [218] and for spin-orbit calculation the rotationally invariant approach by Liechtenstein, Anisimov, and Zaanen [219]. We evaluate the effect of several values of U keeping the onsite exchange J=0, which formally renders the two approaches equivalent [220].

Appendix B

Geometric phase analysis theory

In this appendix, we present the theory that links the phase images obtained by reciprocal space filtering and the local strain maps. We mostly base our description of this theory on the work of Hÿtch, Snoeck, and Kilaas [139]. A full description of the GPA would include the effect of the lenses aberrations on the image. However, the present work was performed on a Cs corrected microscope, therefore the effect of aberrations is neglected here[221]. A typical atomically resolved image of a strained crystal can be decomposed in Fourier series:

$$I(\vec{r}) = \sum_{g} H_g(\vec{r}) e^{2i\pi \vec{g}\cdot\vec{r}} \tag{B.1}$$

$$H_g(\vec{r}) = A_g(\vec{r}) e^{iP_g} \tag{B.2}$$

Where $I(\vec{r})$ is the intensity of the image at point $\vec{r}$ and $\vec{g}$ corresponds to an interplanar distance in the reciprocal space. In the presence of strain or defects, the H_g Fourier coefficients take a general form of Eq. B.2 where A_g is the amplitude of the fringes and P_g is the position (or phase) of the fringes. In the Fourier space the intensity has the following expression:

$$\mathcal{F}(I(\vec{r})) = \hat{I}(\vec{k}) = \int I(\vec{r}) e^{-2i\pi \vec{k}\cdot\vec{r}} \, \mathrm{d}\vec{k} \tag{B.3}$$

Where $\hat{I}(\vec{k})$ is the Fourier transform of I at the reciprocal space position $\vec{k}$. Knowing that $f(r) \cdot g(r) = \hat{f}(k) * \hat{g}(k)$ and $\mathcal{F}(e^{2i\pi \cdot r}) = \delta(k)$ it is possible to demonstrate that :

$$\hat{I}(\vec{k}) = \sum_{g} \hat{H}_g(\vec{k}) * \delta(\vec{k} - \vec{g}) = \sum_{g} \hat{H}_g(\vec{k} - \vec{g}) \tag{B.4}$$

Then $\hat{I}(\vec{k})$ is the sum of each Fourier component centred at its respective $\vec{g}$. The key point of GPA is to focus on a set of reciprocal lattice peaks. By doing so, a projection of lattice variation along the chosen direction is realized

yielding interpretable information. First, considering one reciprocal lattice peak within an area smaller than a Brillouin zone, the intensity is then:

$$\hat{I}(\vec{k}) = \hat{H}_g(\vec{k} - \vec{g}) \tag{B.5}$$

To select one $\vec{g}$, a mask in reciprocal space is used $\hat{M}_g$ that is equal to one within an area of up to one Brillouin zone and zero outside.

$$\hat{H}_g(\vec{k} + \vec{g}) = \hat{I}(\vec{k})\hat{M}_g(\vec{k}) \tag{B.6}$$

The following step is to relate the phase variations to the strain variations. In that aim, two reciprocal lattice peaks with corresponding vectors $\vec{g_1}$ and $\vec{g_2}$ are picked. The corresponding filtered image is then obtained as terms of Eq. B.1:

$$I_{g_1,g_2}(\vec{r}) = A_{g_1}(\vec{r}) \exp((2i\pi\vec{g_1} \cdot \vec{r}) + iP_{g_1}) + A_{g_2}(\vec{r}) \exp((2i\pi\vec{g_2} \cdot \vec{r}) + iP_{g_2}) \tag{B.7}$$

In the presence of a displacement field $\vec{r} \to \vec{r} - \vec{u}(r)$, this change of positions is reflected in the phase of the masked image. It should be noted that considering a displacement field in real space is equivalent to a reciprocal space variation $\vec{g} \to \vec{g} + \Delta\vec{g}$. The phase can then be expressed:

$$P_{g_1}(\vec{r}) = -2\pi\vec{g_1} \cdot \vec{u}(r) = -2\pi g_{1x}u_x - 2\pi g_{1y}u_y \tag{B.8}$$

$$P_{g_2}(\vec{r}) = -2\pi\vec{g_2} \cdot \vec{u}(r) = -2\pi g_{2x}u_x - 2\pi g_{2y}u_y \tag{B.9}$$

These equations are valid for any deformation as long as the derivative of the phase is defined. It implies that in a region close to an interface or within an amorphous region, the strain, as calculated by GPA, is incorrect [166]. A combination of these two equations can be written with the matrix formalism:

$$\begin{pmatrix} P_{g_1} \\ P_{g_2} \end{pmatrix} = -2\pi \begin{pmatrix} g_{1x} & g_{1y} \\ g_{2x} & g_{2y} \end{pmatrix} \begin{pmatrix} u_x \\ u_y \end{pmatrix} \tag{B.10}$$

The displacement field is then obtained by inversion of the previous equation :

$$\begin{pmatrix} u_x \\ u_y \end{pmatrix} = -\frac{1}{2\pi} \begin{pmatrix} g_{1x} & g_{1y} \\ g_{2x} & g_{2y} \end{pmatrix}^{-1} \begin{pmatrix} P_{g_1} \\ P_{g_2} \end{pmatrix} = -\frac{1}{2\pi} \begin{pmatrix} a_{1x} & a_{2x} \\ a_{1y} & a_{2y} \end{pmatrix} \begin{pmatrix} P_{g_1} \\ P_{g_2} \end{pmatrix} \tag{B.11}$$

Where $\vec{a_1}$ and $\vec{a_2}$ are the real space lattice vectors. $\vec{a_i}$ and $\vec{g_j}$ are related by an inversion relation by the equation $\vec{a_i} \cdot \vec{g_j} = \delta_{ij}$. The strain is defined as the gradient of the displacement field :

$$\begin{pmatrix} e_{xx} & e_{xy} \\ e_{yx} & e_{yy} \end{pmatrix} = \begin{pmatrix} \frac{\partial u_x}{\partial x} & \frac{\partial u_x}{\partial y} \\ \frac{\partial u_y}{\partial x} & \frac{\partial u_y}{\partial y} \end{pmatrix} = -\frac{1}{2\pi} \begin{pmatrix} a_{1x} & a_{2x} \\ a_{1y} & a_{2y} \end{pmatrix} \begin{pmatrix} \frac{\partial P_{g_1}}{\partial x} & \frac{\partial P_{g_1}}{\partial y} \\ \frac{\partial P_{g_2}}{\partial x} & \frac{\partial P_{g_2}}{\partial y} \end{pmatrix} \tag{B.12}$$

The strain information is contained within the phase image $Phase[I_{g_1,g_2}(\vec{r})]$. Applying a mask in the reciprocal space enables the projection of the phase along the chosen direction to unwrap the e_{ij} strain components. The e_{ij} components are then obtained by computing the gradient of $P_{g_1}(\vec{r})$ and $P_{g_1}(\vec{r})$. Usually, these two peaks are chosen so that $\vec{g_1} \perp \vec{g_2}$, yielding strain maps that are easier to interpret. A reference area is chosen where the strain is constant. The substrate is usually chosen as a reference area. To obtain quantitative information, the mask is centred at the g vectors of this unstrained lattice a_{sub} yielding an area with a flat phase. The local lattice parameter a_{loc} is related to the strain by the relation[139]:

$$a_{loc} = a_{sub}(1 + e) \tag{B.13}$$

Bibliography

[1] M. Coll et al. "Towards Oxide Electronics: a Roadmap". In: *Applied Surface Science* 482 (July 2019), pp. 1–93. DOI: 10.1016/j.apsusc.2019.03.312.

[2] E. Dagotto and Y. Tokura. "A brief introduction to strongly correlated electronic materials". In: *Multifunctional Oxide Heterostructures*. Ed. by Evgeny Y. Tsymbal et al. Oxford University Press, Aug. 30, 2012, pp. 3–37. ISBN: 978-0-19-958412-3. DOI: 10.1093/acprof:oso/9780199584123.003.0001.

[3] J Coey. "Dilute magnetic oxides". In: *Current Opinion in Solid State and Materials Science* 10.2 (Apr. 2006), pp. 83–92. DOI: 10.1016/j.cossms.2006.12.002.

[4] Fumihiro Matsukura, Yoshinori Tokura, and Hideo Ohno. "Control of magnetism by electric fields". In: *Nature Nanotechnology* 10.3 (Mar. 2015), pp. 209–220. DOI: 10.1038/nnano.2015.22.

[5] T. Hayashi et al. "Magnetic and magnetotransport properties of new III-V diluted magnetic semiconductors: GaMnAs". In: *Journal of Applied Physics* 81.8 (Apr. 15, 1997), pp. 4865–4867. DOI: 10.1063/1.364859.

[6] J M D Coey and S Sanvito. "Magnetic semiconductors and half-metals". In: *Journal of Physics D: Applied Physics* 37.7 (Apr. 7, 2004), pp. 988–993. DOI: 10.1088/0022-3727/37/7/005.

[7] Tomasz Dietl. "A ten-year perspective on dilute magnetic semiconductors and oxides". In: *Nature Materials* 9.12 (Dec. 2010), pp. 965–974. DOI: 10.1038/nmat2898.

[8] M. Wang et al. "Achieving high Curie temperature in (Ga,Mn)As". In: *Applied Physics Letters* 93.13 (Sept. 29, 2008), p. 132103. DOI: 10.1063/1.2992200.

[9] Ashutosh Tiwari et al. "Ferromagnetism in Co doped CeO2: Observation of a giant magnetic moment with a high Curie temperature". In: *Applied Physics Letters* 88.14 (Apr. 3, 2006), p. 142511. DOI: 10.1063/1.2193431.

[10] Wenjian Liu et al. "A room-temperature magnetic semiconductor from a ferromagnetic metallic glass". In: *Nature Communications* 7.1 (Dec. 2016). DOI: 10.1038/ncomms13497.

[11] B. Vertruyen et al. "Curie temperature, exchange integrals, and magneto-optical properties in off-stoichiometric bismuth iron garnet epitaxial films". In: *Physical Review B* 78.9 (Sept. 30, 2008). DOI: 10.1103/PhysRevB.78.094429.

[12] Elena Popova et al. "Magnetic properties of the magnetophotonic crystal based on bismuth iron garnet". In: *Journal of Applied Physics* 112.9 (Nov. 2012), p. 093910. DOI: 10.1063/1.4764345.

[13] M Deb et al. "Magneto-optical Faraday spectroscopy of completely bismuth-substituted Bi3Fe5O12 garnet thin films". In: *Journal of Physics D: Applied Physics* 45.45 (Nov. 14, 2012), p. 455001. DOI: 10.1088/0022-3727/45/45/455001.

[14] Elena Popova et al. "Bismuth iron garnet Bi3Fe5O12: A room temperature magnetoelectric material". In: *Appl. Phys. Lett.* 110 (2017), p. 142404. DOI: 10.1063/1.4979826.

[15] Federico Iori et al. "Bismuth iron garnet : ab initio study of electronic properties". In: *Physical Review B* 100.245150 (2019). DOI: 10.1103/PhysRevB.100.245150.

[16] Carsten Dubs et al. "Sub-micrometer yttrium iron garnet LPE films with low ferromagnetic resonance losses". In: *Journal of Physics D: Applied Physics* 50.20 (May 24, 2017), p. 204005. DOI: 10.1088/1361-6463/aa6b1c.

[17] Carl F. Buhrer. "Faraday Rotation and Dichroism of Bismuth Calcium Vanadium Iron Garnet". In: *Journal of Applied Physics* 40.11 (Oct. 1969), pp. 4500–4502. DOI: 10.1063/1.1657222.

[18] P. Hansen, W. Tolksdorf, and K. Witter. "Recent advances of bismuth garnet materials research for bubble and magneto-optical applications". In: *IEEE Transactions on magnetics* MAG-20.5 (1984), pp. 1099–1104.

[19] T. Okuda et al. "Magnetic properties of Bi3Fe5O12 garnet". In: *Journal of Applied Physics* 67.9 (May 1990), pp. 4944–4946. DOI: 10.1063/1.344740.

[20] K. Satoh et al. "Effect of Substrate Material on Growth of Bi-Fe-Oxide Films by Reactive Ion Beam Sputtering". In: *IEEE Translation journal on magnetics in Japan* 5.12 (1990), p. 1141.

[21] Elena Popova et al. "Interplay between epitaxial strain and low dimensionality effects in a ferrimagnetic oxide". In: *Journal of Applied Physics* 121.11 (Mar. 21, 2017), p. 115304. DOI: 10.1063/1.4978508.

[22] Ming-Yau Chern and Juin-Sen Liaw. "Study of BixY3-xFe5O12 Thin Films Grown by Pulsed Laser Deposition". In: *Japanese Journal of Applied Physics* 36 (Part 1, No. 3A Mar. 15, 1997), pp. 1049–1053. DOI: 10.1143/JJAP.36.1049.

[23] P. Johansson, S.I. Khartsev, and A.M. Grishin. "Comparison of Bi3Fe5O12 film giant Faraday rotators grown on (111) and (001) Gd3Ga5O12 single crystals". In: *Thin Solid Films* 515.2 (Oct. 2006), pp. 477–480. DOI: 10.1016/j.tsf.2005.12.268.

[24] Eva Jesenska et al. "Optical and magneto-optical properties of Bi substituted yttrium iron garnets prepared by metal organic decomposition". In: *Optical Materials Express* 6.6 (June 1, 2016), p. 1986. DOI: 10.1364/OME.6.001986.

[25] N Adachi et al. "Epitaxial Bi3Fe5O1 (001) films grown by pulsed laser deposition and reactive ion beam sputtering techniques". In: *J. Appl. Phys.* 88.5 (2000), p. 7.

[26] S Kahl et al. "Structure, microstructure, and magneto-optical properties of laser deposited Bi3Fe5O12/Gd3Ga5O12 (111) films". In: *J. Appl. Phys.* 91.12 (2002), p. 6.

[27] Elmer E. Anderson. "Molecular Field Model and the Magnetization of YIG". In: *Physical Review* 134.6 (June 15, 1964), A1581–A1585. DOI: 10.1103/PhysRev.134.A1581.

[28] Elena Popova et al. "Magnetic anisotropies in ultrathin bismuth iron garnet films". In: *Journal of Magnetism and Magnetic Materials* 335 (June 2013), pp. 139–143. DOI: 10.1016/j.jmmm.2013.02.003.

[29] S. Kahl, V. Popov, and A. M. Grishin. "Optical transmission and Faraday rotation spectra of a bismuth iron garnet film". In: *Journal of Applied Physics* 94.9 (Nov. 2003), pp. 5688–5694. DOI: 10.1063/1.1618935.

[30] R. Vidyasagar et al. “Giant Zeeman shifts in the optical transitions of yttrium iron garnet thin films”. In: *Applied Physics Letters* 109.12 (Sept. 19, 2016), p. 122402. DOI: 10.1063/1.4962830.

[31] Fu Chen et al. “Room temperature magnetoelectric effect of YFeO 3 –Y 3 Fe 5 O 12 ferrite composites”. In: *Journal of Alloys and Compounds* 656 (Jan. 2016), pp. 465–469. DOI: 10.1016/j.jallcom.2015.09.268.

[32] Marwan Deb et al. “Full spin polarization of complex ferrimagnetic bismuth iron garnet probed by magneto-optical Faraday spectroscopy”. In: *Physical Review B* 87.22 (June 12, 2013). DOI: 10.1103/PhysRevB.87.224408.

[33] P. Hansen and J.-P. Krumme. “Magnetic and magneto-optical properties of garnet films”. In: *Thin Solid Films* 114.1 (Apr. 1984), pp. 69–107. DOI: 10.1016/0040-6090(84)90337-7.

[34] W. Wettling et al. “Optical absorption and Faraday rotation in yttrium iron garnet”. In: *Physica Status Solidi (b)* 59.1 (Sept. 1, 1973), pp. 63–70. DOI: 10.1002/pssb.2220590105.

[35] L. Magdenko et al. “Wafer-scale fabrication of magneto-photonic structures in Bismuth Iron Garnet thin film”. In: *Microelectronic Engineering* 87.11 (Nov. 2010), pp. 2437–2442. DOI: 10.1016/j.mee.2010.04.021.

[36] Yoshinori Ohta. “Growth and Characterizationof 300-pm Thick Bi-Substituted Gadolinium Iron Garnet Films for an Optical Isolator”. In: *IEEE Transactions on magnetics* MAG-22.1 (1986), p. 3.

[37] Gerald F. Dionne and Gary A. Allen. “Spectral origins of giant Faraday rotation and ellipticity in Bi-substituted magnetic garnets”. In: *Journal of Applied Physics* 73.10 (May 15, 1993), pp. 6127–6129. DOI: 10.1063/1.352723.

[38] Ming-Yau Chern et al. “Red Shift of Faraday Rotation in Thin Films of Completely Bismuth-Substituted Iron Garnet Bi3Fe5O12”. In: *Japanese Journal of Applied Physics* 38 (Part 1, No. 12A Dec. 15, 1999), pp. 6687–6689. DOI: 10.1143/JJAP.38.6687.

[39] AK Zvezdin and VA Kotov. *Modern magnetooptics and magnetooptical materials*. IOP Publishing. Studies in condensed matter physics. Bristol and Philadelphia, 1997. ISBN: 0 7503 0362 X.

[40] Gerald F. Dionne and Gary A. Allen. “Molecular-orbital analysis of magneto-optical Bi-O-Fe hybrid excited states”. In: *Journal of Applied Physics* 75.10 (May 15, 1994), pp. 6372–6374. DOI: 10.1063/1.355353.

[41] A V Zenkov and A S Moskvin. "Bismuth-induced increase of the magneto-optical effects in iron garnets: a theoretical analysis". In: *Journal of Physics: Condensed Matter* 14.28 (July 22, 2002), pp. 6957–6968. DOI: 10.1088/0953-8984/14/28/307.

[42] L. E. Helseth et al. "Faraday rotation spectra of bismuth-substituted ferrite garnet films with in-plane magnetization". In: *Physical Review B* 64.17 (Oct. 2, 2001). DOI: 10.1103/PhysRevB.64.174406.

[43] Vladimir Berzhansky et al. "Magneto-optics of nanoscale Bi:YIG films". In: *Applied Optics* 52.26 (Sept. 10, 2013), p. 6599. DOI: 10.1364/AO.52.006599.

[44] A.S. Moskvin et al. "Origin of the magneto-optical properties of iron garnets". In: *Physica B: Condensed Matter* 168.3 (Mar. 1991), pp. 187–196. DOI: 10.1016/0921-4526(91)90670-A.

[45] K. Shinagawa. "Faraday and Kerr Effects in Ferromagnets". In: *Magneto-Optics*. Ed. by Satoru Sugano and Norimichi Kojima. Berlin, Heidelberg: Springer Berlin Heidelberg, 2000, pp. 137–177. ISBN: 978-3-662-04143-7. DOI: 10.1007/978-3-662-04143-7_5.

[46] S. Wittekoek and D. E. Lacklison. "Investigation of the Origin of the Anomalous Faraday Rotation of BixCa3-xFe3.5+0.5xV1.50.5xO12 by Means of the Magneto-optical Kerr Effect". In: *Physical Review Letters* 28.12 (Mar. 20, 1972), pp. 740–743. DOI: 10.1103/PhysRevLett.28.740.

[47] S. Wittekoek et al. "Magneto-optic spectra and the dielectric tensor elements of bismuth-substituted iron garnets at photon energies between 2.2-5.2 eV". In: *Physical Review B* 12.7 (Oct. 1, 1975), pp. 2777–2788. DOI: 10.1103/PhysRevB.12.2777.

[48] J. Suits. "Faraday and kerr effects in magnetic compounds". In: *IEEE Transactions on Magnetics* 8.1 (Mar. 1972), pp. 95–105. DOI: 10.1109/TMAG.1972.1067270.

[49] Tohru Oikawa, Shugo Suzuki, and Kenji Nakao. "First-Principles Study of Spin–Orbit Interactions in Bismuth Iron Garnet". In: *Journal of the Physical Society of Japan* 74.1 (Jan. 15, 2005), pp. 401–404. DOI: 10.1143/JPSJ.74.401.

[50] Richard M. Martin. *Electronic structure: basic theory and practical methods*. Cambridge university press. 2013. ISBN: 978-0-521-78285-2.

[51] Ryan Nakamoto et al. "Properties of rare-earth iron garnets from first principles". In: *Physical Review B* 95.2 (Jan. 31, 2017). DOI: 10.1103/PhysRevB.95.024434.

[52] C. Rödl et al. "Quasiparticle band structures of the antiferromagnetic transition-metal oxides MnO, FeO, CoO, and NiO". In: *Physical Review B* 79.23 (June 8, 2009). DOI: 10.1103/PhysRevB.79.235114.

[53] W Y Ching, Zong-quan Gu, and Yong-Nian Xu. "Theoretical calculation of the optical properties of Y3Fe5O12". In: *Journal of Applied Physics* 89.6883 (2001), p. 4. DOI: /10.1063/1.1357837.

[54] Yong-Nian Xu, Zong-quan Gu, and W. Y. Ching. "First-principles calculation of the electronic structure of yttrium iron garnet (Y3Fe5O12)". In: *Journal of Applied Physics* 87.9 (May 2000), pp. 4867–4869. DOI: 10.1063/1.373185.

[55] Aron Walsh and Graeme W. Watson. "Polymorphism in Bismuth Stannate: A First-Principles Study". In: *Chemistry of Materials* 19.21 (Oct. 2007), pp. 5158–5164. DOI: 10.1021/cm0714279.

[56] J Kane Shenton, David R Bowler, and Wei Li Cheah. "Effects of the Hubbard U on density functional-based predictions of BiFeO3 properties". In: *Journal of Physics: Condensed Matter* 29.44 (Nov. 8, 2017), p. 445501. DOI: 10.1088/1361-648X/aa8935.

[57] D Bahadur, Om Parkash, and Devendra Kumar. "Electron transport in hot pressed YxGdxFe5O12". In: *Bulletin of Materials Science* 3.3 (1981), pp. 325–331.

[58] Adrien Teurtrie et al. "Atmosphere-induced reversible resistivity changes in Ca/Y doped bismuth iron garnet thin films". In: *Accepted in Advanced Functional Materials* 1904958 (2019). DOI: 10.1002/adfm.201904958.

[59] Lucile Soumah et al. "Ultra-low damping insulating magnetic thin films get perpendicular". In: *Nature Communications* 9.1 (Dec. 2018). DOI: 10.1038/s41467-018-05732-1.

[60] R. D. Shannon. "Revised Effective Ionic Radii and Systematic Studies of Interatomic Distances in Halides and Chalcogenides". In: *Acta Crystallographica* A32 (1976), p. 751.

[61] V. J. Fratello et al. "Growth-induced anisotropy in bismuth: Rare-earth iron garnets". In: *Journal of Applied Physics* 60.7 (Oct. 1986), pp. 2488–2497. DOI: 10.1063/1.337163.

[62] P. Hansen et al. "Magnetic and magneto-optical properties of bismuth-substituted lutetium iron garnet films". In: *Physical Review B* 31.9 (May 1, 1985), pp. 5858–5864. DOI: 10.1103/PhysRevB.31.5858.

[63] H. B. Lal, B. K. Verma, and Vijayee Ram Yadav. "Electrical transport in heavy rare-earth iron garnets". In: *Journal of Materials Science* 17.11 (Nov. 1982), pp. 3317–3326. DOI: 10.1007/BF01203501.

[64] Lalitha Sirdeshmukh et al. "Dielectric properties and electrical conduction in yttrium iron garnet (YIG)". In: *Bulletin of Materials Science* 21.3 (June 1998), pp. 219–226. DOI: 10.1007/BF02744973.

[65] T. Schneider et al. "Realization of spin-wave logic gates". In: *Applied Physics Letters* 92.2 (Jan. 14, 2008), p. 022505. DOI: 10.1063/1.2834714.

[66] D. Elwell and A. Dixon. "Mechanism of electrical conduction in garnets". In: *Solid State Communications* 6.8 (Aug. 1968), pp. 585–587. DOI: 10.1016/0038-1098(68)90518-8.

[67] B. Antonini et al. "High conductivity n-type yttrium iron garnet". In: *Journal of Magnetism and Magnetic Materials* 31-34 (Feb. 1983), pp. 149–150. DOI: 10.1016/0304-8853(83)90192-0.

[68] J. M. Costantini, J. P. Salvetat, and F. Brisard. "Dielectric and transport properties of magnetic insulators irradiated with GeV heavy ions". In: *Journal of Applied Physics* 82.10 (Nov. 15, 1997), pp. 5063–5071. DOI: 10.1063/1.366403.

[69] P.K. Larsen and R. Metselaar. "Electrical properties of yttrium iron garnet at high temperatures". In: *Physical Review B* 14.6 (1976), pp. 2520–2527.

[70] R. Metselaar and P.K. Larsen. "Electrical properties of yttrium iron garnet". In: Proceedings of the international school of physics Enrico Fermi. Vol. 70. Varenna, 1978, pp. 417–444.

[71] R. Metselaar and P.K. Larsen. "High-temperature electrical properties of yttrium iron garnet under varying oxygen pressures". In: *Solid State Communications* 15.2 (July 1974), pp. 291–294. DOI: 10.1016/0038-1098(74)90760-1.

[72] P. K. Larsen and J. M. Robertson. "Electrical and optical properties of thin films of Pb2+ and Si4+ doped YIG produced by liquid phase epitaxy". In: *Journal of Applied Physics* 45.7 (July 1974), pp. 2867–2873. DOI: 10.1063/1.1663693.

[73] Y.J. Song et al. "Effects of oxygen vacancies on the magnetic and electrical properties of Ca-substituted yttrium iron garnet". In: *Journal of Magnetism and Magnetic Materials* 154.1 (Mar. 1996), pp. 37–53. DOI: 10.1016/0304-8853(95)00580-3.

[74] A. Tucciarone and P. De Gasperis. "Electrical properties of iron garnet films". In: *Thin Solid Films* 114.1 (Apr. 1984), pp. 109–134. DOI: 10.1016/0040-6090(84)90338-9.

[75] R. Metselaar and M.A.H. Huyberts. "Nonstoichiometry and electronic defects in yttrium iron garnet". In: *Journal of Solid State Chemistry* 22.3 (Nov. 1977), pp. 309–319. DOI: 10.1016/0022-4596(77)90007-X.

[76] V. V. Kharton et al. "Ionic Transport in GdFeO12 and Y3Fe5O12 Based Garnets". In: *Journal of The Electrochemical Society* 150.7 (2003), J33. DOI: 10.1149/1.1574810.

[77] G.B. Turpin, Y.J. Song, and P.E. Wigen. "Room temperature high conduction state in annealed Ca-substituted yttrium iron garnet films". In: *IEEE Transactions on Magnetics* 31.6 (Nov. 1995), pp. 3835–3837. DOI: 10.1109/20.489788.

[78] Jae Sung Lee, Shinbuhm Lee, and Tae Won Noh. "Resistive switching phenomena: A review of statistical physics approaches". In: *Applied Physics Reviews* 2.3 (Sept. 2015), p. 031303. DOI: 10.1063/1.4929512.

[79] A. Odagawa et al. "Colossal electroresistance of a Pr0.7Ca0.3MnO3 thin film at room temperature". In: *Physical Review B* 70.22 (Dec. 3, 2004). DOI: 10.1103/PhysRevB.70.224403.

[80] D. S. Shang et al. "Effect of carrier trapping on the hysteretic current-voltage characteristics in Ag/La0.7Ca0.3MnO3/Pt heterostructures". In: *Physical Review B* 73.24 (June 22, 2006). DOI: 10.1103/PhysRevB.73.245427.

[81] N. Thiery et al. "Electrical properties of epitaxial yttrium iron garnet ultrathin films at high temperatures". In: *Physical Review B* 97.6 (Feb. 26, 2018). DOI: 10.1103/PhysRevB.97.064422.

[82] H M Christen and G Eres. "Recent advances in pulsed-laser deposition of complex oxides". In: *Journal of Physics: Condensed Matter* 20.26 (July 2, 2008), p. 264005. DOI: 10.1088/0953-8984/20/26/264005.

[83] Wing-Tat Chan, X. L. Mao, and Richard E. Russo. "Differential Vaporization during Laser Ablation/Deposition of Bi-Sr-Ca-Cu-O Superconducting Materials". In: *Applied Spectroscopy* 46.6 (June 1992), pp. 1025–1031. DOI: 10.1366/0003702924124510.

[84] L.J. van der Pauw. "A method of measuring the resistivity and Hall coefficient on lamellae of arbitrary shape". In: *Phillips technical review* 20.8 (1958), pp. 220–224.

[85] G. González-Díaz et al. "A robust method to determine the contact resistance using the van der Pauw set up". In: *Measurement* 98 (Feb. 2017), pp. 151–158. DOI: 10.1016/j.measurement.2016.11.040.

[86] Toru Matsumura and Yuichi Sato. "A Theoretical Study on Van Der Pauw Measurement Values of Inhomogeneous Compound Semiconductor Thin Films". In: *Journal of Modern Physics* 01.5 (2010), pp. 340–347. DOI: 10.4236/jmp.2010.15048.

[87] R. C. Miller, R. R. Heikes, and R. Mazelsky. "Model for the Electronic Transport Properties of Mixed Valency Semiconductors". In: *Journal of Applied Physics* 32.10 (Oct. 1961), pp. 2202–2206. DOI: 10.1063/1.1777043.

[88] Florian Werner. "Hall measurements on low-mobility thin films". In: *Journal of Applied Physics* 122.13 (Oct. 7, 2017), p. 135306. DOI: 10.1063/1.4990470.

[89] Marwan Deb. "Magneto-optical spectroscopy of magnetic bismuth iron garnet : static and dynamic studies". PhD thesis. Université Versailles Saint-Quentin en Yvelines, 2013.

[90] Otto Scherzer. "Uber einige fehler von elekronenlinsen". In: *Zeitschritt fur Physik* 101 (1936), p. 593.

[91] Adrew Bleloch and Quentin M. Ramasse. "Lens aberrations: Diagnosis and Correction". In: *Aberration-corrected analytical transmission electron microscopy*. Wiley. RMS-Wiley Imprint. Rik Brydson, 2011, pp. 55–88. ISBN: 978-1-119-97990-6.

[92] Otto Scherzer. "Spharische und chromatische korrektur von eleketronenlinsen". In: *Optik* 2.114 (1947).

[93] O.L. Krivanek et al. "Towards sub-0.5Å electron beams". In: *Ultramicroscopy* 96.3 (Sept. 2003), pp. 229–237. DOI: 10.1016/S0304-3991(03)00090-1.

[94] Max Haider et al. "A spherical-aberration-corrected 200kV transmission electron microscope". In: *Ultramicroscopy* 75.1 (Oct. 1998), pp. 53–60. DOI: 10.1016/S0304-3991(98)00048-5.

[95] Ondrej L. Krivanek et al. "Monochromated STEM with a 30 meV-wide, atom-sized electron probe". In: *Microscopy* 62.1 (Feb. 2013), pp. 3–21. DOI: 10.1093/jmicro/dfs089.

[96] Martin Linck et al. "Chromatic Aberration Correction for Atomic Resolution TEM Imaging from 20 to 80 kV". In: *Physical Review Letters* 117.7 (Aug. 9, 2016). DOI: 10.1103/PhysRevLett.117.076101.

[97] O.L. Krivanek et al. "An electron microscope for the aberration-corrected era". In: *Ultramicroscopy* 108.3 (Feb. 2008), pp. 179–195. DOI: 10.1016/j.ultramic.2007.07.010.

[98] N. Dellby et al. "Dedicated STEM for 200 to 40 keV operation". In: *The European Physical Journal Applied Physics* 54.3 (June 2011), p. 33505. DOI: 10.1051/epjap/2011100429.

[99] Gordon Tatlock. "Introduction to Electron Optics". In: *Aberration-corrected analytical transmission electron microscopy*. Wiley. RMS-Wiley Imprint. Rik Brydson, 2011, pp. 21–38. ISBN: 978-1-119-97990-6.

[100] Mathieu Kociak et al. "Spatially Resolved EELS: The Spectrum-Imaging Technique and Its Applications". In: *Scanning transmission electron microscopy: Imaging and analysis*. Springer. Stephen J. Pennycook and Peter D. Nellist, 2011. ISBN: 978-1-4419-7199-9.

[101] P.D. Nellist and S.J. Pennycook. "The principles and interpretation of annular dark-field Z-contrast imaging". In: *Advances in Imaging and Electron Physics*. Vol. 113. Elsevier, 2000, pp. 147–203. ISBN: 978-0-12-014755-7. DOI: 10.1016/S1076-5670(00)80013-0.

[102] R.F. Egerton. *Electron energy-loss spectroscopy in the electron microscope*. 2nd. New York: Plenum press, 1996. 131–243. ISBN: 0-306-45223-5.

[103] Earl J. Kirkland, Russell F. Loane, and John Silcox. "Simulation of annular dark field stem images using a modified multislice method". In: *Ultramicroscopy* 23.1 (Jan. 1987), pp. 77–96. DOI: 10.1016/0304-3991(87)90229-4.

[104] Dmitri O. Klenov and Susanne Stemmer. "Contributions to the contrast in experimental high-angle annular dark-field images". In: *Ultramicroscopy* 106.10 (Aug. 2006), pp. 889–901. DOI: 10.1016/j.ultramic.2006.03.007.

[105] M. Bosman et al. "Two-Dimensional Mapping of Chemical Information at Atomic Resolution". In: *Physical Review Letters* 99.8 (Aug. 22, 2007). DOI: 10.1103/PhysRevLett.99.086102.

[106] Gatan Inc. *Spectrum imaging*. GATAN. URL: http://www.gatan.com/techniques/spectrum-imaging.

[107] Frank M.F. de Groot and Akio Kotani. *Core level spectroscopy of solids*. Taylor and Francis group. Advances in condensed matter science 6. D.D. Sarma, G. Kotliar and Y. Tokura, 2008. 512 pp. ISBN: 978-0-8493-9071-5.

[108] Vincent Badjeck. "Electron spectro-microscopy study of damage-free and He-implanted ODS steels". PhD thesis. Université Paris-sud: Université Paris-Saclay, 2016. 192 pp.

[109] A.R. Lupini and S.J. Pennycook. "Localization in elastic and inelastic scattering". In: *Ultramicroscopy* 96.3 (Sept. 2003), pp. 313–322. DOI: 10.1016/S0304-3991(03)00096-2.

[110] R.F. Egerton. "Limits to the spatial, energy and momentum resolution of electron energy-loss spectroscopy". In: *Ultramicroscopy* 107.8 (Aug. 2007), pp. 575–586. DOI: 10.1016/j.ultramic.2006.11.005.

[111] C. Dwyer and J. Etheridge. "Scattering of Å-scale electron probes in silicon". In: *Ultramicroscopy* 96.3 (Sept. 2003), pp. 343–360. DOI: 10.1016/S0304-3991(03)00100-1.

[112] Koji Kimoto, Kazuo Ishizuka, and Yoshio Matsui. "Decisive factors for realizing atomic-column resolution using STEM and EELS". In: *Micron* 39 (2008), pp. 653–657. DOI: 10.1016/j.micron.2007.09.011.

[113] D A Muller et al. "Atomic-Scale Chemical Imaging of Composition and Bonding by Aberration-Corrected Microscopy". In: *Science* 319.5866 (2008), p. 1073.

[114] Gianluigi A. Botton, Sorin Lazar, and Christian Dwyer. "Elemental mapping at the atomic scale using low accelerating voltages". In: *Ultramicroscopy* 110.8 (July 2010), pp. 926–934. DOI: 10.1016/j.ultramic.2010.03.008.

[115] Koji Kimoto et al. "Element-selective imaging of atomic columns in a crystal using STEM and EELS". In: *Nature* 450.7170 (Nov. 2007), pp. 702–704. DOI: 10.1038/nature06352.

[116] Alexandre Gloter et al. "Atomically resolved mapping of EELS fine structures". In: *Materials Science in Semiconductor Processing* 65 (July 2017), pp. 2–17. DOI: 10.1016/j.mssp.2016.07.006.

[117] Stuart Turner et al. "Atomic Resolution Coordination Mapping in Ca2FeCoO5 Brownmillerite by Spatially Resolved Electron Energy-Loss Spectroscopy". In: *Chemistry of Materials* 24.10 (May 22, 2012), pp. 1904–1909. DOI: 10.1021/cm300640g.

[118] S. Turner et al. "Site-specific mapping of transition metal oxygen coordination in complex oxides". In: *Applied Physics Letters* 101.24 (Dec. 10, 2012), p. 241910. DOI: 10.1063/1.4770512.

[119] L. Bocher et al. "Direct Evidence of Fe2+ - Fe3+ Charge Ordering in the Ferrimagnetic Hematite-Ilmenite Fe1.35Ti0.65O3-d Thin Films". In: *Physical Review Letters* 111.16 (Oct. 14, 2013). DOI: 10.1103/PhysRevLett.111.167202.

[120] Haiyan Tan et al. "2D Atomic Mapping of Oxidation States in Transition Metal Oxides by Scanning Transmission Electron Microscopy and Electron Energy-Loss Spectroscopy". In: *Physical Review Letters* 107.10 (Sept. 1, 2011). DOI: 10.1103/PhysRevLett.107.107602.

[121] Matthieu Bugnet et al. "Real-space localization and quantification of hole distribution in chain-ladder Sr3Ca11Cu24O41 superconductor". In: *Science Advances* 2.3 (Mar. 2016), e1501652. DOI: 10.1126/sciadv.1501652.

[122] Piter S. Miedema and Frank M.F. de Groot. "The iron L edges: Fe 2p X-ray absorption and electron energy loss spectroscopy". In: *Journal of Electron Spectroscopy and Related Phenomena* 187 (Apr. 2013), pp. 32–48. DOI: 10.1016/j.elspec.2013.03.005.

[123] M. Abbate et al. "Controlled-valence properties of La1-xSrxFeO3 and La1-xSrxmnO3 studied by soft-x-ray absorption spectroscopy". In: *Physical Review B* 46.8 (1992), p. 4511.

[124] Kazuyoshi Tatsumi et al. "Site-specific electronic configurations of Fe 3d states by energy loss by channeled electrons". In: *Applied Physics Letters* 96.20 (May 17, 2010), p. 201911. DOI: 10.1063/1.3429593.

[125] P. A. van Aken and B. Liebscher. "Quantification of ferrous/ferric ratios in minerals: new evaluation schemes of Fe L 23 electron energy-loss near-edge spectra". In: *Physics and Chemistry of Minerals* 29.3 (Apr. 1, 2002), pp. 188–200. DOI: 10.1007/s00269-001-0222-6.

[126] Frank M. F. de Groot et al. "1s2p Resonant Inelastic X-ray Scattering of Iron Oxides". In: *The Journal of Physical Chemistry B* 109.44 (Nov. 2005), pp. 20751–20762. DOI: 10.1021/jp054006s.

[127] C. Mitterbauer et al. "Electron energy-loss near-edge structures of 3d transition metal oxides recorded at high-energy resolution". In: *Ultramicroscopy* 96.3 (Sept. 2003), pp. 469–480. DOI: 10.1016/S0304-3991(03)00109-8.

[128] V. R. Galakhov et al. "Valence Band Structure and X-ray Spectra of Oxygen-Deficient Ferrites SrFeOx". In: *The Journal of Physical Chemistry C* 114.11 (Mar. 25, 2010), pp. 5154–5159. DOI: 10.1021/jp909091s.

[129] J.-S. Kang et al. "Electronic structure of the cubic perovskite SrMn1-xFexO3 investigated by x-ray spectroscopies". In: *Physical Review B* 78.5 (Aug. 21, 2008). DOI: 10.1103/PhysRevB.78.054434.

[130] Svein Steinsvik et al. "THE DEFECT STRUCTURE OF SrTil-xFex03-y (x= 0-0.8)". In: *Journal of Physics and Chemistry of Solids* 58.6 (1997), pp. 969–976.

[131] Armin Feldhoff et al. "Spin-state transition of iron in (perovskite". In: *Journal of Solid State Chemistry* 182.11 (Nov. 2009), pp. 2961–2971. DOI: 10.1016/j.jssc.2009.07.058.

[132] Laurence A. J. Garvie, Alan Craven, and Rik Brydson. "Use of electron-energy loss near-edge fin structure in the study of minerals". In: *American mineralogist* 79 (1994), pp. 411–425.

[133] R. Abrudan et al. "ALICE - An advanced reflectometer for static and dynamic experiments in magnetism at synchrotron radiation facilities". In: *Review of Scientific Instruments* 86.6 (June 2015), p. 063902. DOI: 10.1063/1.4921716.

[134] J. Grabis, A. Nefedov, and H. Zabel. "Diffractometer for soft x-ray resonant magnetic scattering". In: *Review of Scientific Instruments* 74.9 (Sept. 2003), pp. 4048–4051. DOI: 10.1063/1.1602932.

[135] F. Schedin et al. "Magnetic properties of ultrathin epitaxial Fe3O4 films on Pt(111)". In: *Journal of Magnetism and Magnetic Materials* 211 (2000), pp. 266–270.

[136] F.M.F. de Groot et al. "Fluorescence yield detection: Why it does not measure the X-ray absorption cross section". In: *Solid State Communications* 92.12 (Dec. 1994), pp. 991–995. DOI: 10.1016/0038-1098(94)90027-2.

[137] Jan Vogel and Maurizio Sacchi. "Polarization and angular dependence of the L 2,3 absorption edges in Ni(110)". In: *Physical Review B* 49.5 (Feb. 1, 1994), pp. 3230–3234. DOI: 10.1103/PhysRevB.49.3230.

[138] Michel van Veenendaal, J. B. Goedkoop, and B. T. Thole. "Polarized X-ray Fluorescence as a Probe of Ground State Properties". In: *Physical Review Letters* 77.8 (Aug. 19, 1996), pp. 1508–1511. DOI: 10.1103/PhysRevLett.77.1508.

[139] M.J. Hÿtch, E. Snoeck, and R. Kilaas. "Quantitative measurement of displacement and strain fields from HREM micrographs". In: *Ultramicroscopy* 74.3 (Aug. 1998), pp. 131–146. DOI: 10.1016/S0304-3991(98)00035-7.

[140] Yuanyuan Zhu et al. "Interface lattice displacement measurement to 1pm by geometric phase analysis on aberration-corrected HAADF STEM images". In: *Acta Materialia* 61.15 (Sept. 2013), pp. 5646–5663. DOI: 10.1016/j.actamat.2013.06.006.

[141] N Bonnet, N Brun, and C Colliex. "Extracting information from sequences of spatially resolved EELS spectra using multivariate statistical analysis". In: *Ultramicroscopy* 77.3 (July 1999), pp. 97–112. DOI: 10.1016/S0304-3991(99)00042-X.

[142] F. de la Peña. *Hyperspy*. Version 1.4.1.

[143] Michael R. Keenan and Paul G. Kotula. "Accounting for Poisson noise in the multivariate analysis of ToF-SIMS spectrum images". In: *Surface and Interface Analysis* 36.3 (Mar. 2004), pp. 203–212. DOI: 10.1002/sia.1657.

[144] Stijn Lichtert and Jo Verbeeck. "Statistical consequences of applying a PCA noise filter on EELS spectrum images". In: *Ultramicroscopy* 125 (Feb. 2013), pp. 35–42. DOI: 10.1016/j.ultramic.2012.10.001.

[145] F. de la Peña et al. "Mapping titanium and tin oxide phases using EELS: An application of independent component analysis". In: *Ultramicroscopy* 111.2 (Jan. 2011), pp. 169–176. DOI: 10.1016/j.ultramic.2010.10.001.

[146] Nicolas Dobigeon and Nathalie Brun. "Spectral mixture analysis of EELS spectrum-images". In: *Ultramicroscopy* 120 (Sept. 2012), pp. 25–34. DOI: 10.1016/j.ultramic.2012.05.006.

[147] Lior Rokach. "A survey of clustering algorithms". In: *Data mining and knowledge discovery handbook*. Springer. Oded Maimon and Lior Rokach, 2010, pp. 269–298. ISBN: 978-0-387-09822-7.

[148] Pau Torruella et al. "Clustering analysis strategies for electron energy loss spectroscopy (EELS)". In: *Ultramicroscopy* 185 (Feb. 2018), pp. 42–48. DOI: 10.1016/j.ultramic.2017.11.010.

[149] Ahmet Kertmen et al. "Photoelectrochemically Active N-Adsorbing Ultrathin TiO2 Layers for Water-Splitting Applications Prepared by Pyrolysis of Oleic Acid on Iron Oxide Nanoparticle Surfaces under Nitrogen Environment". In: *Advanced Materials Interfaces* (Dec. 10, 2018), p. 1801286. DOI: 10.1002/admi.201801286.

[150] Jakob Spiegelberg et al. "Analysis of electron energy loss spectroscopy data using geometric extraction methods". In: *Ultramicroscopy* 174 (Mar. 2017), pp. 14–26. DOI: 10.1016/j.ultramic.2016.12.014.

[151] Fabian Pedregosa et al. "Scikit-learn: Machine Learning in Python". In: *MACHINE LEARNING IN PYTHON* 12 (2011), pp. 2825–2830.

[152] L Roth. "THE MAGNETIC STRUCTURE OF Co3O4". In: *Journal of Physics and Chemistry of Solids* 25 (1963), pp. 1–10.

[153] Fernando Morales et al. "In Situ X-ray Absorption of Co/Mn/TiO2 Catalysts for Fischer-Tropsch Synthesis". In: *The Journal of Physical Chemistry B* 108.41 (Oct. 2004), pp. 16201–16207. DOI: 10.1021/jp0403846.

[154] F. de la Peña. "Advanced methods for electron energy-loss spectroscopy core-loss analysis". PhD thesis. Orsay: Université Paris-sud, 2010. 181 pp.

[155] E. Popova et al. "Structure and magnetic properties of yttrium-iron-garnet thin films prepared by laser deposition". In: *Journal of Applied Physics* 90.3 (Aug. 2001), pp. 1422–1428. DOI: 10.1063/1.1379344.

[156] Yiguang Wang et al. "Synthesis, Characterization, and Optical Properties of Pristine and Doped Yttrium Aluminum Garnet Nanopowders". In: *Journal of the American Ceramic Society* 88.2 (Feb. 2005), pp. 284–286. DOI: 10.1111/j.1551-2916.2005.00071.x.

[157] C. Colliex, T. Manoubi, and C. Ortiz. "Electron-energy-loss-spectroscopy near-edge fine structures in the iron-oxygen system". In: *Physical Review B* 44.20 (Nov. 15, 1991), pp. 11402–11411. DOI: 10.1103/PhysRevB.44.11402.

[158] F. M. F. de Groot et al. "Oxygen 1s x-ray-absorption edges of transition-metal oxides". In: *Physical Review B* 40.8 (Sept. 15, 1989), pp. 5715–5723. DOI: 10.1103/PhysRevB.40.5715.

[159] Ragnhild Sæterli et al. "Electronic structure of multiferroic BiFeO 3 and related compounds: Electron energy loss spectroscopy and density functional study". In: *Physical Review B* 82.6 (Aug. 6, 2010). DOI: 10.1103/PhysRevB.82.064102.

[160] Huairuo Zhang et al. "Stabilisation of Fe2O3-rich Perovskite Nanophase in Epitaxial Rare-earth Doped BiFeO3 Films". In: *Scientific Reports* 5.1 (Oct. 2015). DOI: 10.1038/srep13066.

[161] Hélène Béa et al. "Investigation on the origin of the magnetic moment of BiFeO 3 thin films by advanced x-ray characterizations". In: *Physical Review B* 74.2 (July 17, 2006). DOI: 10.1103/PhysRevB.74.020101.

[162] M. Murakami et al. "Microstructure and phase control in Bi–Fe–O multiferroic nanocomposite thin films". In: *Applied Physics Letters* 88.11 (Mar. 13, 2006), p. 112505. DOI: 10.1063/1.2184892.

[163] X. Wang et al. "Morphology and orientation of iron oxide precipitates in epitaxial BiFeO3 thin films grown under two non-optimized oxygen pressures". In: *Philosophical Magazine* 90.34 (Nov. 28, 2010), pp. 4551–4567. DOI: 10.1080/14786435.2010.515261.

[164] Y. Sharma et al. "Studies on structural, optical, magnetic, and resistive switching properties of doped BiFe1-xCrxO3 thin films". In: *Journal of Applied Physics* 120.19 (Nov. 21, 2016), p. 194101. DOI: 10.1063/1.4967993.

[165] Anshu Gaur et al. "Structural, optical and magnetic properties of Nd-doped BiFeO3 thin films prepared by pulsed laser deposition". In: *Physica B: Condensed Matter* 406.10 (May 2011), pp. 1877–1882. DOI: 10.1016/j.physb.2011.02.046.

[166] J.L. Rouvière and E. Sarigiannidou. "Theoretical discussions on the geometrical phase analysis". In: *Ultramicroscopy* 106.1 (Dec. 2005), pp. 1–17. DOI: 10.1016/j.ultramic.2005.06.001.

[167] S. H. Lim et al. "The Effects of Multiphase Formation on Strain Relaxation and Magnetization in Multiferroic BiFeO3 Thin Films". In: *Advanced Functional Materials* 17.14 (Sept. 24, 2007), pp. 2594–2599. DOI: 10.1002/adfm.200700055.

[168] L. Fitting Kourkoutis et al. "Atomic-resolution spectroscopic imaging of oxide interfaces". In: *Philosophical Magazine* 90.35 (Dec. 14, 2010), pp. 4731–4749. DOI: 10.1080/14786435.2010.518983.

[169] Mengchao Liu et al. "Atomic-scale structure and chemistry of YIG/GGG". In: *AIP Advances* 8.8 (Aug. 2018), p. 085117. DOI: 10.1063/1.5018795.

[170] James C. Gallagher et al. "Exceptionally high magnetization of stoichiometric Y3Fe5O12 epitaxial films grown on Gd3Ga5O12". In: *Applied Physics Letters* 109.7 (Aug. 15, 2016), p. 072401. DOI: 10.1063/1.4961371.

[171] A. Mitra et al. "Interfacial Origin of the Magnetisation Suppression of Thin Film Yttrium Iron Garnet". In: *Scientific Reports* 7.1 (Dec. 2017). DOI: 10.1038/s41598-017-10281-6.

[172] F. A. Kröger and H. J. Vink. "Relations between the concentrations of imperfections in crystalline solids". In: *Solid State Physics* 3 (1956), pp. 307–435. DOI: 10.1016/S0081-1947(08)60135-6.

[173] Yifang Ouyang et al. "Codoping Er-N to Suppress Self-Compensation Donors for Stable p -Type Zinc Oxide". In: *Advanced Theory and Simulations* 2.2 (Feb. 2019), p. 1800133. DOI: 10.1002/adts.201800133.

[174] Ananya Dey. "Semiconductor metal oxide gas sensors: A review". In: *Materials Science and Engineering: B* 229 (Mar. 2018), pp. 206–217. DOI: 10.1016/j.mseb.2017.12.036.

[175] H.-J. Hagemann and D. Hennings. "Reversible Weight Change of Acceptor-Doped BaTiO3". In: *Journal of the American Ceramic Society* 64.10 (Oct. 1981), pp. 590–594. DOI: 10.1111/j.1151-2916.1981.tb10223.x.

[176] T. Tsuyama et al. "X-ray spectroscopic study of BaFeO 3 thin films: An Fe4+ ferromagnetic insulator". In: *Physical Review B* 91.11 (Mar. 2, 2015). DOI: 10.1103/PhysRevB.91.115101.

[177] Ulrich Aschauer et al. "Strain-controlled oxygen vacancy formation and ordering in CaMnO 3". In: *Physical Review B* 88.5 (Aug. 19, 2013). DOI: 10.1103/PhysRevB.88.054111.

[178] V.V. Mesilov et al. "Valence states of iron ions in nanostructured yttrium iron garnet Y3Fe5O12 studied by means of soft X-ray absorption spectroscopy". In: *Journal of Electron Spectroscopy and Related Phenomena* 185.12 (Dec. 2012), pp. 598–601. DOI: 10.1016/j.elspec.2013.01.010.

[179] Laurence A. J. Garvie and Peter R. Buseck. "Ratios of ferrous to ferric iron from nanometre-sized areas in minerals". In: *Nature* 396.6712 (Dec. 1998), pp. 667–670. DOI: 10.1038/25334.

[180] Shih-Yun Chen et al. "Electron energy loss spectroscopy and ab initio investigation of iron oxide nanomaterials grown by a hydrothermal process". In: *Physical Review B* 79.10 (Mar. 5, 2009). DOI: 10.1103/PhysRevB.79.104103.

[181] Huarui Wu et al. "Grain size and Fe2+ concentration-dependent magnetic, dielectric, and magnetodielectric properties of Y3Fe5O12 ceramics: Magnetic, dielectric, and magnetodielectric properties of Y3Fe5O12 ceramics". In: *physica status solidi (a)* 213.1 (Jan. 2016), pp. 146–153. DOI: 10.1002/pssa.201532582.

[182] E. Goering, S. Gold, and G. Schütz. "Ho-Fe-Garnet soft XMCD measurements below and above the compensation temperature". In: *Journal of Synchrotron Radiation* 8.2 (Mar. 1, 2001), pp. 422–424. DOI: 10.1107/S0909049500018355.

[183] H. B. Vasili et al. "Direct observation of multivalent states and 4 f ->3 d charge transfer in Ce-doped yttrium iron garnet thin films". In: *Physical Review B* 96.1 (July 27, 2017). DOI: 10.1103/PhysRevB.96.014433.

[184] Richard A.D. Pattrick et al. "Cation site occupancy in spinel ferrites studied by X-ray magnetic circular dichroism: developing a method for mineralogists". In: *European Journal of Mineralogy* 14.6 (Nov. 25, 2002), pp. 1095–1102. DOI: 10.1127/0935-1221/2002/0014-1095.

[185] Jinhua Li et al. "Controlled cobalt doping in the spinel structure of magnetosome magnetite: new evidences from element- and site-specific X-ray magnetic circular dichroism analyses". In: *Journal of The Royal Society Interface* 13.121 (Aug. 31, 2016), p. 20160355. DOI: 10.1098/rsif.2016.0355.

[186] Michel Sassi et al. "First-Principles Fe L2,3 -Edge and O K-Edge XANES and XMCD Spectra for Iron Oxides". In: *The Journal of Physical Chemistry A* 121.40 (Oct. 12, 2017), pp. 7613–7618. DOI: 10.1021/acs.jpca.7b08392.

[187] S. Brice-Profeta et al. "Magnetic order in - nanoparticles: a XMCD study". In: *Journal of Magnetism and Magnetic Materials* 288 (Mar. 2005), pp. 354–365. DOI: 10.1016/j.jmmm.2004.09.120.

[188] C.I. Pearce et al. "Synthesis and properties of titanomagnetite (Fe3-xTixO4) nanoparticles: A tunable solid-state Fe(II/III) redox system". In: *Journal of Colloid and Interface Science* 387.1 (Dec. 2012), pp. 24–38. DOI: 10.1016/j.jcis.2012.06.092.

[189] W. Noun et al. "Determination of yttrium iron garnet superexchange parameters as a function of oxygen and cation stoichiometry". In: *Physical Review B* 81.5 (Feb. 9, 2010). DOI: 10.1103/PhysRevB.81.054411.

[190] A E Berkowitz and Kentaro Takano. "Exchange anisotropy: a review". In: *Journal of Magnetism and Magnetic Materials* (1999), p. 19.

[191] P. Novák. "Contribution of Fe3+ ions to the growth induced anisotropy in garnet films". In: *Czechoslovak Journal of Physics* 34.10 (Oct. 1984), pp. 1060–1074. DOI: 10.1007/BF01590100.

[192] Bin Liu et al. "Origin of antipolar clusters in BiFeO3 epitaxial thin films". In: *Journal of the European Ceramic Society* 38.2 (Feb. 2018), pp. 621–627. DOI: 10.1016/j.jeurceramsoc.2017.09.041.

[193] Sibylle Meyer et al. "Anomalous Hall effect in YIG-Pt bilayers". In: *Applied Physics Letters* 106.13 (Mar. 30, 2015), p. 132402. DOI: 10.1063/1.4916342.

[194] L. Joly et al. "Versatile variable temperature insert at the DEIMOS beamline for *in situ* electrical transport measurements". In: *Journal of Synchrotron Radiation* 23.3 (May 1, 2016), pp. 652–657. DOI: 10.1107/S1600577516002551.

[195] Etienne Janod et al. "Resistive Switching in Mott Insulators and Correlated Systems". In: *Advanced Functional Materials* 25.40 (Oct. 2015), pp. 6287–6305. DOI: 10.1002/adfm.201500823.

[196] Nikolai E. Khokhlov et al. "Electric-field-driven magnetic domain wall as a microscale magneto-optical shutter". In: *Scientific Reports* 7.1 (Dec. 2017). DOI: 10.1038/s41598-017-00365-8.

[197] Jaroslav Fabian, Igor Zutic, and S. Das Sarma. "Theory of spin-polarized bipolar transport in magnetic p-n junctions". In: *Physical Review B* 66.16 (Oct. 1, 2002). DOI: 10.1103/PhysRevB.66.165301.

[198] M. I. Dyakonov and V. I. Perel. "Theory of optical spin orientation of electron and nuclei in semiconductors". In: *Optical orientation*. Elsevier. Modern problems in condensed matter sciences 8. New York: Meier F. and Zakharchenya B. P., 1984.

[199] K. B. Omarov et al. "Thermodynamic analysis of Mn-As-H2O, Mn-Sb-H2O, Mn-Bi-H2O systems". In: *6th International Conference on Biological, Chemical & Environmental Sciences (BCES-2016) August 8-9, 2016 Pattaya (Thailand)*. 6th International Conference on Biological, Chemical & Environmental Sciences. Pattaya (Thailand): International Institute of Chemical, Biological & Environmental Engineering (IICBEE), Aug. 8, 2016, pp. 23–25. ISBN: 978-93-84468-66-8. DOI: 10.15242/IICBE.C0816212.

[200] Qing Qin et al. "Ultra-low magnetic damping of perovskite La0.7Sr0.3MnO3 thin films". In: *Applied Physics Letters* 110.11 (Mar. 13, 2017), p. 112401. DOI: 10.1063/1.4978431.

[201] Michael C. Martin et al. "Magnetism and structural distortion in the La0.7Sr0.3MnO3 metallic ferromagnet". In: *Physical Review B* 53.21 (June 1, 1996), pp. 14285–14290. DOI: 10.1103/PhysRevB.53.14285.

[202] S. Kolesnik et al. "Magnetic phase diagram of cubic perovskites SrMn1-xFexO3". In: *Physical Review B* 67.14 (Apr. 2, 2003). DOI: 10.1103/PhysRevB.67.144402.

[203] M. Abbate et al. "X-ray absorption of the negative charge-transfer material SrFe1-xCoxO3". In: *Physical Review B* 65.16 (Apr. 15, 2002). DOI: 10.1103/PhysRevB.65.165120.

[204] T.C. Lovejoy et al. "Advances in Ultra-High Energy Resolution STEM-EELS". In: *Microscopy and Microanalysis* 24 (S1 Aug. 2018), pp. 446–447. DOI: 10.1017/S1431927618002726.

[205] David Cooper et al. "Anomalous Resistance Hysteresis in Oxide ReRAM: Oxygen Evolution and Reincorporation Revealed by In Situ TEM". In: *Advanced Materials* 29.23 (June 2017), p. 1700212. DOI: 10.1002/adma.201700212.

[206] Deok-Hwang Kwon et al. "Atomic structure of conducting nanofilaments in TiO2 resistive switching memory". In: *Nature Nanotechnology* 5.2 (Feb. 2010), pp. 148–153. DOI: 10.1038/nnano.2009.456.

[207] A. C. Twitchett, R. E. Dunin-Borkowski, and P. A. Midgley. "Quantitative Electron Holography of Biased Semiconductor Devices". In: *Physical Review Letters* 88.23 (May 24, 2002). DOI: 10.1103/PhysRevLett.88.238302.

[208] Rafael Ballabriga, Michael Campbell, and Xavier Llopart. "Asic developments for radiation imaging applications: The medipix and timepix family". In: *Nuclear Instruments and Methods in Physics Research Section A: Accelerators, Spectrometers, Detectors and Associated Equipment* 878 (Jan. 2018), pp. 10–23. DOI: 10.1016/j.nima.2017.07.029.

[209] Takashi Yamamoto. "Assignment of pre-edge peaks in K-edge x-ray absorption spectra of 3d transition metal compounds: electric dipole or quadrupole?" In: *X-Ray Spectrometry* 37.6 (Nov. 2008), pp. 572–584. DOI: 10.1002/xrs.1103.

[210] K.-W. Lee et al. "Disproportionation, Metal-Insulator Transition, and Critical Interaction Strength in Na1/2CoO2". In: *Physical Review Letters* 94.2 (Jan. 18, 2005). DOI: 10.1103/PhysRevLett.94.026403.

[211] W. Kohn and L. J. Sham. "Self-Consistent Equations Including Exchange and Correlation Effects". In: *Physical Review* 140.4 (Nov. 15, 1965), A1133–A1138. DOI: 10.1103/PhysRev.140.A1133.

[212] P. Hohenberg and W. Kohn. "Inhomogeneous Electron Gas". In: *Physical Review* 136.3 (Nov. 9, 1964), B864–B871. DOI: 10.1103/PhysRev.136.B864.

[213] Paolo Giannozzi et al. "QUANTUM ESPRESSO: a modular and open-source software project for quantum simulations of materials". In: *Journal of Physics: Condensed Matter* 21.39 (Sept. 30, 2009), p. 395502. DOI: 10.1088/0953-8984/21/39/395502.

[214] Andrea Dal Corso. "Pseudopotentials periodic table: From H to Pu". In: *Computational Materials Science* 95 (Dec. 2014), pp. 337–350. DOI: 10.1016/j.commatsci.2014.07.043.

[215] John P. Perdew, Kieron Burke, and Matthias Ernzerhof. "Generalized Gradient Approximation Made Simple". In: *Physical Review Letters* 77.18 (Oct. 28, 1996), pp. 3865–3868. DOI: 10.1103/PhysRevLett.77.3865.

[216] U von Barth and L Hedin. "A local exchange-correlation potential for the spin polarized case. i". In: *Journal of Physics C: Solid State Physics* 5.13 (July 10, 1972), pp. 1629–1642. DOI: 10.1088/0022-3719/5/13/012.

[217] John P. Perdew et al. "Restoring the Density-Gradient Expansion for Exchange in Solids and Surfaces". In: *Physical Review Letters* 100.13 (Apr. 4, 2008). DOI: 10.1103/PhysRevLett.100.136406.

[218] Matteo Cococcioni and Stefano de Gironcoli. "A linear response approach to the calculation of the effective interaction parameters in the LDA+U method". In: *Physical Review B* 71.3 (Jan. 18, 2005), p. 035105. DOI: 10.1103/PhysRevB.71.035105. arXiv: cond-mat/0405160.

[219] A. I. Liechtenstein, V. I. Anisimov, and J. Zaanen. "Density-functional theory and strong interactions: Orbital ordering in Mott-Hubbard insulators". In: *Physical Review B* 52.8 (Aug. 15, 1995), R5467–R5470. DOI: 10.1103/PhysRevB.52.R5467.

[220] Pio Baettig, Claude Ederer, and Nicola A. Spaldin. "First principles study of the multiferroics Bi Fe O 3 , Bi 2 Fe Cr O 6 , and Bi Cr O 3 : Structure, polarization, and magnetic ordering temperature". In: *Physical Review B* 72.21 (Dec. 6, 2005). DOI: 10.1103/PhysRevB.72.214105.

[221] Jayhoon Chung and Lew Rabenberg. "Effects of strain gradients on strain measurements using geometrical phase analysis in the transmission electron microscope". In: *Ultramicroscopy* 108.12 (Nov. 2008), pp. 1595–1602. DOI: 10.1016/j.ultramic.2008.05.010.

université PARIS-SACLAY

ÉCOLE DOCTORALE
Physique en Île-de-France (EDPIF)

Titre : Vers un semi-conducteur magnétique utilisant des couches minces de grenat de fer de bismuth co-substitué au Ca et à l'Y

Mots clés : oxydes fonctionnels, microscopie électronique en transmission, dichroïsme circulaire magnétique, semi-conducteur magnétique, spectroscopie de perte d'énergie des électrons, grenat de bismuth fer

Résumé : Ce travail s'inscrit dans le domaine des oxydes multifonctionnels pour l'électronique "tout-oxyde" afin de développer un matériau semi-conducteur magnétique combinant à la fois des porteurs de charge et un ordre magnétique. Le couplage de ces deux propriétés à 300 K est un enjeu majeur qui permettrait de contrôler le magnétisme par un champ électrique ou les porteurs de charge par un champ magnétique. De nombreux travaux ont été réalisés sur le dopage de semi-conducteurs classiques comme GaAs (DMS) ou des oxydes semi-conducteurs comme ZnO (DMO) par des cations magnétiques 3d. Pour les DMS, le couplage entre les propriétés électriques et magnétiques n'est présent que jusqu'à 190 K. Tandis qu'une température de Curie (T_C) de 900 K est atteinte pour les DMO sans toutefois présenter de couplage avec les propriétés électriques.

Dans cette thèse, l'approche inverse a été appliquée où des cations aliovalents et/ou isovalents sont substitués au sein d'un oxyde magnétique isolant afin d'induire des porteurs de charge. Le grenat de bismuth fer (BIG) présente des propriétés remarquables dont la rotation Faraday géante induite par la présence de Bi, un couplage magnéto-électrique à 300K et une T_C de 660 K résultant du couplage ferrimagnétique entre les sous-réseaux tétraèdriques et octaèdriques de fer. Des calculs théoriques montrent que la structure électronique du BIG favoriserait un transport électronique polarisé en spin.

La croissance de grenats de fer riche en Bi ne pouvant pas être réalisée sous forme de monocristaux massifs, des films de BIG co-dopés à l'Y (0.2 à 0.5 Y par formule unitaire) et au Ca (0 à 0.3 Ca par formule unitaire) sur le site du Bi ont été synthétisés par dépôt laser pulsé sur un substrat isostructural. Le Ca^{2+} tend à induire la formation de $Fe^{3+/4+}$ et une conduction de type p alors que le co-dopage d'Y^{3+} permet de maintenir constante la concentration de Bi (2.5 par formule unitaire) préservant la rotation Faraday géante.

Les films présentent une phase grenat majoritaire bien cristallisée et epitaxiée. Une phase minoritaire d'hématite faiblement cristallisée et texturée est aussi présente sans toutefois former de chemin de percolation. Cette phase n'est pas détectable par diffraction des rayons X et n'altère pas les propriétés physiques des films. La distribution des dopants et des charges au sein de ces films a été étudiée notamment par microscopie électronique (Cs-STEM) et spectroscopie de pertes d'énergie des électrons (EELS) jusqu'à l'échelle atomique. Le Ca et l'Y se substituent dans la maille de grenat sans former d'agrégats. Les films présentent une sous-stoechiométrie en oxygène s'ajustant à l'aide de recuits sous atmosphère contrôlée tout en conservant leurs propriétés structurales et microstructurales. Ces grenats co-dopés au Ca et à l'Y présentent un comportement semi-conducteur de type p ($\rho(450K) = 3 \times 10^4\ \Omega\ cm$) tandis que le BIG dopé uniquement à l'Y révèle un comportement semi-conducteur de type n ($\rho(450K) = 1 \times 10^1\ \Omega\ cm$); ce qui est dix ordres de grandeur inférieur au grenat d'yttrium fer. En outre, les films de type n montrent un changement de résistivité réversible de trois ordres de grandeur lors de recuits sous atmosphère inerte ou oxydante. La présence de Fe^{4+} au sein des films de type p n'a pas pu être mise en évidence ni par EELS ni par spectroscopie d'absorption des rayons X ; les porteurs de type p sont à priori compensés par des lacunes d'oxygène. Les films de type n présentent une concentration de porteurs correspondant à 12% de Fe^{2+} principalement localisés sur les sites tétraédriques du fer. Les films conservent une rotation Faraday géante ainsi qu'une $T_C > 590$ K.

La présence simultanée d'un comportement semi-conducteur de type p ou n, d'une $T_C > 600$ K, d'une rotation Faraday géante ainsi que des calculs indiquant la polarisation en spin du haut de la bande de valence font de ces phases de BIG co-dopés à l'Y et au Ca des candidats prometteurs en tant que semi-conducteur magnétique.

Title : Towards a magnetic semiconductor using Ca and Y co-substituted bismuth iron garnet thin films

Keywords : functional oxides, transmission electron microscopy, magnetic circular dichroism, magnetic semiconductor, electron energy-loss spectroscopy, bismuth iron garnet

Abstract : This work belongs to the field of multifunctional oxides for "all-oxide" electronics in order to develop a magnetic semiconductor i.e. combining the presence of both charge carriers and a magnetic order. The coupling of these two properties at 300 K is a major challenge that would allow the control of magnetism by an electric field or the control of charge carriers by a magnetic field. Many works were carried out on the doping of conventional semiconductors such as GaAs (DMS) or semiconductor oxides such as ZnO (DMO) by 3d magnetic cations. For DMS, the coupling between the electrical and magnetic properties is only present up to 190 K. While a Curie temperature (T_C) of 900 K is achieved for DMOs without however presenting a coupling with the electrical properties.

In this thesis, the inverse approach was applied by substituting aliovalent and/or isovalent cations within an insulating magnetic oxide in order to induce charge carriers. Bismuth iron garnet (BIG) has remarkable properties including the giant Faraday rotation induced by the presence of Bi, a magneto-electric coupling at 300K and a T_C of 660 K resulting from the ferrimagnetic coupling between the tetrahedral and octahedral iron sublattices. Theoretical calculations show that the electronic structure of BIG would favor a spin-polarized electronic transport.

The growth of Bi-rich iron garnets cannot be obtained in the form of bulk single crystals. Thus, BIG films co-substituted with Y (0.2 to 0.5 Y per formula unit) and Ca (0 to 0.3 Ca per formula unit) on the Bi site have been synthesized by pulsed laser deposition on an isostructural substrate. The Ca^{2+} tends to induce the formation of $Fe^{3+/4+}$ and a p-type conduction while the co-substitution of Y^{3+} allows to keep the concentration of Bi (2.5 per formula unit) preserving the giant Faraday rotation.

The films are mostly composed of a well crystallised and epitaxial garnet phase. A minor secondary phase of weakly crystallized and textured hematite is also present but does not form a percolation path. This phase is not detectable by X-ray diffraction and does not alter the physical properties of the films. The distribution of dopants and charges within these films was studied notably by electron microscopy (Cs-STEM) and electron energy loss spectroscopy (EELS) down to the atomic scale. Ca and Y substitute within the garnet lattice without forming aggregates. The oxygen stoichiometry of the films can be adjusted by means of controlled atmosphere annealing while maintaining their structural and microstructural properties. These Ca and Y co-substituted garnets have a p-type semiconductor behaviour ($\rho(450K) = 3 \times 10^4\ \Omega\ cm$) while the Y-only substituted BIG exhibits a n-type semiconductor behavior ($\rho(450K) = 1 \times 10^1\ \Omega\ cm$); this resistivity is ten orders of magntitude lower than that of yttrium iron garnet. In addition, n-type films exhibit a reversible resistivity change of three orders of magnitude upon annealing under an inert or oxidizing atmosphere. The presence of Fe^{4+} in p-type films could not be identified neither by EELS nor by X-ray absorption spectroscopy as p-type charge carriers are a priori compensated by oxygen vacancies. N-type films have a carrier concentration corresponding to 12% of Fe^{2+} mainly located on the Fe tetrahedral sites. The films conserved the giant Faraday rotation Faraday and a $T_C > 590$ K.

The simultaneous presence of either n- or p-type semiconductor behaviour, a $T_C > 600$ K, a giant Faraday rotation and calculations indicating a spin-polarization of the top of the valence band make these Y and Ca co-substituted BIG phases promising candidates as magnetic semiconductors.

Université Paris-Saclay
Espace Technologique / Immeuble Discovery
Route de l'Orme aux Merisiers RD 128 / 91190 Saint-Aubin, France